NASA. CR-122450

EVALUATION OF ACOUSTIC TESTING
TECHNIQUES FOR SPACECRAFT SYSTEMS
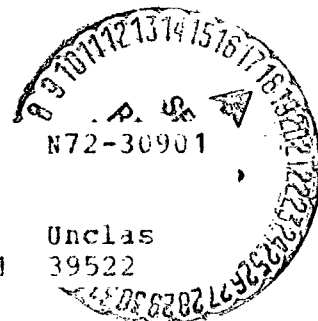
James A. Cockburn
Wyle Laboratories
7800 Governors Drive, West
Huntsville, Alabama 35807

June 1971
Final Report — WR 71-7
Contract Number: NAS 5-21203

Prepared for

NATIONAL AERONAUTICS AND SPACE ADMINISTRATION
GODDARD SPACE FLIGHT CENTER
Greenbelt, Maryland 20771

Wyle Research Staff Report
WR 71-7

EVALUATION OF ACOUSTIC TESTING
TECHNIQUES FOR SPACECRAFT SYSTEMS

June 1971

James A. Cockburn

Wyle Laboratories Research Staff
Huntsville, Alabama

ERRATA

August 1971

ERRATA

The following pages are replaced in their entirety: 101, 102, 219, 220, 237 and 238.

Page 103   **Reporting Requirements**

Item (1)d should read:

d.   Description of the use of any "Q multiplication" (i.e., enhanced
sound pressure levels through placement of local sources at wall—
floor junctions and corners) or other special techniques employed
to enhance the acoustic field.

Pages 196 and 197;   Figures 68(a) and 68(b)

The ordinates of these figures (i.e., Octave Band Sound Pressure Levels)
should be identical to Figure 19, i.e., 100 to 170 dB in 10 dB increments.

Page 216,   Lines 3 and 8

Replace   v   by   V.

Page 216   Step 3 of Procedure should read:

3.   Determine OA and ....

Page 233;   Figures 4(a) and 4(b)

The frequency bandwidth columns shown in these figures for the
purposes of curve identification should read as follows:

Figure 4(a):   150/300
                    75/150
                  300/600
                     OA
                  37.5/75

Figure 4(b):   2400/4800
                  4800/9600
                     OA
                  1200/2400
                   600/1200

The ordinate should read:

$$\text{Source Distance, } X_0/D_e$$

should read:

.... The general form of the co-power spectral density ....

$$\frac{\eta \zeta}{U_c} \quad \text{should read} \quad \frac{\omega \eta}{U_c}$$

     L.H.S. of Equation (28):

Superscript NA should be NH.

     Equation (31):

Subscript A in L.H.S. and R.H.S. should be subscript S.

     Second term in Equation (33):

Subscript A should read subscript S.

1. Report No.	2. Government Accession No.	3. Recipient's Catalog No.

4. Title and Subtitle	5. Report Date
EVALUATION OF ACOUSTIC TESTING TECHNIQUES FOR SPACECRAFT SYSTEMS	JUNE 1971
	6. Performing Organization Code COPY NO. ___ 05 .

7. Author(s)	8. Performing Organization Report No.
JAMES A.COCKBURN	WR 71-7

9. Performing Organization Name and Address	10. Work Unit No.
Wyle Laboratories — Huntsville Facility 7800 Governors Drive West Huntsville, Alabama 35807	11. Contract or Grant No. NAS5-21203
	13. Type of Report and Period Covered

12. Sponsoring Agency Name and Address	13. Type of Report and Period Covered
MR. JOSEPH P. YOUNG National Aeronautics and Space Administration Goddard Space Flight Center, Greenbelt, Md. 20771	FINAL REPORT March 1970 - February 1971
	14. Sponsoring Agency Code

15. Supplementary Notes

16. Abstract

External acoustic environments, structural responses, noise reductions, and the internal acoustic environments have been predicted for a typical shroud/spacecraft system during lift-off and various critical stages of flight. Spacecraft responses caused by energy transmission from the shroud via mechanical and acoustic paths have been compared and the importance of the mechanical path has been evaluated. Theoretical predictions have been compared extensively with available laboratory and in-flight measurements. Equivalent laboratory acoustic fields for simulation of shroud response during the various phases of flight have been derived and compared in detail. Techniques for varying the time-space correlations of laboratory acoustic fields have been examined, together with methods for varying the time and spatial distribution of acoustic amplitudes. Possible acoustic testing configurations for shroud/spacecraft systems have been suggested and trade-off considerations have been reviewed. The problem of simulating the acoustic environments versus simulating the structural responses has been considered and techniques for testing without the shroud installed have been discussed.

17. Key Words	18. Distribution Statement
Testing techniques — Acoustic Environments — Shroud — Spacecraft — Noise Reduction	Availability is unlimited. Document may be released to the Clearinghouse for Federal Scientific and Technical Information, Springfield, Virginia 22151, for sale to the public.

19. Security Classif. (of this report)	20. Security Classif. (of this page)	21. No. of Pages	22. Price
Unclassified	Unclassified	339	$3.00

PREFACE

The purpose of the study described in this report was to evaluate the effectiveness and technical basis of laboratory acoustic testing techniques for shroud/spacecraft systems. The external acoustic environments, structural responses, noise reductions and the internal acoustic environments were determined for a typical shroud/spacecraft system during lift-off and during various phases of flight. Spacecraft responses caused by energy transmission from the shroud via mechanical and acoustic paths were compared and the importance of the mechanical path was evaluated. The problem of simulating the acoustic environments versus simulating the structural responses was considered and techniques for testing with and without the shroud installed were reviewed.

Techniques for the prediction of the acoustic environment surrounding shroud/spacecraft systems during lift-off have been presented, and the results are generally in good agreement with measured data. The aerodynamic environments were found to be extremely complex at transonic Mach numbers, involving regions exposed to separated flow, shock-wave oscillation and thickened boundary layers. The most significant internal noise levels were found to occur during lift-off, and internal sound pressure levels generally decreased with increasing flight Mach number over the range $M=0.7$ to $M=2.0$. Relatively poor agreement has been observed between predicted and measured noise reductions, pointing up the fact that space-averaging of the internal acoustic field is a critical factor in establishing noise reduction from experimental measurements. The low-order shroud modes appear to exhibit strong coupling with the spacecraft adapter structure; this result suggests that mechanical excitation of the adapter is an essential requirement when attempting to test with the shroud removed. Because of the complexity and cost of direct simulation of in-flight acoustic environments, simulation of the shroud responses utilizing equivalent acoustic fields offers a practical alternative. Recommendations for further study include limited laboratory investigations of (a) noise reduction of model-scale shrouds utilizing different external acoustic fields, (b) the relative roles played by the mechanical and acoustic transmission paths for a range of acoustic environments, and (c) the relative contributions via the mechanical path for different adapter design concepts.

TABLE OF CONTENTS

v

TABLE OF CONTENTS (Continued)

TABLE OF CONTENTS (Continued)

LIST OF ILLUSTRATIONS

PRECEDING PAGE BLANK NOT FILMED

LIST OF ILLUSTRATIONS (Continued)

LIST OF ILLUSTRATIONS (Continued)

LIST OF ILLUSTRATIONS (Continued)

LIST OF ILLUSTRATIONS (Concluded)

1.0 INTRODUCTION

The random vibration environment in shroud/spacecraft systems results directly from external pressure fluctuations. During launch and low speed flight these fluctuations are caused by acoustic noise radiated from the propulsion systems, whereas during the higher speed portions of flight the pressure fluctuations are generated by unsteady aerodynamic flows over the vehicle. The acoustic environment at lift-off results primarily from the noise field produced by the rocket exhaust flows. The actual characteristics of this environment depend on the size of the rocket engines, the deflector configuration, and the distance between the spacecraft shroud and the base of the vehicle. During the transonic flight phase, shock waves generated at various points on the vehicle move towards the nose, prior to their eventual stabilization in supersonic flight. In addition to their gross motion, the shocks may oscillate and be coupled with, or supplemented by, possible severe buffeting. The magnitudes of these external pressure fluctuations are highly dependent on vehicle geometry. Examination of flight vehicle records obtained during this flight regime typically show transient vibration response. When the vehicle accelerates through the maximum dynamic pressure flight phase, the excitation results primarily from turbulent fluctuations in the aerodynamic flow over the spacecraft shroud.

These pressure fluctuations excite the external shroud and vehicle structure and are transmitted to the spacecraft through two distinct paths; an air path and a mechanical path. The air path is simply that air space between the inside surface of the shroud and the spacecraft. The mechanical path is that connection between the base of the shroud and the adapter, which is in turn connected to the base of the spacecraft. In addition to the vibration environment resulting from noise impinging directly on the shroud, there are some additional low frequency vibration components resulting from acoustic excitation of the basic modes of the entire launch vehicle. This vibration is transmitted to the spacecraft via the vehicle structure and adapter.

Because of the differences in these acoustic environments, their often localized nature, and the complicated way in which the spacecraft, the shroud, and the launch vehicle interact, it follows that realistic acoustic testing of shroud/spacecraft systems in the laboratory is fraught with difficulties. Simulation of the in-flight acoustic environment is not, of course, always a realistic proposition in view of the facility costs, power requirements and space-time correlation properties of the environments to be simulated. Thus a simulation based upon duplicating structural responses of the shroud often becomes a necessary alternative to be considered. Ideal shroud response simulation also implies simulation of the boundary conditions and a portion of the vehicle structure below the shroud-launch vehicle connection plane. Acoustic testing is further complicated by any requirement to remove the shroud; it is often convenient to remove the shroud in order to reduce the acoustic power output from the facility or to excite the spacecraft with a specific type of acoustic field. Removal of the shroud effectively eliminates the mechanical path by which shroud vibrations are transmitted to the spacecraft.

1

The purpose of the study described in this report was to evaluate the effectiveness and technical basis of laboratory acoustic testing techniques for shroud/spacecraft systems. The specific objectives of this study were as follows:

o   To establish the acoustic field characteristics external to and within the spacecraft shroud for all significant flight events.

o   To determine the essential characteristics of these noise fields which must be simulated in the laboratory, based upon their effects on structural response and noise reductions.

●   To evaluate the importance of simulating the atmospheric pressure environment.

o   To evaluate the influence of boundary conditions and adjacent structure on the structural response and the interior acoustic field within the shroud.

o   To investigate variations in time-space correlation functions that can be attained in a laboratory within reasonable levels of effort and expense.

o   To investigate the influence of test article volume relative to reverberant room volume on the acoustic field characteristics.

o   To evaluate the option of true simulation of the noise fields versus simulation of the responses by adjusting the laboratory acoustic field.

o   To evaluate the feasibility and possible techniques for testing the spacecraft with the shroud removed.

o   To develop an acoustic test specification format to ensure consistency between accustic tests performed in different facilities.

A comprehensive review of the general characteristics of shroud/spacecraft systems and their free vibration behavior is presented in Section 2.0. This includes a discussion of shroud mode shapes and resonant frequencies, structural coupling of the shroud and space- craft, the effects of differential pressure and a vacuum environment, and structural and acoustic radiation damping effects.

Theoretical techniques for predicting the lift-off and in-flight acoustic environments, the structural responses of the shroud, and the shroud noise reductions are summarized in Section 3.0. This is followed by a detailed presentation of theoretical and experimental results in Section 4.0. Predicted external acoustic environments, shroud responses, and internal acoustic environments for a typical shroud/spacecraft system during lift-off and various

2

critical stages of flight are presented. Spacecraft responses due to energy transmission from the shroud via mechanical and acoustic paths are examined and the importance of the mechanical transmission path is evaluated in detail. Theoretical predictions of the acoustic environments, the structural responses, and the shroud noise reductions are compared extensively with available laboratory and in-flight measurements. Equivalent laboratory acoustic fields are derived from the theoretical results to provide acoustic simulation techniques based upon identical laboratory and in-flight shroud responses.

A comprehensive review of acoustic testing technology is presented in Section 5.0. This discussion includes a review of time-space correlations which can be achieved in the laboratory, together with techniques for varying time and spatial distribution of the acoustic amplitudes. Various acoustic testing configurations for shroud/spacecraft systems are examined and trade-off considerations are reviewed. The effects of reverberation room dimensions on the lowest test frequency and the volume occupied by the test specimen relative to the room volume are discussed. Simulation of the acoustic environment versus simulation of the structural responses is examined in detail and techniques for testing without the shroud are reviewed. A test specification format, to ensure consistency of acoustic testing, together with suitable tolerances, is also outlined in this section.

Finally, in Section 6.0, each of the specific objectives listed above is discussed in turn, and the conclusions resulting from this study are presented. Recommendations for further work are discussed in Section 7.0.

3

2.0 SHROUD/SPACECRAFT SYSTEMS

2.1 General Characteristics of Shroud/Spacecraft Systems

Shroud/Spacecraft Systems can be divided into several basic categories according to the physical size and weight of the spacecraft, and the particular launch vehicle employed. Typical overall dimensions for a range of shroud designs are illustrated in Figure 1. The smaller shrouds such as the Delta bulbous or Agena short shroud, house communications satellites, while the larger shrouds, such as the 50 ft Titan shroud, are intended for multiple payload applications. The principal functions of the shroud are to: (a) provide an aerodynamically "clean" shape around the spacecraft, (b) protect the spacecraft from aerodynamic loads, acoustic loads and thermal loads, and (c) provide a contamination-free environment for the spacecraft.

The spacecraft are generally attached to the vehicle structure through single or multiple adapters. The adapter may be in the form of a truss or may be a short cylindrical section. In either case the adapter is rigidly connected to the final stage of the launch vehicle, while the upper edge of the adapter (i.e., the adapter-spacecraft interface) is provided with some form of separable connection. The spacecraft shroud normally extends below the separable connection to the final stage of the vehicle and is usually connected rigidly to either the adapter-vehicle stage interface ring or some portion of the final vehicle stage below this interface ring. A typical shroud/spacecraft system is shown in Figures 2 and 3 for the Surveyor spacecraft and Atlas/Centaur launch vehicle. These figures illustrate the cylindrical payload adapter concept, where the lower edge of the shroud is well removed from the spacecraft-adapter interface. The simple truss adapter concept is illustrated in Figure 4 for the OGO spacecraft—Atlas/Agena B launch vehicle combination. This figure shows the lower edge of the shroud connected through an interface ring directly to the spacecraft truss; in this design the lower edge of the shroud is closer to the spacecraft—adapter interface.

    2.1.1 Classification of Shroud Structures — In spite of the variations in the size of shrouds, the materials employed in their construction are generally confined to magnesium, aluminum and fiberglas; similarly the constructional details fall into two general classes, i.e., unstiffened sheet construction and rib-stiffened sheet construction. A comprehensive literature survey was conducted to define the properties of typical shroud and spacecraft structures (References 1-4). A sufficiently wide range of shroud structures was investigated to enable definition of the parameter ranges encountered in practice. Properties which were investigated included; overall diameter and length, materials, type of construction,

4

skin thickness, stiffener properties and total weight. From a knowledge of these properties, the surface weight densities and orthotropic (or isotropic) bending stiffnesses were estimated.

A summary of typical shroud properties is shown in Table I, where each shroud is defined in terms of its overall dimensions, skin thickness, surface weight, orthotropic bending stiffnesses, and extensional stiffness. In the following paragraphs, a number of the shrouds identified in Table I are discussed in greater detail.

Mariner D Shroud

The Mariner D shroud consists of a magnesium cone-cylinder body with a beryllium nose cap. The lengths of thé cylindrical and conical sections are 88 inches and 65 inches respectively, and the nose cap radius is 12 inches. The cylindrical and conical sections are stiffened by magnesium L-section ring frames. Overall length and diameter are 165 inches and 60 inches respectively, the skin thickness is 0.08 inch and the total weight is approximately 160 pounds. The surface weight density of the shroud has been calculated to be approximately 0.006 lb/in² and the circumferential and longitudinal bending stiffnesses in the cylindrical section are 3.64×10^4 lb in. and 305 lb in., respectively.

Delta Low Drag Shroud

The Delta Low Drag shroud consists of a fiberglas cone-cylinder body stiffened in the cylindrical section by aluminum ring frames. The lengths of the cylindrical and conical sections are 78 inches and 39 inches respectively, and the nose radius is approximately 7 inches. Overall length and diameter are 124 inches and 33 inches respectively, the average skin thickness is 0.17 inch and the total weight is 154 pounds. The cone angle is 15 degrees and the surface weight density has been computed to be approximately 0.0135 lb/in² . The circumferential and longitudinal bending stiffnesses in the cylindrical section have been computed to be approximately 1.66×10^3 lb in. (The shell has been assumed to be isotropic since there are only two ring frames in the cylindrical portion of the shroud).

Agena Long (or Nimbus) Shroud

The Nimbus shroud consists of a fiberglas cone-cylinder body stiffened in both the conical and cylindrical sections by aluminum ring frames. The lengths of the cylindrical and conical portions are 130 inches and 81 inches respectively, and the nose radius is approximately 12 inches. Overall length and diameter are 224 inches and 65 inches respectively, and the average skin thickness varies between 0.1 and 0.14 inch in the cylindrical section and is 0.14 inch in the conical section. The total shroud weight is approximately 535 pounds, the cone angle is 15 degrees and the surface weight density has been computed to be approximately 0.012 lb/in² in the cylindrical portion. The equivalent circumferential and longitudinal bending stiffnesses for the cylindrical portion have been computed to be approximately 1.04×10^6 lb in. and 9.3×10^2 lb in. respectively. The conical portion can be replaced for the purposes of structural analysis

5

TABLE I

TYPICAL SHROUD CONFIGURATIONS

Representative Payloads	Launch Vehicle	Shroud Properties						
		Shroud Geometry	Length of Cylindrical Section in.	Skin Thickness $\frac{1}{2}$	Surface Weight Density lb/in². $\frac{1}{2}$	Circumferential Bending Stiffness lb in. $\frac{1}{2}$	Longitudinal Bending Stiffness lb in. *	In-Plane Extensional Stiffness lb/in. $\frac{1}{2}$
o Mariner D	Atlas/ Agena B	Mariner D Shroud: Cone-cylinder 60 in. diameter x 165 in. long. Magnesium skin with ring stiffeners - 160 lb weight	88	0.08 / 0.08	0.006 / 0.006	3.64×10^4 / 3.9×10^4	3.05×10^2	5.2×10^5*
o Echo • Relay o SYNCOM	Delta	Delta Low Drag Shroud. Cone-Cylinder 33 in. diameter x 124 in. long. Fiberglas skin with aluminum ring stiffeners - 154 lb wt.	78	0.17 / 0.17	0.0136 / 0.0136	1.66×10^3 / 1.66×10^3	1.66×10^3	6.3×10^5*
o Nimbus o EOGO • AOSO o OGO	Atlas/ Agena B	Agena Long (or Nimbus) Shroud: Cone-Cylinder, 65 in. diameter x 228 in. long. Fiberglas skin with aluminum ring stiffeners - 535 lb wt.	130	0.14 / 0.14	0.012 / 0.0131	1.04×10^6 / 6.33×10^5	9.3×10^2	5.18×10^5*
o Lunar Module	Saturn V	Spacecraft Lunar Adapter: Conical Frustum 260 in. diameter tapering to 155 in. diameter x 336 in. long. (349 in. slant height). Aluminum honeycomb - unstiffened - 3070 lb wt.	--	1.7	0.0139	3.24×10^5	3.24×10^5	4.7×10^5
o Oscar o Vela	Titan 3A and C	Fiberglas Honeycomb Shroud: Cone-cylinder 120 in. diameter x 216 in. long. - unstiffened honeycomb fiberglas - 688 lb wt.	30	1.0(nom) / 1.0(nom)	0.0127	1.65×10^5	1.65×10^5	--
o IDCSP o Comsats	Titan 3	Standard Aluminum Titan Shroud: Cone-cylinder 120 in. diameter x 216 in. long. Aluminum skin with ring and stringer stiffeners - 919 lb wt.	30	0.063 / 0.075	0.0169	5.56×10^5	4.72×10^5	6.3×10^5 / 7.5×10^5
o MOL o Multiple Payloads	Titan 3	Large Titan Shroud: Cone-cylinder 120 in. diameter x 600 in. long. Aluminum skin with ring and stringer stiffeners - 2260 lb wt.	492	0.025-0.07 / 0.08-0.09	0.01025	2.73×10^5	4.72×10^5	2.5×10^5 / 8.5×10^5
o OAO	Atlas/ Agena D	OAO Shroud: Cone-cylinder 120 in. diameter x 347 in. long. Unstiffened honeycomb fiberglas - 860 lb wt.	153	1.82 / 1.835	0.0084 / 0.0084	3.16×10^5 / 3.16×10^5	3.16×10^5	2.59×10^5 / 2.96×10^5
o Surveyor	Atlas/ Centaur	Surveyor Shroud: Cone-cylinder 120 in. diameter x 264 in. long. Unstiffened honeycomb fiberglas.	72	1.75(nom) / 1.75(nom)	0.0084 / 0.0084	3.16×10^5 / 3.16×10^5	3.16×10^5	2.59×10^5 / 2.96×10^5

Note: 1   Cylindrical Section
        2   Conical Section
        *   Same in both Cylindrical and Conical Sections

by an equivalent cylindrical shell 47 in. diameter and 72 in. long. The surface weight density for this equivalent shell is approximately 0.0131 lb/in² and the equivalent circumferential and longitudinal bending stiffnesses have been computed to be approximately 6.33×10^5 lb in. and 9.3×10^2 lb in. respectively.

Titan Fiberglas Shroud

The Titan IIIA and C fiberglas shrouds consist of a phenolic impregnated fiberglas honeycomb cone-cylinder body. The lengths of the cylindrical and conical portions are 30 inches and 171 inches respectively, and the nose cap radius is 15 inches. Overall length and diameter are 216 inches and 120 inches respectively, and the average skin thickness is 1.0 inch. The total shroud weight is approximately 688 lbs, the cone angle is 15 degrees, and the surface weight density has been computed to be approximately 0.0127 lb/in². The isotropic bending stiffness has been computed to be approximately 1.65 $\times$ 10^5 lb in.

Standard Aluminum Titan Shroud

The Standard Titan shroud consists of an aluminum cone-cylinder body having the same overall dimensions as the fiberglas Titan shroud. This shroud is stiffened circumferentially by aluminum ring frames (5 inches pitch) and longitudinally by stringers (6 inches pitch). The average skin thickness is approximately 0.05 inch in the nose region, 0.1 inch in the conical section and 0.063 inch in the cylindrical section. The total shroud weight is approximately 919 pounds and the surface weight density has been computed to be approximately 0.0169 lb/in². The circumferential and longitudinal bending stiffnesses have been computed to be approximately 5.56×10^5 lb in. and 4.72×10^5 lb in. respectively.

Large Titan Shroud

The large Titan shroud (or Universal shroud) consists of an aluminum cone-cylinder body which is stiffened longitudinally by stringers (6 inches pitch) and circumferentially by ring frames (5 inch pitch in the conical section, and 15 inch pitch in the cylindrical section). The basic shroud has standard conical and base modules, the former being 60 inches long and the latter 72 inches long. The nose cap is 48 inches in radius and the intermediate section (between the lower edge of the conical section and the upper edge of the base module) is assembled from seven separate cylindrical modules each 60 inches long. The overall length of the shroud can be varied by adding or removing these intermediate modules. The maximum length of the shroud is 50 feet, the overall diameter is 10 feet and the cone angle is approximately 10 degrees. Skin thickness varies from 0.08 to 0.09 inch in the conical section, 0.025 inch in the intermediate modules, to 0.04 to 0.07 inch in the base section. The total weight of the shroud is 2,260 pounds and the surface weight density has been computed to be approximately 0.01025 lb/in². The circumferential and longitudinal bending stiffnesses have been computed to be approximately 2.73×10^5 lb in. and 4.72×10^5 lb in., respectively.

7

OAO Shroud

The OAO shroud consists of an unstiffened honeycomb fiberglas cone-cylinder body. The lengths of the cylindrical and conical section are 153 inches and 179 inches respectively, and the nose radius is 15 inches. Overall length and diameter are 347 inches and 120 inches respectively, and the total wall thickness varies between 1.82 inches and 1.84 inches. The shroud wall consists of a 1-3/4 inch thick honeycomb core, an inner face sheet 0.03 in. thick, and an outer face sheet ranging in thickness from 0.04 in. (in the cylindrical section) to 0.06 in. (at the forward stations on the conical section). The total shroud weight is approximately 860 lb, the cone angle is 15 degrees and the surface weight density has been computed to be approximately 0.0084 lb/in^2. The circumferential and longitudinal bending stiffnesses have been calculated to be approximately 3.16×10^5 lb in..

Surveyor Shroud

The Surveyor shroud is identical to the OAO shroud described above except for the overall lengths which in this case are 72 inches in the cylindrical section and 177 inches in the conical section. Design details for the Surveyor shroud are shown in Figures 2 and 3.

   2.1.2 Spacecraft Structures — In this sub-section a number of typical spacecraft structures are discussed in order to illustrate the particular design concepts and their important structural properties from the standpoint of vibro-acoustic response.

Mariner Spacecraft

The Mariner spacecraft is mounted on two cylindrical adapters that constitute the structural interface between the spacecraft and the launch vehicle. The primary structure or "bus" forms the structural core of the spacecraft, providing support for the other sub-systems. It consists of two octagonal rings approximately 55 inches in diameter joined at the eight corners by longerons approximately 16 inches long (Reference 5). Shear plates are attached to seven of the eight bays while the eighth bay houses the propulsion system.

A truss-type structure inside the bus supports the planetary scan platform, which is latched to the lower octagon ring during launch. Four solar panels, hinged at the upper octagon ring, are coupled together through spring-dampers at their tips during launch, forming a box-like structure. A parabolic reflector approximately 36 inches in diameter is mounted on a truss-type superstructure which is also attached to the upper ring of the bus. The total spacecraft weight is approximately 830 pounds, while the combined weight of the two adapter assemblies is about 85 pounds.

Each solar panel has a rectangular platform with an 84 inch span and a 35 inch chord. The panels are of lightweight construction (approximately 0.6 lb/ft^2) and the main load carrying structure consists of two hat-section spars, cross-braced and joined by inter-costals. The 0.005 inch face sheet, which supports solar cells, is bonded to a corrugated

backing which is constructed from 0.005 inch sheet formed to a depth of about 0.5 inch. This assembly, or "substrate," is bonded to the spars which are hinged to the bus through fittings at their inboard ends.

The lower order modes of vibration of these solar panels all involve bending or twisting of the hat-section stiffeners and occur in the frequency range of from 20 Hz to 100 Hz (Reference 5). Vibrations in the higher order modes, which are most likely to be caused by the acoustic field within a given shroud, will involve small panel segments bounded by the stiffeners. For this particular case, the panel will undergo in-plane bending and a typical panel size will be about 28 inches by 22 inches.

Orbiting Geophysical Observatory (OGO Spacecraft)

The main body of the OGO spacecraft is a box-like structure approximately 3 feet by 3 feet square and 6 feet long with projecting panels, antennas and experiments. The box is constructed from corrugated aluminum sandwich built up from three sheets (two panels plus the core) each 0.016 inch thick (Reference 6). Four longerons in the corners of the spacecraft box, together with the side panels, form the basic load carrying members. The spacecraft is mounted on a truss-type adapter which is in turn rigidly connected to the interface ring attached to the launch vehicle, in the manner shown in Figure 4.

Orbiting Astronomical Observatory (OAO Spacecraft)

The external design of the OAO spacecraft consists of an octagonal shaped box which is approximately 80 inches across the flats and 120 inches long. The structural framework consists of eight rectangular cross-braced trusses radiating from a cylindrical core, and attached to a base ring with clamp points for joining the spacecraft to the second stage of the launch vehicle. Trusses, rings and core are connected together and stiffened by beams and panels, and capped at each end by a sheet bulkhead to form a hollow center octagonal prism. Each of the eight bays between the trusses is sub-divided into six compartments such that typical external panel dimensions are 20 inches along the longitudinal axis of the spacecraft and 40 inches along a direction at right angles to this axis. All primary structure is aluminum, and the solar panels are approximately 60 inches square in planform.

2.2 Free Vibration Characteristics

2.2.1 Conical Shell Behavior — Since the majority of payload shrouds consist of cone-cylinder bodies, methods of predicting the vibration behavior of conical shells were investigated. For subsequent analytical predictions of the structural response and noise reduction of shrouds utilizing the modal analysis, it is first necessary to compute the resonant frequencies and the "joint acceptances" of the structural modes for the particular fluctuating pressure environment. The joint acceptance, which is a measure of the efficiency with which the fluctuating pressures couple with and excite a particular structural mode, is usually derived by integrating the product of a narrow-band space correlation coefficient and the functional form for the mode shapes of the structure. However, a

9

review of the literature concerning the vibration behavior of conical shells (Reference 7) has indicated that due to the difficulty of analytical treatment of the problem, most investigators have either employed energy methods with simple assumed mode shape functions or have resorted to numerical integration techniques. To obtain sufficient accuracy in the prediction of mode shapes and resonant frequencies, considerable computational effort is required, and in addition, five or more terms of an infinite series expansion for the mode shapes must be reatined.

Since the use of such complicated mode shapes leads to difficulty in deriving closed-form expressions for the joint acceptances of a conical shroud structure to random fluctuating pressures, the concept of the "equivalent" cylindrical shell becomes a practical alternative. The equivalent cylindrical shell (having a length equal to the slant height of the conical frustum and a radius equal to the mean radius) will exhibit substantially the same resonant frequencies as the conical shell for the low order modes up to a circumferential wave number of about $n = 6$, but above this wave number the predicted frequencies will be greater than those for the actual conical sheli, the error increasing with increasing circumferential mode number and semi-vertex angle. Watkins and Clary (Reference 8) have examined experimentally the frequencies of a fixed-free conical frustum and compared their results with the "equivalent" cylinder theory. These results confirmed the divergence between theory and experiment as the number of circumferential waves was increased beyond $n = 6$. They also observed that at higher frequencies there were a greater number of circumferential waves at the major diameter than at the minor diameter. This difference in the number of waves increased with increasing conicity.

More recent experimental work by Miller and Hart (Reference 9) is shown in Figure 5. Also shown in the figure are theoretical curves derived from a closed-form expression for the resonant frequencies of a conical frustum, proposed by Miller and Hart. The results obtained from the "equivalent" cylinder theory are also shown in the figure for the purposes of comparison. For the particular conical frustum geometry indicated in this figure, the results derived from equivalent cylinder theory are seen to be in good agreement with the experimental results.

The errors introduced by the equivalent cylinder assumption become much less important when considering the power spectral density of the response of the shroud to fluctuating pressure fields, since this response is obtained by super-position of the responses of a large number of normal modes. This is especially true at higher frequencies where the structural modal density is high.

2.2.2 Shroud Mode Shapes and Resonant Frequencies

2.2.2.1 Mode Shapes and Resonant Frequencies of Flat Plates — When certain portions of the shroud structure are subjected to separated flows or oscillating shock waves, it is convenient to be able to predict the acceleration power spectral density of the localized structural region which is affected. For such special cases, the local structure can be idealized to a flat plate.

The mode shape for the (m n) mode of a simply supported flat plate is given by:

10

$$\phi_{mn}(\bar{x}, \bar{y}) = \sin m\pi\bar{x} \cdot \sin n\pi\bar{y} \tag{1}$$

where

m	$=$	number of elastic half-waves in the x-direction
n	$=$	number of elastic half-waves in the y-direction
$\bar{x}$	$=$	$\dfrac{x}{L_x}$
$\bar{y}$	$=$	$\dfrac{y}{L_y}$
L_x	$=$	panel length
L_y	$=$	panel width

The resonant frequencies of a simply supported flat isotropic plate are determined from the relation:

$$\omega_{mn} = \pi^2 \cdot \left[\frac{D}{\mu}\right]^{\frac{1}{2}} \left[\left(\frac{m}{L_x}\right)^2 + \left(\frac{n}{L_y}\right)^2\right] \tag{2}$$

For an orthotropic flat plate, the resonant frequency equation can be derived from plate theory (Reference 10) as follows:

$$\omega_{mn} = \frac{\pi^2}{\sqrt{\mu}} \left[D_x\left(\frac{m}{L_x}\right)^4 + 2H\left(\frac{m}{L_x}\right)^2\left(\frac{n}{L_y}\right)^2 + D_y\left(\frac{n}{L_y}\right)^4\right]^{\frac{1}{2}} \tag{3}$$

2.2.2.2 Mode Shapes and Resonant Frequencies of Cylindrical Shells -- The mode shapes and resonant frequencies of typical shroud structures can be determined with sufficient accuracy by simplifying the complex shroud structure to equivalent simply supported isotropic or orthotropic cylindrical shells. For the general case of a simply supported cylindrical shell subjected to an internal pressure, Reissner (Reference 11) and Fung, et al., (Reference 12) have shown that the resonant frequencies can be predicted from the relation:

11

$$\omega_{mn} = \frac{1}{R} \left[\frac{K_e}{\mu} \cdot \frac{\lambda_m^4}{\left(\lambda_m^2 + n^2\right)^2} + \frac{D}{\mu R^2} \left(\lambda_m^2 + n^2\right)^2 + \frac{pR}{\mu} \left(\frac{\lambda_m^2}{2} + n^2\right) \right]^{\frac{1}{2}} \quad (4)$$

where

R = radius of shell

K_e = in-plane extensional stiffness per unit length of cylinder
(= Eh for isotropic shells)

h = thickness of shell

μ = mass per unit area

λ_m = axial wave number parameter = $\dfrac{m \pi R}{L_x}$

m = number of elastic half-waves along the axis of the cylinder

L_x = axial length of cylinder

n = number of full elastic waves around the circumference of the cylinder

D = isotropic bending stiffness = $\dfrac{EI}{1-v^2}$

p = internal pressure (psig)

The first term on the righthand side of the above equation is associated with the extensional (membrane) deformations, the second term is associated with bending of the shell wall, while the third term represents the contribution from the internal pressure.

For small values of n the resonant frequency is determined largely by the first term whereas for large values of n the resonant frequency is determined largely by the second term. This phenomenon, which governs the vibratory behavior of cylindrical shells, leads to the interesting result that at higher frequencies, the vibration characteristics of the shell approach those of an equivalent flat plate, since bending deformations are significantly greater than membrane deformations.

12

To account for this behavior at high frequencies, Forsberg (Reference 13) has developed an approximate correction to the usual mathematical forms describing the vibration mode shapes. These corrected mode shapes are as follows (Reference 14):

Radial Components of Mode Shape

$$\phi_{mn1}(\bar{x}, \bar{y}) = \sin(m\pi\bar{x}) \cdot \sin(2n\pi\bar{y})$$

$$\phi_{mn2}(\bar{x}, \bar{y}) = \sin(m\pi\bar{x}) \cdot \cos(2n\pi\bar{y})$$

(5)

where

$$\bar{x} = x/L_x$$
$$\bar{y} = y/L_y$$
$$L_y = 2\pi R$$

Circumferential Components of Mode Shape

$$\psi_{mn1}(\bar{x}, \bar{y}) = \sin(m\pi\bar{x}) \qquad\qquad n = 0$$

$$= \frac{1}{n} \sin(m\pi\bar{x}) \cdot \cos(2n\pi\bar{y}) \qquad n \geq 1$$

(6)

$$\psi_{mn2}(\bar{x}, \bar{y}) = 0 \qquad\qquad n = 0$$

$$= \frac{1}{n} \sin(m\pi\bar{x}) \cdot \sin(2n\pi\bar{y}) \qquad n \geq 1$$

A single structural mode shape is denoted by the pair of functions

$$\left[\phi_{mni}(\bar{x}, \bar{y}), \ \psi_{mni}(\bar{x}, \bar{y}) \right]$$

13

where (m n i) is a triplet of integers with $i = 1$, or $i = 2$. Orthogonality between two different modes (m n i) and (r s j) is expressed by the equation:

$$\int_{x=0}^{L_x} \int_{y=0}^{L_y} \left[\phi_{mni}(x,y) \, \phi_{rsj}(x,y) + \psi_{mni}(x,y) \, \psi_{rsj}(x,y) \right] dx \, dy = 0 \quad (7)$$

if   (r s j) $\neq$ (m n i)

Equation (6) implies that the amplitudes of the circumferential deflection components approach zero as n increases. Thus, at higher frequencies only the radial deflection components are significant so that the shell characteristics approximate those of a flat plate.

This transition from shell behavior to flat plate behavior is particularly noticeable for the case of a thin cylindrical shell which is reinforced by relatively heavy ring frames and longitudinal stringers. In this case the vibratory behavior changes from overall shell deformation to deformations occuring in a single panel which is bounded by adjacent ring frames and stringers.

Between this transition from shell behavior to individual panel behavior however, an intermediate region exists which involves the motion of coupled sets of panels which in turn cause stringer bending and torsion. This intermediate frequency range, which has been discussed by Lin (Reference 15), is characterized by the grouping of sets of panels (including stringers) which are bounded by adjacent ring frames.

A similar frequency equation describes the resonances of an orthotropic (or stiffened) cylindrical shell. This can be derived approximately by expanding the second term in Equation (4) and comparing the resulting expression with that for an orthotropic flat plate (Equation 3).

Expanding the second term in Equation (4)

$$D \left(\lambda_m^2 + n^2 \right)^2 = D \lambda_m^4 + 2D \lambda_m^2 n^2 + D n^4 \quad \text{(for an isotropic shell)}$$

$$\doteqdot D_x \lambda_m^4 + 2H \lambda_m^2 n^2 + D_y n^4 \quad \text{(for an orthotropic shell)}$$

(8)

14

where

$$H = \sqrt{D_x D_y}$$

D_x = Longitudinal bending stiffness

D_y = Circumferential bending stiffness

The equivalent orthotropic bending stiffnesses are given by the equations:

$$D_x = \frac{EI_x}{1 - \nu^2} \quad \text{lb} \cdot \text{in.}$$

$$\tag{9}$$

$$D_y = \frac{EI_y}{1 - \nu^2} \quad \text{lb} \cdot \text{in.}$$

where D_x, D_y are the longitudinal and circumferential bending stiffnesses respectively and

I_x = Moment of inertia (per unit length) of the structural cross-section about the neutral axis of the skin and longitudinal stringer combination (i.e., longitudinally)

I_y = Moment of inertia (per unit length) of the structural cross-section about the neutral axis of the skin and ring frame combination (i.e., circumferentially)

ν = Poisson's ratio

E = = Modulus of elasticity

For the case of an isotropic cylindrical shell:

$$D_x = D_y = D$$

15

2.2.3 Structural Coupling of the Shroud and Spacecraft — Apart from excitation of the basic modes of the entire launch vehicle, the spacecraft vibrations are caused predominantly by the acoustic field within the shroud, and the vibratory energy transmitted mechanically from the shroud via the adapter. Additional vibratory energy is transmitted from below the shroud interface ring due to local vibration of the vehicle skin and tank structure.

For the low order translation-type modes of the shroud ($n=1$), some degree of coupling will exist between the shroud and the final vehicle stage. For higher order circumferential mode numbers however, the shroud will essentially de-couple from the final vehicle stage and will respond independently of the basic modes of the overall vehicle. Thus, the dominant coupling mechanism will be that which exists between the shroud and the interface ring and then to the adapter and the spacecraft.

Prediction of the spacecraft response to mechanical excitation transmitted from the shroud is most conveniently achieved by use of statistical energy techniques (References 16 and 17). Three power balance equations can be defined to describe the coupling between the shroud and the shroud stiffeners, the shroud stiffeners and the spacecraft adapter, and the adapter and the spacecraft. Solving these power balance equations leads to an expression for the spacecraft response in terms of (a) the shroud response to the external acoustic excitation, and (b) the physical properties, modal densities, dissipation loss factors, and coupling loss factors of the structural sub-systems.

This type of analysis has been reported by Manning (Reference 18) for a crude model of the OGO spacecraft and Nimbus shroud (consisting of a rectangular box mounted within a stiffened cylinder), and by Conticelli (Reference 19) for a cylindrical payload mounted within a baffled honeycomb cylinder. In both cases the simulated shrouds were subjected to a diffuse acoustic field.

2.2.4 The Effects of Pressure Differential and a Vacuum Environment — As a space vehicle rises through the atmosphere following launch, the external ambient pressure surrounding the vehicle is reduced. Simultaneously, venting of the interior volume within the payload shroud takes place to prevent the buildup of a pressure differential. The reduction in external atmospheric pressure has two principal effects:

o   Firstly, the time lag associated with venting of the interior volume causes a finite differential pressure across the shroud, the interior volume being at a slightly higher pressure than the external atmosphere. This pressure differential causes a shift in the resonant frequencies, which can be verified by observing the third term on the righthand side of Equation (4).

o   Secondly, as the vehicle rises through the atmosphere, the reduction in ambient pressure is accompanied by a reduction in ambient density according to the relation:

16

$$\rho = \frac{P_A}{R\,T}$$

where P_A = ambient pressure

T = ambient temperature

and R = universal gas constant $(= 1716 \text{ ft}^2/\text{sec}^2\ {}^\circ\text{R})$

This change in density therefore modifies the acoustic field within the shroud, since the noise reduction is approximately inversely proportional to ρc. However, since the speed of sound is dependent on temperature according to the relation

$$c = \sqrt{\gamma\,R\,T}$$

a constant level of external acoustic excitation would result in the approximate noise reduction versus ambient pressure relation;

$$NR \quad \alpha \quad \frac{1}{P_A}\ \sqrt{\frac{R\,T}{\gamma}} \qquad\qquad (10)$$

Hence for constant temperature and a constant level of external excitation, the increase in noise reduction would be approximately inversely proportional to ambient pressure.

Excitation of the spacecraft structure via the acoustic path would therefore be reduced; however, excitation of the spacecraft via the mechanical path would not change appreciably, except for small changes due to a reduction in the air damping of such items as solar panels. These effects have been reported by Bruck (Reference 20) for the OGO structural model and Nimbus-type shroud during combined environment testing. The results of this experimental study showed that the noise reduction increased with decreasing ambient pressure for a constant level of acoustic excitation. However, instead of an inverse proportionality between noise reduction and ambient pressure it was found that the noise reduction varied inversely with the square root of the ambient pressure. No data on the temperature or the stabilizing time of the test set-up following pressure reduction were reported.

2.2.5 Damping Effects — The sources of damping in shroud structures are predominantly in the structural joints (where ring frames or stringers are employed) and in

the adjacent air into which acoustic energy can be radiated and lost. The relative magnitude of these sources depends largely on the mode in which the structure vibrates. Additional damping is provided in the form of material damping, though for typical stiffened skin structures this is of much less significance than the other two sources. For honeycomb panels the predominant damping mechanisms are structural damping at the boundaries, acoustic radiation damping, and the material damping arising from the complex stress distribution within the cellular core and laminations of the panels.

2.2.5.1 Acoustic Damping— Theoretical expressions for the acoustic damping ratio of a simply supported or fully fixed plate vibrating in its fundamental mode have been developed by Mead (Reference 21) as follows:

$$\zeta_{ac} = \frac{0.156}{c} \frac{\rho}{\rho_m} \left(\frac{E_m}{\rho_m}\right)^{\frac{1}{2}} \left(n + \frac{1}{n}\right) \quad \text{(simply supported)}$$

$$\zeta_{ac} = \frac{0.245}{c} \frac{\rho}{\rho_m} \left(\frac{E_m}{\rho_m}\right)^{\frac{1}{2}} n \left(1 + \frac{2}{3n^2} + \frac{1}{n^4}\right)^{\frac{1}{2}} \quad \text{(fully fixed)}$$

(11)

where

c	=	speed of sound in the medium
ρ	=	density of the medium
ρ_m	=	density of the plate material
E_m	=	Young's modulus of the plate
n	=	length, breadth ratio of the plate

These equations are based upon the assumption that the wavelength of the radiated sound is large compared to the plate dimensions so that the damping pressure is constant over the plate. Meads' theory (Reference 21), which is a simplification of the work of Junger (Reference 22) predicts that the damping factor for a panel of given material vibrating in a particular mode is dependent only on the density of the surrounding medium and the dimensionless length to breadth ratio of the panel.

To extend this work to the case of a practical structure, Mead (Reference 21) considered the acoustic radiation damping of a stiffened plate vibrating in two predominant types of mode, stringer torsion modes, and stringer bending mode.

18

For a stiffened panel vibrating in an ideal stringer torsion mode, it is assumed that it can be regarded as an array of single plates with elastically restrained edges, each plate vibrating in its fundamental mode in counterphase with the adjacent plate. If the radiated sound wavelength is much greater than the individual plate width, then the acoustic damping pressure on one plate due to its own motion will be almost cancelled by the pressure from the opposing motion of the adjacent plate. Under these conditions the acoustic damping ratio will be extremely small and negligible compared to the structural damping (Reference 21).

When the same stiffened panel vibrates in the stringer bending mode however, it is suggested (Reference 21) that it can be regarded as an array of fixed edge plates all vibrating in phase with each other. Under these conditions it is assumed that the damping pressure on one individual plate due to the motion of an adjacent plate is $\sin (2\pi d/\lambda)/2\pi d/\lambda$ times the pressure on this other plate due to its own motion. The acoustic damping ratio of the whole array of panels is then approximately λ/d times that of a single fully-fixed panel, where λ = wavelength of plate vibration and d = distance between centers of adjacent plates. Meads' expression for the acoustic damping ratio of an infinitely long stiffened panel vibrating in the ideal stringer bending mode then reduces to (Reference 21):

$$\zeta_{ac} = 0.222 \left(\frac{b}{t} \right) \left(\frac{\rho}{\rho_m} \right) n, \tag{12}$$

where

t = plate thickness

b = panel width

If a second array of panels is connected along side the first array, it is suggested (Reference 21) that reinforcement of the damping pressure should occur if the two arrays vibrate in phase; alternatively, cancellation should occur if they vibrate anti-phase. During experiments with a Caravelle fuselage however, little correlation between the vibrations of adjacent panel arrays was observed, (Reference 23) and it was concluded that each panel array (between ringframes) vibrated independently.

It has been claimed (Reference 21) that the acoustic damping of stringer torsion modes is likely to be negligible compared with the structural damping, but that of the stringer bending mode may be considerably larger than the structural damping (for typical structural damping ratios of about 0.01). Acoustic damping in the intermediate modes is claimed to be at least of the same order of magnitude as the structural damping (Reference 21). However, comparison of predicted acoustic damping ratios with measured total damping ratios (where the total damping

19

is the sum of the structural and acoustic components) suggests that the simple theory proposed by Mead (Reference 21) considerably overestimates the acoustic damping ratio. From the experimental work of Clarkson and Ford (Reference 24), involving acoustic excitation of a curved skin-stringer panel, the total damping ratio in the stringer bending mode was found to be 0.008 at a frequency of 600 Hz. Using Meads simple theory (Equation 12) the calculated acoustic damping ratio for this mode is 0.02, which is a factor of 2.5 greater than the measured total damping ratio. Thus the application of this simple theory to complex structural geometries appears questionable.

Meads' original work has been extended by Mangiarotty (Reference 25) to cover the condition of a non-uniform damping pressure over the panel surface. The resulting equations for the acoustic damping coefficient are highly complex, and results have been given for the fundamental panel mode only. These results show that for the fundamental panel modes, the difference between the uniform pressure theory (Reference 21) and the non-uniform pressure theory (Reference 25) is relatively insignificant. Reinforcement or cancellation effects, due to the vibration of multiple panel structures, were not considered by Mangiarotty.

Due to the uncertainties associated with theoretical prediction of the acoustic damping ratio, and the fact that most experimental damping measurements are in terms of the total damping ratio (which automatically accounts for the acoustic radiation components), there appears to be little advantage in defining an acoustic damping coefficient for use in structural response predictions of payload shrouds. However, acoustic damping effects are likely to be very important when defining the interior acoustic field within the payload shroud, and also when subjecting the payload shroud to progressive wave testing. For the former case, Morse (Reference 26) has shown that for a three-dimensional acoustic field:

$$Q_{ac} = \frac{4 V \omega}{c \, \overline{\alpha}_n} \left[\frac{1}{S_x + \dfrac{S_R/2}{1 - (n/\pi \psi_{ns})^2}} \right] \tag{13}$$

where

V = enclosed cylindrical volume within the shroud

α_n = average normal absorption coefficient at the walls

S_x = $2\pi R$ (area of end walls)

S_R = $2\ R\ L_x$ (area of side walls)

n = radial mode number

ψ_{ns} = roots of the characteristic equation $J'_n(\overline{R}) = 0$
(tabulated in Reference 26)

20

The above equation can be approximated by:

$$Q_{ac} \approx \frac{4 V \omega}{c \, \overline{\alpha}_n \, S_R} \tag{14}$$

Further, by utilizing the approximation that $\overline{\alpha} = 2 \alpha_n$ (i.e., the random incidence absorption coefficient) the equation for acoustic damping is simplified to:

$$Q_{ac} \approx \frac{8 V \omega}{c \, a} \tag{15}$$

where

$$a = \sum_i \alpha_i \, S_i$$

the total square feet of absorption.

For the case of progressive wave testing, Bozich (Reference 27) has shown that acoustic radiation damping can be a significant factor in determining the response of the lower modes of a typical vehicle skin panel. Radiation damping in the low modes has been shown to be of significant magnitude when the ratio of panel area to duct cross sectional area approaches unity. The effects of panel area and duct cross sectional area on the acoustic damping ratios are illustrated in Figure 6 (from Reference 27). In terms of acoustic testing of shroud structures utilizing ducts, these results suggest that the low order modes (involving odd numbered axial half waves) may be subjected to relatively high acoustic damping.

2.2.5.2 Total Damping — A compilation of damping data by Rader, et al., (Reference 28) covering skin and rib construction, bonded honeycomb panels, and aircraft structural sections shows that the range of damping varies typically from a Q of 15 to a Q of 100, the honeycomb panels tending to exhibit a lower Q than the skin and rib construction. This tendency for honeycomb panels to exhibit a lower Q has also been reported by Ballentine, et al., (Reference 29) during fatigue testing of rib-stiffened and honeycomb panels; average damping (Q) in the lower panel modes varied from 15 to 38 for honeycomb panels and from 27 to 50 for rib-stiffened panels. However, most of the available damping data was obtained from single panels or multiple panel sections having fully fixed boundary conditions of the type normally utilized for fatigue testing (References 28 and 29).

During a recent study of Conticelli, et al., (Reference 30) of the impedance characteristics of stiffened cylindrical shells, an attempt was made to obtain practical damping data without the restrictions imposed by boundary conditions. The cylindrical shells were placed in the upright position on top of a foam rubber mat and impedance measurements were taken on the unstiffened portion of the shell wall, on the ring frames, on the stringers, and at the intersections of the ring frames and stringers. A definite trend toward a lower Q was observed as the number of stiffeners was increased. However for a given design, no definite trends in the variation of Q with frequency were observed; in some cases Q was found to increase with frequency while in other cases Q was found to decrease with frequency. The range of frequencies investigated varied from individual panel resonance at 50 Hz to the ring frequency of the cylinders at about 1300 Hz.

More recent damping studies utilizing a stiffened cylindrical shell have been reported in Reference 31. The damping data was deduced from free vibration decay measurements, the transducer signal being passed through a third-octave filter centered at various frequencies. These experiments have shown that average third-octave band values of Q varied from a Q of 50 for the lowest modes to a Q of 100 or greater for the highest modes of the shell. The high Q values were attributed to the low number of skin-stiffener joints and the fact that the test specimen had only a moderate degree of stiffening.

The unpredictable variation of Q with frequency is an apparent feature of the total damping exhibited by complex structures. Existing methods of predicting response to fluctuating pressure fields (References 14 and 16) normally take into account the overall Q by assuming it to be constant for all modes. Based upon a review of the available experimental measurements, this appears to be a reasonable assumption.

22

3.0 THEORETICAL TECHNIQUES FOR PREDICTING ACOUSTIC LOADS, STRUCTURAL RESPONSES AND NOISE REDUCTION

3.1 Introduction

To predict structural responses and the noise reduction for typical shroud structures, subjected to arbitrary fluctuating pressure environments, it is first necessary to define the acoustic loads acting on the external surface of the shroud. The key statistical properties necessary for a complete definition of the environment are:

    i)   The Overall Level

    ii)   The Power Spectrum

    iii) The Narrow-band Space Correlation Coefficients

Once these characteristics have been defined, the structural responses and the resulting noise reduction can be computed using modal analysis methods or statistical energy methods.

In Section 3.2, theoretical and empirical methods for predicting the essential characteristics of the various flight environments are discussed. This is followed in Section 3.3 by a discussion of the important properties (from a structural analysis view point) of laboratory acoustic environments. Finally, a summary of the analytical techniques for predicting structural responses and noise reduction is presented in Section 3.4.

3.2 Definition of Flight Environments

    3.2.1 <u>Rocket Noise</u> — The rocket noise environment is an important par. of the overall environment experienced by the vehicle and its payload. The payload/shroud system on a launch vehicle can be considered to be located in the acoustic mid-field of the rocket exhaust. The most severe a__ustic loading from the rocket noise environment occurs during lift-off. Thus the configuration of the first stage boosters as well as the deflector geometry are important parameters to be considered in determining the overall acoustic environment.

    3.2.1.1 <u>Overall Level and Power Spectrum</u> — Several precise methods of rocket noise prediction have been developed in recent years. Due to the semi-empirical nature of these methods, however, none of them is general enough to cover all situations, although each method has its own merit for its relevance to certain special conditions.

    Four different methods for rocket noise prediction have been considered during the present study. The first is a method introduced by Cole, et al., (Reference 32). This is one of the earliest methods which can provide a precise definition of rocket noise environments, and is based on a series of rocket engine tests with thrusts

ranging from 1000 lbs to 130,000 lbs. The second method was developed by the Wyle Laboratories research staff (Reference 33) through a series of rocket noise studies. In this approach, the rocket exhaust flow is divided into segments of apparent noise sources and the acoustic pressu,e fluctuations at various points on the vehicle can be computed by summing the contributions from these source segments. The appaient source location and the strength of the sources are derived from experimental data, and presented in terms of normalized parameters. The third method follows a different approach and was developed by Franken and Wiener in 1963 (Reference 34). Acoustic measurements of launch noise environments on vehicles such as the Titan and Jupiter, were synthesized into a set of three normalized curves. These curves represent approximately the top, mid—section and bottom section of the launch vehicles. A correction factor is available to take into account variations in thrust for individual launch vehicles. This method has been shown to be accurate for predictions of the noise environments for large launch vehicles with thrusts up to about 10^6 lbs. Finally, a fourth method which deals with very large boosters, such as the Saturn V, was introduced by Wilhold, et al., (Reference 35). This method takes into account the importance of noise source distribution and the deflected geometry of the rocket exhaust. The basic non—dimensional spectrum is compiled from data obtained during launch and static testing of large booster engines. This method, which provides the flexibility of dealing with advanced strap-on launch vehicles such as Titan III C or projected post-Saturn launch vehicles, has been shown to be very accurate (Reference 36).

The detailed procedure for each method, as well as its range of application, is discussed in detail in Appendix A. For launch vehicles with simple geometry, the noise environment can usually be predicted by using one of these four methods. For strap-on launch vehicles, however, two different methods may be required to handle the main rocket booster and the strap-on rockets separately.

3.2.1.2 Narrow-Band Space Correlation Coefficients — A necessary preliminary to any study of structural response of a shroud to a random pressure field is the calculation of the surface pressure correlation function. The greatest structural response occurs for any given mode when the spatial correlation or phase of the pressures corresponds to the mode shape. Spatial correlation is defined in terms of a pressure correlation coefficient, which is the long time average of the instantaneous product of two acoustic pressure signals divided by the product of their root mean square values. A correlation coefficient of one implies that the two signals are in phase at all times. A correlation coefficient of zero indicates that the two signals are completely independent, while a correlation coefficient of minus one indicates that the two pressures would be exactly out of phase.

The narrow band space correlation function $R(\zeta, \eta, \omega)$ can be thought of physically as a measure of the time average value of the relative phase between pressures acting at two points (x, y) and (x', y') which are separated by component distances ζ and η. This implies that the pressure acting at any point (x', y') within the central region of positive correlation will, over a long time average, be in-phase

24

for an R fraction of this time with the pressure acting at the center (x, y) of the region. The correlation length, C_L, is defined as equal to that length over which the excitation may be considered as perfectly correlated in space, i.e., the correlation length times unit correlation is equal to the area under the normalized space correlation curve. Thus for a diffuse acoustic field where the narrow band space correlation coefficient has the form $C(k\zeta; \omega) = \sin k\zeta/k\zeta$, where ζ is the spatial separation and k is 2π divided by the wavelength, the correlation length is obtained from the relation:

$$(C_L \times 1) = 2 \int_0^\infty \frac{\sin k\zeta}{k\zeta} \, d(k\zeta) \qquad (16)$$

giving the result that $\quad C_L = \dfrac{\lambda}{2}$

A second method of defining the correlation length which is sometimes preferred, is to replace the upper limit of the above integration by the distance to the first zero crossing of the narrow band space correlation coefficient.

It is known that, for a three-dimensional diffuse field without the structure present, the pressure correlation function is of the form $\sin k\zeta/k\zeta$, where ζ is the spatial separation. For a plane wave, the correlation function is simply $\cos k(x - x')$, where x is in the direction of wave propagation. However, the pressure correlation function will be changed in the presence of the vehicle due to diffraction effects. Dyer discussed in Reference 37 some pressure correlation results determined from measurements along a missile surface. The longitudinal correlation is shown in Figure 7 and the angular correlation is shown in Figure 8. Dyer found that the longitudinal correlation agreed very well with $\cos k(x - x')$, the correlation function for a plane wave, for small non-dimensional separation distances. The angular correlation function shown in Figure 8 is plotted versus $k a (\phi - \phi')$. Since the structural radius is a, then $a(\phi - \phi')$ is the circumferential separation on the missile surface. Thus it can be seen that for a given separation, angular correlation is equal to or greater than the longitudinal correlation. Dyer interpreted this result as follows: consider the largest separation possible in the circumferential direction, to be $a\pi$, i.e., observation points on opposite sides of the missile. At low frequencies, the sound source is centered relatively far down stream of the nozzle, consequently the noise reaching the missile appears to originate from a single source point, rather than from the volume distribution of the source. Thus the pressure signals separated by $a\pi$ are still correlated. At high frequencies, the sound source is centered relatively close to the nozzle. Thus the noise propagating along opposite sides of the missile originates from different portions of the noise source, and because the high frequency noise follows essentially straight-line paths, the signals are uncorrelated.

25

In the mid-field, the peak octave band sound pressure level occurs near a Strouhal number of 0.1. By considering that the shroud diameter is approximately the same as the effective diameter of the first stage rocket engines, the peak wavelength will be about twice the shroud diameter. Hence, most of the acoustic pressure functions are well correlated. Although the rocket exhaust flow may be deflected with respect to the ground plane, the directional effect in the low frequency range is not significant.

The mid-field pressure correlation function on a vehicle for a given launch configuration has been predicted by Potter (Reference 38). In this method, the noise for a given frequency is assumed to originate from an apparent source location in the exhaust stream. The wave front spreads out spherically and when it arrives at the vehicle, it is practically a plane wave with a definite angle of incidence. According to the classical theories of diffraction around a cylinder, a correlation function for this particular wave length can be computed. The details of this computation have been reported in Reference 38.

A summary of the angular correlation results obtained by Potter (Reference 38) for the S-IC vehicle is shown in Figure 9. These results, for a range of octave band center frequencies, are plotted versus the normalized separation angle ka $(\phi - \phi')$ or $2\pi \eta/\lambda$ (where a is the vehicle radius and η is the circumferential separation distance). The correlation results show a much wider range than those suggested by Franken (see Figure 8). For the purposes of comparison, the reverberant correlation coefficient

$$C(\eta;\omega) = \sin 2\pi\eta/\lambda \bigg/ \frac{2\pi\eta}{\lambda} \qquad (17)$$

is also shown in Figure 9; this comparison shows that the low frequency correlation is lower than the reverberant case, but the higher frequencies show substantially greater correlation lengths than the reverberant case.

These theoretical results have been partially collapsed by replotting the correlation coefficients versus the parameter $\eta\, f^{1/4}/c$ (where c is the speed of sound and f is the appropriate center frequency). The data collapse is shown in Figure 10. For the purposes of estimating the structural response, a functional form for the narrow band correlation coefficient which lay reasonably close to the collapsed data shown in Figure 10, was assumed. This correlation coefficient, given by the general expression $\sin 2\pi\eta_0 / 2\pi\eta_0$ (where η_0 is equal to $10\,\eta\, f^{1/4}/c$) is also shown in Figure 10. The functional form for the correlation coefficient, is of course, similar to that for a reverberant acoustic field; however the characteristic variations in correlation for the various frequencies, illustrated in Figure 9, have been retained. Although the assumed correlation coefficient is a relatively crude approximation to the collapsed data shown in Figure 10, it is considered to be reasonable for the purposes of predicting structural response.

26

The longitudinal correlation coefficient can be approximated reasonably well by the function $\cos\left\{2\pi\,\zeta/\lambda \cdot \sin\beta\right\}$ where β is the angle between the normal to the incident plane wave and the horizontal. In order to use this form for the correlation coefficient in structural response predictions, it is necessary to know the relationship between the angle of incidence β, and the predominant frequencies in the exhaust flow. Since all of the shrouds analyzed during the present study are mounted on launch vehicles powered by an Atlas first stage booster, investigation of the relationship between the angle β and frequency was confined to this particular booster. Noise sources were allocated in the rocket exhaust flow according to the rocket noise prediction technique outlined in Reference 33. From the geometry of the exhaust flow and the allocated sources, the angle of incidence for each noise source was plotted versus frequency, as shown in Figure 11. Based upon these calculated results, the angle of incidence can be assumed to be given by the following;

$$\beta \approx 38 \text{ degrees} \qquad\qquad 0 \leq f \leq 25 \text{ Hz}$$

$$\beta \approx (26.2 \log_{10} f + 1.452) \text{ degrees} \qquad 25 \text{ Hz} \leq f \leq 2500 \text{ Hz} \qquad (18)$$

$$\beta \approx 90 \text{ degrees} \qquad\qquad f > 2500 \text{ Hz}$$

To summarize the discussion of the narrow band space correlation coefficients, the equations used for subsequent calculation of structural response are given below;

$$C\left(\overline{\zeta}\,;\omega\right) = \cos\gamma_x\,\overline{\zeta} \qquad\qquad - \text{ Longitudinal}$$

$$(19)$$

$$C\left(\overline{\eta}\,;\omega\right) = \frac{\sin\left\{20\pi\,L_y\,\dfrac{f^{1/4}}{c}\,\overline{\eta}\right\}}{20\pi\,L_y\,\dfrac{f^{1/4}}{c}\,\overline{\eta}} \qquad - \text{ Lateral}$$

where

$$\gamma_x = \frac{\omega\,L_x}{c}\cdot\sin\beta$$

$$\overline{\zeta} = \zeta/L_x$$

$$\overline{\eta} = \eta/L_y$$

$$L_x = \text{axial length of structure}$$

$$L_y = \text{circumferential length of structure}$$

27

3.2.2 Aerodynamic Environments

3.2.2.1 Introduction — This discussion is devoted to the specification of surface fluctuating pressures resulting from unsteady aerodynamic phenomena during the launch phase of flight. Previous wind tunnel and flight data show that fluctuating pressures are proportional to free-stream dynamic pressure (q_{∞}) for a given unsteady flow phenomenon. However, peak fluctuating pressures do not necessarily occur at maximum q_{∞} for certain regions of a vehicle due to the non-homogeneous nature of the flow field. For example, regions of the vehicle exposed to separated flow and the impingement of oscillating shock waves will experience fluctuating pressures at least an order of magnitude greater than regions exposed to attached flow. Thus, if separated flow and oscillating shock waves are present, say at Mach numbers other than the range of maximum q_{∞}, then peak fluctuating pressures will also be encountered at conditions other than at maximum q_{∞}. Thus, it is easily seen that vehicle configuration is very important in the specification of fluctuating pressure levels since the source phenomena are highly configuration dependent in addition to varying with Mach number and angle of attack.

In light of the foregoing discussion, one general statement can be made in regard to aerodynamic fluctuating pressures. Regions exposed to the same unsteady phenomenon will experience fluctuating pressure levels which are proportional to free-stream dynamic pressure. Thus, it can be readily seen that a fundamental parameter in the specification of the surface excitation is free-stream dynamic pressure and its variation with Mach number. For a given configuration, Mach number and angle of attack define the phenomena, and dynamic pressure defines the fluctuating pressure levels associated with the phenomena.

Unsteady aerodynamic flow and the attendant fluctuating pressures experienced by aerospace vehicles naturally depend on the flight environments and the geometry of the vehicle. There are an infinite number of possible configurations and any discussion of their fluctuating pressure environment must be general. Practically all experimental data for unsteady aerodynamic flow have been acquired for bodies of revolution which are typical of missile configurations. As a result of these studies, it is well known that certain basic unsteady flow conditions will occur regardless of the detailed geometry of the vehicle. The occurrence of these basic fluctuating pressure phenomena and their statistical properties can be predicted quite accurately. It is convenient to discuss these basic flow conditions for bodies of revolution; however, this is certainly no restriction on either the feasibility or the practicality of predicting their occurrence on more complicated configurations.

A complete discussion of the general features of typical bodies of revolution, the unsteady flow fields which they encounter, and the methods of predicting the statistical properties of each flow field, is presented in Appendix B.

28

The remainder of this section is devoted to a summary of the particular fluctuating pressures encountered at different Mach numbers by several typical shroud – launch vehicle combinations. Three shrouds, each having a cone angle of 15 degrees, were considered during the present study, as follows:

- Nimbus shroud
- OAO shroud
- Mariner D shroud

For these 15-degree cone-cylinder bodies the significant flight Mach numbers (in terms of fluctuating pressures) are Mach 0.7, Mach 0.8, and the flight Mach number corresponding to maximum dynamic pressure. Maximum dynamic pressures for typical shroud/spacecraft-launch vehicle combinations generally occur in the Mach number range $M = 1.25$ to $M = 2.0$. This is illustrated in Figure 12 which shows dynamic pressure time histories for the Thor/Agena B, Delta, Atlas/Agena B and Atlas/Centaur vehicles. Altitude and Mach number versus time for the Atlas/Centaur vehicle are also shown in this figure. This data was obtained from References 39 and 40. In the following sub-section the significant fluctuating pressure environments encountered by the 15-degree cone-cylinder shrouds are discussed and equations for predicting the statistical properties of each environment are summarized. This summary is based upon the detailed discussion presented in Appendix B and the extensive cone-cylinder wind tunnel study reported by Robertson in Reference 41. Typical 15 degree cone-cylinder body results from this study are shown in Figure 13. This figure describes the axial distributions of fluctuating pressures for various free stream Mach numbers, M_∞; the results are presented in terms of $\sqrt{\overline{P^2}}/q_\infty$ versus the distance downstream in vehicle diameters, D, where D is the cylinder diameter.

3.2.2.2 <u>Significa· ; Fluctuating Pressure Environments</u> — The fluctuating pressures acting on typical 15-degree cone-cylinder shrouds are illustrated in Figure 14. This figure defines the environments by type and by zone for Mach numbers $M = 0.7$, $M = 0.8$, and $1.0 \leq M \leq 2.0$. Firstly it should be noted that the flow is attached over the conical section of the shroud for all of the above Mach numbers.

At Mach 0.7 the flow over the cylindrical section is characterized by a separated flow region in Zone 1 followed by modified attached flows in Zones 2 and 3. The modified attached flows are characterized by thickened boundary layers, the boundary layer thickness being substantially greater (by a factor of 3) than that for regular undisturbed attached flow. Although Zones 2 and 3 have basically the same type of flow phenomenon, i.e., attached, the overall levels differ, and it is therefore convenient to consider them separately.

At Mach 0.8 the flow over the cylindrical section is characterized by a regular attached flow region in Zone 1, followed by both separated flow and shock-wave oscillation in Zone 2, and a modified attached flow in Zone 3.

29

For Mach numbers equal to or greater than $M = 1$, the flow is attached over the whole of the cylindrical section. The length of each zone, in terms of the shroud diameter D, is also indicated in Figure 14.

3.2.2.3 Overall Levels — The overall levels in each zone for the three Mach number ranges have been derived from the general results for cone-cylinder bodies presented in Appendix B. For example, the overall levels for blunt body separated flow over a 25 degree cone-cylinder body can be deduced from the results shown in Figure 5 in Appendix B. For the 15 degree cone-cylinder shrouds considered here, extensive use has been made of the results obtained by Robertson (Reference 41) for a range of model sizes and cone angles, typical results being as shown in Figure 13. In defining the overall levels in a shroud zone of finite length, the average fluctuating pressure levels (over the finite length) have been utilized rather than maximum local levels.

The overall levels in each zone for the three Mach number ranges are as follows:

Mach 0.7

$$\sqrt{\overline{P^2}/q_\infty^2} = 0.03$$

Zone 1
(Separated Flow)

$$\sqrt{\overline{P^2}/q_\infty^2} = 0.022 \qquad (20)$$

Zone 2
(Modified Attached Flow)

$$\sqrt{\overline{P^2}/q_\infty^2} = 0.013$$

Zone 3
(Modified Attached Flow)

For the conical section of the shroud, where the flow is attached, the overall level is given by the equation;

$$\sqrt{\overline{P^2}/q_\infty} = 0.006/(1 + 0.14\, M_\infty^2) \qquad (21)$$

where
$$M_\infty = 0.7$$

Mach 0.8

Zone 1
(Regular Attached Flow)
Same as Equation (21) with $M_\infty = 0.8$

Zone 2
(Separated Flow Influence)
$$\sqrt{\overline{P^2}/q_\infty^2} = 0.0259 \qquad (22)$$

Zone 2
(Shock-Wave Oscillation Influence)
$$\sqrt{\overline{P^2}/q_\infty^2} = 0.054$$

30

Zone 3
(Modified Attached Flow)
$$\sqrt[4]{\overline{P^2}/q_\infty^2} \;\; = \;\; 0.008$$

For the conical portion of the shroud, where the flow is attached, the overall level is given by Equation 21 with $M_\infty = 0.8$.

$1.0 \leq M \leq 2.0$

At these Mach numbers the flow is attached over both the conical and cylindrical sections of the shroud. The overall levels are thus given by Equation (21) with the appropriate free-stream Mach number substitution.

3.2.2.4 Power Spectra — For the cylindrical section of the shrouds, a generalized equation for the power spectrum has been derived from the results discussed in Appendix B. This generalized equation, which combines Equations (2), (10), (34) and (35) of Appendix B, allows the normalized power spectrum to be computed in any individual zone, as follows:

$$
\frac{\phi(f)\, U_\ell}{q_\infty^2 \, \delta_\ell} = A \cdot \frac{(\overline{P^2}/q_\infty^2)_A}{\left(\dfrac{f_0\,\delta_\ell}{U_\ell}\right)_A \left\{1 + (f/f_0)^{0.9}\right\}^2}
$$

$$
+ \; B \cdot \frac{(\overline{P^2}/q_\infty^2)_B}{\left(\dfrac{f_0\,\delta_\ell}{U_\ell}\right)_B \left\{1 + (f/f_0)^{0.83}\right\}^{2.15}}
$$

$$
+ \; C \cdot \frac{(\overline{P^2}/q_\infty^2)_T - (\overline{P^2}/q_\infty^2)_B}{\left(\dfrac{f_0\,\delta_\ell}{U_\ell}\right)_C \left\{1 + (f/f_0)^{1.55}\right\}^{1.7}}
$$

$$
+ \; D \cdot \frac{(\overline{P^2}/q_\infty^2)_T - (\overline{P^2}/q_\infty^2)_A}{\left(\dfrac{f_0\,\delta_\ell}{U_\ell}\right)_C \left\{1 + (f/f_0)^{1.55}\right\}^{1.7}}
$$

(23)

where

$\phi(f)$ = Pressure spectral density $(\text{psi})^2/\text{Hz}$

U_ℓ = Local velocity (in./sec)

q_∞ = Free-stream dynamic pressure (lb/in².)

δ_ℓ = Local boundary layer thickness (in.)

31

A refers to zones having wholly attached flow.

B refers to zones having wholly separated flow.

C refers to zones having separated flow beneath a shock wave.

D refers to zones having attached flow beneath a shock wave.

and the subscript T denotes total conditions, i.e., the total fluctuating pressure due to the shock wave superimposed on the separated or attached flow.

It should be noted that in this generalized equation, the power spectrum has been normalized by local velocity, local boundary layer thickness and free stream dynamic pressure.

Over the range of Mach numbers considered during the present study, the flow over the conical section of the shrouds is attached. Thus, the power spectra can be derived from the above equation with the following substitutions (for 15-degree cone-cylinder shrouds)

$$B = C = D = 0$$
$$A = 1.0$$

$$\overline{(P^2/q_\infty^2)}_A = \frac{3.6 \cdot 10^{-5}}{(1 + 0.14\, M_\infty)^2} \; ; \quad \left(\frac{f_0\, \delta_\ell}{U_\ell}\right)_A = 0.346$$

(24)

where

M_∞ = free-stream Mach number

$U_\ell = U_\infty$

U_∞ = free-stream velocity corresponding to each Mach number

$\delta_\ell = \delta_b$

For the 15-degree cone-cylinder shrouds the appropriate substitutions in Equation (23) for the computation of the power spectrum in each zone are outlined below for the various Mach numbers.

Mach 0.7

Zone 1 $A = D = 0$

                         $B = C = 1.0$

$$\left(\overline{P^2}/q_\infty^2\right)_B = 6.75.10^{-4}; \quad \left(\frac{f_0 \, \delta_\ell}{U_\ell}\right)_B = 0.17 \tag{25}$$

$$\left(\overline{P^2}/q_\infty^2\right)_T = 9.0.10^{-4}; \quad \left(\frac{f_0 \, \delta_\ell}{U_\ell}\right)_C = 1.0.10^{-3}$$

where

$U_\ell = $ 1077 ft/sec

$\delta_\ell = 3 \, \delta_b$

$\delta_b = $ boundary layer thickness for regular attached flows

$$= x \left[0.37 \, R_e^{-0.2} \left\{ 1 + \left(\frac{R_e}{6.9.10^7}\right)^2 \right\}^{0.1} \right] \tag{26}$$

$x = $ distance from shroud nose cone to center of fluctuating pressure zone of in? ....

$R_e = $ Reynolds number $= U_\infty x / \nu$

$\nu = $ kinematic viscosity

$U_\infty = $ free-stream velocity

Zone 2 $\qquad\qquad$ B = C = D = 0

$\qquad\qquad\qquad\qquad$ A = 1.0

$$\left(\overline{P^2}/q_\infty^2\right)_A = 4.84.10^{-4}; \quad \left(\frac{f_0 \, \delta_\ell}{U_\ell}\right)_A = 0.346 \tag{27}$$

where

$U_\ell = U_\infty ; \quad \delta_\ell = 3 \delta_b$

Zone 3 $\qquad$ B = C = D = 0

$$A = 1.0$$

$$(\overline{P^2}/q_\infty^2)_A = 6.4 \cdot 10^{-5}; \quad \left(\frac{f_0\,\delta_\ell}{U_\ell}\right)_A = 0.346 \qquad (31)$$

where

$$U_\ell = 965 \text{ ft/sec} \; ; \quad \delta_\ell = 3\,\delta_b$$

$1.0 \leq M \leq 2.0$

In this Mach number range the flow is attached over the entire cylinder; thus the power spectra can be computed utilizing the substitutions outlined earlier in this section for the conical sections.

3.2.2.5 Narrow-band Space Correlation Coefficients — In Summarizing the functional forms for the narrow-band space correlation coefficients (or the cross-power spectra) it is convenient to consider each type of environment separately rather than define explicitly the correlation in each zone. Thus, the correlation coefficients can be grouped under the following headings: attached boundary layers (both regular and thickened cases), separated flows, and shock-wave oscillation. To apply these formulae to the particular Mach numbers and zones, it is necessary to substitute the appropriate numerical values for the free-stream conditions, and the local conditions i.e., local velocities, local boundary layer thicknesses and free stream velocities.

Attached Turbulent Boundary Layers

$$C\,(\overline{\zeta};\omega) = \exp\left[-\,\delta_x\,\left|\,\overline{\zeta}\,\right|\right] \cdot \cos\,\gamma_x\,\overline{\zeta} \qquad - \text{Longitudinal}$$

$$(32)$$

$$C\,(\overline{\eta};\omega) = \exp\left[-\,\delta_y\,\left|\,\overline{\eta}\,\right|\right] \qquad\qquad - \text{Lateral}$$

where

$$\gamma_x = \omega\,L_x/U_c$$

$$\gamma_y = \omega\,L_y/U_c$$

$$\delta_x = a\gamma_x + b\,L_x/\delta_\ell \qquad (33)$$

35

$$\delta_y = c\,\gamma_y + d\,L_y/\delta_\ell$$

$$U_c = 0.6984\,U_\infty \left(\frac{U_\infty}{\omega\delta^*}\right)^{0.09} \quad - \text{Bies Equation (Reference 42)} \quad (34)$$

$$\delta^* = \delta_\ell/8 \quad \text{for} \quad M < 1.0$$

$$\delta^* = \frac{(1.3 + 0.43\,M_\infty^2)\,\delta_\ell}{10.4 + 0.5\,M_\infty^2 \left[1 + 2.10^{-8}\,R_e\right]^{1/3}} \quad \text{for} \quad M > 1.0 \quad (35)$$

L_x = axial length of structure

L_y = circumferential length of structure

$\overline{\zeta}$ = ζ/L_x

$\overline{\eta}$ = η/L_y

ζ, η = axial and circumferential separation distances

δ_ℓ = local boundary layer thickness

a, b, c, d = constants, equal to 0.1, 0.27, 0.72, and 2.0, respectively

R_e = Reynolds number

Separated Flows

$$C\left(\overline{\zeta};\omega\right) = \exp\left[-\delta_x\left|\overline{\zeta}\right|\right]\cos\gamma_x\,\overline{\zeta} \quad - \text{Longitudinal}$$

$$(36)$$

$$C\left(\overline{\eta};\omega\right) = \exp\left[-\delta_y\left|\overline{\eta}\right|\right] \quad - \text{Lateral}$$

where

$$\delta_x = 0.75\, L_x \quad \text{for} \quad \frac{f\,\delta_\ell}{U_\ell} < 6.10^{-3}$$

$$= 0.75\, L_x \left[\frac{f\,\delta_\ell / U_\ell}{(f\delta_\ell / U_\ell)_0} \right]^{0.3} \quad \text{for } 6.10^{-3} \le \frac{f\,\delta_\ell}{U_\ell} \le 6.10^{-2} \tag{37}$$

$$= 1.5\, L_x \quad \text{for} \quad \frac{f\,\delta_\ell}{U_\ell} > 6.10^{-2}$$

$$\left(\frac{f\,\delta_\ell}{U_\ell} \right)_0 = 6.10^{-3} \tag{38}$$

$$\gamma_x = \frac{\omega\, L_x}{U_c}$$

$$U_c = 0.3\, U_\ell \quad \text{for} \quad \frac{f\,\delta_\ell}{U_\ell} < 0.1$$

$$= U_\ell \left[0.3 + \log_{10} \left(\frac{10\, f\delta_\ell}{U_\ell} \right)^{0.5} \right] \text{for } 0.1 \le \frac{f\,\delta_\ell}{U_\ell} \le 1.0 \tag{39}$$

$$= 0.8\, U_\ell \quad \text{for} \quad \frac{f\,\delta_\ell}{U_\ell} > 1.0$$

$$\delta_y = 0.75\, L_y \quad \text{for} \quad \frac{f\,\delta_\ell}{U_\ell} < 6.10^{-3}$$

$$\tag{40}$$

$$= 0.75\, L_y \left[\frac{(f\,\delta_\ell / U_\ell)}{(f\,\delta_\ell / U_\ell)_0} \right]^{0.3} \quad \text{for} \quad \frac{f\,\delta_\ell}{U_\ell} > 6.10^{-3}$$

37

Shock-Wave Oscillation

The correlation coefficient in the longitudinal direction may be written as (see Equation (25) of Appendix B):

$$C(\overline{\zeta};\omega) = \exp\left[-\delta_x \left|\overline{\zeta}\right|\right] \cdot \cos\gamma_x\overline{\zeta} \tag{41}$$

where

$$\delta_x = \frac{3.18 \, \omega \, L_x}{U_0}$$

$$\gamma_x = \frac{\omega \, L_x}{U_0} \tag{42}$$

U_0 = local velocity upstream of the shock wave

Published data is ....ole on the transverse spatial characteristics of shock—induced fluctr · . ssures. However, it is anticipated that these disturbances will be reason. . correlated over much larger distances in the transverse direction than in the longitudinal direction because of the continuity of the shock wave in the plane normal to the flow. Therefore, it is physically reasonable to assume that the correlation coefficient is unity over one-quarter of the shroud circumference, i.e., the circumference of the shroud can be divided into 4 uncorrelated spans, the correlation coefficient being equal to 1.0 in each span.

Thus, the narrow band correlation coefficient in the lateral direction may be written as:

$$C(\overline{\eta};\omega) = \text{UNITY over each of four quadrants} \tag{43}$$

3.2.2.6 Other Shroud Geometries — The discussion so far has been limited to 15 degree cone-cylinder shrouds. Typical fluctuating pressure levels for other cone-cylinders, boattails, steps and wedges, have been presented in Appendix B. It is of interest here, however, to present typical axial distributions of fluctuating pressures for three other shroud configurations. These data were obtained by Coe (Reference 43) utilizing the Ames 14-foot transonic wind tunnel.

38

Axial distributions of fluctuating pressures for: (1) an ellipsoidal nose cone on a 6° 30' converging body section, (2) an ellipsoidal nose cone on a cylindrical body with a 30 degree step, and (3) a 14° 28' cone-cylinder staged vehicle, are shown in Figures 15, 16 and 17, respectively. These results are presented in terms of $\sqrt{\overline{P^2}}/q_\infty$ (or P_{rms}/q_∞) versus the distance downstream in vehicle diameters, D, for a range of free-stream Mach numbers, where D is the maximum body diameter.

For the bulbous shroud, shown in Figure 15, the peak fluctuating pressure levels are associated with the shock wave at the beginning of the converging section. As the free-stream Mach number increases, the region of peak fluctuating pressure moves aft with the shock wave.

For the boattail shroud, shown in Figure 16, two regions of peak fluctuating pressure level are observed, depending upon the free-stream Mach number. The upstream region, which occurs at transonic Mach numbers of about $M_\infty = 0.8$, is associated with the separation at the beginning of the cylindrical section. The second region of peak fluctuating pressure level is associated with re-attachment behind the boat-tail region; the levels can be seen to diminish steadily with increasing free-stream Mach number. Figure 17, shows a similar effect for the cone-cylinder staged vehicle, there being two regions of peak fluctuating pressure level; both are associated with shock wave oscillation at free-stream Mach numbers above $M_\infty = 0.8$.

In comparing Figures 15, 16 and 17, the severity of the boattail geometry, in terms of peak levels, can be immediately observed. The local peak fluctuating pressure levels (P_{rms}/q_∞) for these three shroud geometries are typically on the order of 0.06. Thus for a dynamic pressure of say 860 lb/ft², this corresponds to an overall level of about 162 dB.

In summary, the results presented in Figures 13, 15, 16 and 17 show the detailed effects of shroud geometry on the fluctuating pressure levels. Clearly, there are certain basic unsteady flow conditions which occur regardless of the detailed geometry of the vehicle, e.g., flow separation, re-attachment, and shock-wave oscillation. The magnitudes of the peak fluctuating pressure levels associated with any one of these unsteady flow phenomena are quite similar over the range of shroud geometries, though the size of the region affected (in terms of vehicle diameters) may vary.

3.3 Characteristics of Laboratory Acoustic Environments

The essential characteristics of laboratory acoustic environments from a structural analysis view point are the space correlation functions. Therefore, this subsection is limited to a discussion of the correlation functions for reverberant acoustic fields and ducted progressive wave acoustic fields.

Reverberant Acoustic Field

The reverberant acoustic field is assumed to be an ideal diffuse field that is composed of plane waves which impinge on the structural surface with an equal probability for all angles of incidence. In an ideal reverberation room, the narrow band space correlation function relative to any two points separated by a distance r is $[\sin k r]/k r$ where $k = \omega/c = $ acoustic wave number. The presence of the structure being analyzed is assumed to have no influence on the impinging wave field, as for example, a small flat plate flush mounted in a wall of the room.

For both flat and cylindrical surfaces, the narrow band space correlation functions are:

$$C(\overline{\zeta};\omega) = \frac{\sin k\overline{\zeta}}{k\overline{\zeta}}$$

$$C(\overline{\eta};\omega) = \frac{\sin k\overline{\eta}}{k\overline{\eta}}$$

(44)

It has been shown (Reference 44) that the above equation for $C(\overline{\zeta};\omega)$ is quite accurate for a cylinder even when scattering is considered. Because of scattering, the above equation for $C(\overline{\eta};\omega)$ introduces some errors for a cylinder; however, the errors diminish with increasing frequency.

Reflections of the acoustic waves from the structural surface cause effective increases in surface pressures. At low frequencies, the reflection factor on pressure level is unity, while at high frequencies this factor is 2.0. In all subsequent structural response calculations described in this report, the responses have been normalized to the actual surface pressures. Thus in comparing responses of a given structure to a number of different environments, it should be borne in mind that the fluctuating pressures used in the analysis are true surface pressures.

Ducted Progressive Wave Field

The ducted progressive wave field consists of N independent plane wave fields that propagate at parallel incidence along the length, L_x, of a cylindrical shell or rectangular plate. This field is formed within a rigid shroud that completely covers the structural surface and that is internally baffled so as to create a set of N straight, parallel ducts which act as acoustic wave guides. The intermediate walls between adjacent ducts are separated from the structural surface by a set of flexible seals that minimize acoustic leakage between adjacent ducts and minimize structural constraints introduced by the shroud. The ducts have uniform widths of $2\pi R/N$ around the circumference of the shell, and L_y/N across the width of a rectangular plate. Each duct is driven at one end by a broadband random acoustic noise source and has an anechoic termination at the other end. The N acoustic noise sources are driven by uncorrelated random signals in order to produce N uncorrelated progressive wave fields. In the analysis of structural response, it is assumed that plane wave fronts exist in each duct. The acoustic field along the axis of any one duct is said to be axially correlated if at any frequency the axial pressure distributions are sinusoidal. Due to various acoustic phenomena in the ducts, these axial pressure distributions may not be sinusoidal, in which case axial correlation lengths may be limited.

Assuming that the sound pressure level is uniform along the ducts, the axial space correlation coefficient for the acoustic field is;

$$C(\overline{\zeta};\omega) = \cos \gamma_x \overline{\zeta} \tag{45}$$

where

$$\gamma_x = \frac{\omega L_x}{c}$$

The circumferential correlation is assumed to have a value of unity, since the acoustic waves generated within each duct are assumed to be plane waves.

3.4 Structural Response and Noise Reduction Equations

3.4.1 Modal Analysis — In the modal analysis, the classical method is adopted to treat systems having a large number of modes whose natural frequencies are closely spaced and whose bandwidths may overlap. It is assumed that the mean square response amplitude of each mode can be obtained independently, and that the summation of these mean square responses is insensitive to damping coupling between modes. The total mean square response of a structure at any point depends upon the summation of the mean square modal responses and upon the summation of the cross-correlations between pairs of modes. The latter term is in some cases significant; however, each term in this summation becomes equal to zero when the space average of the mean square response is obtained. The cancellation of modal cross-correlations for space average response is due to orthogonality between the modes.

41

Response Equations

The analysis of structural response to random pressure fields utilizing normal modes was initially formulated by Powell (References 45, 46 and 47); detailed results were derived for the response of structures to plane acoustic waves and to a two-dimensional reverberant acoustic field (Reference 47). The theory was extended to predict the response of panels to turbulent boundary layer pressure fluctuations by Wilby (Reference 48) and to a three—dimensional reverberant acoustic field by Crocker and White (Reference 49). More recently, this work has been extended to predict the responses of cylindrical shells to random pressure fields (References 14 and 50).

A detailed derivation of the response equations is given in References 14 and 45-50; for the purposes of the present study, only the final equation is presented.

It can be shown (Reference 14) that the space-average acceleration response spectrum is given by the equation;

$$\frac{S[\ddot{U}; f]}{S[P; f]} = \frac{1}{(\mu g)^2} \sum_{m=1}^{\infty} \sum_{n=0}^{\infty} \beta_{mn} H^2 \left(\frac{f_{mn}}{f}\right) \cdot j^2_{mn}(f) \qquad (46)$$

where

$S[\ddot{U}; f]$ = space-average power spectral density of acceleration; g^2/Hz

$S[P; f]$ = pressure power spectral density; $(psi)^2/Hz$

μg = weight per unit area of surface of shell or plate; (lb/in^2)

β_{mn} = 2, $\qquad m=1,2,3,\ldots;\quad n=0$ } Cylindrical Shell

     = $4n^4/(1+n^2)^2$, $m=1,2,3,\ldots;\quad n=1,2,3,\ldots$ }

     = 4, $\qquad m=1,2,3,\ldots;\quad n=1,2,3,\ldots$ Plate

$H\left(\frac{f_{mn}}{f}\right)$ = single degree of freedom dynamic magnification factor for acceleration response of the (m, n)-mode

$$= \left[\left\{\left(\frac{f_{mn}}{f}\right)^2 - 1\right\}^2 + \frac{1}{Q^2_{mn}}\left(\frac{f_{mn}}{f}\right)^2\right]^{-1/2}$$

Q = dynamic magnification factor for the $(m-n)$ mode

$j^2_{mn}(f)$ = joint acceptance for the (m, n) structural mode

42

It is usually assumed that the structural mode shapes can be written in separable form (i.e., $\phi_{mn}(\overline{x}, \overline{y}) = \phi_m(\overline{x}) \cdot \phi_n(\overline{y})$), so that the joint acceptance for the (m,n,) mode may be re-defined as:

$$j_{mn}^2(f) = j_m^2(f) \cdot j_n^2(f) \tag{47}$$

where

$$j_m^2(f) = \text{joint acceptance for mth mode}$$

$$j_n^2(f) = \text{joint acceptance for nth mode}$$

Equation (46) may be used for estimating the response of a plate or cylindrical shell. The assumptions inherent in this equation include the following:

- Mode shapes can be expressed as products of modes along the principal axes of the plate or shell.

- Space-correlation functions for the fluctuating pressure fields can be expressed as products of space-correlation functions along the two principal axes of the plate or shell.

- Mode shapes of the plate or shell are orthogonal with respect to the mass, stiffness and damping distributions of the structure; and this condition is valid if the structure is uniform.

The above equation treats each mode of the structure as a single degree of freedom system whose response is independent of the responses of all other modes. The total mean-square response of the structure is then equal to the sum of the ensemble of mean-square responses of all of the structural modes. The influence of cross-correlations between the responses of any pair of modes is automatically deleted by space averaging the response. Thus, Equation (46) contains no cross-product terms associated with two different modes. The influence of modal cross-correlations on response has been demonstrated for a simple pinned beam (Reference 14). The cross-correlations essentially describe the variation of response from the space average, and such variations are expected to be important only for structures with localized excitations. In the latter case, response levels are expected to be high near the source of excitation and to decrease with increasing distance from the source. Therefore when analyzing structural response to a localized excitation, responses should be computed by two methods. First, Equation (46) can be used to give a reasonably good estimate of the average response of the unforced portion of the structure. Secondly, the

43

response of only the forced portion of the structure should be computed to give an upper bound to the localized response levels. Actual response levels near the source will be lower tha, 'ose computed in the second calculation, while response levels far from the source should be higher than those predicted by the first calculation.

Joint Acceptances for the Various Environments

The joint-acceptance equations for the various fluctuating pressure environments are presented in Appendix C. Most of these equations were developed in References 14 and 45 - 50.

3.4.2 <u>Statistical Energy Analysis</u> — The statistical energy analysis is based on the principle that the time average power flow between two simple oscillators, linearly coupled and excited by a wide-band excitation, is proportional to the difference in their time-average total energy, the power flow being always from the oscillator of higher energy to that of lower energy. The extension of this principle to multi-modal systems is described in Appendix C; only the final equations will be presented here.

For the case of a cylindrical structure excited by a reverberant acoustic field, the response can be predicted from the following equation (Reference 19);

$$\frac{S_{a2}}{S_{p1}} = \frac{\pi c_0}{A \rho_s \rho_0} \left[\frac{\eta_{2AF,1}\, \eta_{2AF}}{2\eta_{2AF,1} + \eta_{2AF}} + \frac{\eta_{2AS,1}\, \eta_{2AS}}{2\eta_{2AS,1} + \eta_{2AS}} \right] \left[1 + \frac{S_{p3}}{S_{p1}} \right] \cdot \qquad (48)$$

$$\cdot \left[\frac{1}{g^2} \right] \left(\frac{g^2}{psi^2} \right)$$

Similarly, it can be shown (Reference 19) that the noise reduction is given by the relation;

$$\frac{S_{p1}}{S_{p3}} = \frac{\eta_{2AS,1}\, \eta_{2AS} + \eta_{1AF,1}\, \eta_{2AF} + \eta_3\, \eta_3}{\dfrac{\eta_{2AS,1}\, \eta_{2AS}}{2\eta_{2AF,1} + \eta_{2AS}} + \dfrac{\eta_{2AF,1}^2\, \eta_{2AF}}{2\eta_{2AF,1} + \eta_{2AF}}} - 1 \qquad (49)$$

In the above equations;

S_{a2} = acceleration spectral density

S_{p1} = pressure spectral density of the external acoustic field

S_{p3} = pressure spectral density of the internal acoustic field

44

c_0 = speed of sound in air

ρ_0 = mass density of air

A = surface area of cylinder

ρ_s = surface mass density of cylinder

g = gravity acceleration

n_{2AF} = modal density of the resonant acoustically fast (AF) modal group

n_{2AS} = modal density of the resonant acoustically slow (AS) modal group

n_3 = modal density of the resonant interior space modes

$\eta_{2AF,1}$ = coupling loss factor between the acoustic field and the resonant AF mode group

$\eta_{2AS,1}$ = coupling loss factor between the acoustic field and the resonant AF mode group

η_{2AF} = dissipating loss factor of the resonant AF modal group

η_{2AS} = dissipating loss factor of the resonant AS modal group

η_3 = dissipating loss factor of the interior space modal group

A more detailed discussion of this method, together with the appropriate equations for the modal densities and coupling loss factors is presented in Appendix C.

3.4.3 Structural Models for Theoretical Analyses — For the purposes of analyzing the response and noise reduction of typical spacecraft shrouds, three shroud designs were selected. The selection was based upon the availability of design data and the necessity for determining response characteristics of various forms of shroud construction. The three shrouds selected for analysis were as follows:

o   Agena Long (or Nimbus) Shroud — This shroud is typical of orthotropic designs employing Fiberglas skin and aluminum ring-frame stiffeners.

o   OAO Shroud — This shroud is typical of isotropic designs employing honeycomb Fiberglas skin.

o   Mariner D Shroud — This shroud is typical of orthotropic designs employing Magnesium skin and ring-frame stiffeners.

Details of these three shrouds are shown in Figure 18. Each shroud was analyzed in two stages; the lower cylindrical section, and the upper conical section. For the latter case, the conical shell was idealized to an "equivalent" cylindrical shell. In each case the upper and lower sections of the shroud were treated as simply-supported cylindrical shells. For the stiffened shells, the equivalent orthotropic bending stiffnesses were computed in the manner discussed in Section 2.2. The length of each "equivalent" cylinder utilized for analyzing the conical section was measured from the cone-cylinder junction to a forward station which was well removed from the nose cap, approximately mid-way between the upper two ring frames.

The properties of the cylindrical shells which were analyzed are summarized in Table II. For analyses involving the responses of local portions of the shrouds, short cylindrical sections between ring frames were chosen; these cylindrical sections were also assumed to be simply-supported at each end.

TABLE II

PROPERTIES OF SHROUDS SELECTED FOR THEORETICAL ANALYSIS

SHROUD TYPE		Axial Length L_x in.	Diameter D in.	Circumf. Length L_y in.	Surface Weight Density (μg) lb/in.^{2}	Axial Bending Stiffness D_x lb in.	Circumf. Bending Stiffness D_y lb in.	In-Plane Extensional Stiffness K_e lb/in.
Nimbus	Lower Section	130	65	204	.012	930	$1 \cdot 04 \cdot 10^6$	$5 \cdot 18 \cdot 10^5$
	Upper Section	72	47	147.5	.0131	930	$6 \cdot 33 \cdot 10^5$	$5 \cdot 18 \cdot 10^5$
OAO	Lower Section	153	120	376.5	.0084	$3 \cdot 16 \cdot 10^5$	$3 \cdot 16 \cdot 10^5$	$2 \cdot 59 \cdot 10^5$
	Upper Section	148	84	264	.0084	$3 \cdot 16 \cdot 10^5$	$3 \cdot 16 \cdot 10^5$	$2 \cdot 96 \cdot 10^5$
Mariner D	Lower Section	88	60	188	.006	305	$3 \cdot 64 \cdot 10^4$	$5 \cdot 2 \cdot 10^5$
	Upper Section	58	46	144.5	.006	305	$3 \cdot 94 \cdot 10^4$	$5 \cdot 2 \cdot 10^5$

4.0 THEORETICAL RESULTS AND COMPARISON WITH MEASURED DATA

4.1 Introduction

As discussed in Section 3.4.3, three typical shroud/launch vehicle configurations were chosen for theoretical analysis of response and noise reduction. These configurations were as follows: the Nimbus-Atlas/Agena B, the OAO-Atlas/Agena D, and the Mariner D-Atlas/Agena B. Of these three configurations, the Nimbus-Atlas/Agena B was analyzed in detail. As a result of these analyses, the following characteristics were determined:

- The lift-off acoustic environment

- The acoustic environments due to unsteady aerodynamic fluctuating pressures at Mach 0.7, Mach 0.8, Mach 1.0, Mach 1.4 and Mach 2.0.

- The space-average acceleration responses of the shroud during lift-off and at the flight Mach numbers indicated above.

- The space-average acceleration responses of localized segments of the shroud during lift-off and at critical flight Mach numbers.

- The noise reductions of the shrouds at lift-off and during various phases of flight.

- The internal acoustic fields within the shroud at lift-off and during flight.

- The space-average acceleration responses of the shroud to reverberant acoustic fields, ducted progressive wave acoustic fields and localized reverberant fields.

In the remainder of Section 4.0, these theoretical results are presented together with relevant laboratory and flight data where appropriate.

4.2 Flight Environments

4.2.1 Acoustic Environment at Lift-Off — The acoustic environment at lift-off for typical payloads mounted on the Atlas Booster has been estimated by using two of the prediction techniques discussed in Section 3.2.1. These results are shown in Figure 19. The octave band spectra in Figure 19 were computed using the Franken and Weiner method (Reference 34) and the method developed by Wyle Laboratories (Reference 33).

In computing the lift-off acoustic environment of the Atlas Booster, the following engine parameters were used:

Number of engines   = 3

47

Thrust = 2 outer engines at 165,000 lbs and 1 center engine at 57,000 lbs

Nozzle exit diameter = 51 in.

Distance from nozzle exit plane to deflector bucket = 12 ft

Distance from nozzle exit plane to point of interest on payload shroud = 95 ft

Acoustic efficiency = 0.003

Exhaust velocity = 8200 ft/sec

Because of the engine spacing and nozzle exit geometry (three engines in line, 63 inches between centers), the acoustic spectrum was initially calculated for one of the outer engines. A correction of 3 dB was added to this spectrum to account for the other out-board engine and a correction of about 0.7 dB was added to account for the additional thrust provided by the center engine.

To account for pressure doubling at the surface of the payload shroud, the predicted free field levels were corrected by adding an average of 3 dB for frequencies in the range:

$$ f \geq \frac{c_o}{2 \pi R} \quad Hz \tag{50} $$

where c_o = speed of sound in air

R = Radius of payload shroud

This 3 dB correction represents an average increase in sound pressure level around the circumference of the shroud due to the impingement of random phase acoustic waves (Reference 51). In computing the free field sound pressure levels, a directivity index of 0 dB was assumed for radiation directions of 90 to 135 degrees to the exhaust flow. For radiation directions between 135 and 180 degrees, the directivity index was assumed to vary from 0 dB to -5 dB. Also shown in Figure 19 are the octave band sound pressure levels measured on the umbilical tower during launch of the Atlas/Centaur AC-16 vehicle and OAO-A2 spacecraft (Reference 52). Since these measurements are essentially free—field sound pressure levels, an average 3 dB correction was applied in the same manner as for the predicted sound pressure levels. The corrected octave band surface sound pressure levels are indicated in Figure 19. The levels at the umbilical tower represent measured averages in each octave band between times (T-3) sec and (T+2) sec. At time (T-0) sec the vehicle had lifted 2 inches off the pad, while at (T+3) sec the vehicle had lifted 20 feet off the launch pad. Since the maximum levels in each octave band occurred at different times during this five second period (Reference 52), interpretation of this measured data is difficult; the overall sound pressure level computed from this averaging process is 147.5 dB, whereas the time history of the overall sound pressure level (shown in Reference 52). ver exceeded 145 dB during this five second period.

48

Examination of the predicted and measured sound pressure levels shows that typical scatter between the predicted and measured data is approximately 4 dB at low frequencies, increasing to about 9 dB at 8 K Hz.

A comparison between the acoustic levels at lift-off measured on the launch umbilical tower near the surface of the payload shroud for three different first-stage boosters is shown in Figure 20. This data, reported in References 52 and 53, was obtained during launchings of Thrust-assisted Thor/Agena, Improved Delta, and Atlas/Centaur vehicles. The basic Thor booster consists of a single engine developing approximately 172,000 lbs of thrust. The Improved Delta and Thrust-assisted Thor/Agena vehicles described in Reference 53 had additional thrust provided by three strap-on solid-propellant motors, each developing a thrust of 54,000 lbs. The Atlas first stage booster was rated at approximately 386,500 lbs thrust. Figure 20 shows that despite the differences in thrust and rocket nozzle geometry, the resulting free-field octave-band spectra in the vicinity of the shroud are basically similar.

Typical one-third octave band sound pressure levels measured at the surface of payload shrouds during lift-off and static firing for a range of Titan vehicles are shown in Figures 21 and 22. These measurements have been included for the purposes of comparison with the Atlas, Delta and Thor acoustic data. Figure 21 shows the sound pressure levels measured during static firing of three different Titan II vehicles. These results are reasonably consistent over the frequency range of 100 Hz - 2000 Hz, however outside this range considerable scatter exists. Also shown in Figure 21 are the sound pressure levels obtained during lift-off for a Titan IIIA vehicle. Although the Titan II and Titan IIIA have basically identical first stage boosters (2 engines developing a total of 430,000 lbs of thrust), the sound pressure levels exhibited by the latter are slightly higher than those for the Titan II at frequencies above 250 Hz. The differences between the launch pad configuration and the static firing test stand, and the different angular locations of the microphones may account for this. Lift-off data obtained from three Titan IIIC launches is shown in Figure 22. The Titan IIIC vehicle is basically a Titan IIIA with an additional pair of strap-on solid-propellant boosters, each developing approximately 1,203,600 lbs of thrust. At lift-off the thrust is provided by the two solid motors. The data shown in Figure 22 for the Titan IIIC is more consistent than the Titan II data though the levels are somewhat lower. This is considered to be due primarily to the deflector configuration, which was basically a 90-degree closed bucket which extended 135 feet in the horizontal direction (approximately 17 nozzle exit diameters). Additionally, some shielding effects due to the two 120 inch diameter strap-on motors are thought to be present.

One-third octave band sound pressure levels measured at the surface of the Instrument Unit during lift-off for Saturn 1B and Saturn V vehicles are shown in Figure 23. The Saturn 1B data was obtained from vehicles AS203 and AS204 (Reference 54), and the Saturn V data represents the mean from vehicles AS501, AS502 and AS503 (Reference 54). Except for the AS203 data at low frequencies, the sound pressure levels measured on the Saturn V and Saturn 1B Instrument Units are reasonably consistent throughout the frequency range. Again, these measurements have been included only for the purposes of comparison with the Atlas, Delta and Thor acoustic data.

4.2.2 Aerodynamic Environments — As discussed in Section 3.2.2, for typical 15 degree cone-cylinder shrouds the significant flight Mach numbers, in terms of fluctuating pressures, are Mach 0.7, Mach 0.8 and the flight Mach number corresponding to maximum dynamic pressure. For the analytical studies, the Atlas/Centaur dynamic pressure time history (Reference 40) was utilized. Dynamic pressure, altitude and Mach number versus time from lift-off are shown in Figure 12. Maximum dynamic pressure, which was assumed to occur at Mach 2.0, was equal to approximately 810 lb/ft^2.

For Mach numbers less than $M = 1.0$, the flow over the conical portion of the shroud is completely attached whereas the flow over the cylindrical portion is characterized by 3 distinct zones.

These zones, which were discussed in Section 3.2.2.2, are shown in Figure 24 for the Nimbus shroud. At Mach 0.7 the three zones are characterized by the following environments:

 ⊚ Zone 1 — Separated flow

 ⊚ Zone 2 — Modified attached flow (i.e., a thickened boundary layer)

 ⊚ Zone 3 — Modified attaches flow.

Although the space-correlation properties in Zones 2 and 3 are identical, the overall fluctuating pressure levels are different. These overall levels were defined in Section 3.2.2.3.

At Mach 0.8, the three zones are characterized by the following environments:

 ⊚ Zone 1 — Attached flow

 ⊚ Zone 2 — Separated flow and shock wave oscillation superimposed

 ⊚ Zone 3 — Modified attached flow.

At Mach 2.0 (the maximum dynamic pressure condition), the flow is attached over both conical and cylindrical portions of the shroud.

Fluctuating pressure spectra for the Nimbus shroud at Mach 0.7, Mach 0.8, and Mach 2.0 have been calculated utilizing the prediction schemes discussed in Appendix B and summarized in Section 3.2.2. These spectra are shown in Figures 25, 26 and 27, for Mach numbers $M=0.7$, $M=0.8$ and $M=2.0$, respectively. In each case, the reference point for the computation of the boundary layer thickness and the fluctuating pressure spectrum was taken to be the mid-point in each zone.

The calculated spectrum levels were converted to one-third octave band sound pressure levels and re-plotted for the three Mach numbers, as shown in Figure 28. It can be seen in this figure that the sound pressure levels over the conical section of the shroud do not vary substantially with increasing Mach number and are also significantly lower

50

than the levels over the cylindrical section, as expected. The highest sound pressure levels during flight occur in Zone 2 of the cylindrical section at Mach 0.8; this particular zone is subjected to the combined influence of the separated flow and the shock—wave oscillation. Significantly high sound pressure levels occur in all three zones of the cylindrical section at Mach 0.7. This figure illustrates the importance of the transonic portion of flight.

Apparently there are no in-flight measurements of the surface sound pressure levels (for these vehicle configurations) available for direct comparison with the theoretical results. However, limited measurements obtained from Titan IIIC and Saturn V vehicles have been reported (References 55 and 56). This flight data is shown in Figure 29. The Titan IIIC data which were obtained from three separate vehicles at Mach 1.0 show typical scatter of from 5 dB to 8 dB at low and high frequencies. All of these measurements were recorded by a flush-mounted microphone in the payload region. The Saturn V data, also shown in Figure 29, represents the space-average of the sound pressure levels measured on the surface of the Service Module at Mach 1.6. (Reference 56).

4.3 Shroud Responses

4.3.1 Introduction — Acceleration Power Spectral Densities for the Nimbus shroud, the Mariner D shroud, and the OAO shroud were computed for the following environments:

- ● Lift-off acoustic environment

- ● In-flight aerodynamic environments (Mach numbers 0.7, 0.8, 1.0, 1.4 and 2.0)

- ● Laboratory acoustic environments (reverberant acoustic field, 8, 4 and 1 progressive wave axial ducts, and localized reverberant acoustic fields).

The structural responses of the shrouds were computed using the modal analysis as described in Section 3.4. The response data is presented in terms of normalized acceleration spectra, i.e., the acceleration PSD divided by the pressure PSD, the units being $g^2/(\text{psi})^2$. For conversion to Acceleration Spectrum Level in dB, referenced to 1g and 2.10^{-5} Newtons/m^2, the following relation may be utilized: $[AL - SPL] - dB$ (Re 1g and 2.10^{-5} N/m^2) = $\{10 \log_{10} (g^2/(\text{psi})^2 - 170.75\} - dB$.

For those cases where more than one fluctuating pressure environment acts on the shroud, e.g., the aerodynamic environment at Mach 0.7 and Mach 0.8, the overall space-average acceleration response was obtained by adding the mean-square responses of the shroud to each separate environment. In the following section, the response results for the Nimbus shroud are discussed in detail.

4.3.2 Vibration Response of Nimbus Shroud

Launch Acoustic Environment

The acceleration response of the cylindrical portion of the Nimbus shroud to the launch environment is shown in Figure 30. Two separate spectra are shown in this figure; the solid curve denotes the overall space average acceleration, while the dashed curve denotes the space average acceleration of a cylindrical section of the shroud between ring frame stations 115.0 and 159.0 (see Figure 18). The effects of the ring frequency (approximately 630 Hz) and the acoustic critical frequency (i e., the coincidence frequency for grazing incidence waves) at 5220 Hz are clearly evident. The slight frequency shift between the two structural cases at the ring and coincidence frequencies results from the different surface weights of the two structures; for the case of the whole cylindrical section of the shroud, the ring frame weights were distributed over the surface area. The response of the section between ring frames represents an upper bound to the space-average response of the cylindrical portion of the Nimbus shroud. The acceleration response of the conical portion of the Nimbus shroud to the launch environment is shown in Figure 31. Again the response was computed for a section between ring frames in addition to the overall response of the total conical portion.

In order to determine the accuracy of the structural response theory for a rocket noise environment, the response of the SLA structure to the Saturn 1B lift-off environment was computed and compared to flight measurements. This comparison is shown in Figure 32 in terms of one-third octave band normalized acceleration. The flight data shown in Figure 32 was recorded by two accelerometers located 40 in. from the base of the SLA and 70 in. from the top of the SLA. It can be seen that the agreement between the predicted and measured responses is reasonably good throughout the frequency range; however, no data above 500 Hz are available. A comparison between the measured SLA responses at lift-off, during transonic flight, and during supersonic flight is shown in Figure 33, which was taken from Reference 57.

Mach 0.7

The acceleration response of the Nimbus shroud to the aerodynamic environment at Mach 0.7 is shown in Figure 34. Since the environment consisted of three distinct zones (see Figure 24), the overall space average response of the cylindrical portion to each environment was computed separately. The total response of the cylindrical portion is obtained by adding the mean square responses for each fluctuating pressure environment; this is shown in Figure 35. Note that the total mean square responses are absolute accelerations; i.e., g^2 averaged in one-third octave bands. The effects of the separated flow environment can be clearly seen in Figures 34 and 35; at low frequencies the contribution to the overall response is quite small compared to the contributions from the other two environments (concentrated over Zones 2 and 3), whereas at high frequencies the contribution to the overall response is highly significant.

The acceleration responses of localized regions in the cylindrical portion of the Nimbus shroud are shown in Figure 36 for the Mach 0 7 flight environment. The section between ring frames stations 115.0 and 159.0 was analyzed for both the separated flow environment (which extends over a length of 32.5 in.) and the modified attached flow environment (which extends over the remaining 11.5 in.). In addition, the acceleration response of the section between ring frame stations 198.5 and 221.5 was analyzed for the modified attached flow environment. These responses represent an upper bound to the overall responses presented in Figure 34. The total mean square response of the segment between ring frame stations 115.0 and 159.0 is shown in Figure 37; again the significance of the separated flow environment at high frequencies can be observed.

Mach 0.8

The acceleration response of the Nimbus shroud to the aerodynamic environment at Mach 0.8 is shown in Figure 38. Again, these responses are the overall space average responses of the shroud to separate environments which are concentrated over discrete areas. The significance of the shock wave oscillation environment over the whole frequency range is clearly observed. It can be inferred from Figure 26, however, (which shows a rapid decay in sound pressure level with increasing frequency) that the absolute response to a shock wave oscillation does not contribute significantly to the total response at high frequencies. The total mean square response of the cylindrical portion of the shroud, obtained by adding the individual mean square responses, is shown in Figure 39.

The acceleration responses of the section between ring frame stations 115.0 and 159.0 are shown in Figure 40 for the Mach 0.8 flight environment. This particular section of the Nimbus shroud has four separate fluctuating pressure environments superimposed, namely; attached flow over the forward 6.5 in., separated flow and shock wave oscillation over the next 19.5 in. and modified attached flow over the remaining 18 in. Again, these responses represent an upper bound to the responses shown in Figure 38.

Mach 2.0

The acceleration response of the Nimbus shroud to the aerodynamic environment at Mach 2.0 is shown in Figure 41. For this Mach number, the flow is attached over the whole shroud. For the purposes of comparing the mean-square response levels of the shroud at different Mach numbers, the mean square responses for the Mach 2.0 environment are shown in Figure 42. The responses at Mach 2.0 are generally lower than those at Mach 0.7 or Mach 0.8 over the frequency range investigated, except in the vicinity of the acoustic critical frequency (5220 Hz), where response levels during Mach 2.0 flight are higher by a factor of 2 to 3.

Reverberant Acoustic Field

The acceleration responses to a reverberant acoustic field are shown in Figure 43. Three curves are shown in this figure; the dashed curve represents the overall space average acceleration of the cylindrical portion of the Nimbus shroud, the solid curve describes the acceleration response of a section between ring frame stations 115.0 and 159.0, and the third curve shows the acceleration response of a section between ring frame stations 198.5 and 221.5. The absence of a peak at the acoustic critical frequency for the dashed curve is due to the "joint acceptance" characteristics of the larger structure at high frequencies. Similar acceleration spectra for the conical portion of the Nimbus shroud are shown in Figure 44.

Localized Reverberant Acoustic Fields

The responses of the cylindrical portion of the Nimbus shroud subjected to localized reverberant acoustic fields are shown in Figure 45. The three acceleration spectra represent the overall space average responses to excitation applied over Zone 1, Zone 2 and Zone 3 separately, (the three zones corresponding to a simulation of the Mach 0.7 flight environment). Zones 1 and 2 each extended over one-quarter of the cylindrical length, while Zone 3 extended over the remaining one-half of the cylindrical length. A detailed comparison between Figure 45 and Figure 43 shows that the space-average response of the shroud is approximately proportional to the ratio of the excitation area divided by the total surface area of the shroud.

Progressive Wave Axial Ducts

The acceleration responses of the Nimbus shroud to one, four, eight and sixteen progressive wave axial ducts are shown in Figures 46 and 47. The responses of the cylindrical portion are shown in Figure 46 and those of the conical portion in Figure 47. In each case it can be seen that above the ring frequency the number of progressive wave ducts does not play an important role in determining the response to a unit pressure spectrum. The acceleration spectra for the one duct cases include responses of the $n = 0$ modes only (i.e., breathing modes) since for all other values of n (the number of full circumferential waves) the lateral joint acceptance is zero.

One-Third Octave Band Response Spectra

Acceleration responses of the shroud were also computed in terms of normalized one—third octave band levels, i.e., $[AL - SPL]$ in dB re 1 g and 2×10^{-5} Newtons/m^2. The acceleration levels are shown in Figure 48 for the lift-off environment, Mach 2.0 flight environment, reverberant acoustic field and the 1 duct and 8 duct progressive wave configurations. Because of the significant differences in the sound pressure levels for the various shroud zones at Mach 0.7 and Mach 0.8, this acceleration data was not normalized and is therefore not shown in Figure 48.

4.3.3 Special Effects —

Differential Pressure

The effects of a differential pressure across the shroud were discussed in Section 2.2.4, where it was pointed out that the principal effect was the shift in the resonant frequencies of the shroud. To determine more precisely the effects of a differential pressure, the responses of the Nimbus shroud to a reverberant acoustic field and the aerodynamic environment at Mach 2.0 were computed for differential pressures of 0.5 psi, 1.0 psi, and 2.0 psi. These results indicated that a very slight frequency shift of the low order modes took place between zero differential pressure and 0.5 psi. This shift was approximately 20 Hz. The results for 0.5 psi, 1.0 psi, and 2.0 psi were almost identical. These trends were observed for both the reverberant and the aerodynamic excitation. No change in response levels was observed.

Sound Pressure Level Decay in Progressive Wave Ducts

As sound waves propagate along the axes of ducts, acoustic energy is absorbed by the structure and as a result, the sound pressure levels decay along the duct axes. The effects of this sound pressure level decay can be estimated if it is assumed that the decay is exponential along the length of the duct. For this condition the longitudinal spatial correlation function can be expressed as (Reference 14):

$$C\left(\overline{\zeta}; \omega\right) = \exp\left[-A\gamma_x \left|\overline{\zeta}\right|\right] \cos \gamma_x \overline{\zeta} \tag{51}$$

where

$$\gamma_x = \omega L_x / c$$

$$\overline{\zeta} = \zeta / L_x$$

ζ = separation distance

c = speed of sound

L_x = axial length of the structure

A = damping term or axial decay parameter

= 0.693 for 6 dB decay between top and bottom of duct

= 1.286 for 12 dB decay between top and bottom of duct

The sound pressure level decay is given by: $20 \log_{10} \left[\dfrac{1}{e^{-A}}\right]$ dB.

55

The effects of decaying sound pressure level along the length of a duct are shown in Figure 49 for the SLA structure subjected to a 16-duct progressive wave environment. This data (obtained from Reference 14) shows the SLA response for zero decay, 4.5 dB decay, and 8.7 dB decay. The responses shown in this figure are normalized by the pressure spectral density which exists at the beginning of the axial duct. Th> most significant effect caused by the sound pressure level decay is the increase in high frequency response of the SLA in the region above the acoustic critical frequency (which for the SLA is approximately 300 Hz). The response in the region of the ring frequency (approximately 175 Hz for the SLA) is reduced by a factor of between 2 and 3 due to the sound pressure level decay.

Acoustic Radiation Damping in Progressive Wave Ducts

The general properties of acoustic radiation damping were discussed in Section 2.2.5, and the importance of the radiation damping inherent in progressive wave duct systems was pointed out. For a given progressive wave duct configuration. The acoustic damping ratio, ζ_r, can be evaluated using the results of Reference 27 shown in Figure 6. The effective damping of the structure-duct configuration is then given by:

$$Q_e = Q_0 + Q_r \tag{52}$$

where $\qquad Q_r = \dfrac{1}{2\zeta_r}$

and $\qquad Q_0 = $ total damping of the structure without the progressive wave ducts.

Since the power spectral density of the acceleration response of the shroud is proportional to Q^2 (see Equation (46)), the low order odd-numbered axial modes of the shroud can be modified by multiplying the response PSD by the factor, $\left(\dfrac{Q_e}{Q_0}\right)^2$. It is generally assumed that for even numbered axial modes the effective radiation damping is negligible due to cancellation effects.

4.4 Shroud Noise Reduction

4.4.1 Introduction — The noise reductions of the Nimbus, OAO, and Mariner D shrouds were computed utilizing the statistical energy method described in Section 3.4. These computations were based upon the usual assumption of diffusivity of external and internal acoustic fields. Because the conical and cylindrical sections of the shroud were analyzed separately, it was necessary to account for this in the computation of the space—

average internal acoustic field. This correction procedure is discussed later in Section 4.5. In the remainder of this section, the theoretical results are discussed in detail and compared with available experimental data.

4.4.2 Theoretical Results — The calculated noise reduction for the lower section of the Nimbus shroud is shown in Figure 50 for three values of internal absorption. These noise reduction curves display the characteristic minima at the ring frequency (632 Hz) and the acoustic critical frequency (5220 Hz). Increasing the average internal absorption coefficient from 0.1 to 0.3 results in an increase in noise reduction of approximately 4 dB over the frequency range. The results shown in Figure 50 are not considered to be very precise at frequencies below about 300 Hz because of the limitations in extending the statistical energy method further than about one octave below the ring frequency.

The effects of varying altitude on the shroud noise reduction are shown in Figure 51 for the lower section of the Nimbus shroud. Three curves are shown in this figure, corresponding to sea level, 18,000 ft and 45,000 ft, which represent the lift-off, Mach 0.8 and Mach 2.0 flight environments respectively. In computing the noise reductions, appropriate values of ρc were utilized, based upon the flight Mach number and altitude profiles shown in Figure 12, together with standard atmospheric properties (Reference 58). Similar curves for the upper section of the Nimbus shroud are shown in Figure 52.

The effects of altitude are observed to be twofold; firstly the acoustic critical frequency is shifted because of the change in the speed of sound, and secondly the noise reduction is increased in proportion to the reduction in ρc. It has previously been shown (Reference 59) that for the same media on both sides of the structure, the change in transmission loss due to increasing altitude can be determined approximately from the relation:

$$\Delta (TL) \approx 20 \log \left(\frac{\rho_0 c_0}{\rho_1 c_1} \right) \quad dB \tag{53}$$

where the subscripts $_0$ and $_1$ refer to the conditions at sea level and at altitude, respectively. The calculated increments in transmission loss for 18,000 ft and 45,000 ft altitude, based upon the above simple relationship, are approximately 5.5 dB and 15 dB respectively. It can be seen from Figures 51 and 52 that the results of this simple calculation are in close agreement with the noise reduction trends computed using the statistical energy analysis.

Noise reduction results for the OAO and Mariner D shrouds are shown in Figure 53, based on sea level conditions and an average internal absorption of 0.2. These results can be compared directly with those shown in Figure 50 for the Nimbus shroud.

A comparison between flight and laboratory noise reduction data for the Nimbus shroud is shown in Figure 54. This figure shows the measured noise reduction at lift-off during launch of the OGO-C spacecraft (Reference 60) and spacecraft (Reference 53).

Also shown in the figure are three noise reduction curves measured during acoustic testing of the Nimbus shroud. Two of these curves were determined from tests at the GSFC Launch Phase Simulator — Progressive Wave Duct Facility (References 61 and 20) while the other curve was determined from tests at the Langley Research Center (Reference 60) utilizing the discharge from a blowdown wind tunnel. As can be seen in the figure, there is considerable scatter in the noise reduction results. This scatter is caused by a number of factors; the different characteristics of the external acoustic fields, configuration changes within the shroud, and the number and locations of the microphones. Details of the external acoustic fields, together with the relevant microphone locations corresponding to these noise reduction measurements, are given in Figure 55. Comparisons between Figures 54 and 55 indicate that over the test frequency range, the scatter in the noise reduction data is considerably greater than the variation in the external sound pressure levels.

Envelopes to the noise reduction data of Figure 54 have been plotted in Figure 56. These envelopes show more clearly the spread in the results. Also shown in Figure 56 are two theoretical curves describing the noise reduction of the Nimbus shroud for a diffuse external acoustic field. The solid curve represents the noise reduction at sea level for an absorption coefficient of 0.2 (see Figure 50), and the dashed curve represents the simple "mass law" noise reduction (Reference 62).

Noise reduction data for the SLA and for the Ranger, OAO, and Titan (fiberglas and metal) shrouds are shown in Figure 57. The SLA data was obtained during lift-off and during acoustic testing utilizing 16 progressive wave ducts (References 54 and 57). The Titan data (Reference 55) and the OAO data (References 52 and 53) represent the noise reduction at lift-off. The noise reduction for the Ranger shroud was presented by Kaplan (Reference 63) and the characteristics of the environment were not reported. The noise reduction data shown in Figure 57 has been presented for comparison purposes only.

Interpretation of the measured noise reduction data shown in Figures 54 and 57 is very difficult. In many cases the noise reduction curves are derived from measurements obtained by a single external microphone and a single internal microphone. Also, additional uncertainty is introduced by the fact that the internal microphone was in many cases located in close proximity to the inner wall of the shroud. Recent experimental measurements of noise reduction through shells (Reference 31) using microphones spaced throughout the interior volume, have shown that the sound pressure levels vary considerably between measurement points close to the inner wall and measurement points removed from the wall. This point is illustrated in Figure 58, which was taken from Reference 31. Large deviations in the noise reduction determined from three microphone measurements can be observed; these deviations are substantially reduced as the frequency increases and the internal acoustic field becomes more diffuse.

    4.4.3 Low Frequency Noise Reduction — At very low frequencies, below the fundamental modal frequencies of both the interior acoustic field and the shroud, the shroud-interior volume system is completely non-resonant. Under these conditions it is possible to calculate the transmission loss, where the motion of the shroud and the

58

contained air is one of "breathing" in a radial direction (Reference 59). The lowest acoustic modal frequencies for the interior of a cylindrical shroud are given by the expressions (Reference 26):

$$f = \frac{1.85\,c}{2\pi R} \quad \text{(radial and circumferential modes)}$$

$$f = \frac{c}{2L} \quad \text{(axial modes)} \tag{54}$$

where: R and L are the radius and length of the shroud, respectively, and c is the speed of sound.

The low frequency noise reduction theory can be applied up to a frequency f_a, given by whichever is lower of the above two frequencies. At frequencies below f_a, the air in the shroud undergoes compression and rarefaction such that the complete system "breathes". The sound pressure inside the shroud is essentially constant throughout the whole volume.

If it is assumed that the external driving sound pressure is due to a diffuse sound field, the action of this pressure will be to periodically increase and decrease the radius of the shroud about the mean, unexcited value in accordance with the frequency of excitation. Under these conditions, the stiffness K_s of the cylindrical shroud is given by:

$$K_s = \frac{Eh}{R^2} \quad \text{per unit length} \tag{55}$$

where h is the thickness of the cylindrical skin, and E is the elastic modulus.

The cylindrical skin is effectively in series with the internal air, which behaves as a pure stiffness K_a of value

$$K_a = \frac{2\rho c^2}{R} \tag{56}$$

where ρ is the density of air.

Utilizing impedance concepts, together with the above relations, it has been shown (Reference 59) that the transmission loss is given by:

$$TL \approx 20 \log_{10} \left\{ \frac{Ehg}{2R\rho c^2} \right\} - 3 \quad \text{dB} \tag{57}$$

59

The noise reduction of an enclosure can be obtained from the following general equation:

$$NR = 10 \log_{10} \left[1 + \frac{\bar{\alpha} \bar{S}}{\bar{\tau} S_t} \right]$$ (58)

where

$\bar{\alpha} = (\Sigma \alpha_i S_i) / \Sigma S_i$, the average absorption coefficient

$\bar{S} = \Sigma S_i$, the total absorbing surface area

$\alpha_i =$ the absorption coefficient associated with area S_i

$\bar{\tau} =$ the average transmission coefficient of the structure through the transmitting area $S_t = (\Sigma \tau_j S_j) / \Sigma S_j$

$S_t = \Sigma S_j$, the total transmitting surface area

$\tau_j =$ the transmission coefficient associated with area S_j.

However, for the simple case of a shroud having a uniform external wall and subjected to constant incident sound power over the entire external surface, the noise reduction can be obtained for the relation (Reference 33):

$$NR = T.L. - 10 \log_{10} \left(\frac{S_t}{\bar{\alpha} \bar{S}} \right)$$ (59)

An alternative scheme for the prediction of low frequency noise reduction, reported in Reference 64, is as follows:

$$NR = 20 \log_{10} \left(\frac{P_0}{P_i} \right) = 20 \log_{10} \left[1 + \frac{C_{con}}{C} \right]$$ (60)

60

where

$$C_{con} = \text{acoustic compliance of the contained volume} = \frac{V_{con}}{\gamma \cdot P_{con}}$$

$$V_{con} = \text{volume contained within the shroud}$$

$$C = \frac{\pi R^3 L}{EA}\left(\frac{5}{2} - 2\nu\right) \quad \text{for a cylindrical shroud}$$

$$\gamma = 1.4 \text{ for air}$$

$$P_{con} = \text{initial pressure within the shroud (psi absolute)}$$

$$\nu = \text{Poisson's ratio}$$

$$A = \text{longitudinal cross-section area of the shroud wall}$$

$$= 2h \text{ in.}^2 \text{ per unit length of shroud.}$$

The low frequency noise reduction for the Nimbus shroud was computed using both of the above prediction schemes. An average absorption coefficient of 0.1 was assumed in order to convert the transmission loss computed from Equation (57) to noise reduction. The results of these two calculations were 38 dB noise reduction from Equation (59) and 59 dB noise reduction from Equation (60). These two results are shown in Figure 50. The lowest acoustic mode for the cylindrical section of the shroud occurs at about 50 Hz; thus, the low frequency noise reduction should be constant up to about 30 Hz or 40 Hz and then begin to decrease as the 50 Hz resonance is approached.

Similar calculations for the SLA structure, using Equation (59), resulted in a low frequency noise reduction of 27 dB. For the latter calculation the depth of the honeycomb section was ignored and the effective wall thickness was assumed to be given by the two aluminum face sheets. The first acoustic mode occurs at approximately 20 Hz. Thus the computed low frequency noise reduction should begin to decrease as this frequency is approached. This low frequency noise reduction result is shown in Figure 57.

61

4.5 Shroud Interior Acoustic Fields

4.5.1 Introduction — The space-average internal sound pressure levels within the Nimbus shroud were computed for the lift-off acoustic environment and the Mach 0.7, Mach 0.8 and Mach 2.0 flight environments. The procedure adopted for computing the internal acoustic fields was as follows:

(1) Convert the actual external sound pressure level spectrum to an "equivalent" reverberant sound pressure level spectrum, i.e., the reverberant acoustic field producing the same structural response as the flight environment being considered. This is a necessary step since the calculated noise reductions are based upon the assumption of diffusivity of external and internal acoustic fields.

As an example, the equivalent reverberant field for the rocket noise environment is given by the ratio of the normalized acceleration responses, as follows:

$$\frac{S[P;\omega]_{Reverberant}}{S[P;\omega]_{Rocket\ Noise}} = \frac{\left\{S[\ddot{U};\omega] \Big/ S[P;\omega]\right\}_{Rocket\ Noise}}{\left\{S[\ddot{U};\omega] \Big/ S[P;\omega]\right\}_{Reverberant}} \tag{61}$$

The quantity $10 \log_{10} \left\{ \dfrac{S[P;\omega]_{Reverberant}}{S[P;\omega]_{Rocket\ Noise}} \right\}$ therefore

represents the dB correction to be added to the Rocket Noise Spectrum to give the equivalent reverberant spectrum.

For the transonic Mach numbers, where more than one fluctuating pressure environment exists at the surface of the shroud, the equivalent reverberant spectrum is given directly from the relation:

$$S[P;\omega]_{Reverberant} = \frac{S[\ddot{U};\omega]_{Transonic}}{\left\{S[\ddot{U};\omega] \Big/ S[P;\omega]\right\}_{Reverberant}} \tag{62}$$

where $S[\ddot{U};\omega]_{Transonic}$ represents the sum of the mean-square responses of the shroud to the various fluctuating pressures. For this case the equivalent reverberant spectrum is therefore given directly in units of $(psi)^2/Hz$.

(2) Subtract the calculated Noise Reductions for the upper and lower sections of the shroud from the equivalent reverberant spectra to obtain internal sound pressure levels within the conical and cylindrical sections of the shroud. At low frequencies (more than 1 to 1-1/2 octaves below the ring frequency) the lower envelope to the measured noise reductions shown in Figure 54 was utilized rather than the predicted noise reduction.

(3) Combine the two sound pressure levels to obtain an estimate of the space—average sound pressure level within the shroud.

This final step is accomplished by use of the following relationships:

$$PWL_1 = SPL_1 + 10 \log_{10} A_1 - 0.5 \quad dB$$

$$PWL_2 = SPL_2 + 10 \log_{10} A_2 - 0.5 \quad dB \tag{63}$$

$$PWL_{Total} = SPL_{Average} + 10 \log_{10} A_{Total} - 0.5 \quad dB$$

where

PWL = Acoustic Power Level — dB

SPL = Sound Pressure Level — dB

A = Surface area enclosing the volume of air being considered — ft^2

Subscripts $_1$, $_2$, and Total refer to the cylindrical portion of the shroud, the conical portion of the shroud, and the overall shroud respectively.

4.5.2 Space-Average Internal Sound Pressure Levels — The space—average internal sound pressure levels for the Nimbus shroud are shown in Figures 59, 60, 61 and 62 for the lift-off, Mach 0.7, Mach 0.8, and Mach 2.0 flight environments, respectively. Also shown, for the purpose of comparison, are the computed external sound pressure levels existing at the shroud surface during each significant flight phase. It can be seen that the most significant internal acoustic levels occur at lift-off. At Mach 0.7, the internal levels are lower than at lift-off, by about 10 dB over the frequency range. The Mach 0.8 internal levels are very similar to those occurring at Mach 0.7, while at Mach 2.0 the internal levels are again reduced, by 10 dB - 20 dB at frequencies up to 2,000 Hz. Above this frequency the internal levels at Mach 2.0 are very similar to the Mach 0.7 and Mach 0.8 flight conditions.

63

Measured internal sound pressure levels during flight of the Nimbus shroud/OT-2 Space-craft configuration are shown in Figure 63; these curves show the internal octave band sound pressure levels at lift-off, the transonic portion of flight, and the max. q portion of flight. A single microphone located close to the inner wall of the shroud at the cone—cylinder intersection was employed for these measurements; consequently the internal sound pressure level data should be interpreted with care. Because the interior wall is a location of pressure maxima for all radial acoustic modes of the shroud, it is expected that sound pressure levels measured at this location would be substantially higher than those measured further from the wall. This effect was discussed earlier in Section 4.4.2 and is illustrated in Figure 58. Therefore the results shown in Figure 63 should be viewed as being indicative of the trends, rather than the magnitudes, of the internal sound pressure levels. Direct comparison between the theoretical results and these measured results is thus not justified, since the former are essentially spatial averages within the shroud.

4.6 Spacecraft Response

Theoretical predictions of spacecraft response to the energy transmitted from vibrating shrouds have been reported extensively in References 16, 18, 19 and 65. In each case the total spacecraft response was computed in three stages: (a) the spacecraft response to energy transmitted via the mechanical path, (b) the spacecraft response to energy transmitted via the acoustic path and (c) the total mean-square response of the space-craft obtained by adding the mean-square responses contributed via the mechanical and acoustic paths. The theoretical studies reported in References 16, 18 and 65 dealt with a relatively crude one-half scale shroud/spacecraft system (an approximate model of the OGO spacecraft and Nimbus-type shroud), while in Reference 19 a much larger system, the MARL simulated shroud/payload assembly, was analyzed. The dimensions of the one—half scale and the MARL shrouds were 32 inches in diameter by 78.5 inches long by 0.087 inch wall thickness, and 130 inches in diameter by 300 inches long by 1.0 inch wall thickenss, respectively. The shroud materials were Fiberglas and Aluminum honeycomb respectively. In both cases, the shrouds were simple cylindrical shells with end baffles.

The most significant conclusion resulting from the small-scale study (Reference 65) was that at low frequencies (up to about 2,000 Hz) the energy transmission via the acoustic path exceeded that transmitted via the mechanical path, while above 2,000 Hz the converse was true. This result is illustrated in Figure 64. In order to verify this conclusion, experiments were conducted with the one-half scale model in a rever-berant chamber. Firstly, the total response of the spacecraft was measured while sub-jecting the shroud-spacecraft assembly to a diffuse acoustic field. Secondly, the space-craft response to energy transmitted via the mechanical path was determined by eliminating the acoustic path and repeating the experiment; the acoustic path was eliminated by placing a sound proof enclosure between the inner wall of the shroud and the spacecraft. Finally, the spacecraft response to energy transmitted via the acoustic path was determined by eliminating the mechanical path and repeating the experiment; the mechanical path was eliminated by simply disconnecting the trusses from the shroud.

The results of this experimental study are summarized in Figure 65. These results confirm the predicted result that above 2,000 Hz, the transmission via the mechanical path is greater than the transmission via the acoustic path. For frequencies in the range 630 Hz to 2,000 Hz however, there is no substantial difference between the relative levels of energy transmission. Below 630 Hz these results do confirm the importance of the acoustic path, though no data have been reported for frequencies below 400 Hz.

Similar experiments, utilizing a full-scale OGO-spacecraft and Nimbus shroud, have been reported in Reference 61. The purpose of these experiments was to determine whether or not the spacecraft could be realistically tested with the shroud removed. The first part of the experiment was conducted with the shroud installed; the shroud/spacecraft system was subjected to a progressive wave acoustic environment and the space-average sound pressure levels outside and within the shroud were determined together with the spacecraft responses. The second part of the experiment, conducted with the shroud removed, consisted of reproducing the measured internal space-average sound pressure level and again measuring the spacecraft response. In both experiments detailed measurements of the spacecraft and truss responses, and the sound pressure levels, were obtained. The "internal" space-average sound pressure level was reproduced to within 2 dB - 3 dB over the range 80 Hz to 10,000 Hz except in the frequency range 125 Hz to 400 Hz where the variation ranged from 3 dB - 10 dB, the sound pressure levels with the shroud removed being the higher of the two. No attempt was made to reproduce the spatial characteristics of the internal sound field.

The most significant conclusion arising from the full-scale OGO/Nimbus experiments was that at low frequencies the energy transmission via the mechanical path exceeded that transmitted via the acoustic path. This result is particularly true for measurement locations in the region of the truss. As the measurement point was moved along the spacecraft away from the trusses, the differences between the total responses of the space-craft, with and without the shroud installed, became much less, until at locations well removed from the trusses the responses tended to be very nearly the same. These results are illustrated in Figure 66 for measurement locations at the base of the spacecraft truss and at the top of the spacecraft. Several computed resonant frequencies of the shroud are also indicated in Figure 66. It is clear that the (m=1, n=2) shroud mode at 125 Hz contributes substantially (via the mechanical path) to both the spacecraft truss and the spacecraft responses. Mechanically transmitted contributions from the (m=2, n=2) shroud mode may also be deduced from these results. The response peaks in the range 800 Hz to 1,250 Hz may possibly be associated with resonances of the truss.

A further significant feature of the results shown in Figure 66 is the apparent result that at high frequencies (above about 2,000 Hz) transmission via the acoustic path exceeds transmission via the mechanical path. This result could possibly be due to the different characteristics of the acoustic fields surrounding the spacecraft with and without the shroud installed.

Thus the results of the full-scale OGO-Nimbus experiments apparently contradict the earlier results from the one-half scale model experiments reported in Reference 65. Despite the fact that the characteristics of the internal acoustic field within the shroud were not reproduced exactly, it is considered that the low frequency results shown in Figure 66 are realistic, especially since the effects of the low order shroud modes can be clearly seen.

During a similar study (References 19 and 66), involving the response of the MARL simulated shroud/payload assembly to far-field rocket noise, the theoretical results showed that the energy transmission via the mechanical path was much more significant than transmission via the acoustic path. This finding was partially confirmed by the experimental studies (Reference 66) which were conducted with both Air and Helium within the shroud. During these experiments, the payload/shroud assembly was exposed to the far-field acoustic environments produced by static firings of S-1C and S-II stage rockets. Experimental measurements included free-field sound pressure levels, surface sound pressure levels at the shroud; internal sound pressure levels within the shroud, acceleration responses of the shroud and payload, and strain-gage responses of the truss supporting the payload. A typical result from these experiments is shown in Figure 67 which compares the normalized space average radial accelerations of the payload for the Air-filled shroud and the Helium-filled shroud. The acceleration responses have been normalized by the sound pressure levels at the external surface of the shroud. Figure 67 shows that above 20 Hz the normalized radial acceleration of the payload is unaffected by the substitution of Helium for Air within the shroud, despite the fact that an additional 10 dB of noise reduction was obtained over the entire test frequency range as a result of the substitution (Reference 66). It can therefore be inferred from Figure 67 that energy transmission via the mechanical path is more significant than energy transmission via the acoustic path for this shroud/payload system.

An important feature of the MARL shroud/payload system however, was the method of attachment of the payload to the shroud. The payload truss was attached at eight point. around the mid-height of the shroud, whereas the OGO-Nimbus payload truss was attached to the interface ring at the lower edge of the shroud. The attachment method adopted in the MARL design may well contribute toward the negligible effect of the acoustic path on the total payload response.

It is therefore clear that the geometry of the mounting trusses and the method of attachment to the shroud play an important role in determining the relative contributions of the mechanical and acoustic paths.

4.7 Equivalent Acoustic Environments for Response Simulation

4.7.1 Introduction — Based upon the structural response results for the Nimbus shroud, a number of equivalent acoustic environments have been defined for response simulation during the various phases of flight. These environments include reverberant acoustic fields, single-duct progressive wave configurations, eight-duct progressive wave configurations and local reverberant excitation.

The procedure for computing the equivalent reverberant acoustic field was described earlier in Section 4.5.1. The equivalent single-duct and eight-duct progressive wave spectra were computed in exactly the same way. For example, the equivalent eight—duct progressive wave spectrum for response simulation of Mach 2.0 is given by:

$$\frac{S\left[P;\omega\right]_{8\ Ducts}}{S\left[P;\omega\right]_{Mach\ 2.0}} = \frac{\left\{S\left[\ddot{U};\omega\right]/S\left[P;\omega\right]\right\}_{Mach\ 2.0}}{\left\{S\left[\ddot{U};\omega\right]/S\left[P;\omega\right]\right\}_{8\ Ducts}} \qquad (64)$$

Thus the quantity $10\ \log_{10}\left\{\dfrac{S\left[P;\omega\right]_{8\ Ducts}}{S\left[P;\omega\right]_{Mach\ 2.0}}\right\}$ represents the dB correction to be added to the Mach 2.0 sound pressure level spectrum to give the equivalent eight-duct acoustic spectrum.

For the transonic Mach numbers, where more than one fluctuating pressure environment exists over the surface of the shroud, the equivalent single-duct and eight-duct acoustic spectra are computed in exactly the same manner as for the equivalent reverberant spectrum in Section 4.5.1. (See Equation (62).)

4.7.2 Theoretical Results — The equivalent acoustic environments for simulation of the structural response of the Nimbus shroud during the various phases of flight are shown in Figures 68-71. Each figure is in two parts, (a) and (b), representing the cylindrical and conical sections of the shroud, respectively. A discussion of these equivalent environments and the significant conclusions arising from these results are presented in the following paragraphs.

Lift-Off

Figure 68(a) describes the equivalent acoustic environments for simulation of the response in the cylindrical section of the shroud at lift-off. The actual lift-off acoustic spectrum has also been shown in this figure for the purposes of comparison. The most significant effects which are illustrated in Figure 68(a) can be summarized as follows:

- The low-frequency deficiencies in the one-duct progressive wave configuration are immediately apparent. These are caused primarily by the fact that the ($m=1$, $n=2$) resonant mode of the shroud, at 125 Hz, is not excited by the one-duct acoustic field. This can be verified by examining Figure 46 which shows the acceleration responses of the cylindrical section of the shroud to progressive-wave duct excitation. The acceleration spectrum for the one-duct case, shown in the latter figure, has contributions from the $n=0$ modes only, the joint acceptances (or acoustic—structural coupling factors) being zero for all other modes where $n \neq 0$.

- The similarity between the lift-off environment and the eight-duct progressive wave environment (in terms of exciting the structure to a given response level) is also illustrated in Figure 68(a), except at low frequencies where the eight-duct configuration is substantially more efficient.

- The equivalent reverberant acoustic field displays a sharp dip in the spectrum at 250 Hz, while the actual lift-off acoustic spectrum peaks at this frequency. This characteristic can be verified by comparing the normalized responses at 250 Hz for these two environments, as shown in Figures 30 and 43. The response to the lift-off environment is approximately $4.5 \times 10^2 \ g^2/(psi)^2$, compared to about $6.0 \times 10^4 \ g^2/(psi)^2$ for the reverberant acoustic field. This result is again due to the different joint acceptance characteristics of the lift-off and reverberant environments.

- At low frequencies, below about 80 Hz, it is observed in Figure 68(a) that the eight-duct progressive wave configuration is the most efficient of the equivalent acoustic environments. Over the frequency range of 80 Hz to about 800 Hz however, the reverberant acoustic field is the most efficient acoustic environment. At high frequencies, all three equivalent acoustic environments are very similar except for the peak in the reverberant spectrum at 4,000 Hz.

- The peak in the equivalent reverberant spectrum at 4,000 Hz is due primarily to the fact that the reverberant acoustic field apparently does not excite the structure efficiently in the region of the acoustic critical frequency (which for the lower section of the Nimbus shroud is approximately 5,220 Hz). The reason for this lies in the particular structural models which were analyzed, and this point can be explained with the aid of Figure 43. The latter figure shows the space-average responses of the cylindrical section and a smaller section between ring frames, for the case of a reverberant acoustic field. It is observed

68

that the difference between the responses in the region of the acoustic critical frequency is quite significant. This difference is caused by the relative magnitudes of the joint acceptances for the two structural models in this frequency region as follows:

Defining "coincidence" as wavelength matching between the structural and acoustic waves, or $\lambda_e = \lambda_a$, it follows that the condition of axial coincidence is given by the equality $\dfrac{2L_x}{m} = \lambda_a$, where L_x is the structural length and m is the number of axial half-waves (or the axial mode number); thus, the axial mode number corresponding to the coincidence condition is given by $m = 2L_x f/c_0$, where f is the acoustic critical frequency and c_0 is the speed of sound in air. For the cylindrical section of the Nimbus shroud this axial mode number has been computed to be about $m = 100$ for the acoustic critical frequency of 5,220 Hz, whereas for the section between ring frames the axial mode number is about $m = 30$. The axial joint acceptance $j_m^2(\omega)$, is approximately equal to $1/4m$ at coincidence (Reference 50), where m is the axial mode number corresponding to the coincident condition. Thus, for the section between ring frames, the joint acceptance at coincidence is about three times as great as the joint-acceptance for the total cylindrical section.

In contrast, the results presented in Figure 30 show that for the lift-off environment the response in the region of coincidence is relatively unaffected by the characteristics of the structural models chosen. Thus the result shown in Figure 68(a) for the equivalent reverberant acoustic field in the region of coincidence is directly attributable to the structural model. If in practice, the cylindrical section of the shroud responded in the form of individual cylindrical segments bounded by nodes at each ring frame, the peak in the equivalent reverberant spectrum at 4,000 Hz would not be observed.

o   It should be noted that the results presented in Figures 68(a) and 68(b) represent the equivalent acoustic fields necessary for simulation of the space-average responses of the cylindrical and conical sections of the shroud, respectively. Since the lift-off acoustic environment is virtually the same for both sections, and the dimensions of the two structural models analyzed are not vastly different, the results shown in Figures

69

68(a) and 68(b) are very similar. Thus the above discussion concerning the cylindrical section is also applicable to the conical section. Although the differences between the equivalent acoustic environments for the two sections of the shroud are not too great except in the case of the one-duct progressive wave configuration, they must nevertheless be considered when applying excitation over the whole shroud. Thus if the equivalent reverberant acoustic field shown in Figure 68(a) was applied over the whole shroud, the responses in the conical section would not exactly duplicate those experienced at lift-off, particularly in the 125 Hz and 500 Hz third-octave bands.

Mach 0.7

The equivalent acoustic environments for simulation of the response to the aerodynamic fluctuating pressures at Mach 0.7 are shown in Figures 69(a) and 69(b). The actual external sound pressure levels predicted for this flight event are also shown in these figures for the purposes of comparison. The most significant effects observed in these figures can be summarized as follows:

- The low frequency deficiencies in the one-duct progressive wave configuration are again immediately apparent in the results for the cylindrical section. These effects are particularly noticeable in the region of the (m=1, n=2) shroud mode, which occurs at 125 Hz in the cylindrical section and at 210 Hz in the conical section. However the one-duct progressive wave configuration for the conical section is observed to be substantially more efficient than that for the cylindrical section in the frequency region below the (m=1, n=2) structural mode. The general comments given earlier for the lift-off environment are also relevant here.

- At low frequencies, below about 80 Hz (125 Hz for the conical section) the eight-duct progressive wave configuration is the most efficient of the equivalent acoustic environments. Over the frequency range of 100 Hz to 500 Hz (160 Hz-630 Hz for the conical section) however, the reverberant acoustic field is the most efficient acoustic environment. At higher frequencies all three equivalent acoustic environments display the same levels, except for the absence of a sharp dip in the reverberant spectrum at 5,000 Hz. As discussed previously this characteristic is caused by the joint acceptance properties of the cylindrical structural model.

- A detailed comparison between Figures 69(a) and 69(b) shows that, unlike the lift-off portion of the flight, the in-flight external sound pressure levels (and thus the equivalent acoustic fields) differ substantially between the cylindrical and conical sections of the shroud. This presents an immediate problem when considering the application of an equivalent

70

acoustic environment to the whole shroud structure. Obviously the
reproduction of an equivalent acoustic spectrum defined for the cylindrical
section would result in over-testing of the conical section. A number of
techniques can be adopted to overcome this problem. These techniques
include absorbing materials or attenuators for the conical section, double
reverberation room configurations, or alternatively, enhanced excitation
of the cylindrical section while maintaining reverberation rcom levels
to within those specified for the conical section. However, the noise
reduction calculations for this particular flight environment demonstrated
that the average sound pressure levels within the shroud were determined
essentially by those external levels existing over the cylindrical section;
the lower external sound pressure levels over the conical section had an
insignificant effect on the final results. Furthermore the mechanical
path from the shroud to the spacecraft involves primarily the cylindrical
section. Thus it is anticipated that the application of an equivalent
acoustic field over the cylindrical section only (i.e., the conical section
would not be subjected to acoustic excitation) would result in a proper
simulation of the spacecraft vibration response, since the energy transmission
via the acoustic and mechanical paths would be almost identical to that
experienced in flight.

Mach 0.8

The equivalent acoustic environments for simulation of the response to the aerodynamic
fluctuating pressures at Mach 0.8 are shown in Figures 70(a) and 70(b). The actual
external sound pressure levels predicted for this flight event are also shown in these
figures for the purposes of comparison. The most significant effects observed in these
figures can be summarized as follows:

⊚   The low frequency dificiencies in the one-duct progressive wave
     configuration are again observed in these results for the cylindrical
     section. This configuration is again more efficient for the conical
     section than for the cylindrical section, as was the case for the
     Mach 0.7 flight event.

o   For the cylindrical section of the shroud, the one-third octave band
     levels in the low frequency region are considerably higher than those
     predicted for Mach 0.7; this is the result of the shock wave oscillation
     over the cylindrical section at Mach 0.8. In contrast, the one-third
     octave band levels over the conical section follow more closely those
     predicted for the Mach 0.7 case.

71

o   At low frequencies, the eight-duct progressive wave configuration is
        the most efficient of the equivalent acoustic environments, while over
        the mid-frequency range the reverberant acoustic field is the most
        efficient acoustic environment. At higher frequencies all three
        equivalent acoustic environments display the same levels except for
        the reverberant acoustic field in the 5,000 Hz one-third octave band,
        for the reasons discussed earlier.

•   Again, significant differences between the in-flight external sound
        pressure levels over the cylindrical and conical sections of the shroud
        have resulted in substantial differences between the equivalent
        acoustic spectra for the two shroud sections. The discussion of this
        problem given earlier for the Mach 0.7 case is applicable to the
        Mach 0.8 case also. A further simplification may be possible in the
        very low frequency region; although the one-third octave band sound
        pressure levels necessary to simulate the shroud response are somewhat
        higher in this frequency region due to the shock wave oscillation (see
        Figure 70(a)), the predominant resonant frequencies of the spacecraft
        may occur at significantly higher frequencies. In such a case the
        equivalent acoustic spectra shown in Figure 70(a) could be modified
        considerably in the lowest one-third octave bands.

Mach 2.0

The equivalent acoustic environments for simulation of the response to the aerodynamic
fluctuating pressures at Mach 2.0 are shown in Figures 71(a) and 71(b). The actual
external sound pressure levels predicted for this flight event are also shown in these
figures for the purposes of comparison. The most significant effects observed in these
figures can be summarized as follows:

⊚   The general characteristics of the equivalent acoustic fields are very
        similar to those discussed for the Mach 0.7 case, though the relative
        one-third octave band levels are considerably lower in the cylindrical
        section of the shroud.

o   Although the predicted in-flight external sound pressure levels over the
        cylindrical and conical sections vary by only 3 dB-4 dB over the
        frequency range, the differences in the equivalent acoustic environments
        are slightly greater. This is particularly true for the one-duct progressive
        wave configuration at low frequencies, where the maximum variation
        between levels over the cylinder and the cone approaches 20 dB in the
        125 Hz one-third octave band. These differences however, are due
        primarily to the shift in the resonant frequencies between the cylindrical

72

and conical sections; this point can be verified by comparing the cylinder and cone responses for aerodynamic turbulence, the reverberant acoustic field, and the progressive wave duct environments. Such a comparison shows that in general the peak responses and trends in the response curves are very similar in magnitude for the two geometries, but are shifted in frequency.

These differences between the equivalent acoustic spectra for the two sections of the shroud, although relatively small (except in the case of the one-duct progressive wave configuration), should be carefully considered when applying acoustic excitation over the whole shroud. However, it was again found during the noise reduction calculations that the average sound pressure levels within the shroud were determined essentially by those external leveis existing over the cylindrical section. This effect was discussed earlier for the Mach 0.7 flight event.

Special Cases

At Mach 0.7 the turbulent flow over the cylindrical section of the shroud is divided into three distinct zones, as discussed previously; these zones involve separated flow followed by two zones having modified attached flows. The structural responses of two cylindrical segments between ring frames were discussed earlier in Section 4.3.2 for this case, and the results were presented in Figure 36. These structural segments extend from station 115 to station 159, and from station 198.5 to station 221.5, respectively. The former segment is subjected to separated flow over the forward region and modified attached flow over the aft region at Mach 0.7; the latter segment is subjected to modified attached flow over the whole length.

For these special structural cases, the equivalent reverberant acoustic fields necessary for simulation of the space-average responses have been computed, and are shown in Figures 72 and 73, respectively. The predicted external sound pressure levels are also shown in these figures for reference.

The result shown in Figure 72 indicates that the localized reverberant acoustic field is less efficient than the aerodynamic environment in the very low frequency region, but is generally more efficient over the remainder of the frequency range. The general shape of the equivalent reverberant spectrum is very similar to that shown in Figure 69 for simulation of the response in the whole cylindrical section.

The result shown in Figure 73, for the cylindrical segment between stations 198.5 and 221.5, indicates that the localized reverberant acoustic field is substantially less efficient for frequencies below about 500 Hz, but more efficient for frequencies above about 1,600 Hz. This result can be verified by comparing the responses of the cylindric ' segment to the aerodynamic and reverberant environments, shown in Figures 36 and 43, respectively.

73

5.0 ACOUSTIC TESTING TECHNOLOGY

5.1 Introduction

In the previous section, the in-flight acoustic environments and the structural responses of typical shroud/spacecraft systems were discussed extensively. Based upon simulation of the space-average shroud responses, equivalent acoustic environments were defined and compared in detail. In the present section, a comprehensive review of acoustic testing technology is presented. Firstly, a discussion of practical acoustic test environments, which includes the various spatial correlations that can be achieved, together with techniques for varying the time and spatial distribution of the acoustic field, is presented in Section 5.2. Various acoustic testing configurations for shroud/spacecraft systems are examined and technical trade-off considerations are reviewed. The effects of the reverberation room dimensions on the lowest test frequency, and the volume occupied by the test specimen relative to the room volume are discussed in Section 5.3. This is followed in Section 5.4 by a general discussion of the simulation problem, where simulation of the acoustic environment versus simulation of the structural response is examined in detail. Finally, a typical test specification format, together with testing tolerances, is presented in Section 5.5.

5.2 Acoustic Test Environments

The results presented in Section 4.0 have demonstrated the important differences between the structural responses of the shroud when excited by the various in-flight environments and typical laboratory acoustic fields. These differences depend primarily on the spatial variations of the phase of the pressure fluctuations in narrow bands of frequency over the vehicle. These differences in phase, generally expressed in terms of spatial correlation, can be approximately accounted for by suitable adjustment in the spectrum and intensity of the acoustic simulation. However, for such adjustment to be practical, the acoustic field must have at least some of the important correlation properties of the flight environment. For example, it is exceedingly difficult to excite structural bending waves around the circumference of a cylinder if the acoustic pressures are in phase and of the same amplitude over the entire circumference. There are two pure types of acoustic field which can be employed for acoustic testing; the reverberant field and the progressive plane wave field. These environments, together with practical testing applications, are discussed in detail in the following sub-sections.

5.2.1 The Reverberant Acoustic Field

5.2.1.1 Basic Characteristics of the Pure Reverberant Field — The ideal reverberant field is diffuse when excited by a wide band acoustic source, in that the field is continuous in both narrow band frequency spectrum and angular distribution of energy. A practical reverberation room does not fulfill this definition at low frequencies, but sometimes approaches the ideal diffuse condition at high frequencies. Nevertheless, the reverberation room furnishes a test tool of high utility for tests in which the spectrum and level are uniform over the entire specimen

74

surface. Diffusivity may be defined as being a condition whereby there is equal probability that sound will pass through a given point from any direction, having any frequency and any amplitude. Ideally, an ordinary pressure sensitive micro-phone, when exposed to a diffuse field, will give the same reading at all points in the field. Also, a narrow-band filter will show little or no variation in output as it is tuned across the spectrum of the diffuse sound field. Another definition of diffusivity states that if an omni-directional broadband microphone is moved around the room in some random manner, all space having the same sound pressure level within 1 dB can be considered to be within the diffuse field. This will not, of course, include space close to the walls, the sound sources, or highly absorptive or reflective surfaces.

In mathematical terms, it has been stated (Reference 59) that as a general rule, if there are at least five normal modes within the bandwidth of one acoustic mode, then the sound field can be considered to be reasonably diffuse.

The modal density or number of modes per unit bandwidth, of a rectangular room is given by the expression (Reference 26):

$$\frac{dN}{df} \approx \frac{4\pi V f^2}{c^3} + \frac{\pi S f}{2c^2} + \frac{L}{8c} \qquad (65)$$

where

$$V \quad = \quad \text{Volume of the room}$$

$$S \quad = \quad \text{Surface area of the room}$$

$$L \quad = \quad 4(L_x + L_y + L_z)$$

$$c \quad = \quad \text{Speed of sound}$$

$$f \quad = \quad \text{Frequency}$$

$$L_x, \, L_y, \, L_z \quad = \quad \text{Dimensions of the room}$$

This equation is usually approximated to give the number of individual modes, $N(f)$, accurring within a frequency range, Δf, as follows:

$$N(f) \approx \frac{4\pi V f^2}{c^3} \cdot \Delta f \qquad (66)$$

The relationship between the bandwidth of an acoustic mode, δf, and the resonant frequency of the mode, f, is;

75

$$\frac{f}{\delta f} = Q = \frac{ca}{8\pi V} \qquad (67)$$

where Q is the amplification factor of the acoustic mode and a is the acoustic absorption for the mode considered, given by the product of the absorption coefficient α of the surfaces and the area of the surfaces.

Thus for the condition of five or more normal modes within the bandwidth of any one mode, it is required that:

$$\frac{N(f)}{\Delta f} \cdot \delta f \geq 5$$

i.e.,
$$\frac{4\pi V f^3}{c^3 Q} \geq 5 \qquad (68)$$

In the above equations, the modal frequencies of a rectangular enclosure are given by the relation:

$$f_{\ell m n} = \frac{c}{2}\left[\left(\frac{\ell}{L_x}\right)^2 + \left(\frac{m}{L_y}\right)^2 + \left(\frac{n}{L_z}\right)^2\right]^{\frac{1}{2}} \qquad (69)$$

where ℓ, m and n are integers.

Since these integers may be varied independently over the range from zero to infinity, it may be seen that a large number of allowed frequencies or Eigentones may be accumulated within the first decade above the first such frequency. It has long been known that a cubical room, or a room having definite integral relations between the lengths of its walls, will show a tendency for the modes to congregate, leaving large gaps in frequency space. To obtain a room shape which spreads the modes in a uniform manner, Sepmeyer (Reference 67), studied the performance of various reverberation room sizes using this equation and has determined some ideal shapes. Among these is a room having the dimensional ratio of 1:0.79 : 0.63.

The discussion so far has been concerned with the modal properties of reverberation rooms and the various definitions of diffusivity. Ultimately however, it is necessary to consider the requirements of the test specimen in determining if the sound field is useful for the test. The aforementioned general rule concerning five resonances

76

within the bandwidth of a given room mode does not specify that these five resonances have peaks at each and every point in the room; this would in fact be an impossible requirement. In the limit therefore, it is not necessary that the sound field be ideally diffuse, if it can be arranged that all points in the frequency domain of the specimen be matched to points in the frequency domain of the test chamber so that all specimen resonances are driven by chamber resonances. The subject of diffusivity and the influence of the test specimen on the characteristics of reverberation rooms is discussed further in Section 5.3.2.

In an ideal reverberant test facility, the sound field is perfectly diffuse and the space correlation coefficient at a given frequency is fixed and given by:

$$R(x, x') = \frac{\overline{P(x) \cdot P(x')}}{\sqrt{\overline{P^2(x)} \cdot \overline{P^2(x')}}}$$

$$= \frac{\sin 2\pi f \Delta x/c}{2\pi f \Delta x/c} \tag{70}$$

where $P(x)$ = instantaneous pressure at point x

          f = frequency

          Δx = separation between points x and x'

          c = speed of sound

          $\overline{}$ = signifies the long time average

Only by adding localized sources within a reverberant facility would it be possible to modify this inherent spatial correlation.

5.2.1.2 Testing Concepts for Varying the Time and Spatial Distribution of Acoustic Amplitudes — While a primary purpose for using a reverberation chamber is to expose the whole of a given specimen to a uniform sound field, it is not always desirable that all areas of the specimen receive the same sound pressure level. This is particularly so for typical shrouds where the levels over the conical and cylindrical sections have been shown to differ substantially during certain flight events. Accordingly, laboratory techniques have been studied for varying the sound pressure level in order to expose certain areas to higher or lower levels than the average level. These techniques make it possible to expose the bulk of a shroud/spacecraft system to an average level simulating say general aerodynamic noise.

77

Small, or even large areas of the structure may be simultaneously exposed to higher or lower levels by installing sound sources or sinks near these areas.

Possible acoustic test configurations are reviewed in the following paragraphs, and the degree to which they can simulate the required environment is discussed.

Simple Reverberation Room

In this configuration, the specimen is normally standing free near the center of a reverberation room. This represents the most common method of performing an acoustic test of a large component. The specimen is readily available for instrumentation installation and requires no special purpose facilities for the test. The main disadvantage of this configuration is that it is unable to produce any sound level gradients over the surface of the shroud to simulate the effect of any protuberances. In addition, it would generally be necessary either to simulate the maximum loading that will occur at any one point on the shroud or to conduct the test at a lower level and attempt to scale up the vibration response of the structure to include the effect of local areas of higher excitation.

Reverberant Field with Absorption

This concept is similar to the simple reverberation room method, except that an absorbent skirt of varying thickness is placed around the sections of the vehicle which are required to be exposed to a lower level. For a typical shroud/spacecraft system, the absorbent skirt would be positioned over the conical section of the vehicle. The absorbent material is designed to reduce the sound pressure levels around the conical section of the vehicle from the higher levels occurring in the rest of the reverberation room.

Reverberant Field with Local Excitation

This configuration consists of the specimen mounted in a reverberant chamber with local sources applied in the regions of high excitation. The problems with this configuration are concerned with designing suitable horns for applying this high level loading without excessively loading the remainder of the structure through the local excitation noise generating systems. To this end, a model program to develop the required horns usually proves necessary and desirable.

Reverberant Field with Short Ducts and Absorbent Panels

In this configuration, the use of progressive wave ducts over only the cylindrical section of a shroud allows higher acoustic levels to be generated locally, while the remainder of the structure is maintained at a lower reverberant level. Such a test configuration would be suitable for simulation of the intense local pressure

78

fluctuations near protuberances or regions of separated flow on the spacecraft shrouds. Absorbent material can be placed over other sections to provide a gradient in acoustic level if desired. The ducts would be powered by acoustic sources connected by transition horns to the duct. The disadvantages of such a configuration are concerned with the application of absorbent material to produce any required sound pressure level gradients, and the difficulty of applying instruments such as strain gages externally to the specimen. This configuration could effectively result in several zones with different or decreasing noise levels along the vehicle axis.

Double Reverberant Field with Local Excitation

When justified by a particular test requirement, substantial flexibility in shaping the spatial distribution of the sound pressure levels could warrant the use of a double reverberant field with local enhanced excitation. The cylindrical and conical sections of the spacecraft shroud would essentially be housed in separate chambers having a common wall, and subjected to independent reverberant acoustic fields with local excitation superimposed where necessary. This arrangement allows somewhat more freedom in generating local high sound pressure levels for testing small areas associated with protuberances or separated flow. However, in applying these local areas of high excitation, care must be taken to insure that the structure is not directly loaded by the air through the local excitation noise generating horn system.

Reverberation Room with Full Length Ducts

In this configuration, which is very similar to the short duct configuration discussed above, several progressive wave ducts are utilized which extend down the complete length of the spacecraft shroud but do not span the entire circumference of the shroud. The primary purpose of the ducts is to enhance the sound pressure levels existing around protuberances and to provide suitable sound pressure level gradients down the axis of the shroud. The ducts can be shaped independently so as to simulate individual protuberance regions and produce the necessary gradient across the structure.

Reverberation Room with Acoustic Attenuators

In this configuration, a reverberant acoustic field is applied to the specimen and "attenuators" are utilized to locally reduce the overall applied acoustic field over certain portions of the test article. The "attenuators" simply consist of muslin sheets (or other material possessing a high flow resistance) attached to a framework which is placed against the test article so that a cavity exists between the muslin sheeting and the test article surface. This technique would normally be attempted during reverberant testing of large shroud/spacecraft systems, and could prove suitable for simulation of the various zones of aerodynamic fluctuating pressure over the cylindrical sections of cone-cylinder shrouds at transonic Mach numbers.

79

The primary function of the attenuators is to provide an even attenuation at all frequencies of interest at the required positions on the test specimen. However, in some special cases it may be desirable to employ attenuators so that acoustic levels will be continuously variable with position on the specimen. The corresponding reduction in the acoustic level applied to the test article is usually referred to as the "insertion loss."

The application of attenuators is complicated, since it is difficult to obtain a flat spectrum of attenuation over a sufficiently wide frequency range because of the fact that single elements of an attenuator structure will only behave as such over a limited frequency range. Experimental results (Reference 68) have shown that the insertion loss associated with attenuators constructed from several layers of muslin sheeting placed over a wooden framework varies with frequency and furthermore is affected by resonance conditions. These resonances are associated with the fundamental dynamic response of the attenuator and the air cavity trapped beneath the attenuator. However, it has been shown (Reference 68) that by proper design, a flat spectrum of attenuation can be obtained within the limits of $\pm$ 2 dB over the frequency range of 200 Hz to 5000 Hz by using a suitable flow resistance for the attenuator. For such a design, the maximum insertion loss over this frequency range is typically 10 dB.

5.2.2   The Progressive Wave Acoustic Field

5.2.2.1   Basic Characteristics of the Progressive Wave Field — The progressive wave is more precisely a plane acoustic wave, differing only in that it may contain cross-modes which are introduced by the geometry of the tube along which the wave is propagated. In a progressive wave facility, the energy travels from a transducer to a coupling horn, and then along a tube to a termination where it is absorbed, reflections being kept to a minimum. For frequencies lower than the cross-mode frequencies, the progressive wave facility can be considered to be a plane wave tube. The frequencies of the cross-modes are given by the relation:

$$f_{mn} = \frac{c}{2} \sqrt{\left(\frac{n}{L_x}\right)^2 + \left(\frac{m}{L_y}\right)^2} \qquad (71)$$

where L_x and L_y are the cross-sectional dimensions of the progressive wave duct, m and n are integers, and c is the speed of sound.

Theoretically, a plane wave tube imposes no particular spectral characteristics upon the acoustic signal introduced, other than the low frequency cut-off of the coupling horn between the transducer and the operating section. In actual practice it is possible to approach this theoretical operation only under ideal conditions, when standing waves have been adequately suppressed. A progressive wave facility offers high efficiency and utility for testing a vehicle which requires continuous variation in level over a portion or all of its surface.

80

In a plane progressive wave acoustic field, the spatial correlation for a single frequency is given by:

$$R(x, x') = \cos(2\pi f \Delta x / \vec{c})\tag{72}$$

where

$\vec{c}$ = trace velocity of the sound wave over the path length Δx

= $c/\cos\theta$

θ = angle between the direction of the path length Δx and the incoming sound wave.

For most plane wave test facilities, θ is zero or very nearly so, so that $\vec{c}$ is very nearly equal to c. Only by using several plane wave sources such as an array of plane wave tubes located circumferentially about a cylindrical or conical specimen, can any significant change be made to the space correlation function in practical plane wave test facilities.

5.2.2.2 The Progressive Wave Duct Testing Configuration — Perhaps the most widely-used configuration for acoustic testing of components and flat panel structural specimens is the progressive wave facility. Such a facility can deliver higher acoustic levels per acoustic watt input than any other type of facility (excluding the standing wave tube). With a proper termination and good quality sound source, frequency response characteristics of such a facility can be quite uniform. To minimize the potential influence of cross-modes in such a facility and to increase the sound levels, the cross-sectional area of the progressive wave duct is made as small as possible. The basic limit on this area, is the increasing effect of radiation damping on the response of the low order structural modes as the ratio of duct cross-sectional area to structural area is decreased. The first cross-mode occurs at a frequency given by the speed of sound divided by twice the largest cross-dimension (i.e., $f_c = c/2L_y$). Above this frequency the sound field within the duct is distorted due to the complications arising from the cross-modes. Typically, the resulting sound pressure is non-progressive, varying laterally across the duct and decaying exponentially in amplitude along the duct axis. The severity of the cross-modes can usually be reduced by careful design utilizing duct walls which possess high self damping.

The basic elements of a progressive wave test facility consist of a noise source, horn coupling device to the progressive wave test section, the test section with provision for mounting to the vehicle, and a termination designed to prevent reflected waves from returning down the progressive wave duct. In applying this configuration to shroud/spacecraft systems, a series of full-length ducts is placed around the entire circumference of the shroud. An example of this type of testing configuration is the Spacecraft Acoustic Laboratory (SAL) described

81

in References 56 and 57. This acoustic facility consisted of 16 progressive wave
ducts arranged around the circumference of the test article (which consisted of
the Apollo Command Module, Service Module and the Spacecraft Lunar Adapter).
The ducts were constructed of wood and steel, and visco-elastic damping com-
pound was used to reduce vibration of the steel components. The outer wall of
each duct was adjustable radially to control the sound pressure levels in the
longitudinal direction by varying the duct to test article clearance space. By
utilizing 16 independent air-modulator noise sources, the sound field was optimized
in each duct for overall level, spectral content and correlation between adjacent
ducts.

Other examples of progressive wave testing configurations for cylindrical vehicles
include the GSFC Launch Phase Simulator — Progressive Wave Facility (References
60 and 69), and the special progressive wave facility constructed for testing a
1/10th scale model Voyager spacecraft and shroud system (Reference 70). In both of
these facilities, the progressive wave test section is formed by placing a concentric
fiberglas cylinder over the particular shroud/spacecraft assembly so as to form a
single annular duct. A considerable number of experiments have been conducted
in the GSFC facility, utilizing a full-scale Nimbus shroud and a structural model
of the OGO spacecraft (References 20, 60 and 61), while the limited experiments
which have been conducted with the Voyager scale model have been largely of an
exploratory nature (Reference 70).

5.2.3 Free-Field Testing — Free-field testing is usually contemplated when the
required correlation characteristics cannot be met in either the reverberation room or the
progressive wave facility; such a test may be performed outdoors or within an anechoic
room. Alternatively, this type of test may be conveniently undertaken in conjunction with
a static test firing of a particular rocket, or even a vehicle launching. A test conducted
in this manner offers a reasonable simulation of the rocket noise environment provided that
the test article is positioned correctly relative to the rocket exhaust flow.

Free-field testing outdoors or in an anechoic room would normally involve exciting the test
article with horn or loudspeaker-generated plane waves at fixed angles of incidence, in an
attempt to simulate, say, the response of a shroud/spacecraft system to the noise produced
by various segments of a deflected rocket exhaust flow. For the lift-off environment the
low frequency noise components arrive at the spacecraft shroud at almost normal incidence,
while the high frequency noise components impinge the shroud essentially at grazing incidence.

A drawback often associated with free-field testing, is the high acoustic power necessary to
provide a given sound pressure level at the specimen surface. However, while free-field
testing may not provide an adequate qualification test, it offers a useful technique for
qualitative studies of response and noise reduction of shroud/spacecraft systems.

82

5.2.4 Technical Tradeoff Considerations — The acoustic testing configurations discussed above illustrate some of the possible ways that a spacecraft/shroud system may be tested in reverberant, progressive wave and free-field acoustic environments to achieve a wide range of spatial distribution of sound levels. Some of the reverberant configurations have been presented only for completeness since they are impractical within the present state of the art. Thus, an optimum testing technique must be chosen which is within the state of the art and which utilizes some of the advantages of the preceeding concepts. Some of the detailed considerations which must be accounted for in selecting an optimum configuration are briefly reviewed in the following paragraphs.

The Pure Reverberant Field

It must be noted immediately that a simple reverberant field test may not be able to provide the high levels often required in localized areas by certain shroud-vehicle combinations. Furthermore, the required acoustic power to generate a sound pressure level of say 167 dB in a large reverberant room imposes a high cost on such a facility. Under some conditions it may be possible to utilize a low test level for fatigue life tests so that a long test at say 155 dB could be considered equivalent to a shorter test at a much higher level. In addition, such a test sould at least allow the basic response modes of the shroud/spacecraft system to be determined. However, it would not be of a form which could be described as sufficient for a structural qualification test of the shroud or spacecraft although it might be highly appropriate for acceptance or systems testing.

One serious drawback of reverberant field testing is the tendency for an approximately uniform distribution of the sound pressure with space. As indicated earlier, flight conditions involve steep gradients in sound pressure levels; in a reverberant field, no such gradients will be produced, normally.

A major advantage of reverberant field testing is, of course, that it has the potential capability for testing an entire structural section or shroud/spacecraft system. If maximum test levels cannot be met, then the lower test levels may often be used initially. The response of the entire specimen to th's low level is then determined in order to establish the size of the sub-systems which can be separated out and tested individually, where necessary, to meet performance criteria for the noise environments. These individual sub-systems may then be constrained by the proper edge conditions, and exposed to higher levels in smaller reverberation rooms as a qualification test. However, it will be recognized that such a technique does not allow the full response of the structure to the individual areas of high loading to be simulated.

The Full Progressive Wave Duct Configuration

For a full duct configuration, such as that described earlier, several identical parallel ducts would be constructed, utilizing separate noise sources through coupling horns to direct the sound energy along the entire length of the shroud under test. The individual ducts would have three sides, two of which were shared with other ducts, the third side

83

being the outer wall. In this way a relatively small amount of acoustic energy can be used to generate very high levels on the test specimen; a consequence of using relatively small amounts of energy is that small losses of energy along the duct add up to large changes in sound pressure level as the energy prop gates down the duct. The most significant source of this loss is the absorption by the vehicle or shroud; insufficient sealing between the duct walls and the test specimen, and radiation through the walls of the duct also will cause the energy to be decreased. This means that the duct must be effectively sealed to the vehicle with all the problems of damage and damping that have been mentioned previously.

Estimates of the absorption of the vehicle or shroud can be derived from model experiments, taking care to insure that a dynamically similar model specimen is created, or from judgment based on previous test p ams. The problem of sealing the ducts to the vehicle can be accomplished by using s ·. seals once the ducts have been carefully contoured to the exact shape of the vehicle. Additionally, soft putty can be used to seal points where sudden discontinuities occur. The problem of radiation of sound through the outside walls of the duct is controlled by mass loading and damping of the walls themselves.

Within each duct, the sound intensity is inversely proportional to the area of the duct, and the position of the outer wall can be controlled to produce the required sound pressures down the length of such a vehicle or shroud. Sudden changes in area have to be avoided because of the impedance mismatch, but gradual changes in area and hence sound pressure are entirely feasible. Thus, it is reasonable to expose a shoulder area on a shroud transition section to a sound pressure level of say 167 dB with the duct having an outer wall six inches away from the vehicle skin. Then by gradually increasing the distance of this wall from the skin, the sound pressure level will be reduced. An increase of the distance to 24 inches will reduce the level to 162 dB. In actual practice, the specimen walls will absorb approximately 0.5 decibels per foot from the ducts so that further increases in area for reduced levels will probably be unnecessary. Again, this is best evaluated by a model study.

Summary of the Possible Testing Configurations

Table III presents a summary of the possible testing configurations which have been reviewed in the discussion so far. This table lists representative sound pressure levels attainable, as well as an indication of the correlation characteristics which will be produced. A note is included concerning the amplitude as a function of space and it is followed by certain brief remarks appropriate to each configuration. The parameters listed can be compared directly with similar parameters for hypothetical flight conditions which are given in the top line of the table. The spectral distribution parameter is excluded from Table III because this limitation is imposed mainly by the acoustic sources rather than by the facility.

84

TABLE III

SUMMARY OF POSSIBLE ACOUSTIC TESTING CONFIGURATIONS

Configuration	Maximum OA SPL (Typical)	Space Correlation Coefficient		Amplitude Function	Remarks
		Longitudinal	Circumferential		
Hypothetical Transonic Flight Conditions	167	$e^{-\delta_x\lvert\xi\rvert} \cdot \cos\gamma_x\,\zeta$	$e^{-\delta_y\lvert\eta\rvert}$	Discontinuous	o Separated flow, shock waves and turbulent wakes complicate the environment over the shroud.
Pure Reverberation	156	$\dfrac{\sin kx}{kx}$	$\dfrac{\sin k\theta}{k\theta}$	Essentially constant	o Mathematically simple sound field
Reverberant Plus Absorbent Skirt					
In Room	156	$\dfrac{\sin kx}{kx}$	$\dfrac{\sin k\theta}{k\theta}$	Constant	o Absorbent skirt prevents overtest of conical section of shroud
In Skirt	154	$e^{-kx}\dfrac{\sin kx}{kx}$	$e^{-kx}\dfrac{\sin k\theta}{k\theta}$	e^{-kx}	o SPL rapidly decreases in skirt
Short Progressive Wave Ducts, Reverberant Field Plus Absorbent Skirt					o Short ducts over cylindrical section of shroud provide high SPL associated with transonic flight.
In Ducts	167	$\cos kx$	1* in each duct	Controllable	
In Skirt	154	Same as skirt above			o Absorbent skirt prevents overtest of conical section exposed to the reverberant field.
In Room	156	Same as room above		Constant	
Double Reverberation Room	157 155	$\dfrac{\sin kx}{kx}$	$\dfrac{\sin k\theta}{k\theta}$	Constant in each room	o Allows two levels in reverberant field to simulate cylindrical and conical sections of the shroud; expensive.
With local sources	161	$\dfrac{\sin kx}{kx}$	$\dfrac{\sin k\theta}{k\theta}$	Slightly discontinuous	. o Adds additional flexibility to the reverberant field, allowing enhancement of SPL's around protuberances and separated flow regions.
Full Length Progressive Wave Ducts and Reverberation Room					o Similar to short duct configuration except that ducts do not span entire shroud circumference. Especially suitable for simulating high SPL's caused by protuberances.
In Ducts	167	$\cos kx$	1* in each duct	Controllable	
In Room	156	$\dfrac{\sin kx}{kx}$	$\dfrac{\sin k\theta}{k\theta}$	Constant	
Full Length Progressive Wave Configuration	167	$\cos kx$	1* in each duct	Controllable	o Suitable for shrouds where the SPL decays axially along its length.
Reverberant Field with Local Attenuators					o Suitable for testing bulk of specimen at high level, and reducing the SPL locally over certain portions of specimen.
In Room	156	$\dfrac{\sin kx}{kx}$	$\dfrac{\sin k\theta}{k\theta}$	Constant	
Between Attenuators and Specimen	146	$\dfrac{\sin kx}{kx}$	$\dfrac{\sin k\theta}{k\theta}$	Almost Constant	

*Below first cross mode

85

5.3 Special Considerations in Reverberant Testing

5.3.1 Test Specimen Size Relative to Reverberation Room Volume — A long standing "rule-of-thumb" concerning the allowed size of a given specimen being tested in a reverberation has been that the specimen volume should not exceed 10% of the volume of the test chamber. In the past, this criterion has been accepted for testing, however, little information has been made available in the literature to show if this rule is overly conservative or too liberal.

Accordingly, a brief study has been made using a model reverberation chamber having the "ideal" dimensional ratio of 1:.816:.707. A "point source" was mounted in one corner of the room. This source consisted of a standard horn driver with a small tube mounted in the place of the horn. This tube had an inside diameter of approximately 1/4 inch and was filled with steel wool to increase its output impedance. The tube extended through the wall of the chamber corner so that the speaker was mounted outside and the opening of the tube was directly in the corner radiating outwards into the chamber. A 1/2 inch B & K microphone Model 4133 was mounted in an opposite corner on the same wall of the chamber. Sine sweep and random signals were radiated into the chamber and recorded by the microphone driving a graphic level recorder. These experiments were conducted firstly using the bare chamber, and then the chamber with cylindrical test specimens inserted having volumes of 9 percent, 25 percent, and 50 percent of the chamber volume.

The results of the random noise tests are shown in Figure 74 where the normalized levels of the occupied reverberation room are plotted in one-third octave bands; all levels are normalized to the bare room levels. Figure 75 shows some of the results from the sine sweep tests. An extended frequency scale was employed in collecting this data so that various individual modes could be distinguished. The random noise data shown in Figure 74 shows that the longer average path lengths followed by the sound rays in passing around the specimen results in a general lowering of the individual resonances of the room. This conclusion is borne out by the sine sweep data of Figure 75, but in much greater detail. The lowering of the resonances has the effect of spreading the peaks out in the lower frequency range so that the room is even less usable at these low frequencies than when it is bare; however, if the lowest test frequency is maintained at 2.5 octaves above the first resonance of the bare room, relatively little degradation of room characterisitcs is seen to take place for specimen sizes between 10% and 50%. For this chamber, the 2.5 octave criterion is met at 1,000 Hz and it may be seen that in the 1/3 octave centered on 1,000 Hz there are approximately nine resonant peaks in the bare room data. The data for the room with specimens also shows that there are at least nine resonances in this same 1/3 octave and in one case 13 distinct Eigentones may be counted in the sine sweep data. In the case where the specimen occupies 50% of the room volume, the levels are higher than they are for the other two specimen for all frequencies above 1,000 Hz and at many frequencies they are higher than for the bare room (See Figure 75). This is probably due to the drastic reduction in volume of the chamber. None of the specimens could be considered to be highly absorbent.

It may be concluded from this brief study that, for the case of a chamber having this particular shape at least, a specimen having a volume of 25% of the chamber volume would not be considered to seriously degrade the room performance. For specimens having resonant magnification factors below 30 to 50, the deep dips shown in the data for the 50% specimen around 3,000 to 4,000 Hz (see Figure 75) would not be considered deleterious, and it may therefore be considered feasible that a specimen as large as this could be tested.

5.3.2 Reverberation Room Size Relative to the Lowest Test Frequency — The basic parameters affecting reverberation chamber size are the size of the test specimen and the lowest test frequency of interest. The specimen size versus reverberation room size has been discussed above, and only minor effects have been observed for specimens having up to 25% of the room volume so that the main consideration for room size falls upon the wavelength of the lowest frequency of interest.

Nearly all computations involving the response of a given specimen in a field of random noise assume that the sound field is diffuse. While this is a convenient assumption, and diffusivity is easy to define, in practice it is very difficult to obtain. In addition, there is no direct method available to measure diffusivity of a sound field. Correlation techniques offer the best of all the methods for determining, indirectly, that a given field is diffuse, but this is frequently cumbersome and of little value when concerned with designing a new facility or a new test in an existing facility. It is slightly easier to conduct a spatial survey in an acoustic field to determine the variation of the sound pressure level in a given frequency band. If this band is held to the same bandwidth as the response bandwidths of the specimen to be tested, and if the size of the room is increased without limit until spatial variations do not exceed $\pm$ 3 decibels in the specified band, then it may be assumed that the specimen will be properly tested, regardless of the position the specimen may occupy in the room.

Studies of the resonant bandwidths of a range of aerospace structures have indicated that, for the general aerospace structure, a 10% bandwidth is quite common at the lower frequencies. Thus, if a room can be designed such that no point in the room will pass through a 10% frequency band without experiencing at least one resonant peak, then each structural resonance should be excited by the acoustic field. It cannot be said that any point in the room will have a 100% chance of experiencing a resonant peak within a given 10% bandwidth. Indeed, the probability of this happening becomes vanishingly small within the first octave above the fundamental resonance of the room. Therefore, it has become common practice to require that the room contain on the average three Eigentones in a given 10% bandwidth, or slightly more than one mode in a 4% bandwidth. This corresponds to an average of approximately seven Eigentones in the lowest 1/3 octave in which the room can be considered acceptable or about 20 Eigentones in the lowest octave band. This is a somewhat arbitrary condition, but is often a sufficient one for most purposes. A properly shed reverberation room will generally reach the above criterion with a 95% confidence limit at approximately 2.5 octaves above the first resonant frequency, and this is generally considered the lowest frequency for which a room can be used with a reasonable

degree of success. However, economic considerations frequently result in utilizing a room as small as possible so that this criterion cannot always be met.

An alternative condition is that there are a certain number of room modes lying within the bandwidth of the lowest structural mode of the specimen to be tested. Eldred (Reference 71) has shown that the number of modes in any desired test specimen bandwidth, Δf, can be related to a room parameter, $f_0 V^{1/3}$, where f_0 is the center frequency of the band. This relationship is shown in Figure 76 which describes the approximate variation in the room parameter $f_0 V^{1/3}$ with the average number of modes $N(f)$ within a test specimen bandwidth Δf. This figure can be derived with the aid of Equation (66) together with the substitution f_0/Q for Δf, where f_0 is the resonant frequency of the lowest structural mode and Q is the amplification factor of the structural mode. The relationship between the room parameter and the average number of modes within a structural bandwidth Δf is shown in Figure 76 for several amplification factors, and hence modal bandwidths. It has been suggested (Reference 71), that a reasonable criterion would be that there is at least one room mode lying within the bandwidth of the lowest structural mode. From Figure 76, it can be seen that the former criterion of 3 modes in a 10% bandwidth sets the room parameter at about $f_0 V^{1/3} = 1485$, while the criterion of 1 mode in the lowest structural bandwidth results in room parameters ranging from about 1020 for a Q of 10, to 1730 for a Q of 50. Thus the criterion of 3 modes in a 10% bandwidth (or seven modes in the lowest 1/3 octave) is slightly conservative for a structural Q of 25 but is insufficient for a Q of 50, on the basis of one room mode within the bandwidth of the lowest structural mode. The lower bound reverberant frequency, f_0, has been replotted against the room volume, V, in Figure 77 for the case of one acoustic mode within the test specimen bandwidth Δf, and five acoustic modes within the test specimen bandwidth. Three values of the amplification factor Q have been included for the single acoustic mode case, corresponding to those shown in Figure 76. From Figure 77 it can be seen that in order to achieve a lower bound reverberant frequency of 60 Hz, it is required that the reverberation room volume be approximately 11,000 ft³, based upon an anticipated Q of 25 for the test specimen resonating at this frequency, and one resonant acoustic mode within the test specimen bandwidth (which would be from 58.8 Hz to 61.2 Hz).

A more conservative criterion frequently applied to a chamber is to move a microphone from place to place in the room and define the lowest one-third octave showing no more than ± 3 dB variation, as the lowest possible test frequency. By this criterion a good reverberation room is limited to use at frequencies no lower than one decade above the first resonance. At the other extreme, the criterion developed for reverberation room use in Mil-Std-810B, Method 515, simply specifies the required spectrum in octave bands with little further requirements placed upon the chamber other than a 10% test specimen volume requirement. Using this standard, it is possible to perform a test with no more than one Eigentone existing in the lowest frequency band specified. Thus, a chamber having less than 1,000 cubic feet can perform a test which would require a 100,000 cubic foot chamber under the ± 3 dB per one-third octave band criterion previously outlined.

It may be concluded then, that after careful consideration of the structure to be tested and the shape of the test chamber, it may be expected that in general, acceptable test results would be obtained down to a lower frequency of at least 2.5 octaves above the first resonance of the chamber. This criterion does not apply to any room shape which results in a large number of redundant modes. For test specimens having a fundamental resonance in which the structural Q substantially exceeds 25, the lowest acceptable test frequency should be verified by applying the condition that at least one room mode exists within the corresponding structural bandwidth.

5.4 Simulation Techniques

5.4.1 Simulation of Acoustic Environment versus Simulation of Structural Response — In general, the ideal testing technique for any system mounted within a vehicle which is exposed to external pressure fluctuations during flight is to subject an appropriate segment of the vehicle to realistically simulated external acoustic pressure fluctuations in the laboratory. As long as the segment of the vehicle is of sufficient size, it can be assumed that it will present to the internal system a vibration environment which is well related to the actual flight vibration environment. If, on the other hand, the internal system is directly exposed to an acoustic field which has been calculated to be of an intensity similar to that anticipated inside the vehicle, the test will be of less value since the structural filtering and the resultant structural vibration input to the internal system will be absent.

This is particularly true for shroud/spacecraft systems where mechanical transmission paths can predominate over the acoustic paths in certain frequency ranges. Thus the appropriate segment of the vehicle for an ideal test would consist of the complete shroud, the interface ring, and a portion of the final stage of the launch vehicle. The shroud and the final stage segment serve primarily as a loading fixture with the unique property that it is identical to the loading fixture utilized in flight.

The basic simulation problem is caused by the fact that in most cases the vibration environment is induced generally by a distributed external fluctuating pressure field (such as that provided by a turbulent boundary layer), which propagates along the entire shroud and vehicle, rather than by several discrete sources of vibratory power. There are cases when the vibration environment over certain frequency ranges is caused by a localized fluctuating pressure field, typical examples being the separated flow field over the cylindrical section of a shroud at transonic Mach numbers. However, the flow field is generally uniformly distributed around the circumference of the shroud and the length over which these flow fields propagate is of the order of one-quarter to one-half of the shroud diameter.

Although the local forces on the shroud due to the distributed pressure fields may be small, the integrated effect of such a field is to transmit large amounts of energy to the shroud. To introduce a comparable amount of energy by local mechanical excitation of the shroud or vehicle could produce extremely high local forces. Hence, any attempt to create with one or more shakers the vibratory field within the shroud which simulates the vibratory field resulting from a distributed environment, necessarily involves compromises. In addition, the vibratory levels at high frequencies are strongly attenuated in the shroud structure, and consequently, in order to impose realistic levels at positions on the shroud remote from the shakers, the shaker excitation levels must be further increased. Alternatively, if small shakers are distributed over the shroud to simulate a distributed pressure loading, local forces near the shaker input are often excessive. Furthermore, shakers often provide unnatural local constraints and mass loading, so that the shroud cannot exhibit its natural dynamic characteristics.

In an effort to alleviate these inherent problems in distributed shaker systems, simulation of aerodynamic fluctuating pressures utilizing impinging wall jets has been attempted (Reference 72). In this particular study, each wall jet behaved effectively as a broadband shaker and the spectrum was controlled by the nozzle diameters and the volume flow of the air jets. Simulation was based upon duplication of the mechanical power absorbed by the structure. The results of this study showed that for the structure tested, the high frequency excitation (above 1,000 Hz) was adequately simulated, but that at lower frequencies the required air flow was excessive. Thus the optimum wall-jet simulation technique requires the use of a sound field to realistically reproduce these lower frequencies.

Because of these inherent difficulties in simulating the actual flight environments, together with the high cost of such laboratory techniques, simulation of the structural response of the shroud becomes a practical alternative. This involves replacing the actual flight environment by an equivalent acoustic environment which duplicates the structural response of the shroud. The flight environments which generally require simulation include the lift-off acoustic environment, attached boundary layer turbulence, separated flow and shock-wave oscillation. Since the spatial correlations for these environments differ from one another, the structural responses are consequently different.

Thus, in order to define the equivalent sound fields for shroud response simulation, it is necessary to predict the responses to both the flight environment and the particular sound field under consideration. (The establishment of equivalent sound fields has been covered extensively in Section 4.0.) The equivalent sound field is thus determined theoretically in the first instance. Additionally, the equivalent sound fields could be derived empirically if adequate laboratory and flight transfer function data (i.e., the ratio of acceleration response to applied sound pressure level) were available. Acoustic testing based upon duplication of measured flight responses has been reported in References 56 and 57 for the Apollo spacecraft. Lift-off and in-flight measurements of the acceleration response of the SLA structure were utilized as the basic testing criteria during the 16-duct acoustic tests of this spacecraft. In the absence of in-flight and laboratory data however, the

90

theoretically equivalent sound fields lead to a satisfactory qualitative comparison of the effects of various acoustic testing configurations.

Finally, the internal acoustic field within the vehicle is related to the structural vibration of the vehicle skin, so that it is generally assumed that if the structural response levels are simulated, then the internal acoustic levels are simulated. This assumes, of course, that the vibration ene.r; is distributed among the various structural modes in a similar manner.

5.4.2 Spacecraft Testing without the Shroud — In testing shroud/spacecraft systems; it is often desirable to remove the shroud and thus subject the spacecraft to acoustic test levels which are substantially lower than would be required external to the shroud. Also, if it can be established that during flight, the acoustic field within the shroud is diffuse, then removal of the shroud for testing purposes has obvious advantages from the point of view of facility requirements.

However, the mechanical transmission path from the shroud to the spacecraft is effectively removed by adopting this procedure. The available theoretical and experimental results (see Section 4.6), although limited in number, have shown that for certain shroud/spacecraft systems, vibration transmission via the mechanical path cannot be ignored. A particularly important effect which has been observed in full-scale testing is the strong mechanical coupling between the low order shroud modes and the spacecraft trusses (Reference 61). One of the primary considerations therefore, when attempting to test without the shroud, would be tl ɔ resonant frequencies of the spacecraft which are of interest relative to the frequencies of the low order shroud modes.

Attempts to simulate the spacecraft response to the vibration transmitted via the mechanical path have been reported in Reference 65. For this study a relatively crude scale model of a spacecraft and shroud system (described earlier in Section 4.6) was used. To investigate transmission via the mechanical path, the shroud was effectively removed, leaving a 2 foot long section attached to the interface ring to form a multi-modal test fixture. This test fixture was excited by a diffuse acoustic field, by a shaker point driven at the upper ring frame (at the top of the 2 foot shroud section), and by a shaker point driven at the shell wall mid-way up the fixture. For the acoustic testing portion of these experiments the spacecraft was enclosed by a sound-proof box.

The results of these experiments are described in Figure 78, which shows the space-averaged normalized acceleration levels of the spacecraft for the different types of fixture excitation. The spacecraft acceleration has been normalized by the average fixture acceleration. Also shown in Figure 78 for the purposes of comparison is the normalized acceleration response of the spacecraft to energy transmitted via the mechanical path, obtained during experiments with the whole shroud installed and subjected to an external diffuse acoustic field. For this latter case, the spacecraft acceleration levels have been normalized by the shroud acceleration levels. It is immediately observed from Figure 78 that the acceleration

responses of the spacecraft obtained by acoustic excitation of the whole shroud and by acoustic excitation of the multi-modal fixture agree to within ± 1 dB. This result is not too surprising since effectively it merely states that the space-average response of the whole shroud (which was approximately 6 ft long) is similar in magnitude to the space average response of the lower 2 ft section of the shroud. However, in the results presented in Figure 78 no data have been reported for frequencies below 400 Hz; thus, the coupling of the low-order shroud modes, particularly the $(m=1, n=2)$ mode at approximately 250 Hz, is not evident.

For shroud excitation by a diffuse external field, the normalized acceleration levels denoted by the open symbols in Figure 78 may thus be regarded as the desired spacecraft response levels or reference levels for adequate simulation of the mechanical transmission path. With this in mind it can be seen that mechanical excitation applied to the upper ring frame of the multi-modal fixture is slightly more efficient in terms of inducing space-craft response, particularly at frequencies above about 5,000 Hz. Conversely, mechanical excitation applied to the shell wall is observed to be much less efficient (typically by 5-10 dB) in terms of inducing spacecraft response up to approximately 5,000 Hz; above this frequency this form of mechanical excitation tends to be more efficient than acoustic excitation of the fixture, but less efficient than mechanical excitation applied to the upper ring frame.

The above result for the fixture wall excitation tends to confirm the earlier remarks concerning shaker excitation of shell-type structures, i.e., the inherent problems of attenuation of vibratory levels in the surrounding structure, and the local constraints and mass loading which prevent the shroud from exhibiting its natural dynamic characteristics.

As a result of the simple model study described above (Reference 65) the following conclusions can be drawn:

- For the particular truss geometry which was studied, the lower section of the shroud provides a realistic loading fixture.

- Acoustic excitation of this lower shroud segment results in an adequate simulation of the spacecraft response due to energy transmission via the mechanical path.

- The application of mechanical excitation to the lower shroud segment results in a reasonable simulation of the space-average spacecraft response over certain frequency ranges, the latter being dependent upon the point of application of the shaker.

- These results apparently do not include the responses of the spacecraft at frequencies in the neighborhood of the low order shroud modes, where other previous work (Reference 61) suggests that the coupling between these modes and the spacecraft adapter is of considerable importance.

92

Clearly the feasibility of shroud removal for acoustic testing must be carefully evaluated for each individual adapter design. The few theoretical and experimental studies which have been beer ...d so far have dealt only with truss-type adapters, where the shroud attachment ...e is in close proximit 'o the base of the truss. In other designs, such as the Surveyor Atlas-Centaur system, the spacecraft adapter consists of a truncated conical section which is mounted to the upper surface of a hemispherical dome. The shroud attachment plane for this design is located at the base of the hemispherical dome (see Figures 2 and 3), considerably more remote from the base of the spacecraft adapter. Thus it may be expected that for the latter design, the vibration transmission characteristics would differ substantially from those of the truss-type adapter employed in the OGO spacecraft/Nimbus shroud design.

To summarize this discussion, several key points should be borne in mind when evaluating the feasibility of testing c given shroud/spacecraft system with the shroud removed. These points can be listed as follows:

(1)   The structural elements which connect the spacecraft to the shroud or to the interface ring are generally designed to withstand inertia or flight acceleration loads. Furthermore, they are designed to achieve maximum strength with minimum weight and are therefore usually small in cross-section and of relatively high surface density. Such structure is inherently less responsive to direct accustic excitation than light-weight non-load carrying skin panel structures.

(2)   At frequencies which are substantially greater than the fundamental bending modes of the load-carrying spacecraft support structure, it is expected that this structure will tend to act as a de-coupling element between the spacecraft itself and the spacecraft mounting points. Only at frequencies above this de-coupling frequency could direct acoustic excitation of the spacecraft system be expected to provide a valid simulation of the flight vibration environment.

(3)   Below this de-coupling frequency, large portions of the spacecraft will be expected to respond more to structurally transmitted vibration from an acoustically-driven shroud, than from acoustic excitation of the spacecraft itself.

(4)   Above this de-coupling frequency, many of the spacecraft components will tend to respond effectively to direct acoustic excitation. This will be particularly true for the spacecraft components located farthest from the shroud attachment points. In other words, the presence of a shroud should not necessarily be required to simulate the acoustically-induced response to the flight environments. This general statement must be qualified, however, by two factors as follows:

(a)   The presence of the shroud serves as a spectrum filtering and attenuating element for any external acoustic field. Although the gross attenuation characteristics of the acoustic environment inside a shroud can be readily simulated, (once the noise reduction through the shroud is known),

93

it is not a simple matter to duplicate the fine structure in this attenuation, namely the detailed spectral filtering provided in the shroud noise reduction. Thus, without this detailed spectral filtering present in the simulation of the internal acoustic environment, the spacecraft could possibly be overtested. However, this would be slightly conservative, and need not be a severe limitation.

(b) During the boost phase of flight, the most intense vibro-acoustic response of spacecraft systems frequently occurs at altitudes of the order of 15,000 - 45,000 feet, during transonic or maximum dynamic pressure flight regimes. In this case, the reduced atmospheric pressure inside an unsealed shroud will reduce the internal noise levels for a given level of fluctuating pressure on the surface of the shroud. Thus, the relative significance of direct acoustic excitation of the spacecraft will be reduced in comparison to the structurally-transmitted excitation which will be undiminished at altitude for a given external fluctuating pressure field on the shroud.

While the above points have dealt with this acoustic testing problem in a purely qualitative manner, (the lack of available experimental data should be emphasized at this point), they are fundamental to the development of any approach for testing spacecraft without the shroud. In defining feasible methods for spacecraft testing without the shroud, the following specific approaches can be suggested.

o As a first choise, no attempt should be made to eliminate the shroud. If necessary, a standard "shroud fixture" should be used to provide some measure of the shroud influence on the vibro-acoustic response of the spacecraft.

o For load-carrying structural portions of a spacecraft, testing should preferably be conducted with the shroud in position. In place of an acoustic test utilizing the shroud, mechanical excitation of this structural portion should be provided, preferably through multiple randomly-phased shakers to cover the lower frequency range where vibratory stresses in such structure may be significant.

o For the remainder of the spacecraft structure, when use of the shroud is undesirable, direct acoustic excitation of the spacecraft components should be accompanied simultaneously, or sequentially if necessary, by mechanical vibration of the spacecraft base in order to cover both forms of excitation which may be significant. For light-weight components well removed from the spacecraft base, the mechanical excitation can probably be eliminated, since these components are usually more responsive to direct acoustic excitation.

94

5.5 Acoustic Test Specification Format and Test Tolerances

For the purposes of improving the repeatability and ensuring consistency of acoustic tests on shroud/spacecraft systems and structural components, an acoustic test specification format is outlined in the following paragraphs. This test specification format covers reverberant and progressive wave environments and deals specifically with facility requirements, test spectra and tolerances, instrumentation and test monitoring requirements.

Acoustic Test Specification Format

Scope: This specification will apply to acoustic testing performed upon structural elements and components . . .

Purpose: The purpose of this specification is to unify acoustic testing of structural components. This will assist in improving the repeatability of a given test in a given facility and improve comparisons of tests performed in different facilities.

Apparatus: The apparatus to be covered in this specification includes reverberation chambers and progressive wave facilities with accompanying instrumentation, *signal conditioning, and readout equipment.*

5.5.1 <u>Test Requirements (Reverberation Chamber)</u> — The specimen shall be tested in a Reverberant Field. The reverberation chamber used to contain this field shall meet the following minimum requirements:

<u>Shape</u>

The room shall be shaped to produce a minimum of redundant modes with a preference for uniform distribution, in the frequency domain, of modes. For rectangular rooms, no dimension shall be rationally related to any other dimension. For non-rectangular rooms, there shall be no parallel surfaces and symmetrical construction shall be avoided. Calculation or test shall be used to verify existence of a minimum of seven allowed resonances within the 1/3-octave centered on the lowest frequency of interest.

<u>Volume</u>

The chamber shall be of sufficient volume such that (a) it will exhibit a minimum of seven resonances within the 1/3 — octave centered on the lowest frequency of interest or (b) that its volume be at least four times the specimen volume, whichever is greater. A well-designed chamber will *generally meet requirement (a) 2-1/2 octaves above its first resonance frequency.*

Additionally, for test specimens having a fundamental resonance in which the structural Q substantially exceeds 25, the lowest acceptable test frequency should be verified by applying the condition that at least one room mode exists within the corresponding structural bandwidth.

96

Specimen Placement	Placement of the specimen in a reverberant field shall be governed by a consideration of the effect of chamber surfaces upon the uniformity of the sound field. All surfaces of the specimen shall be placed at least one-half wavelength from chamber surfaces at the lowest frequency of interest. This will generally mean that the specimen will be at least five feet or more from floors, ceilings, and walls of the test chamber during the test. It is recommended that exact symmetry in the center of a chamber also be avoided where possible.
Boundary Conditions	A portion of the vehicle stage below the lower edge of the shroud should be utilized as a fixture. If this portion of the vehicle cannot be furnished, a suitable fixture should be designed so as to provide a reasonable simulation without unduly influencing the low order vibratory modes of the shroud.
Specimen Closure	Where the test specimen is a section of a cylindrical vehicle, it will generally be found that at least one end of the specimen is open and will admit sound to the inside of the vehicle. In all ··· of this type, a closure shall be designed to seal the open ⁴ ₃) so that the sound reduction through this closure is at ₊ₐ;ᵢ 10 decibels greater than that of the vehicle walls. The attachment line between the closure and the vehicle shall not restrain the vehicle more than would the remainder of the vehicle if it were attached.
Reverberation Time	Reverberation time shall be held to a minimum consistent with sound pressure level requirements and sound power level available. This will tend to increase the probability that specific specimen structural resonances will not lie at chamber minima.

5.5.2 <u>Test Requirements (Progressive Wave Facility)</u> — The test specimen shall be exposed to a progressive wave. Two types of progressive wave testing are possible, depending upon the nature of the specimen. An <u>external</u> test is to be considered when the specimen is a large flat or curved panel and the response of the panel and/or items mounted on it is the major test objective. For this type of test, an existing facility having an adequately sized test opening may be considered. An <u>internal</u> test is to be conducted where a cylindrical or near cylindrical specimen such as a spacecraft shroud is to be exposed to a sound field from all sides. In this case, the specimen should be placed inside a suitably shaped test section composed of longitudinal progressive wave ducts so that it may be surrounded by acoustic energy.

All progressive wave test facilities shall meet the following minimum requirements:

Size

The cross-sectional area of the acoustic duct(s) or channel(s) shall be of adequate size to contain the specimen without causing undue radiation damping, yet have small enough cross-dimensions to minimize the presence of cross-modes in the duct for the test frequency range being considered. This involves a trade-off between; (1) a sufficiently large ratio of duct area to test specimen area, to meet acoustic radiation damping requirements, (2) sufficiently small duct cross-dimensions for suppression of cross-modes, in addition to, (3) the necessary longitudinal variation in duct cross-sectional area for the test sound pressure level requirements.

It should be noted that the cross-mode numbers m and n in Equation (71) denote the number of half-waves between parallel duct wall surfaces. The cross-modes have pressure maxima at the walls and at points which are an integral number of half-waves from the walls. Pressure minima will occur at points located an odd number of quarter waves away from the wall. If the first cross-mode frequency falls within a critical test frequency range of interest, the lateral distribution of the sound pressure level within a plane wave duct should be measured, preferably with the specimen replaced by a dummy rigid specimen, to assist in shaping the test spectrum.

The cross-sectional area of the sound channel for an external test shall be no less than 5% of the surface area of the panel being tested. For an internal test, the cross-sectional area of an individual sound channel shall be no less than 5% of the surface area of the specimen which is covered by this channel. In any test where the specimen curvature causes an area obstruction of more than 10% of the sound channel area, a fairing shall be used upstream to direct sound around the specimen. No specimen shall cause an area obstruction of more than 90% of the channel area.

Fairing

As mentioned above, a fairing shall be used to make a smooth area transition at any point in the cross-section of a progressive wave facility where a specimen or other protuberance occupies more than 10% of the section. Where the transition causes less than a 50% change in area it is permissible to use fairings consisting of conic sections having flare rates no greater than 18°. Where a larger percentage of the cross-sectional area is to be occupied, consideration must be given to the frequency response characteristics of the rate of change of area so that this change rate does not cause reflection of acoustic energy at the lowest frequency of interest.

98

Horn Coupling Frequency Response	Progressive wave facilities are generally driven by acoustic generators through coupling horns. These horns have definite cut-off characteristics which exclude all frequencies below a cut-off frequency from the test section. In acoustic horn design (Reference 73), the cut-off frequency is defined as that frequency, below which no energy is transmitted. In designing such horns, the lowest frequency of interest must be placed at least 1/2 octave above this cut-off frequency.
Boundary Conditions	A panel mounted at the side of a progressive wave facility for an external test will be fastened to the facility in some manner. It shall be the responsibility of the test manager to determine the suitability of the mounting used in relation to the requirements of a specific test. Panel response is critically dependent upon the edge mounting conditions, whether the panel may be considered simply supported, pinned, clamped, or a combin. ·⸱n of these. It will generally be desired that the panel be securely restrained along all edges to produce a clamped-clamped condition or be mounted in a fixture which duplicates, very closely, the actual boundary conditions to be experienced by the specimen in use. Verification that a fixture provides such a simulation shall be made by a suitable engineering study. Actual edge conditions used will be thoroughly documented.
	For the internal test, utilizing a ducted progressive wave configuration surrounding a cylindrical test specimen or shroud, a portion of the vehicle stage below the lower edge of the shroud should be utilized as a fixture. If this portion of the vehicle cannot be furnished, a suitable fixture should be designed so as to provide a reasonable simulation without unduly influencing the low order vibratory modes of the shroud.
Termination	A progressive wave facility must include a termination following the test section to absorb at least 95% of all energy entering it. This will prevent reflection of energy back to the test section where it will combine with the incident energy and cause large gradients in sound pressure level over the specimen length. When such a facility is powered by an airstream modulator, the termination must be designed to allow free passage of air so that static pressure exceeding 2 in. of water is not imposed upon the test section.

Special Requirements for Internal Progressive Wave Facilities

For those internal progressive wave testing configurations utilizing single or multiple progressive wave ducts and horns surrounding a cylindrical specimen, t' e basic requirements outlined in this section regarding fairings, horn coupling and termination are still applicable. However, the duct dimensions and the boundary conditions (between the duct walls and the specimen) must be carefully designed for each testing configuration such that:

(a)   The desired sound pressure l   ls over the specimen are achieved without excessive radiation damping effects or duct cross-mode effects.

(b)   The interfaces between the edges of the duct walls and the test specimen surface do not cause unrealistic constraints which would affect the natural dynamic characteristics of the specimen.

5.5.3 Detailed Test Requirements

Test Spectrum: The test spectrum shall comply with the tabulation as shown in the accompanying table. The overall test level shall be _____ decibels (re: 2×10^{-5} newtons/meter^2) $\pm$ 2 decibels.

TABLE OF ONE-THIRD OCTAVE BAND SOUND PRESSURE LEVELS

1/3 Octave Band Center Frequency	Level in Decibels (re: Overall Level)	Tolerance in Decibels
10	_____	$\pm$ 10
12	_____	$\pm$ 10
16	_____	$\pm$ 9
20	_____	$\pm$ 9
25	_____	$\pm$ 8
31.5	_____	$\pm$ 8
40	_____	$\pm$ 5
50	_____	$\pm$ 4
63	_____	$\pm$ 4
80	_____	$\pm$ 4
100	_____	$\pm$ 3
125	_____	$\pm$ 3
160	_____	$\pm$ 2
200	_____	$\pm$ 2
250	_____	$\pm$ 2
315	_____	$\pm$ 2
400	_____	$\pm$ 2

TABLE OF ONE-THIRD OCTAVE BAND SOUND PRESSURE LEVELS (Continued)

1/3 Octave Band Center Frequency	Level in Decibels (re: Overall Level)	Tolerance in Decibels
500	____	± 3
600	____	± 3
800	____	± 3
1,000	____	± 4
1,250	____	± 4
1,600	____	± 5
2,000	____	± 5
2,500	____	± 5
3,150	____	± 5
4,000	____	± 5
5,000	____	± 5
6,300	____	± 5
8,000	____	± 5
10,000	____	± 8
12,500	____	± 8
16,000	____	± 8
20,000	____	± 8

Mark upper and lower frequency with *

Test Duration: The test shall have a total duration of _____ minutes or until major structural failure is noted. During the test period the facility shall be shut down every _____ minutes for a visual examination of the specimen to detect structural failure. In addition, the test shall be interrupted every _____ minutes for thorough examination of the specimen for minor damage. This will include the following special tests:

      1.

      2.

      3. (Et Cetera)

Acoustic Instrumentation: In order to verify compliance with the requirements of the test spectrum, acoustic instrumentation will be installed to monitor the sound field. Instrumentation shall consist of microphones having a maximum pressure rating of at least 20 decibels higher than the overall test spectrum level. These microphones shall meet ANSI Standard S1.12-1967, as revised, for a type M microphone. They shall be calibrated in accordance with ANSI Standard S1.10-1966, as revised. Field calibration shall be performed upon the entire microphone system at the beginning and end of each working day at a minimum of 1 frequency at a sound pressure level comparable with or above test levels. The frequency response characteristics of the entire microphone system with readout equipment must be known to within ± .5 decibel. Determination of this characteristic shall be performed periodically to manufacturer's recommendations.

Calibration of the instrumentation shall employ laboratory standards traceable to the National Bureau of Standards. All acoustic instrumentation exposed to the sound field shall be resiliently mounted to minimize response to vibration.

Placement of Instrumentation: The purpose of acoustic pressure monitors is to determine the pressure acting upon the specimen itself. A measurement of the sound field near or on a non-rigid surface will inherently include the pressure caused by re-radiation of acoustic energy by the specimen. Thus, the test manager must make some decision as to placement of transducers when a specimen is small compared with the acoustic wavelengths of concern. When such is the case, reflection and re-radiation are of little consequence and the transducers may be placed at convenient locations within one wavelength of the specimen c˙ the peak energy frequency. Thus, for a spectrum peak occurring at 500 Hz, the transducers may be resiliently mounted within two feet of the specimen. When the specimen is large compared with the acoustic wavelengths of concern, flush-mounted microphones are to be preferred. The lower bound frequency, above which pressure reinforcement due to re-radiation may be assumed to occur is given approximately by; $f_0 = \dfrac{c_0}{2\pi R_e}$ where c_0 is the speed of sound and R_e is the vehicle radius. When flush-mounting is not possible, the active face of the transducer shall face the specimen surface and shall be placed with 1/8th wavelength at the highest frequency of interest.

Number of Monitoring Transducers: It is generally acceptable that a minimum of three microphone positions be used to monitor the acoustic field around small test specimens subjected to a uniform acoustic field. Where it is inconvenient to use three separate transducers it is permissible to use a single transducer moved sequentially to the three different positions when the field can be shown to be stationary. Large test specimens will require a minimum of three transducers placed around the specimen. Where very large tests are contemplated, or where large gradients are expected over a specimen, considerably more transducers may be required at the option of the requesting organization. Specific locations inside a large specimen may also require added transducers. Spatial variations between monitor microphones which are greater than ± 3 dB from the average level are considered excessive for tests in a uniform acoustic field, and shall be justification for modifying the test procedure or facility in order to reduce this variation to the specified limits. For testing in a progressive wave duct configuration, this deviation of ± 3 dB may be considered to apply to the distribution of sound pressure levels around the circumference, at a given axial station. This will not of course apply to those tests where localized regions of higher sound pressure level have been specified.

Control Microphone: All acoustic level settings will be determined by reference to one specific transducer or the average of a number of such transducers. The location(s) of these transducer(s) are specified.

1._____ 2._____ 3. Et Cetera

A single microphone may be used for control provided that it measures a sound pressure level within ± 1 dB of the average of all monitor microphones.

<u>Verification of Acoustic Environment Specification</u>: The required acoustic test levels shall be established by the following procedure:

(1)   Prior to inserting the test specimen, trial runs shall be made at levels of approximately -20, -10, -6 and 0 dB below the required levels with monitoring at levels to be made at the same positions that are to be used for measuring with the specimen inserted (to the extent possible).

(2)   Repeat this procedure with the specimen in place, taking particular care to establish the required spectrum shape and required spatial distribution over the test article surface at a test level approximately -20 dB below the specification. For progressive wave test set-up, conduct sweep at constant electrical power to obtain frequency response, measure performance of termination, and investigate standing waves.

(3)   Spectrum analyses shall be conducted at each of these test levels with a spectrum analyzer having a bandwidth no greater than one-third octave.

(4)   For the final verification of test requirements, data shall be analyzed with a sufficient data sample length to achieve at least 100 statistical degrees of freedom (i.e., the product of filter bandwidth and sampling time) in the analysis of each band.

(5)   Indicating, recording or other suitable analysis output indicators shall read in terms of the true rms levels in each band.

<u>Reporting Requirements</u>: Information about the actual parameters used in a test shall be reported and will include the following minimum information:

(1)   Reverberation Room Characteristics

     a.   Diagram of chamber with dimensions, locations of transducers, horns, specimen, special equipment in the field such as local absorbers or sources, etc.

     b.   Reverberation time of the chamber with and without the specimen.

     c.   Description of special wall treatment if any.

          Description of the use of any acoustic "Q multiplication" or other special techniques employed to enhance the acoustic field.

     e.   Verification of transmission loss between outside and inside of "box" specimens.

(2) Progressive Wave Facility Characteristics

    a.   Dimensioned diagram of the facility and the test specimen with transducer locations.

    b.   Horn and termination cutoff characteristics.

    c.   Verification of panel or vehicle mounting characteristics to demonstrate "hard mount" or "soft mount" whatever the case may be.

    d.   Description of fairings used.

    e.   Evaluation of dominant cross-modes by measurements in the progressive wave test section with a dummy rigid specimen if possible.

(3) Characteristics of both Facility Types

    a.   Description of specimen mounting techniques.

    b.   Description of transducer mounting techniques.

    c.   Evidence of the actual required degree of spatial uniformity, or required spatial variation, obtained in the field over the specimen. This will include 1/3 octave analyses made at representative positions near the specimen.

    d.   Temperature and humidity of ambient air around specimen.

    e.   Photographs of pertinent items not clearly shown above.

    f.   Engineering data describing the essential design characteristics, supported where necessary by experimental data, of any special non-standard test facility such as combined reverberant - progressive wave duct facility or multiple duct facility.

(4) Instrumentation List showing pertinent calibration information.

(5) Block diagrams of instrumentation, signal conditioning and readout equipment.

(6) Description of data reduction techniques with sample calculations where appropriate.

(7) All test data requested.

104

<u>Additional Recommendations:</u> It is recommended that the following additional steps be taken when appropriate.

(1)   For panel testing in a plane wave facility, the lower resonance frequencies and damping ratio of at least the first mode of the panel should be measured before and after mounting the specimen in the test opening.

(2)   For shell-like test specimens, the use of strain gages as response transducers is recommended in addition to other appropriate means of monitoring specimen response to acoustic testing.

6.0 DISCUSSION

The external acoustic environments, structural responses, noise reductions, and the internal acoustic environments have been predicted for a typical shroud/spacecraft system during lift-off and various critical stages of flight. Spacecraft responses caused by energy transmission from the shroud via mechanical and acoustic paths have been compared and the importance of the mechanical path has been evaluated. Theoretical predictions have been compared extensively with available laboratory and in-flight measurements. Equivalent laboratory acoustic fields for simulation of shroud response during the various phases of flight have been derived and compared in detail. Techniques for varying the time-space correlations of laboratory acoustic fields have been examined, together with methods for varying the time and spatial distribution of acoustic amplitudes. Possible acoustic testing configurations for shroud/spacecraft systems have been suggested and trade-off considerations have been reviewed. The effects of reverberation room dimensions on the lowest test frequency, and the volume occupied by the test specimen relative to the reverberation room volume have been assessed. The problem of simulating the acoustic environments versus simulating the structural responses has been considered and techniques for testing without the shroud installed have been discussed.

The most significant findings of the present study are summarized in the following paragraphs; these points are arranged in approximately the same order as the specific objectives outlined in the Introduction to this report.

- Several rocket noise prediction methods have been evaluated and their applicability to given launch configurations have been reviewed. Predicted octave-band sound pressure levels at the surface of a typical shroud/spacecraft system agree reasonably well with measured data. Simplified correlation functions based upon plane waves radiating from distributed sources in the rocket exhaust flow were utilized in the structural response calculations; computed responses have been found to be in good agreement with responses measured at lift-off.

- The aerodynamic environments for typical shroud/spacecraft systems employing 15 degree cone-cylinder shrouds are extremely complex for transonic Mach numbers. The flow over the conical section is attached for all Mach numbers up to maximum dynamic pressure (approximately M=2.0 for the range of spacecraft-vehicle combinations investigated); however, the flow over the cylindrical section of the shroud is characterized by distinct zoning. These zones contain separated flows, shock-wave oscillations and thickened boundary layers, the exact characteristics depending upon the particular transonic Mach number and the shroud diameter. The sound pressure levels over the conical section of the shroud do not vary substantially with increasing Mach number and are significantly lower than the levels over the cylindrical section. The highest sound pressure levels (for the Nimbus shroud and Atlas-Agena vehicle) occur on the cylindrical section of the shroud at approximately Mach 0.8, and are associated with the combined influence of a zone of separated flow near the cone-cylinder intersection and a superimposed shock-wave oscillation. The influence

106

of the shock-wave oscillation is confined to low frequencies, typically in the one-third octave bands centered at 16 Hz, 31.5 Hz and 63 Hz.

At transonic Mach numbers, the overall level characteristics of the fluctuating pressure environments for other shroud geometries (such as bulbous and boattail shrouds) are very similar to those for the 15 degree cone-cylinder shrouds.

⊖ The most significant internal acoustic levels for the shroud-vehicle combinations investigated occur at lift-off. At transonic Mach numbers the internal levels are lower than at lift-off by about 10 dB to 15 dB over the frequency range investigated, while during the maximum dynamic pressure flight regime the internal sound pressure levels were found to be significantly lower than at lift-off. Measured internal sound pressure levels during flight are significantly higher than those predicted; this is considered to be due primarily to the fact that these sound pressure levels were measured by a single microphone placed near the inner wall of the shroud which is in fact a point of pressure maxima for all radial acoustic modes within the shroud.

In calculating the space-average internal sound pressure levels due to the aero-dynamic fluctuating pressures, it was found that the levels within the shroud were determined essentially by those external levels existing over the cylindrical section. The lower external sound pressure levels over the conical section had an insignificant effect upon the final space-average result.

⊖ Relatively poor agreement has been observed between predicted and measured noise reductions for typical shrouds. Furthermore, noise reduction measurements for identical shrouds subjected to various acoustic test environments and in-flight environments exhibit considerable scatter. These results point up the fact that space-averaging of the internal acoustic field is a critical factor in establishing realistic noise reduction curves.

⊖ The normalized structural responses of the shroud to the lift-off acoustic environment and the ducted progressive wave environments were found to be very similar. The one-duct progressive wave environment does not excite the low order shroud modes involving non-zero circumferential mode numbers. The separated flow environment over the cylindrical section of the shroud at transonic Mach numbers contributes significantly to the response at high frequencies, typically above 2,000 Hz, while the low frequency response is determined almost exclusively by the pressure fluctuations in the thickened boundary layer over the aft portion of the shroud. The shock wave-oscillation does not contribute significantly to the overall space-average mean-square response of the shroud, except at very low frequencies. During the maximum dynamic pressure portion of flight, the mean-square response levels are in general lower than for the transonic Mach numbers, except at high frequencies in the region of the acoustic critical frequency, where they are substantially higher.

A comparison of the computed equivalent acoustic fields for simulation of shroud responses indicate that the one-duct progressive wave test configuration contains severe low frequency deficiencies due to its inability to excite the low order shroud modes involving non-zero circumferential mode numbers. At low frequencies the eight-duct progressive wave environment was found to be the most efficient of the test environments considered while in the mid-frequency range (typically 100 Hz to 800 Hz) the reverberant acoustic field was more efficient. For frequencies greater than about 800 Hz all three test environments were found to be comparable in efficiency. It can also be concluded, from examination of the normalized response results, that the four-duct and sixteen-duct progressive wave configurations produce very similar results to the eight-duct configuration, small differences being observed in the frequency region between the ring and acoustic critical frequencies. In this frequency region, an increase in the number of ducts causes slight increases in the structural response per unit exciting pressure.

The reduction of atmospheric pressure during flight causes an increase in the shroud noise reduction of approximately 6 dB for an altitude of 18,000 ft (approximately Mach 0.8) and 15 dB for an altitude of 45,000 ft (approximately Mach 2.0). The effects of a finite pressure differential on the shroud response were found to be negligible for increments up to 2.0 psi.

⊕ It has been demonstrated that for certain shroud/spacecraft or shroud/payload systems, vibration transmission via the mechanical path from the shroud to the spacecraft (or payload) is significantly greater than that transmitted via the acoustic path over certain frequency ranges. This has been found to be especially true at lower frequencies where the low-order shroud modes exhibit strong coupling with the spacecraft (or payload) adapter. Because of the importance of the mechanical transmission path, it is essential that a portion of the final vehicle stage below the shroud connection plane be simulated during any acoustic or vibration testing, whether or not the shroud is installed.

⊙ Modification of the spatial correlation properties of the reverberant acoustic field and the progressive wave field can be accomplished only by the addition of localized sources or sinks (for the former), or by using several plane wave sources arranged circumferentially around the shroud (for the latter). These techniques provide a convenient means for varying the time and spatial distribution of the acoustic amplitudes. The most serious drawback associated with testing in a pure reverberant field is the continuous nature of the amplitude function of the sound pressure with space; the pure reverberant field does not lend itself to the provision of sound pressure level gradients over the structure. Inefficiencies associated with the progressive wave duct configuration include the energy losses along the duct due to absorption by the shroud, insufficient sealing between ducts and radiation through the duct walls.

108

o   Model-scale experiments utilizing a reverberation chamber of ideal dimensions together with test specimens occupying different percentages of the room volume have been described. These experiments have shown that as the test specimen volume is increased, the sound rays radiating from the source travel along longer paths around the room, thus lowering the individual room resonances. If the lowest test frequency is maintained at 2.5 octaves above the first room resonance, little degradation of room characteristics can be expected for specimen volumes occupying up to 25% of the room volume. In general, the room performance will not be seriously altered by installing test specimens occupying volumes up to 25% of the room volume; furthermore, the model-scale results suggest that testing with specimens occupying 50% of the room volume may be considered feasible.

o   The basic laboratory simulation problem is caused by the fact that in most cases the vibration environment is induced by a distributed external fluctuating pressure field rather than by several discrete sources of vibratory power. A true simulation of boundary layer turbulence cannot realistically be obtained except by using small localized acoustic noise sources or shakers. Direct insertion of a test specimen into a wind tunnel test section is very rarely feasible due to the limited test section dimensions and the problems associated with tunnel background noise. Simulation of aerodynamic fluctuating pressures by utilizing impinging wall jets has apparently been successful for high frequencies only, typically above 1,000 Hz. Local mechanical excitation of the shroud utilizing shakers often introduces extremely high local forces and, in addition, the vibratory levels induced at high frequencies are attenuated rapidly in the surrounding structure. Also, local constraints and mass loading tend to prevent the shroud from exhibiting its natural dynamic characteristics.

Because of these difficulties and the excessive costs involved, simulation of shroud response by applying an equivalent acoustic field becomes the only practical approach. These equivalent acoustic fields, which may be derived theoretically, or empirically from laboratory and in-flight transfer function data, have been discussed above.

o   For shrouds subjected to a diffuse acoustic field in the laboratory, it has been shown that removal of a section of the shroud, leaving the lower one-third attached to the interface ring intact, results in a realistic loading fixture. Application of a simulated external acoustic environment to the outside surface of this loading fixture provides a realistic simulation of energy transmission via the mechanical path. Mechanical excitation of this loading fixture appears to provide a reasonable simulation of the spacecraft response over certain frequency ranges, the latter being largely a function of the point of application of the driving force. Insufficient experimental data are available to establish the validity of this particular simulation technique at low frequencies where strong coupling between the low order shroud modes and the spacecraft adapter has been shown to exist. It can be concluded that for realistic testing of shroud/spacecraft systems with the shroud removed, mechanical excitation in the region of the spacecraft adapter is an essential requirement.

o   For consistent acoustic tests performed in different reverberant facilities, it is essential that there be a minimum of seven resonances within the one-third octave band centered on the lowest test frequency of interest. For test specimens having a fundamental resonance in which the structural Q is significantly greater than 25, the lowest acceptable test frequency given by this prior condition should be verified by applying the condition that at least one room mode exists within the corresponding bandwidth of the structural resonance. An acoustic test specification format has been prepared to assist in improving the repeatability and consistency of acoustic testing of shroud/spacecraft systems. This specification contains detailed requirements for testing in reverberant enclosures and progressive wave facilities.

7.0 RECOMMENDATIONS

The results of the present study have demonstrated the effects of different types of acoustic environment on both the structural response of the shroud, and the internal sound pressure levels within the shroud. For a given shroud, a correction factor can be determined analytically for the purposes of adjusting the actual in-flight acoustic spectrum to a laboratory acoustic spectrum. This adjustment provides theoretically identical space—averaged structural responses of the shroud. The internal sound pressure levels are then determined by first converting the actual in-flight acoustic spectrum to an equivalent reverberant acoustic spectrum (producing the same structural response levels in the shroud) and then subtracting the computed noise reduction (which is based upon the assumption that the acoustic field is diffuse both outside and inside the shroud) from the reverberant levels. It should be emphasized that theoretical derivation of the equivalent acoustic environments is limited by inherent inaccuracies in the modal analysis theory and the structural modelling; consequently, the absolute decibel corrections to a given flight acoustic spectrum should be viewed with caution. However, it is considered that the theoretically derived correction factors present a reasonable qualitative comparison between the various equivalent laboratory acoustic environments. A more precise method of adjusting the in-flight acoustic spectra would be based upon the results of a program involving detailed measurements of response to excitation transfer functions collected from vehicle flights and laboratory studies, extrapolating where necessary.

In dealing with the shroud/spacecraft response problem theoretically, the most significant weakness is in the determination of shroud noise reduction; agreement between theoretical predictions of noise reduction and measured data is generally poor. This is due partly to the fact that the noise reduction theory is based upon the assumption of diffusivity of external and internal acoustic fields, while many of the experimental studies which have been reported were conducted in non-diffuse acoustic fields. Further uncertainty is introduced by the fact that many measurement programs involved only a single microphone located inside the shroud. Thus any meaningful comparisons between predicted and measured noise reductions for a given shroud are extremely difficult.

Clearly this represents an area for further study, preferably involving model-scale experiments. The objectives of such an experimental study would be to: (a) determine, for a given shroud, the characteristics of the internal acoustic field for a range of external acoustic environments, and (b) evaluate the effects of shroud detail design on the noise reduction characteristics, utilizing a number of shroud design concepts. The range of acoustic environments should include typically, a reverberant acoustic field, plane waves having arbitrary angles of incidence, a ducted progressive wave configuration and possibly a localized form of acoustic excitation. Detailed measurements of the internal sound field should be conducted to determine the typical variations in noise reduction to be expected as a result of a limited number of transducers and their individual locations.

Investigation of the role played by the mechanical path in transmitting energy from the shroud to the spacecraft has to date been limited to a few basic theoretical and experimental studies. The experimental studies have been conducted in acoustic environments ranging from diffuse fields and single-duct progressive wave fields, to far-field rocket noise environments. However, because of the differences in the specific objectives of each of these studies, the available experimental results are fragmentary and only limited comparisons can be made. Additional model-scale experiments are therefore required in order to realistically assess the effects of different acoustic environments on the energy transmission via the two paths. The objectives of such an experimental program would be to eliminate in turn the acoustic and mechanical paths and to: (a) determine the spacecraft response as a function of the type of acoustic field applied to the shroud, and (b) determine the relative roles played by the mechanical path and the acoustic path for each type of acoustic excitation applied to the shroud. The range of acoustic environments to be considered should include those previously outlined above.

Spacecraft adapter designs generally fall into one of two categories: (a) the basic open framework truss, which is attached directly to the interface ring, and (b) the continuous cylindrical or conical adapter, which is usually attached to the upper surfaces of a hemispherical bulkhead. In the former case the shroud is attached directly to the interface ring, while in the latter case the shroud is attached to the lower surfaces of the hemispherical bulkhead. It is anticipated that the mechanical transmission of energy from the shroud to the spacecraft would differ for these two design concepts. Thus an attempt should be made to determine, either analytically or experimentally, the magnitude of this difference.

It has been found during this study that for 15 degree cone-cylinder shrouds, the internal acoustic environment during flight is determined primarily by the external acoustic levels existing over the cylindrical section of the shroud. Furthermore, these external levels are characterized by distinct zoning caused by the turbulent flow over the shroud, the acoustic levels differing significantly from zone to zone in certain cases. These results suggest that acoustic testing which involves the application of a localized acoustic field (concentrated over a small portion of the shroud) may provide a feasible technique for adequate simulation of the spacecraft response during flight. Some attempt should be made to examine, in the laboratory, the effects of applying a localized environment to the shroud, using a suitably scaled model. This investigation should examine the effects of acoustic intensity, the magnitude of the excitation area, and the location of the excitation area, upon the shroud response, adapter and spacecraft response, and the interior acoustic field.

REFERENCES

1. L.C. Rayburn and P.W. Westbury. Shrouds for Space Payloads. Space/Aeronautics, Vol. 47, No. 2, February 1967.

2. McDonnell-Douglas Corporation — Private Communication.

3. Lockheed Missiles and Space Company. Mariner C Spacecraft/S-OIA Interface Preliminary Design Study. LMSC-A306661, Report No. SP-62-20.

4. Titan III A and C Standard Space Launch System (SSL S) Definition for Payload Contractors. SSD-CR-65-18, rev.2, June 1966. Martin Company, Denver, Colorado.

5. H.J. Holbeck, et al. Structural Dynamic Analysis of the Mariner Mars 1969 Spacecraft. Shock and Vibration Bulletin, 39, Part 2, August 1968.

6. I. Stambler. The OGO Satellites. Space/Aeronautics, Vol. 39, No. 2, February 1963.

7. W.C.L. Hu. Free Vibrations of Conical Shells. NASA TN D-2666, February 1965.

8. J.D. Watkins and R.R. Clary. Vibrational Characteristics of Thin-Wall Conical Frustum Shells. Paper No. 64-78 presented at AIAA Aerospace Sciences Meeting, New York, New York. January 1964.

9. D.K. Miller and F.D. Hart. The Density of Eigenvalues in Thin Circular Conical Shells. NASA CR-1497, March 1970.

10. S. Timoshenko and S. Woinowsky-Krieger. Theory of Plates and Shells. McGraw-Hill Book Co., 1959.

11. E. Reissner. Notes on Vibrations of Thin, Pressurized Cylindrical Shells. Aero-mechanics Report AM 5-4. Ramo-Wooldridge Corporation, November 1955.

12. Y.C. Fung, E.E. Sechler and A. Kaplan. On the Vibration of Thin Cylindrical Shells Under Internal Pressure. Journ. of the Aeron. Sciences, September 1957.

13. K. Forsberg. A Review of Analytical Methods Used to Determine the Modal Characteristics of Cylindrical Shells. NASA CR-613, June 1965.

14. D. Bozich and R.W. White. A Study of the Vibration Responses of Shells and Plates to Fluctuating Pressure Environments. NASA CR-1515, March 1970.

15. Y.K. Lin. Stresses in Continuous Skin-Stiffener Panels Under Random Loading. J. Aero. Sci., January 1962.

16. J.E. Manning, et al. Transmission of Sound and Vibration to a Shroud-Enclosed Spacecraft. BBN Report No. 1431, October 1966.

17. P.W. Smith and R.H. Lyon. Sound and Structural Vibration. NASA CR-160, March 1965.

18. J.E. Manning. Experimental Study of Sound and Vibration Transmission to a Shroud-Enclosed Spacecraft. BBN Report No. 1592, August 1968.

19. V.M. Conticelli. Study of Vibratory Response of a Payload Subjected to a High-Frequency Acoustic Field. Wyle Laboratories Research Staff Report prepared under Contract No. NAS8-21260 for NASA Marshall Space Flight Center, May 1969.

20. L.R. Bruck. Response of a Shroud Enclosed Spacecraft to Combined Acoustic — Vacuum Environments. Memorandum Report No. 701-5 DIRS No. 02094, Goddard Space Flight Center, May 1970.

21. D.J. Mead. The Effect of Certain Damping Treatments on the Response of Idealized Aeroplane Structures Excited by Noise. WPAFB, AFML-TR-65-284, August 1965.

22. M.C. Junger. The Physical Interpretation of the Expression for an Outgoing Wave in Cylindrical Coordinates. JASA, 25, 40, 1953.

23. D.J. Mead. The Damping of Stiffened Plat Structures. Chapter 26 of Acoustical Fatigue in Aerospace Structures, edited by W.J. Trapp and D.M. Forney, Syracuse Univ. Press, 1965.

24. B.L. Clarkson and R.D. Ford. The Response of a Model Structure to Noise — Part II, Curved Panel. University of Southampton AASU Report 206, 1962.

25. R.A. Mangiarotty. Acoustic Radiation Damping of Vibrating Structures. JASA, 35 3. March 1963.

26. P.M. Morse. Vibration and Sound. McGraw-Hill Book Co., 1948.

27. D.J. Bozich. Radiation Damping of Panels Mounted in Ducts. Wyle Laboratories Research Staff Report prepared under Contract No. NAS8-5113 for Marshall Space Flight Center, 1964.

28. Rader, et al. Load Computations used in Acoustical Fatigue Tests of DC-8 Structure. Douglas Aircraft Co. Report SM-23234, N001958.

29. J.R. Ballentine, et al. Refinement of Sonic Fatigue Structural Design Criteria. WPAFB, AFFDL-TR-67-156, January 1968.

30. V.M. Conticelli, G.C. Kao and R.W. White. Experimental Evaluation of Input Impedances of Stiffened Cylindrical Shells. Wyle Laboratories Research Staff Report prepared under Contract No. NAS8-24497 for NASA — Marshall Space Flight Center, August 1970.

31. V.M. Conticelli and R.W. White. Experimental Study of Vibro-Acoustic Response of Stiffened Cylindrical Shells. Wyle Laboratories Research Staff Report prepared under Contract No. NAS9-10423 for NASA — Manned Space Center, January 1971.

32. J.N. Cole, et al. Noise Radiation from Fourteen Types of Rockets in the 1000 to 130,000 Pound-Thrust Range. WADC TR 57-354, December 1957.

33. L.C. Sutherland, Editor. Sonic and Vibration Environments for Ground Facilities — A Design Manual. Wyle Laboratories Research Staff Report WR 68-2, 1968.

34. P.A. Franken and F.M. Wiener. Estimation of Noise Levels at the Surface of a Rocket-Powered Vehicle. Shock and Vibration Bulletin No. 31, Pt. 3, pp. 27-31, 1963.

35. G.A. Wilhold, et al. A Technique for Predicting for Field Acoustic Environments Due to a Moving Rocket Sound Source. NASA TN D-1832, 1963.

36. G.A. Wilhold. Acoustic Environments of Rocket Exhausts. Aero-Astrodynamics Research Review No. 7. NASA TM-X 53782, October 1968, pp. 2-13.

37. I. Dyer. Estimation of Sound Induced Missile Vibration. Random Vibration, Chapter 9, ed. S.H. Crandall, MIT Press 1958.

38. R.C. Potter. Correlation Patterns of the Acoustic Pressure Fluctuations on the S-IC Vehicle Due to the Exhaust Noise at the Test and Launch Hand. Wyle Research Report WR 66-15, 1966.

39. W.J. Neff and R.A. Montes de Oca. Launch Environment Profiles for Sounding Rockets and Spacecraft. NASA TN D-1916, January 1964.

40. Lewis Research Center, Cleveland, Ohio. Atlas-Centaur AC-11 Flight Performance for Surveyor IV. NASA TN X-1768, March 1969.

41. J.E. Robertson. Wind Tunnel Investigation of the Effects of Reynolds Number and Model Size on the Steady and Fluctuating Pressures Experienced by Cone-Cylinder Missile Configurations at Transonic Speeds. Arnold Engineering Development Center Report No. AEDC-TR-66-266, March 1967.

42. D.A. Bies. A Review of Flight and Wind Tunnel Measurements of Boundary Layer Pressure Fluctuations and Induced Response. NASA CR-626, October 1966.

43. C.F. Coe. The Effects of Some Variations in Launch-Vehicle Nose Shape on Steady and Fluctuating Pressures at Transonic Speeds. NASA TM X-646, March 1962.

44. A.R. Wenzel. Pressure Correlation for a Cylinder in a Diffused Sound Field. J. Acoustic Soc. Am., Vol. 41, pp. 1459-1466, 1967.

45. A. Powell. On the Fatigue Failure of Structures Due to Vibrations Excited by Random Pressure Fields. JASA, Vol. 30, No. 12. December 1958, pp. 1130-1135.

46. A. Powell. On the Approximation to the Infinite Solution by the Method of Normal Modes for Random Vibrations. JASA, Vol. 30, No. 12, December 1958, pp. 1136-1139.

47. A. Powell. On the Response of Structures to Random Pressures and to Jet Noise in Particular. Chapter 8 of "Random Vibration", edited by S.H. Crandall, Technology Press.

48. M.K. Bull, J.F. Wilby and D.R. Blackman. Wall Pressure Fluctuations in Boundary Layer Flow and Response of Simple Structures to Random Pressure Fields. University of Southampton (England) A.A.S.U. Report No. 243, July 1963 (AD 631 521).

49. M.J. Crocker and R.W. White. Response of an Aircraft Fuselage to Turbulence and to Reverberant Noise. Wyle Laboratories Research Staff Consulting Report No. WCR 66-11, September 1966.

50. R.W. White. Theoretical Study of Acoustic Simulation of In-Flight Environments. Shock and Vibration Bulletin 37, Part 5, January 1968.

51. P.A. Franken and E.M. Kerwin. Methods of Flight Vehicle Noise Prediction. WADC Tech. Report 58-343, November 1958.

52. L.A. Williams. Flight Vibration, Shock and Acoustic Data from Atlas/Centaur AC-16 for OAO-A2 Spacecraft. NASA— GSFC Memorandum Report No. 691-17, July 1969.

53. L.A. Williams and W.B. Tereniak. Noise Level Measurements for Improved Delta, Atlas/Agena D, and TAT/Agena-D Launch Vehicles. Shock and Vibration Bulletin 36, Part 7, pp. 89-102, February 1967.

54. R.W. Peverley and D.E. Newbrough. A Summary of the Acoustic and Vibration Testing in Support of the Apollo Spacecraft Program, Volumes I and II. Report prepared for NASA — MSC by General Electric Co., Apollo Systems, Houston, Texas.

55. K.W. Shogren, W.G. Spalthoff and M. Goldberg. Acoustic and Vibration Data from SSLV 5-08, SSLV 5-11, and SSLV 5-13 Flights. Aerospace Corporation Report Numbers ATM-66 (6116-40) -203, ATM-67 (2116-40) -10, and ATM-67 (2116-40) -61, April 1966, August 1966 and March 1967, respectively.

56. R.J. Wren, W.D. Dorland and K. McK. Eldred. Concept, Design and Performance of the Spacecraft Acoustic Laboratory. Shock and Vibration Bulletin 37, Part 5, pp. 25-54, January 1968.

57. W.D. Dorland, R.J. Wren and K. McK. Eldred. Development of Acoustic Test Conditions for Apollo Lunar Module Flight Certification. Shock and Vibration Bulletin 37, Part 5, pp. 139-152, January 1968.

58. U. S. Standard Atmosphere Supplements, 1966. Prepared under sponsorship of Environmental Science Services Administration, NASA and U.S.A.F.

59. B. Sharp. Transmission of Sound through Structures. Technical notes prepared for NASA-GSFC under Contract No. NAS5-10962, May 1970.

60. L.R. Bruck. Evaluation of the Launch Phase Simulator as an Acoustic Testing Facility. Memorandum Report No. 701-11, DIR S02251, Goddard Space Flight Center, August 1970.

61. L.R. Bruck. Acoustic Response Comparison for a Spacecraft Tested with and without a Shroud. Memorandum Report No. 701-1, DIR S01977, Goddard Space Flight Center, January 1970.

62. L.L. Beranek. Noise Reduction. McGraw-Hill Book Company, 1960.

63. S.M. Kaplan. Criterion for Estimating Spacecraft Shroud Acoustic Field Reductions. Journal of Environmental Sciences, pp. 27-29, February 1969.

64. R.H. Lyon, et al. Low-Frequency Noise Reduction of Spacecraft Structures. NASA CR-589, September 1966.

65. J.E. Manning. A Theoretical and Experimental Model-Study of the Sound-Induced Vibration Transmitted to a Shroud-Enclosed Spacecraft. BBN Report No. 1891, May 1970.

66. K.Y. Chang and R.W. White. Empirical Evaluation of Vibro-Acoustic Data from MARL/Static Firing Tests. Wyle Laboratories Research Staff Report prepared under Contract No. NAS8-21260 for NASA-Marshall Space Flight Center, February 1971.

67. L.W. Sepmeyer. Computed Frequency and Angular Distribution of the Normal Modes of Vibration in Rectangular Rooms. JASA, Vol. 37, No. 3, March 1965, pp. 413-423.

68. B.H. Sharp. Development of Practical Attenuators for Acoustic Testing of Aerospace Structures. Wyle Laboratories Research Staff Report. Work performed under Contract Purchase Order 028-H59-19, June 1969.

69. E.J. Kirchman, and C.J. Arcilesi. Advanced Combined Environmental Test Facility. The Shock and Vibration Bulletin, No. 37, Part 3, January 1968.

70. W.E. Noonan, and J.R. Daiber. Acoustic Tests of a Flexible Spacecraft Model. NASA CR-1618, June 1970.

71. K. McK. Eldred. Problems in the Laboratory Qualification of Structures and Equipment Exposed to Intense Acoustic Environments. Paper presented at I.E.S. Symposium, 1964.

72. R.H. Lyon, et al. Aerodynamic Noise Simulation in Sonic Fatigue Facility. WPAFB Technical Report, AFFDL-TR-66-112, November 1966.

73. H.F. Olson. "Acoustical Engineering". D. Van Nostrand Company, Inc., 1957.

74. Compilation of Shock, Vibration, and Acoustic Data from Titan Vehicles, — Vol. 3, Titan II Shock, Vibration and Acoustic Data. Martin Company Report CR-64-86, January 1965.

75. Summary Report: Titan IIIA Vibration and Acoustic Data, BBN Report No. 1268, December 1965.

ACKNOWLEDGEMENT

FIGURES

Figure 1. Shroud Designs

Type	Ranger	Mariner D	Delta Bulbous	Delta Low Drag	Agena Long	Agena Short	Titan 3 (Standard)	OAO	Titan 3 (Large)
Weight (lb)	178	160	192	154	535	265	919	860	2260
Typical Mission	Ranger	Mariner D	Telstar, Tiros, OSO	Echo 1, Relay, Syncom	Nimbus, EOGO, OGO	Echo 2, Fire, Gemini Docking Adapter	IDCSP Comsats	OAO Surveyor	Multiple Payloads, MOL
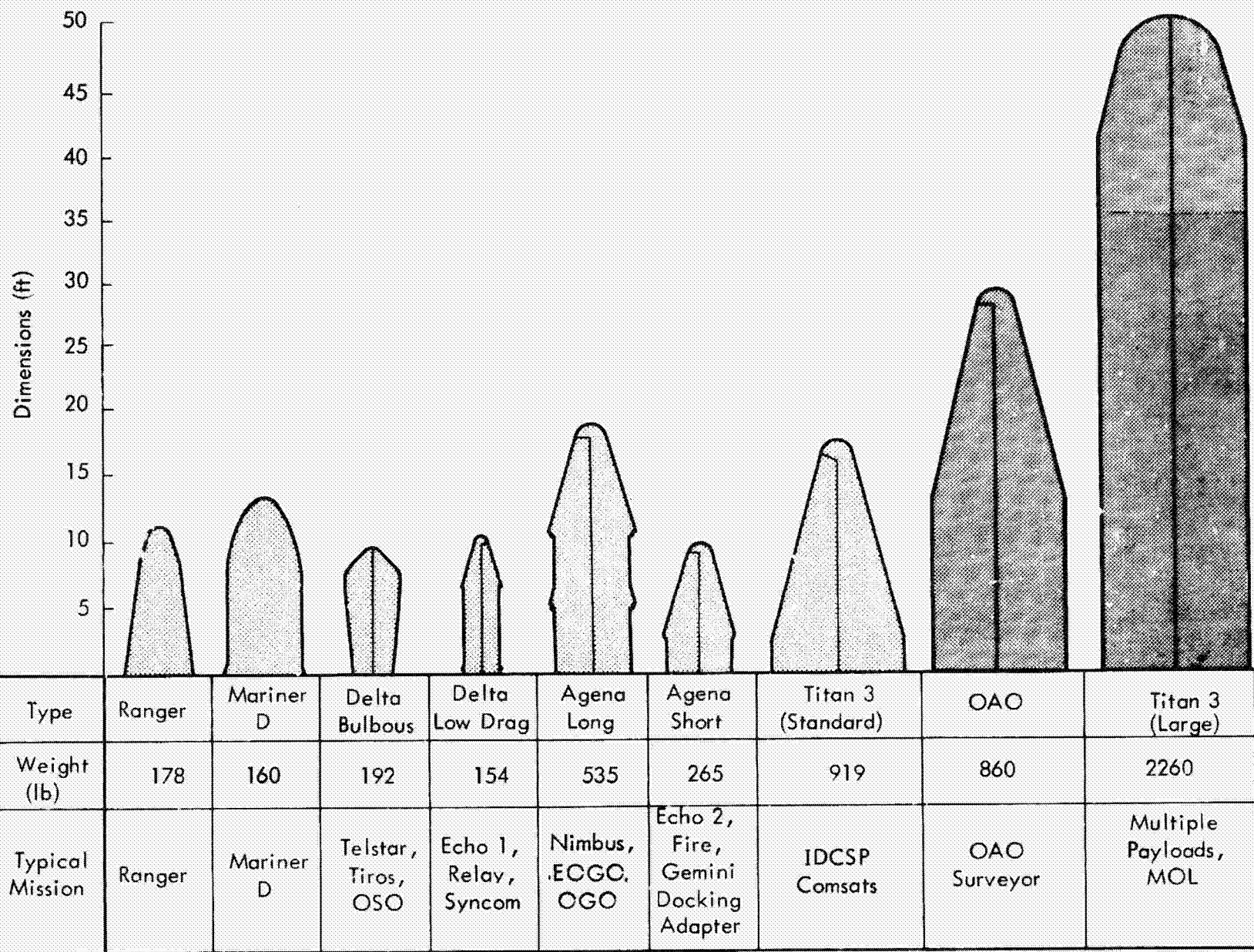
Section A-A
(Scale: Approx. 5/8 Full Size)

Figure 2. Surveyor Shroud (Atlas/Centaur Launch Vehicle). (Reference 40)

124
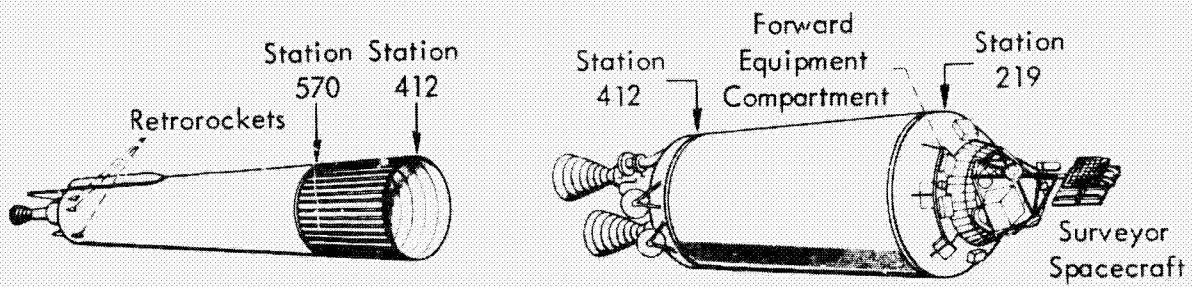
Atlas-Centaur Separation
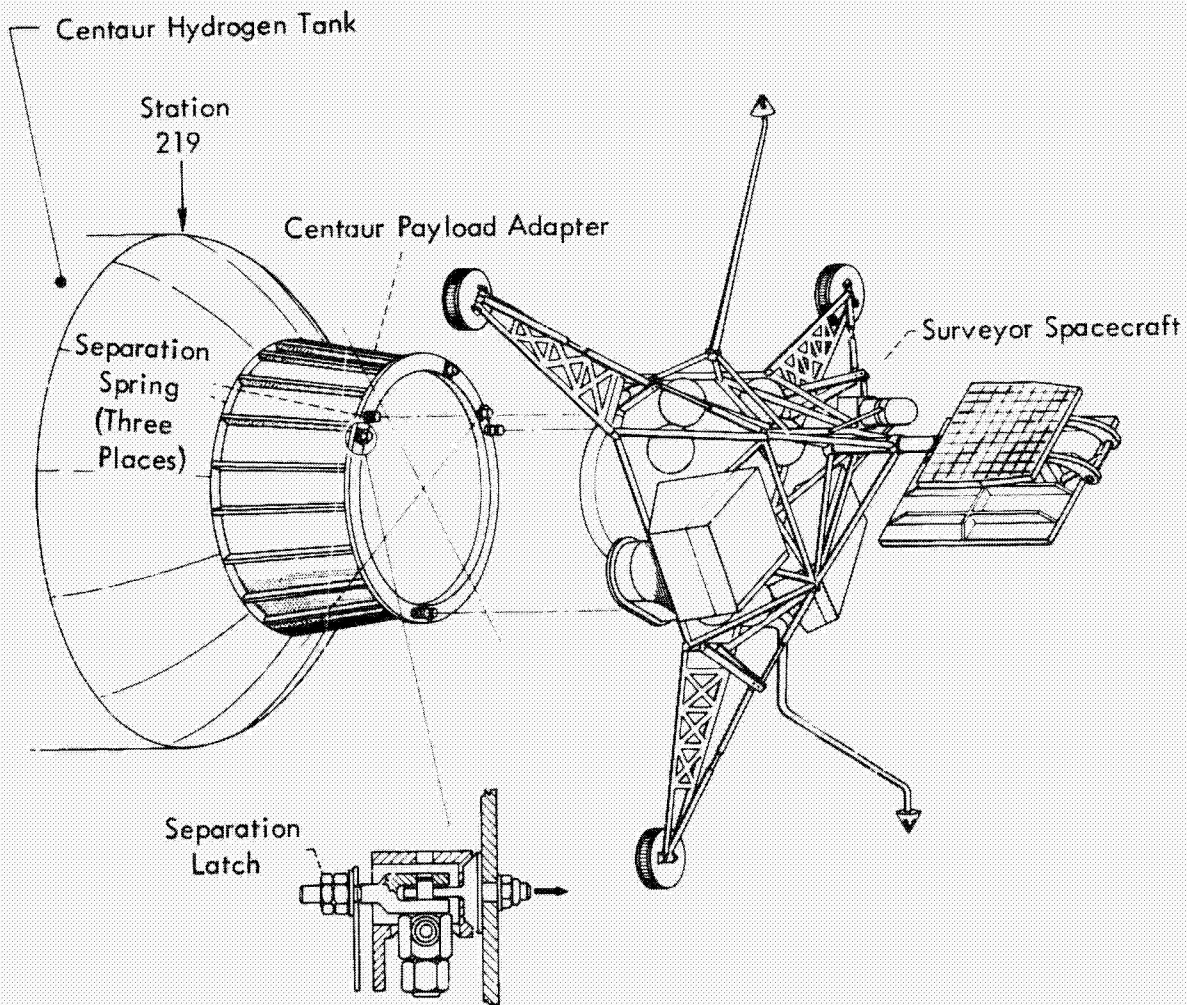
Figure 3. Details of the Atlas/Centaur Payload Adapter and Spacecraft Mounting (Reference 40)

Shroud

Base of
Spacecraft

Shroud

Adapter
Truss

Interface Ring

Base of
Spacecraft

Adapter
Truss

DETAIL
A

Final Vehicle Stage
(Agena)

Final Vehicle Stage (Agena)

DETAIL A

NIMBUS SHROUD PROFILE
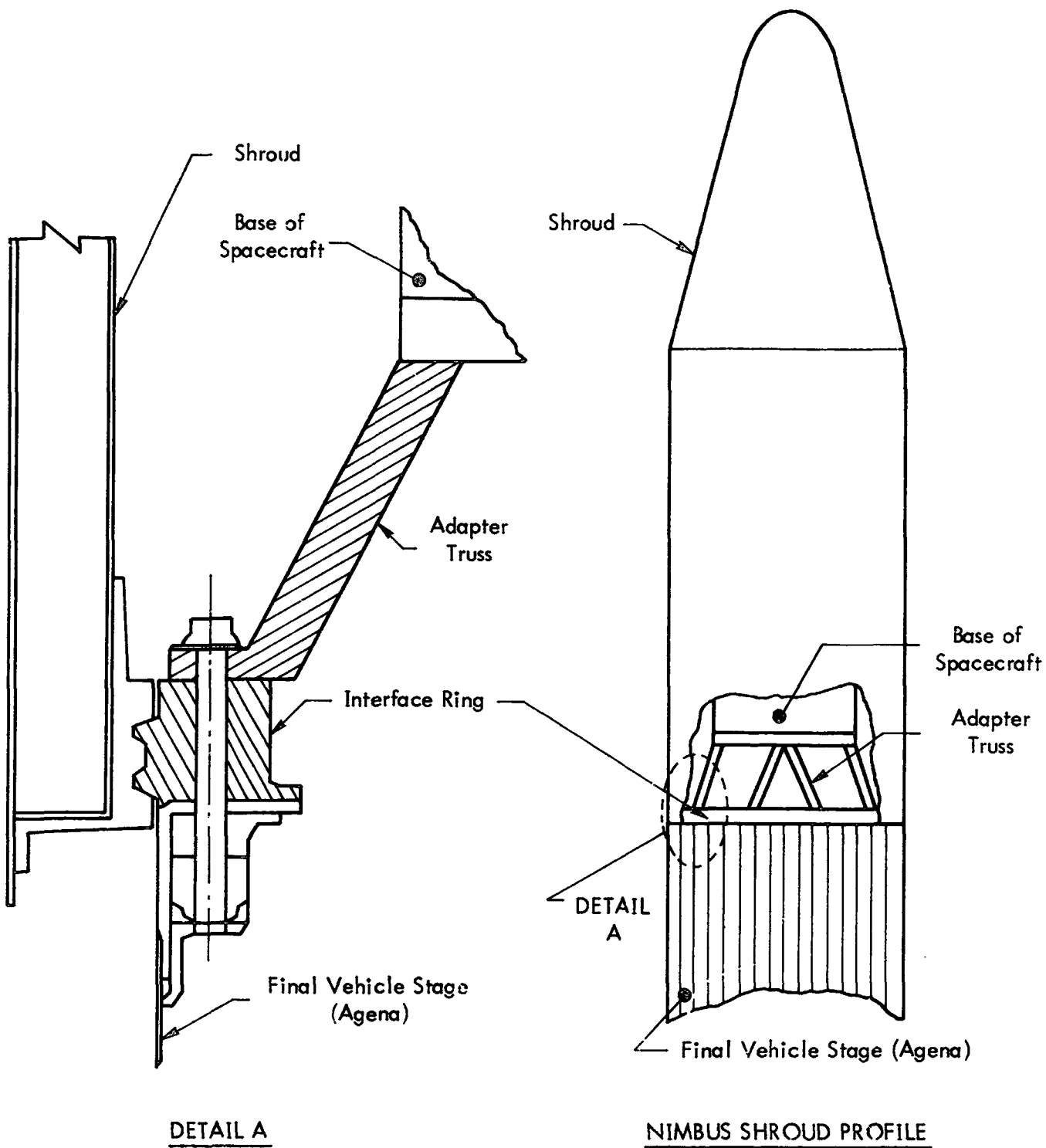
Figure 4. Schematic of Typical Truss-Type Adapter
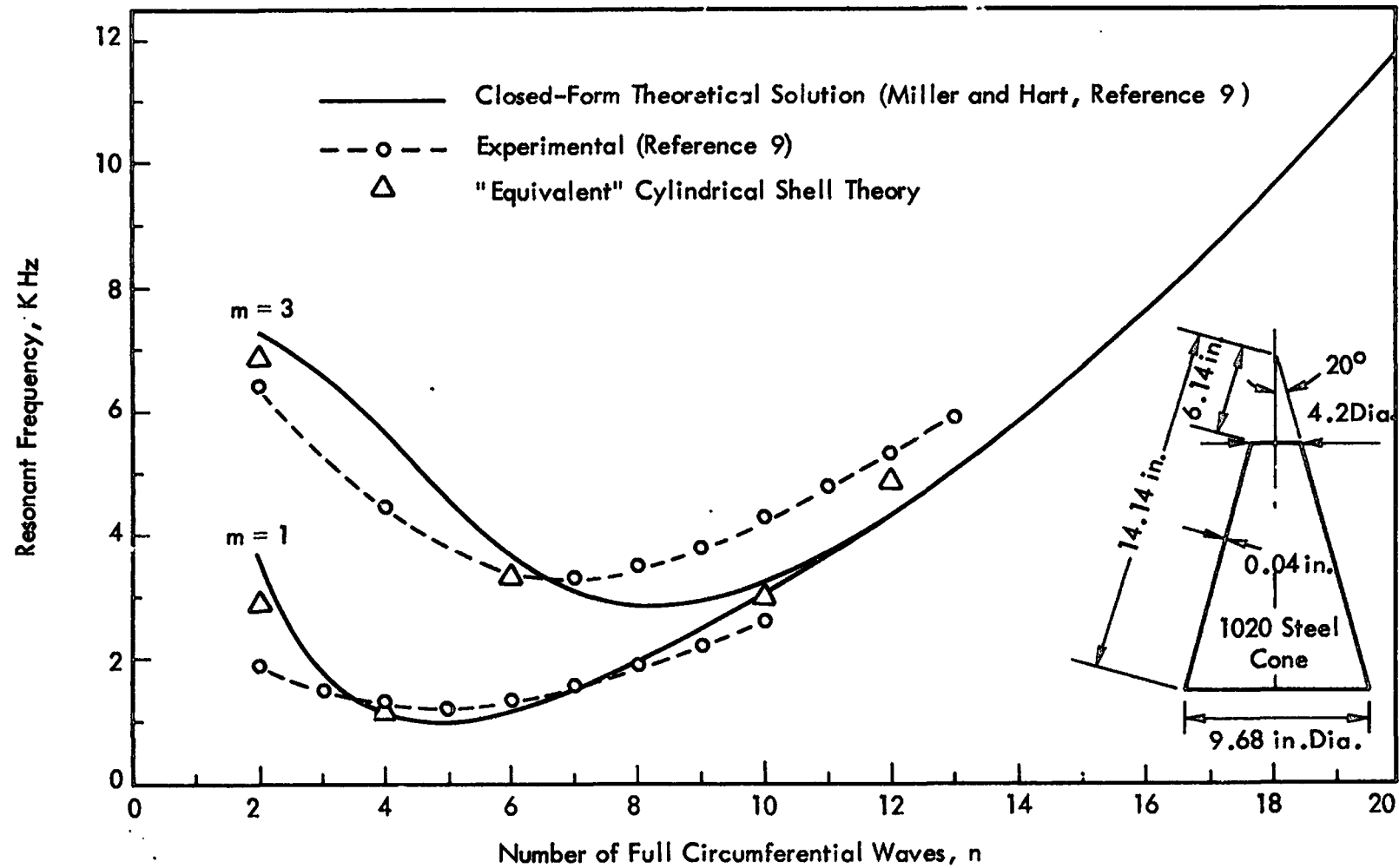
Figure 5. Resonant Frequencies of a Conical Shell: Comparison of Equivalent Cylindrical Shell Theory with Experimental Results
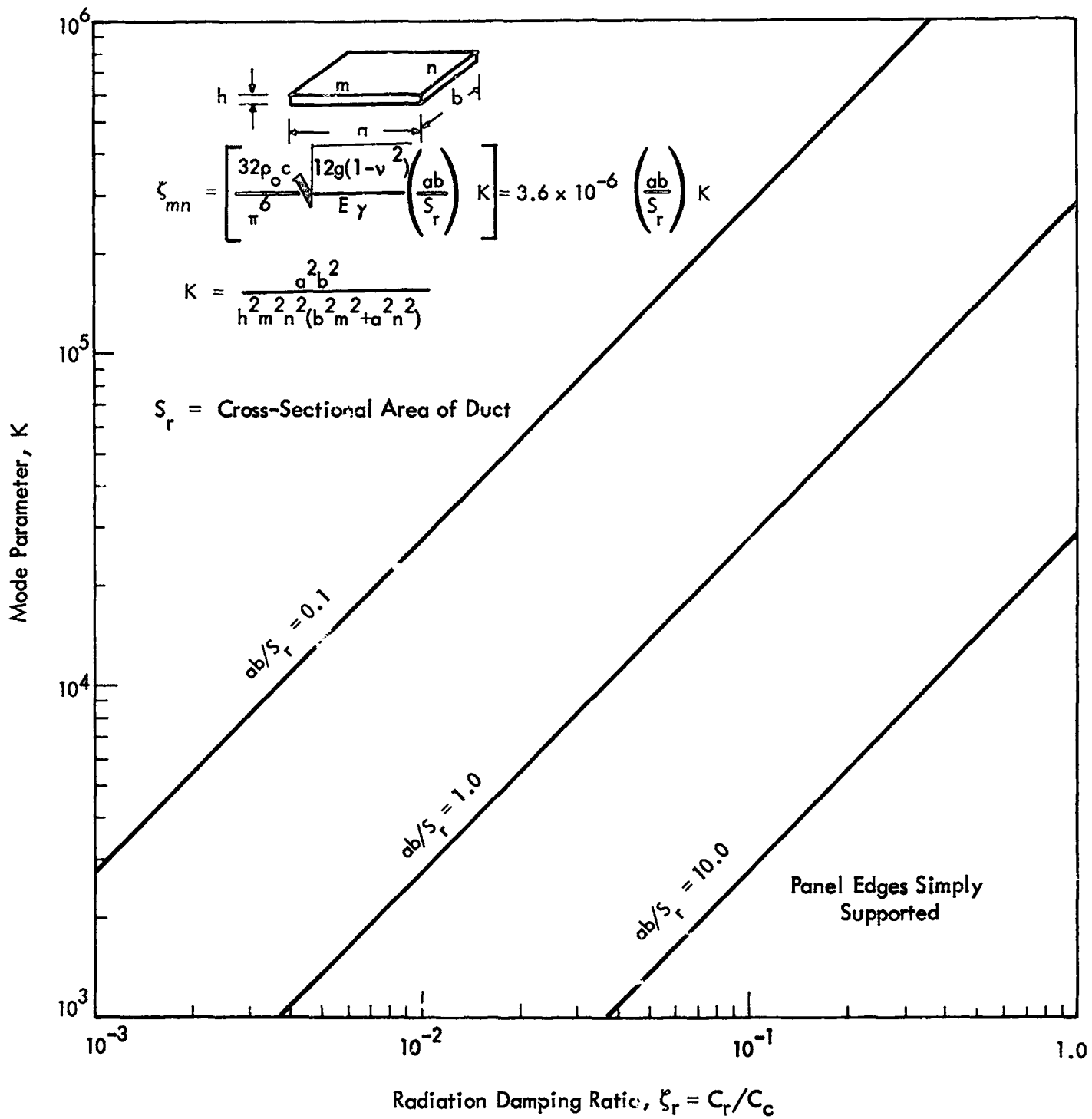
Figure 6. Radiation Damping Ratio in a Progressive Wave Test Section
for Various Values of the Area Ratio ab/S_r (from Reference 27)
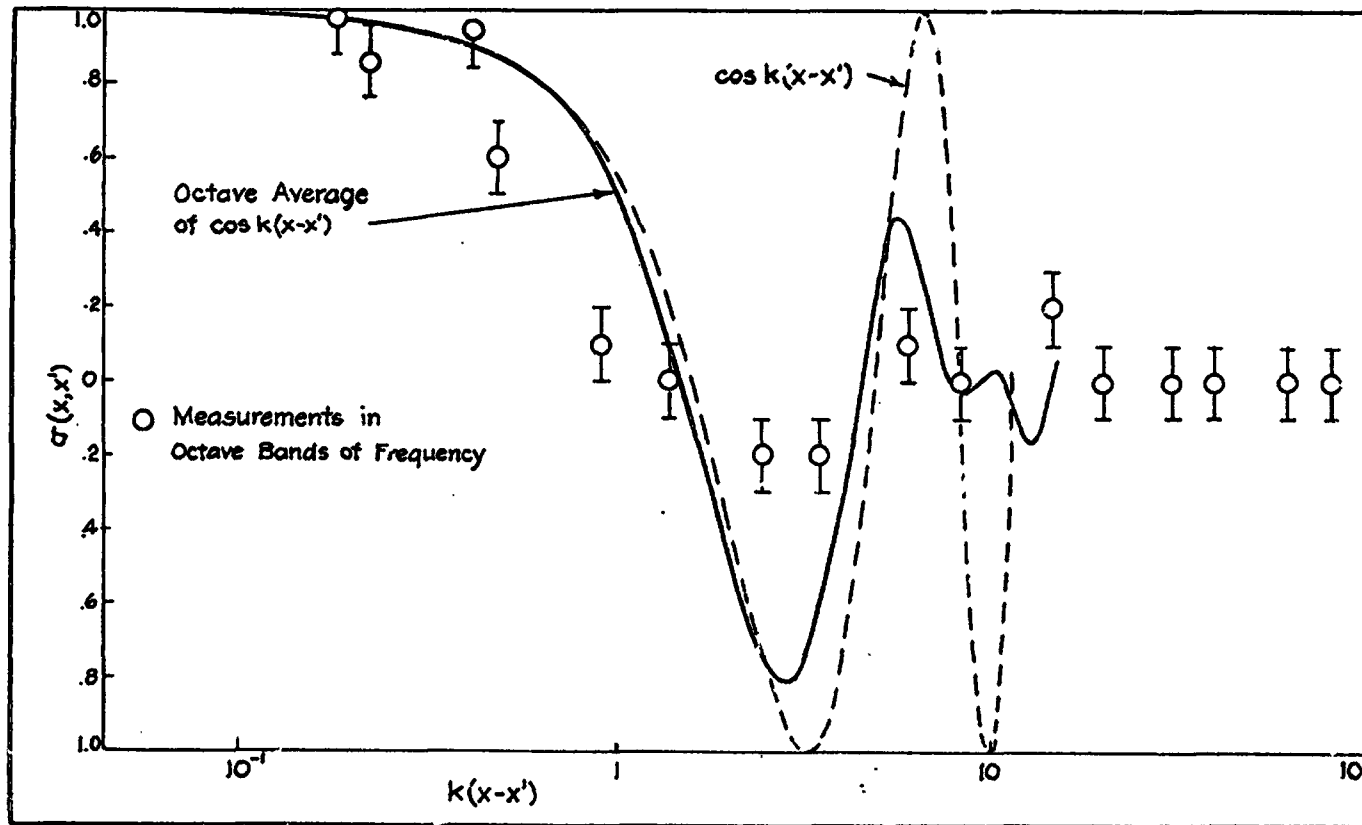
Figure 7. Longitudinal Correlation of Rocket Noise (Reference 37)
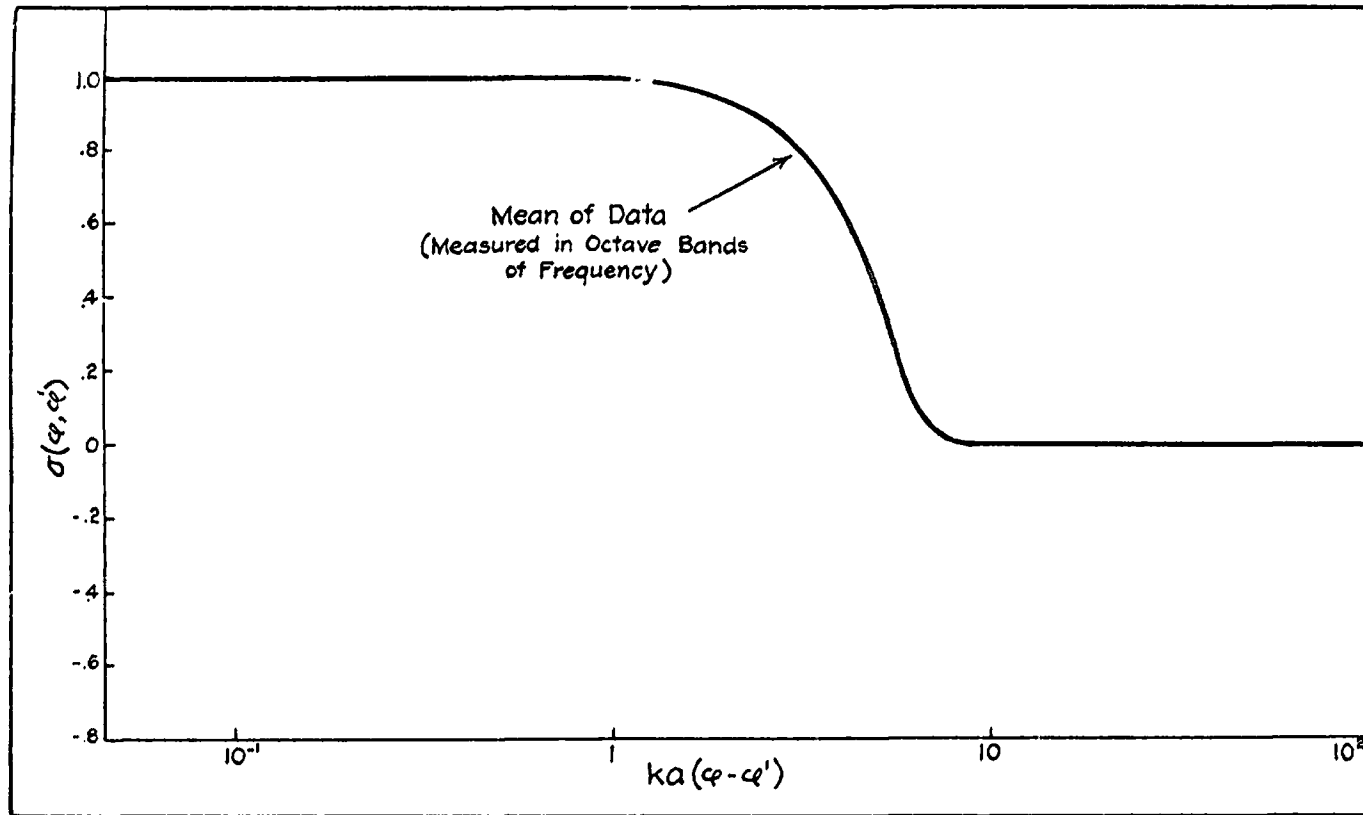
Figure 8. Angular Correlation of Rocket Noise $0 \leq \phi - \phi' \leq \pi$ (Reference 37)
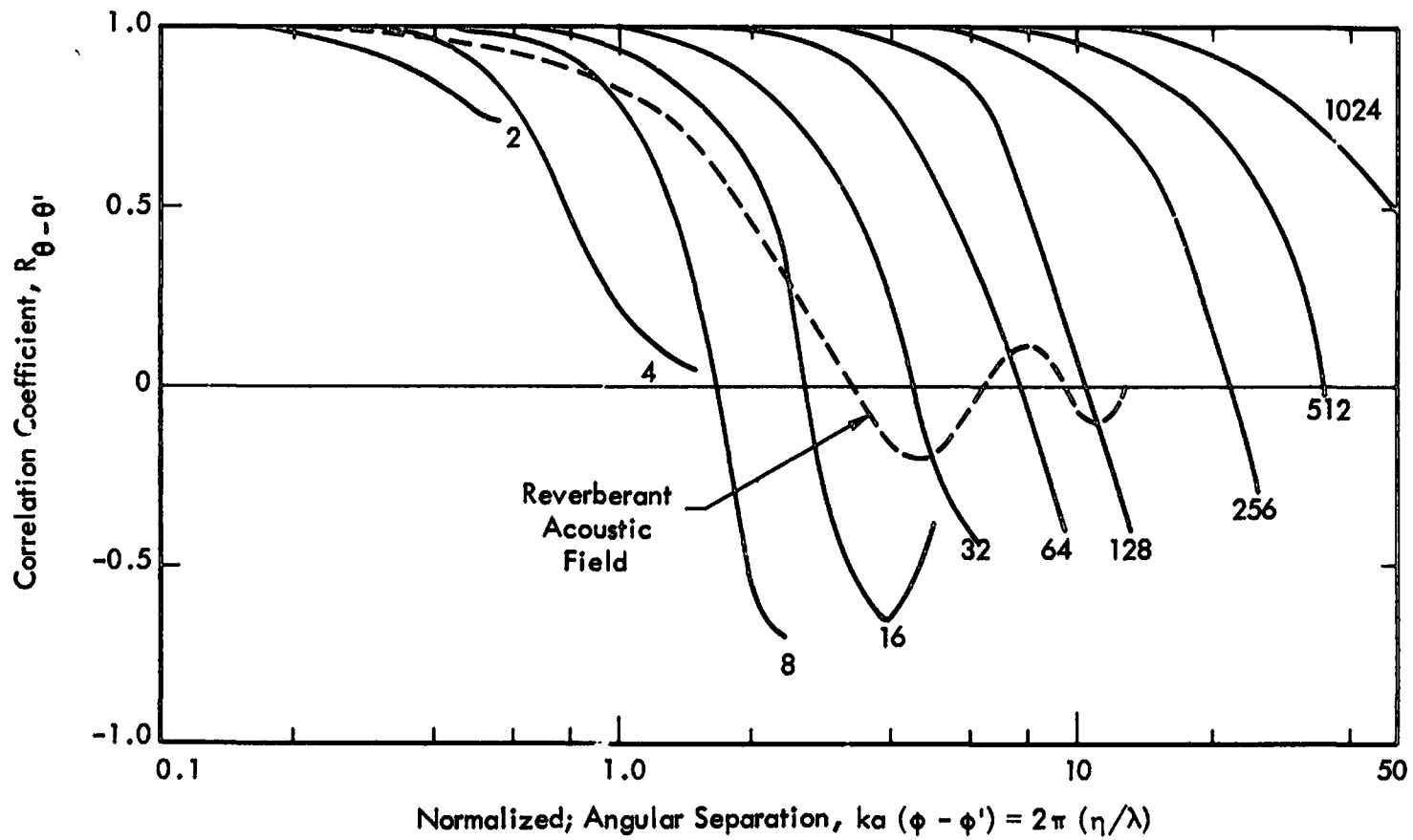
Figure 9. Circumferential Correlation Results for the S-IC Vehicle (Reference 38)

131
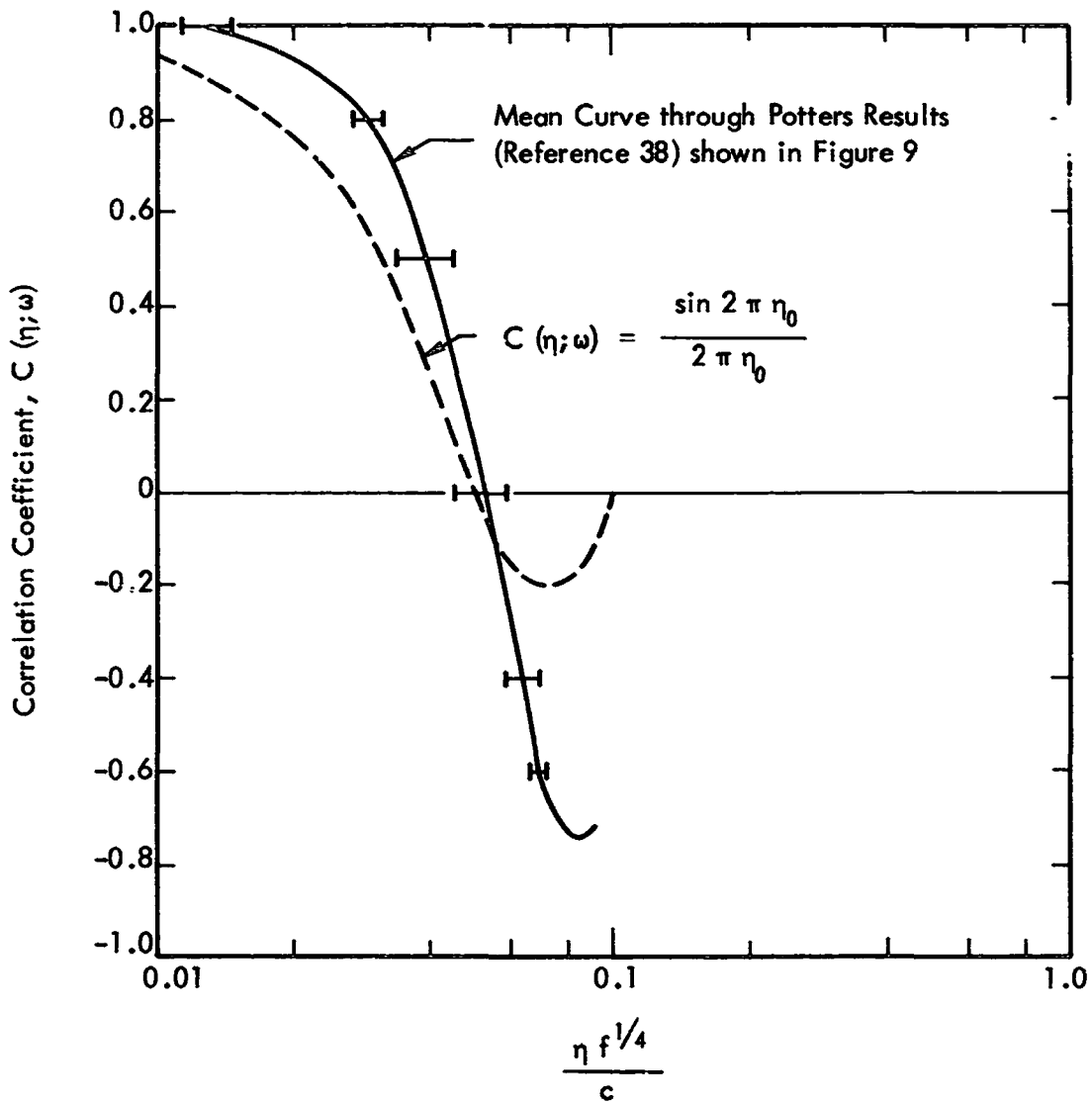
Figure 10. Angular Correlation around Surface of Vehicle; Collapse of Data
Plotted in Figure 9
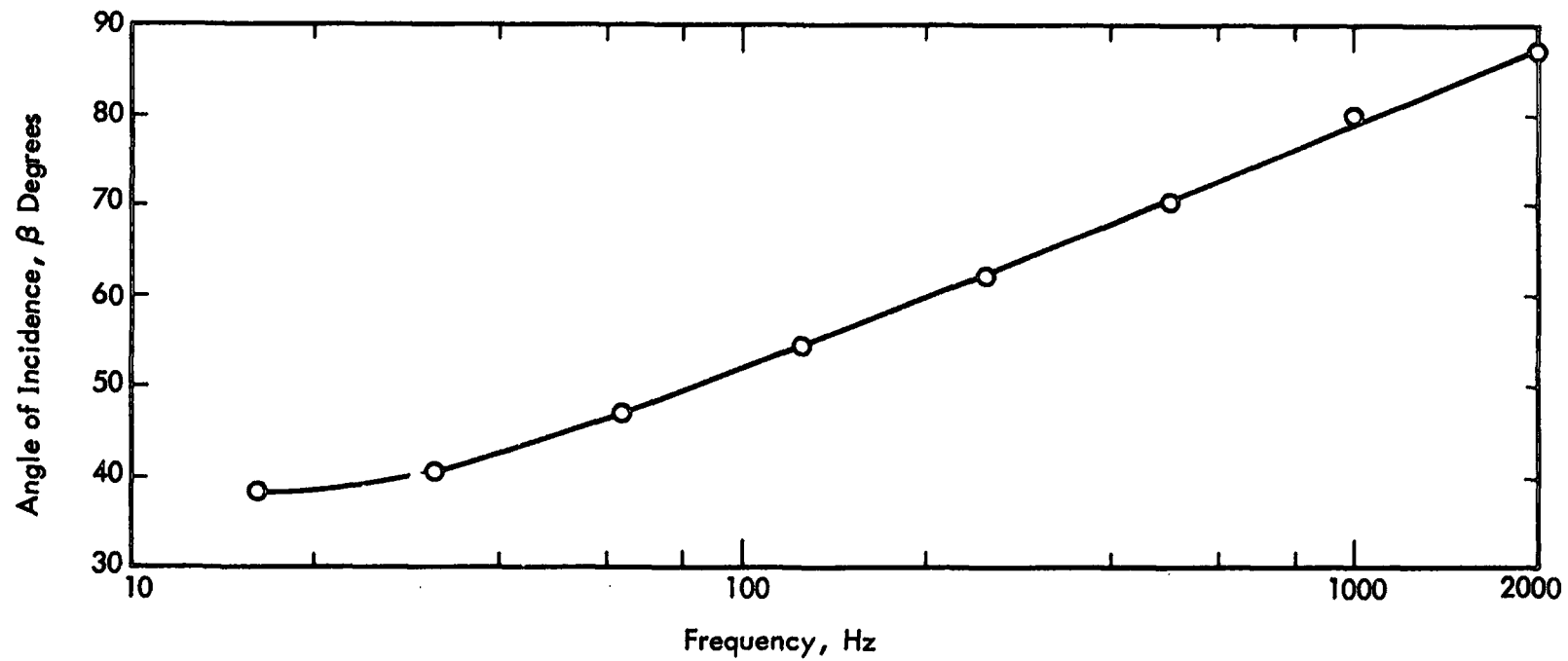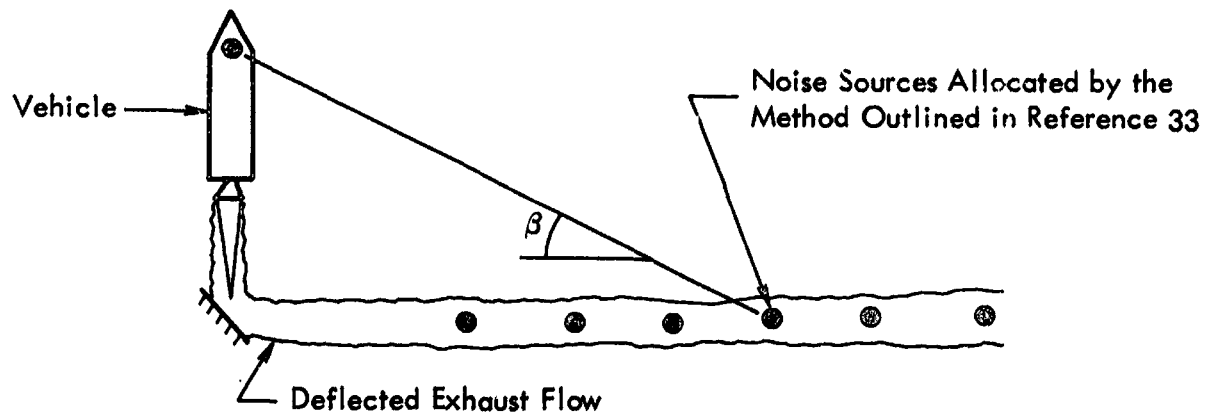
Figure 11. Variation of Angle of Incidence with Noise Source Frequency for the Atlas Booster
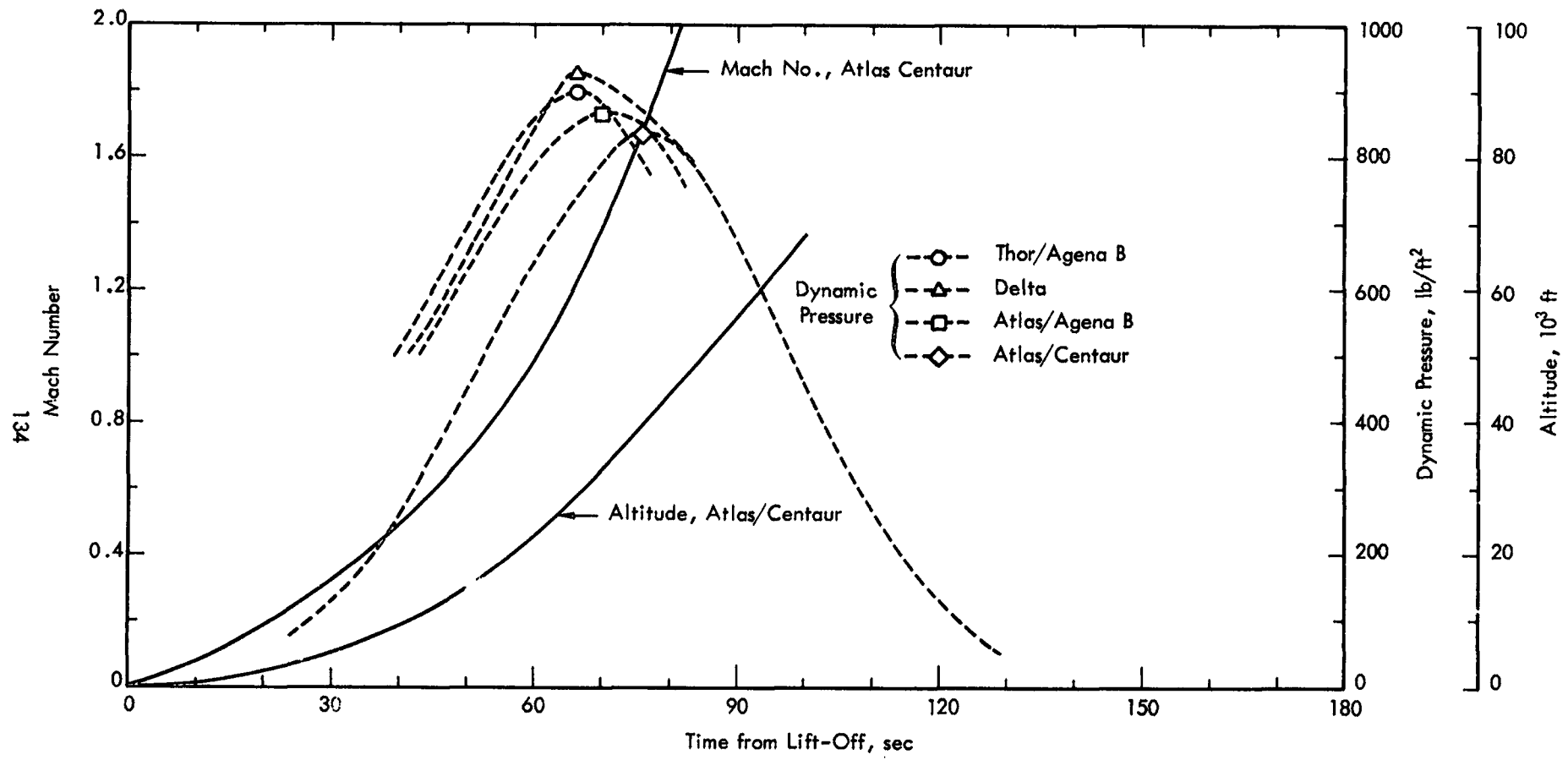
Figure 12. Dynamic Pressure, Mach Number and Altitude versus Time for Typical Launch Vehicles
(Data from References 39 and 40)
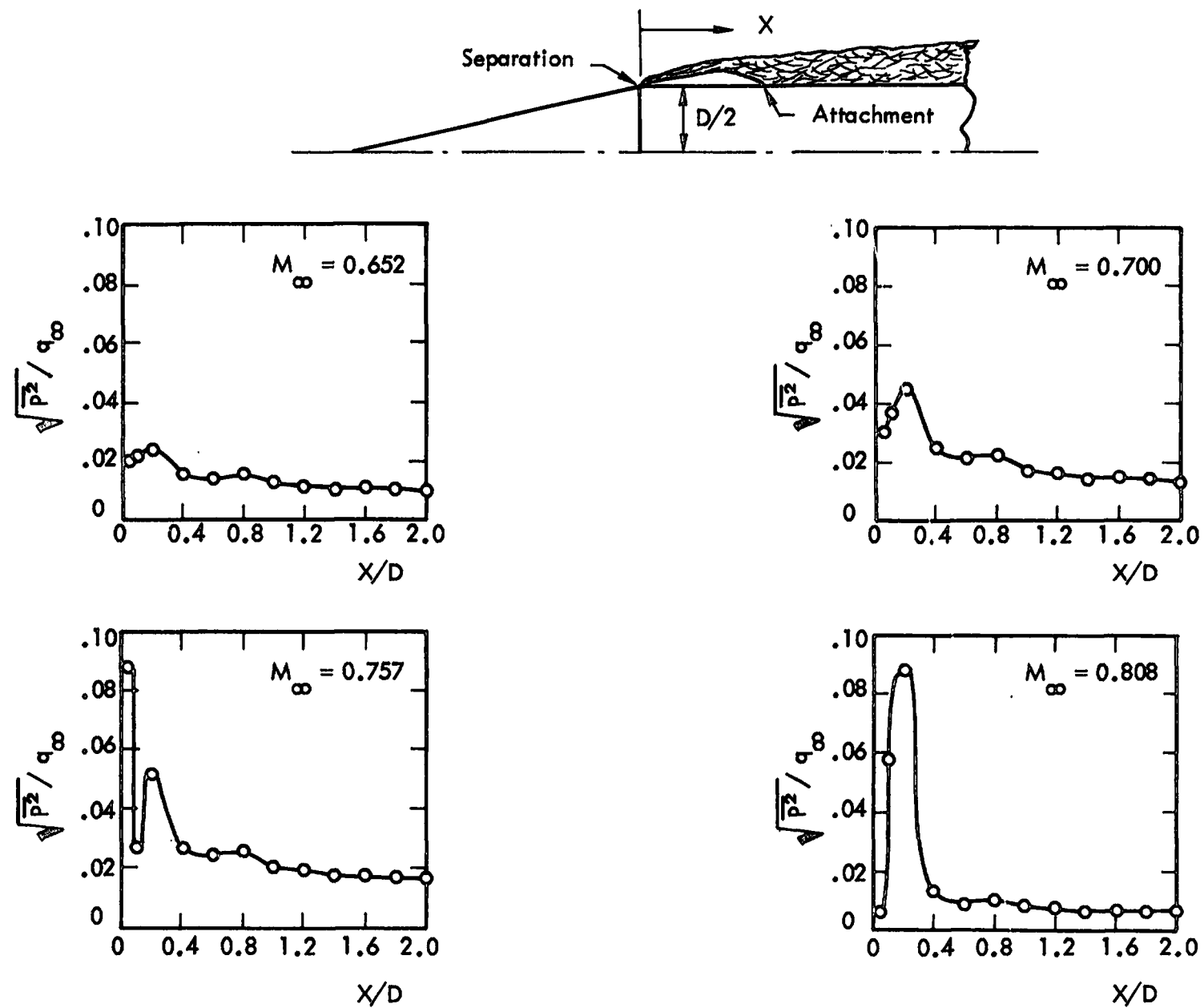
Figure 13. Axial Distributions of Fluctuating Pressures for Blunt Body Separated Flow; 15 Degree Cone-Cylinder (Reference 41)

Mach 0.7

Zone	X_s
1	0–0.5D
2	0.5D–1.0D
3	1.0D–L_x/D

Mach 0.8

Zone	X_s
1	0–0.1D
2	0.1D–0.4D
3	0.4D–L_x/D

$1.0 \leq M \leq 2.0$
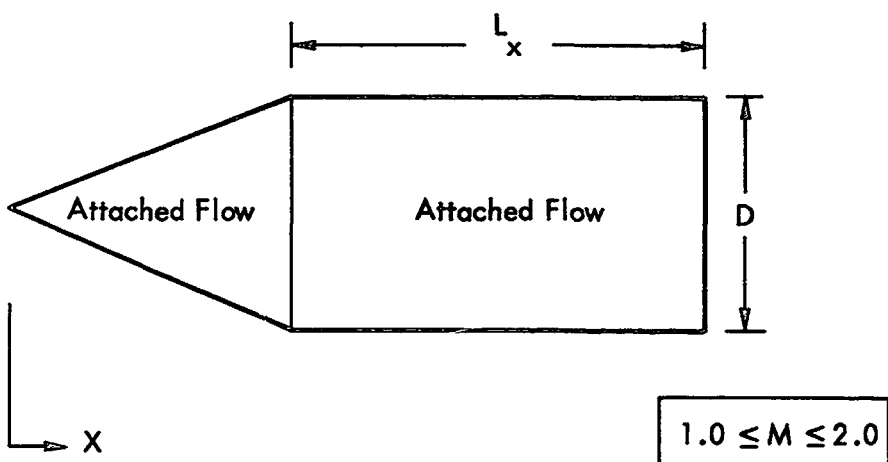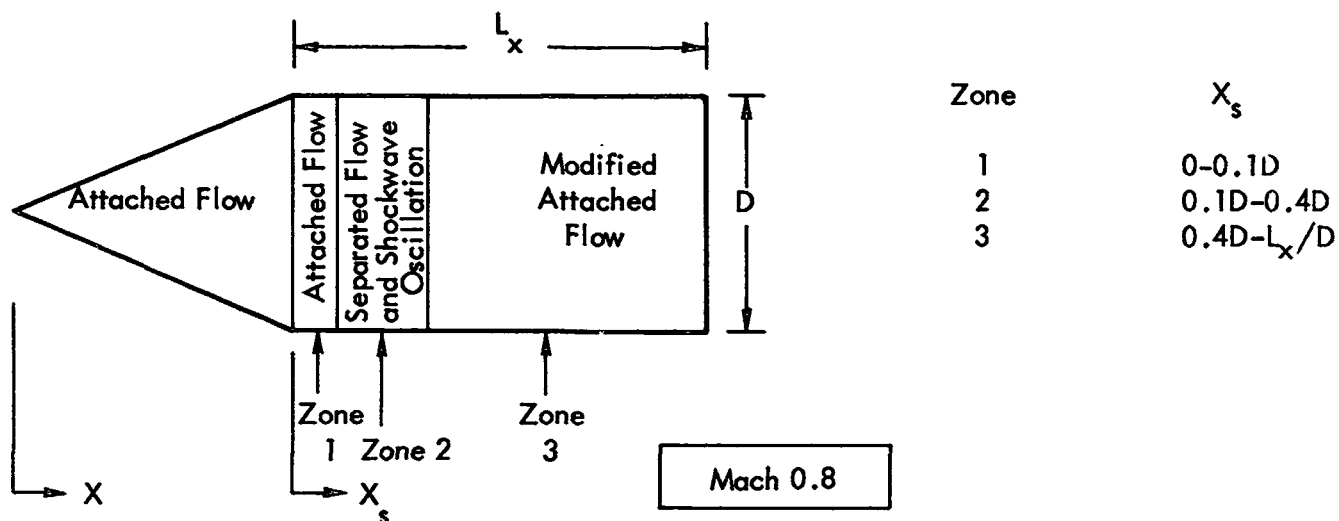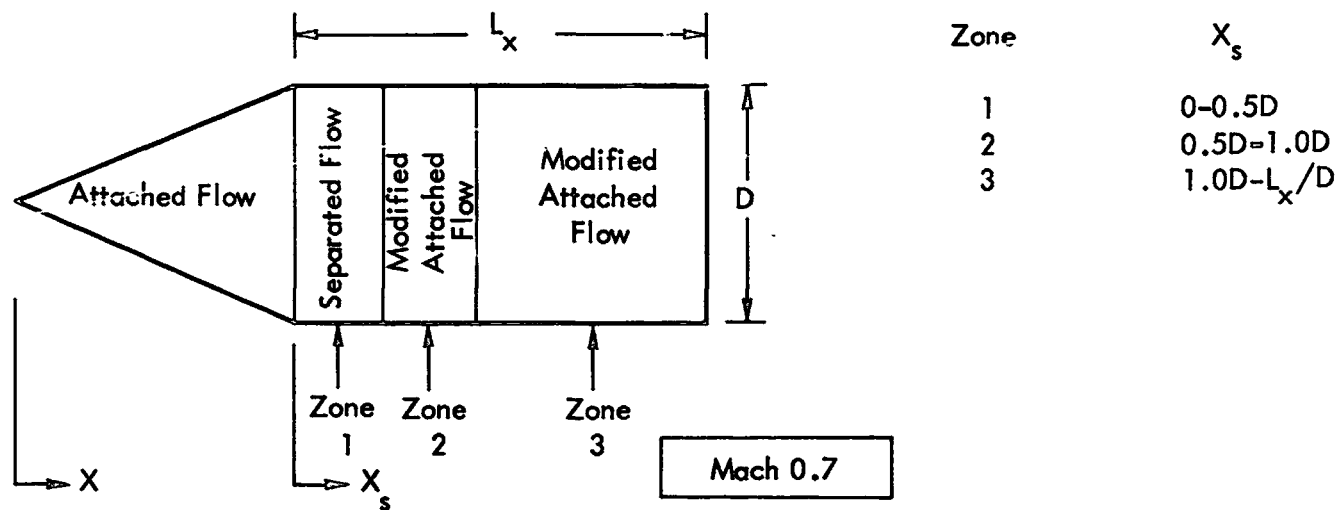
Figure 14. Significant Flight Environments for 15-Degree Cone-Cylinder Shrouds
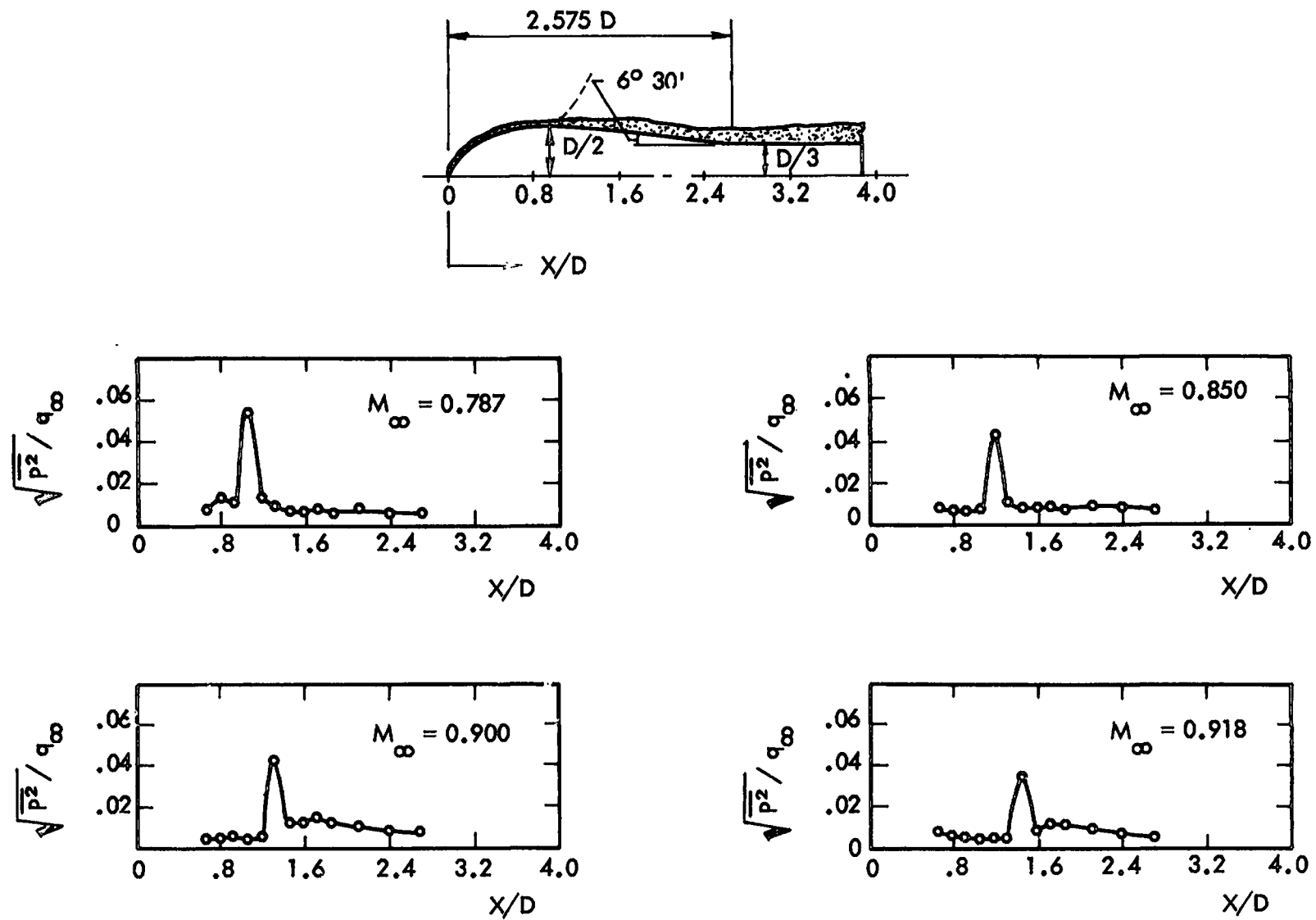
Figure 15. Axial Distributions of Fluctuating Pressures for Blunt Body Separated Flow;
Ellipsoidal Nose Cone on a 6° 30' Converging Body Section (Reference 43)
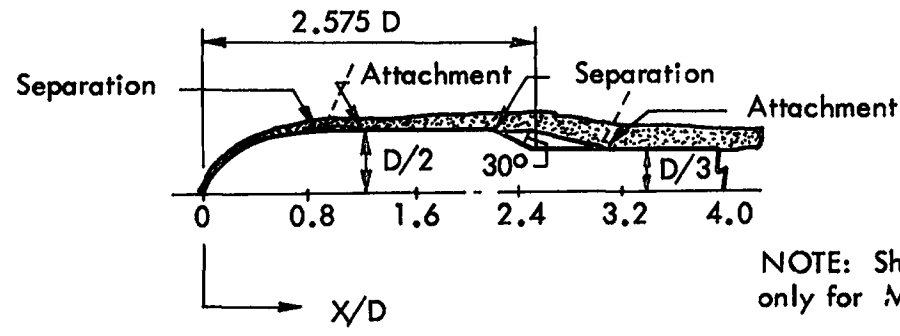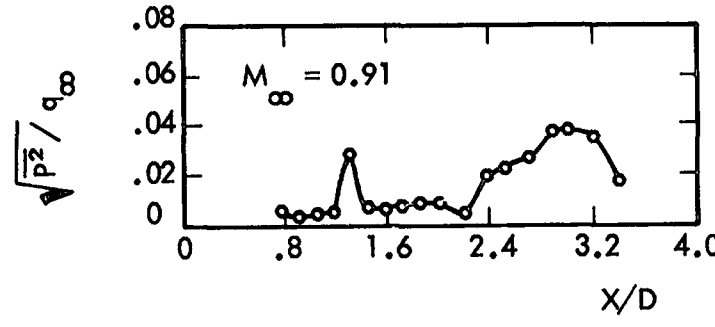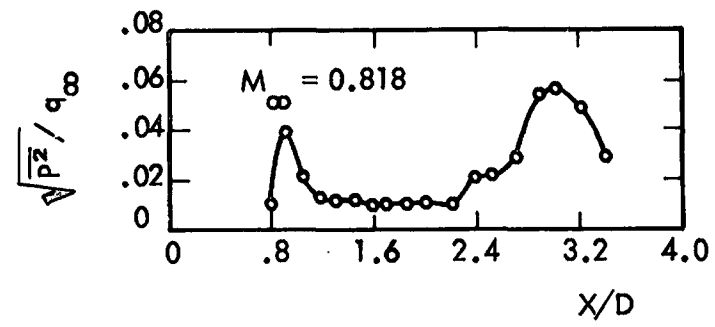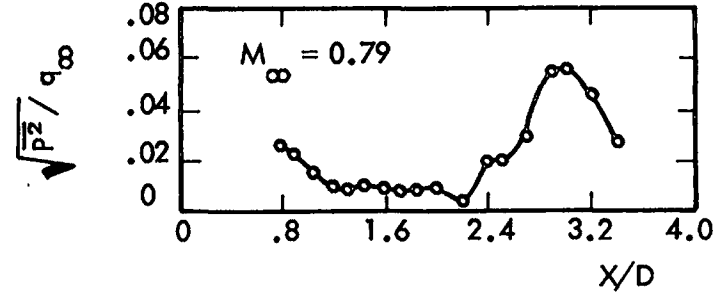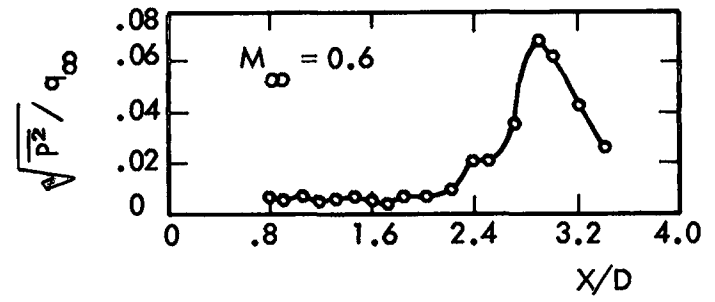
Figure 16. Axial Distributions of Fluctuating Pressures for Blunt Body Separated Flow; Ellipsoidal Nose Cone on a Cylindrical Body with a 30 Degree Step (Reference 43)
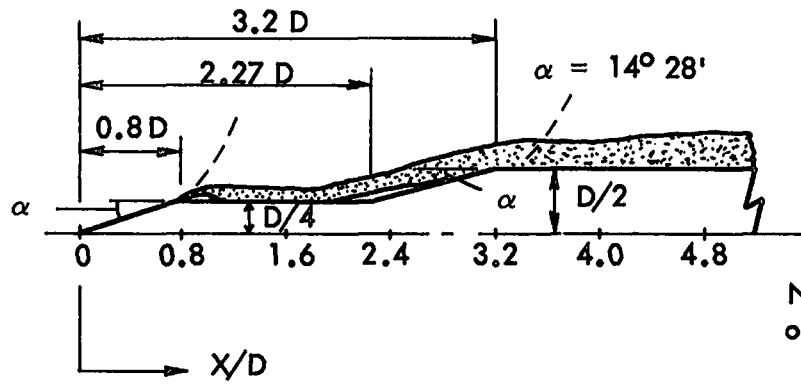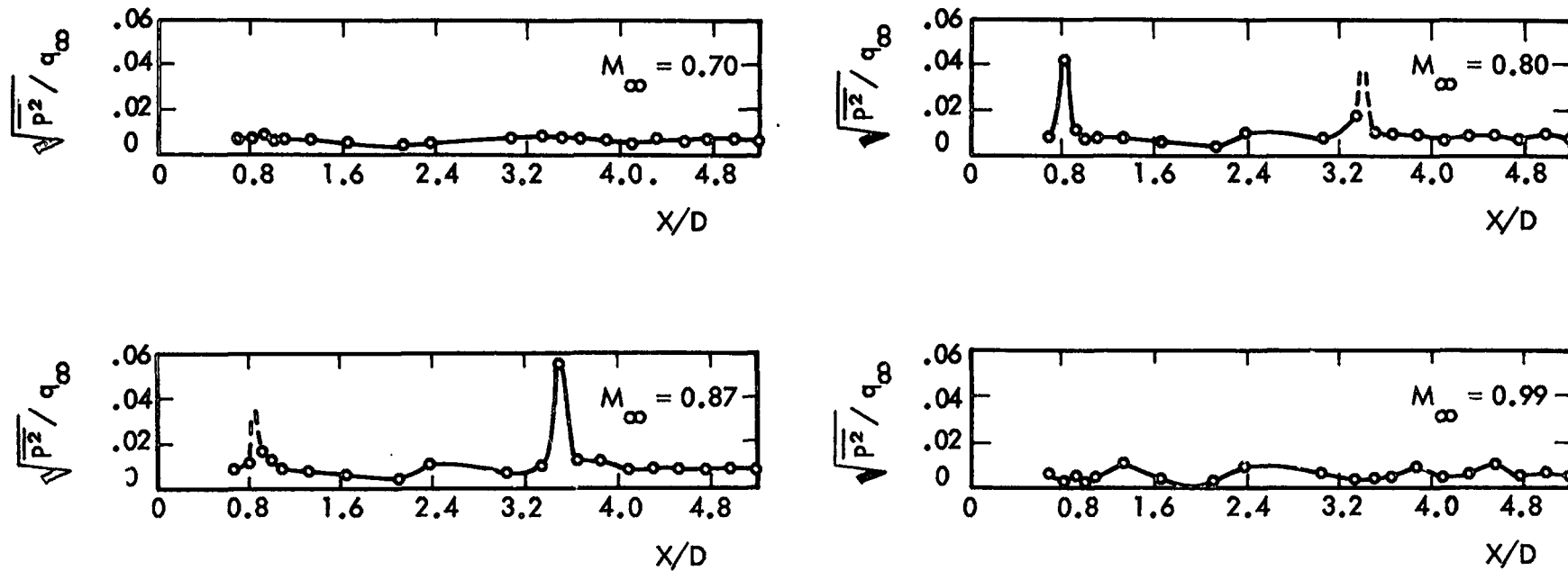
Figure 17. Axial Distributions of Fluctuating Pressures for Blunt Body Separated Flow;
14° 28' Cone-Cylinder Staged Vehicle (Reference 43)
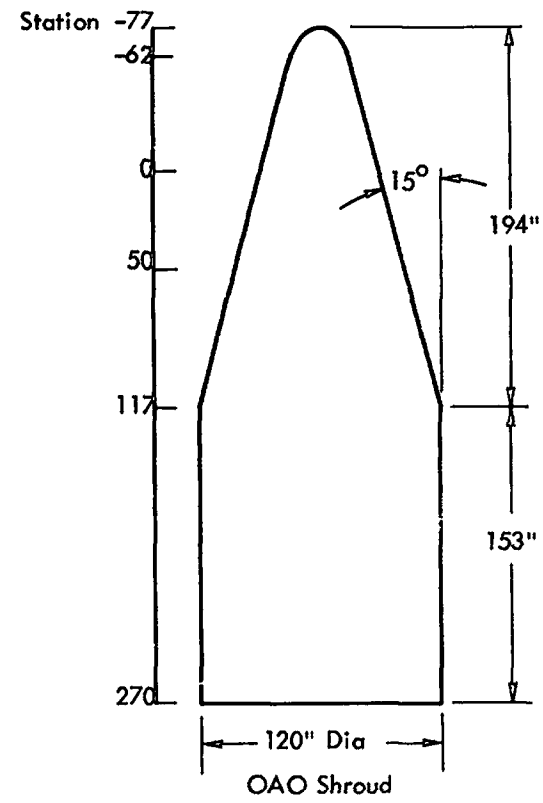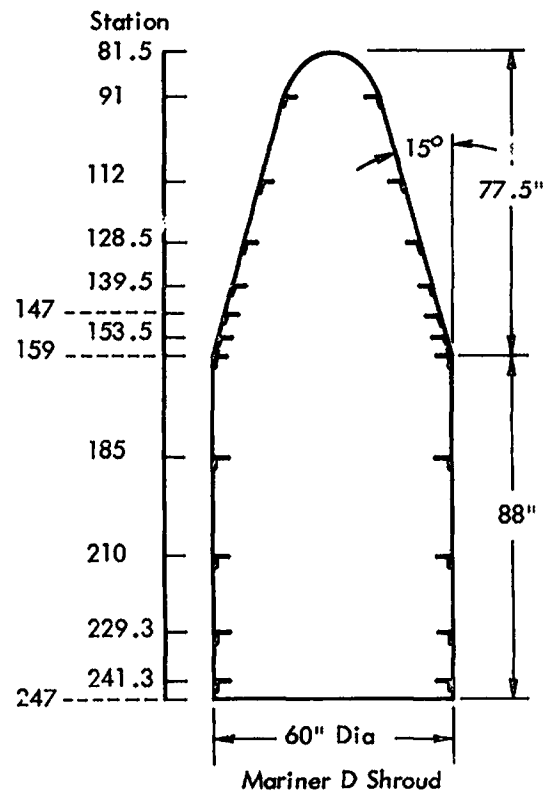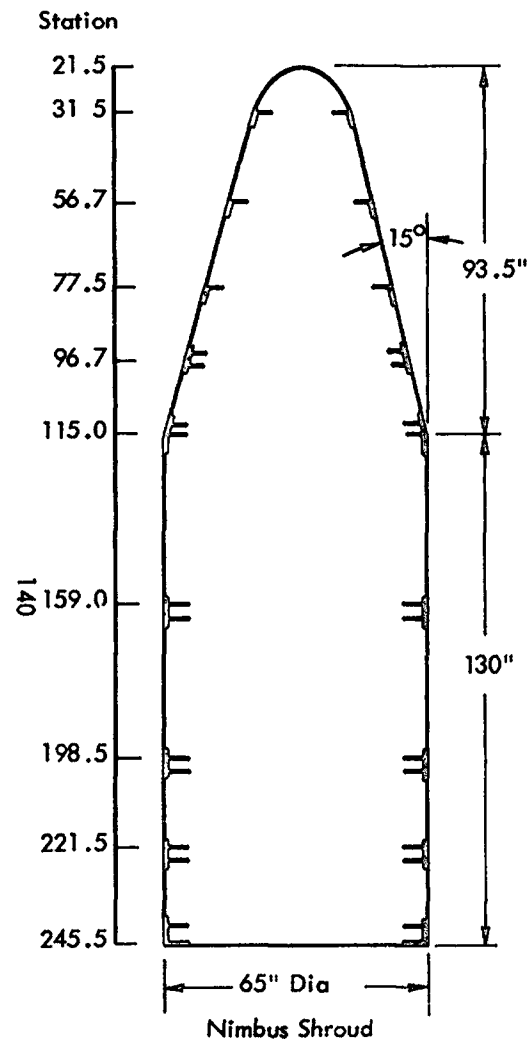
Figure 18. Details of Shroud Structures Analyzed

Octave Band Center Frequencies

One-Third Octave Band Center Frequencies – Hz

— · · — · ·   Predicted Surface Pressures based upon Franken and Weiner Method } See
───────────   Predicted Surface Pressures based upon Wyle Method   } Appendix
   ⊙   Measured Maximum Free-Field Sound Pressure Levels between   A
                (T–3) sec and (T+2) sec. Microphone located on Umbilical Tower
                about 25 ft from Vehicle Surface (Atlas/Centaur AC-16) Ref. 52
— — — — —   Measured Umbilical Tower Data Corrected to Surface Pressures
                at the Shroud

Figure 19. Rocket-Noise Spectra at External Surface of Payload Shrouds for the Atlas
Booster at Lift-Off — Comparison between Various Prediction Schemes
and Measured Data
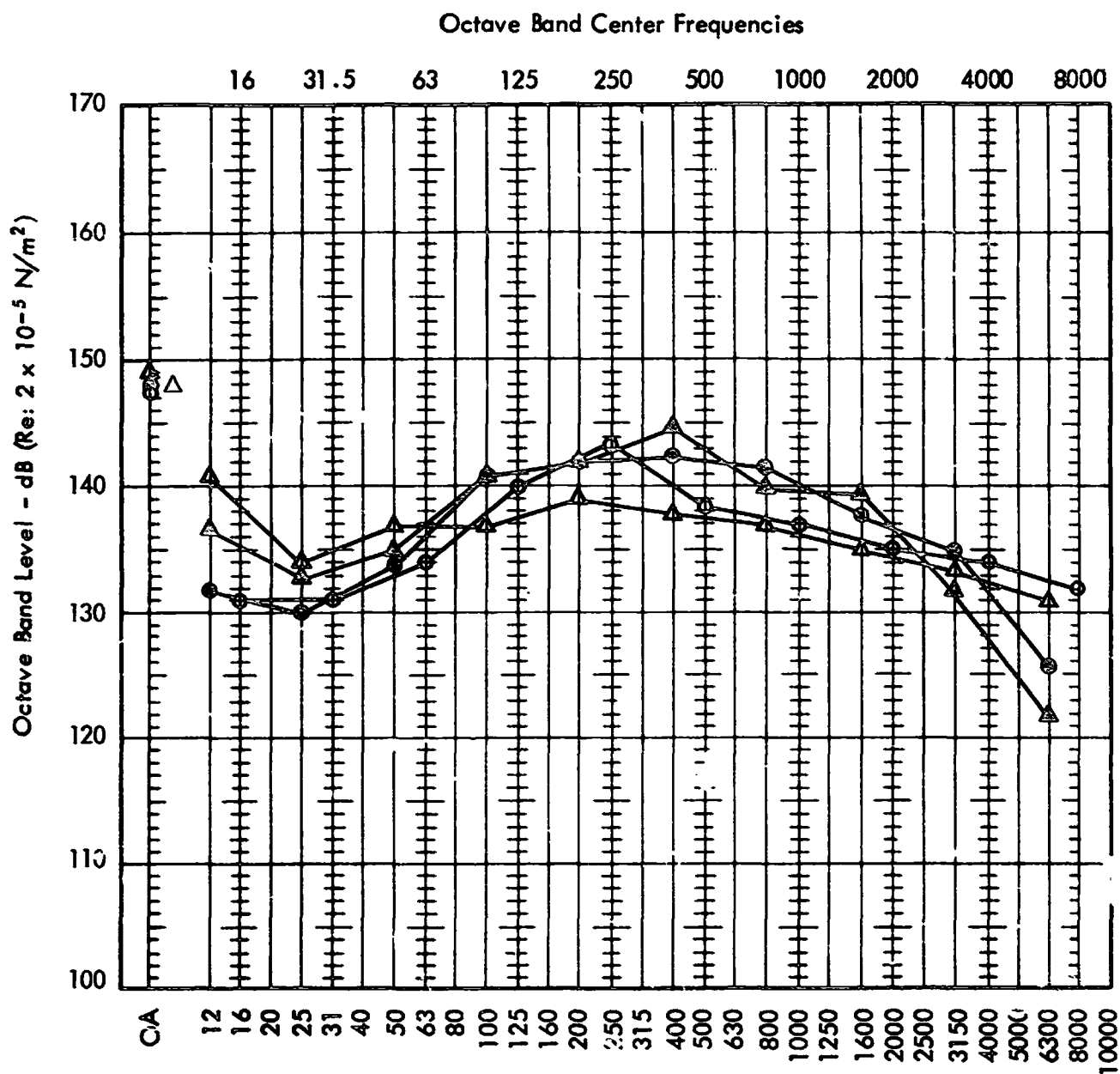
141

Figure 20. Measured Octave Band Sound Pressure Levels on the Umbilical Tower
near External Surface of Nimbus and OAO Shrouds at Lift-Off
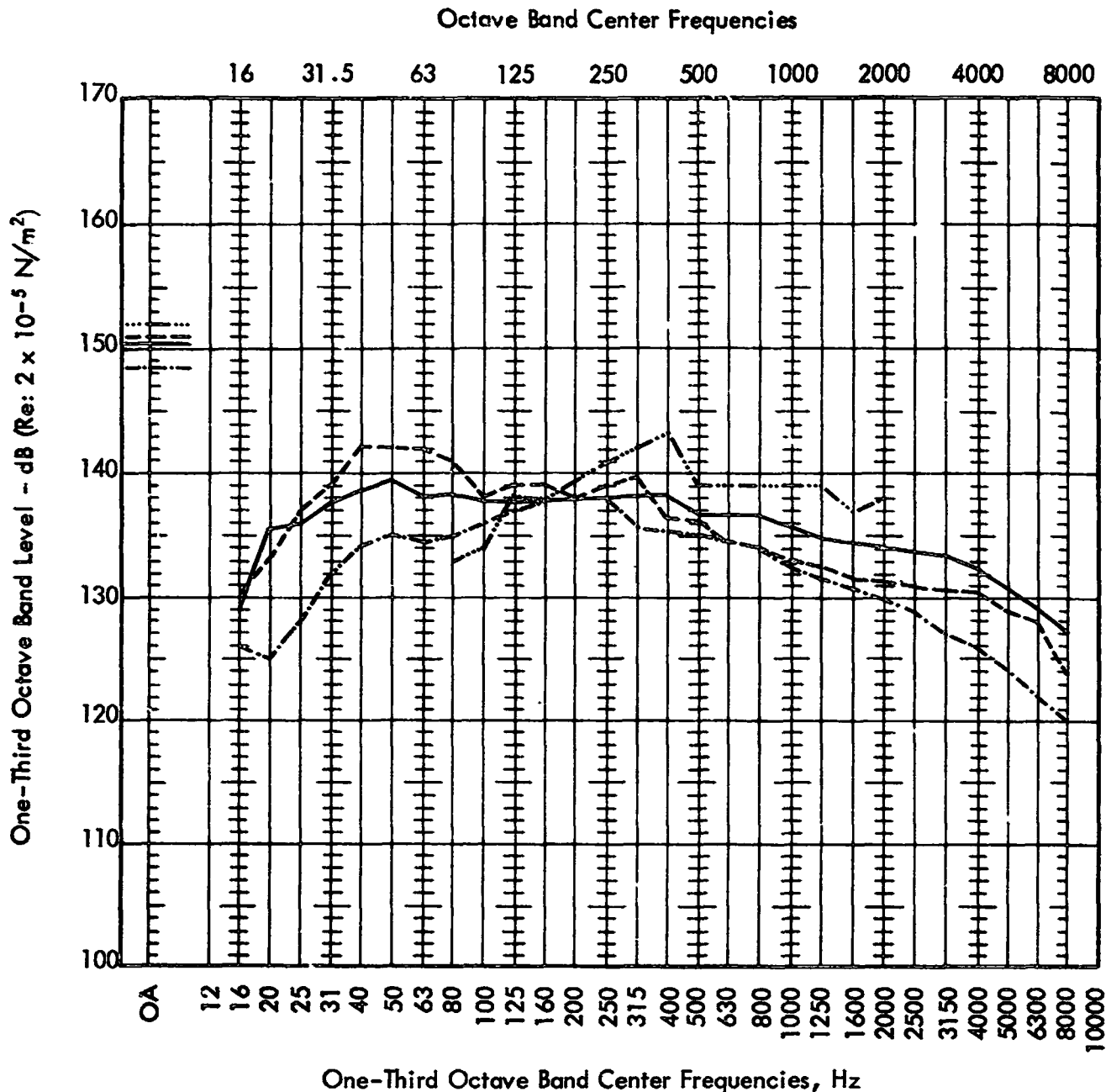
O OGO-C/Thrust Assisted Thor-Agena: External SPL at Lift-Off (microphone on
   umbilical towei near mid-section of Nimbus shroud) Reference 53

△ OGO-C/Thrust Assisted Thor-Agena: External SPL at Lift-Off (microphone on
   umbilical tower near base of Nimbus shroud) Reference 53

△ OT-2/Improved Delta (TAD): External SPL at Lift-Off (microphone on umbilical
   tower near cone-cyiinder junction of Nimbus shroud) Reference 53

O OAO-A2/Atlas-Centaur: External SPL at Lift-Off (microphone on umbilical
   tower near base of OAO shroud) Reference 52

142

Figure 21. Titan II and Titan IIIA; One-Third Octave Band External Sound Pressure
Levels at Shroud Surface during Lift-Off and Static Firing
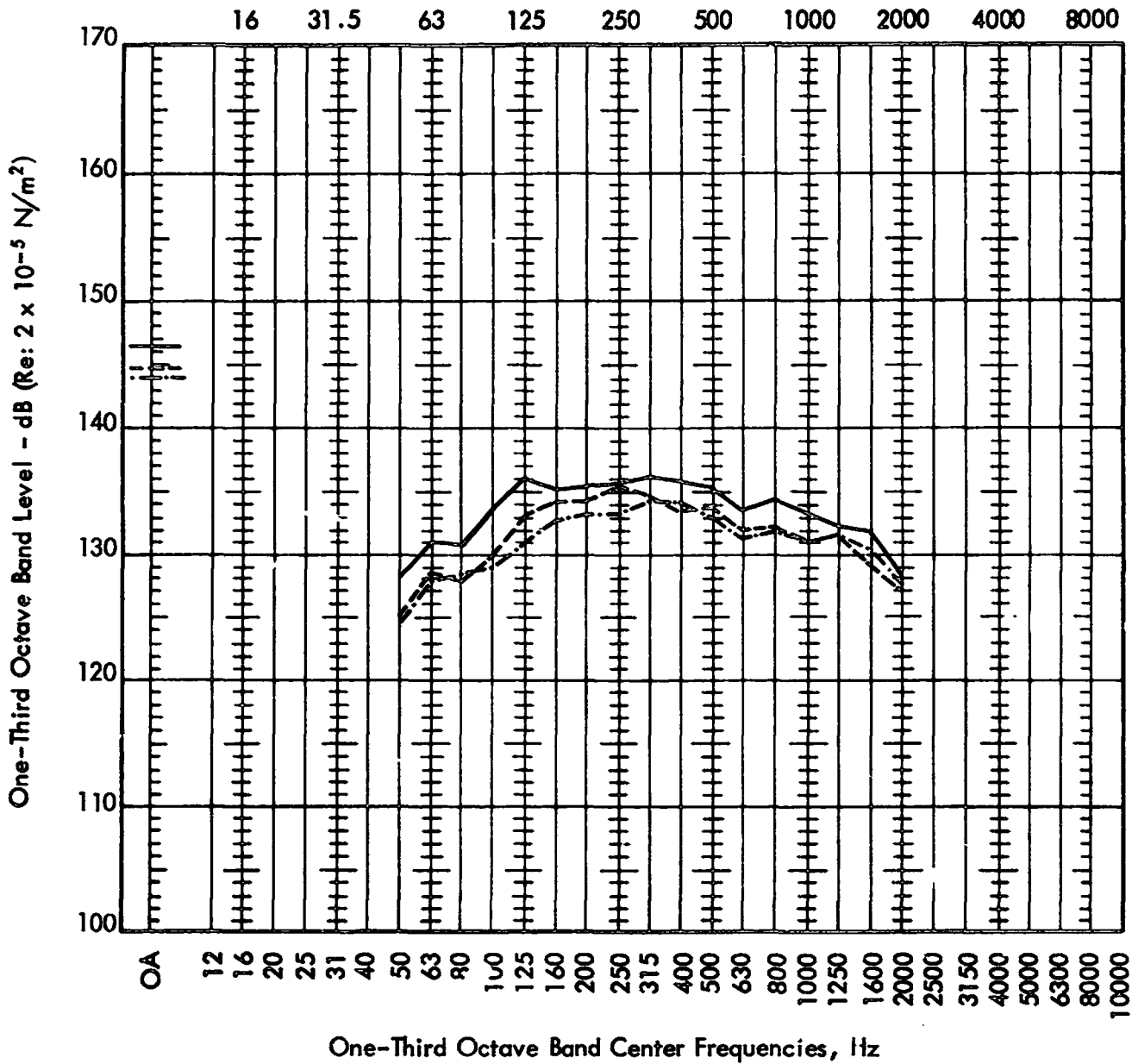
Figure 22.   Titan IIIC; One-Third Octave Band External Sound Pressure Levels at Shroud Surface during Lift-Off
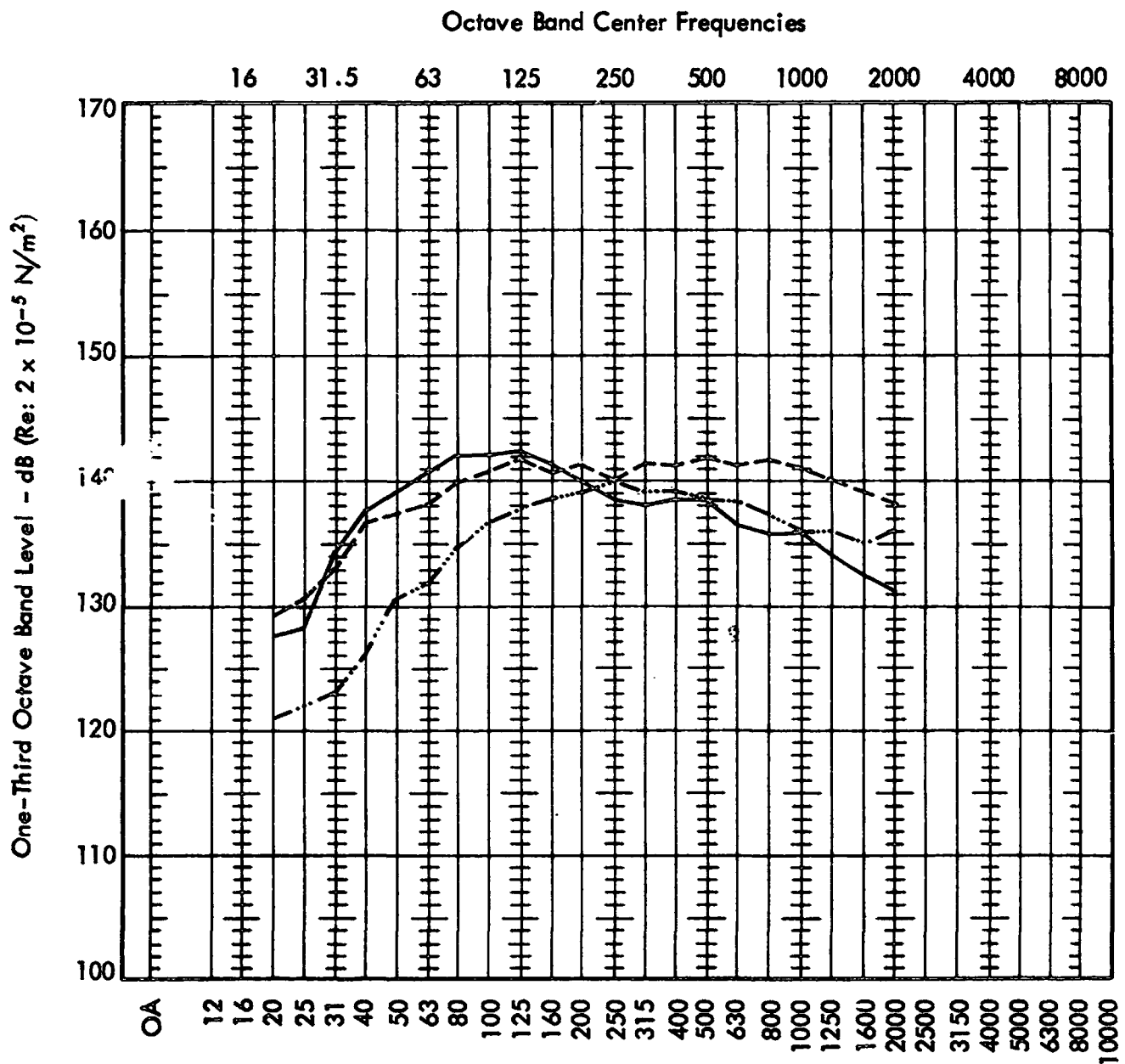
144

Figure 23. One-Third Octave Band Sound Pressure Levels on the External Surface of the SLA; Measured Lift-Off Data

145
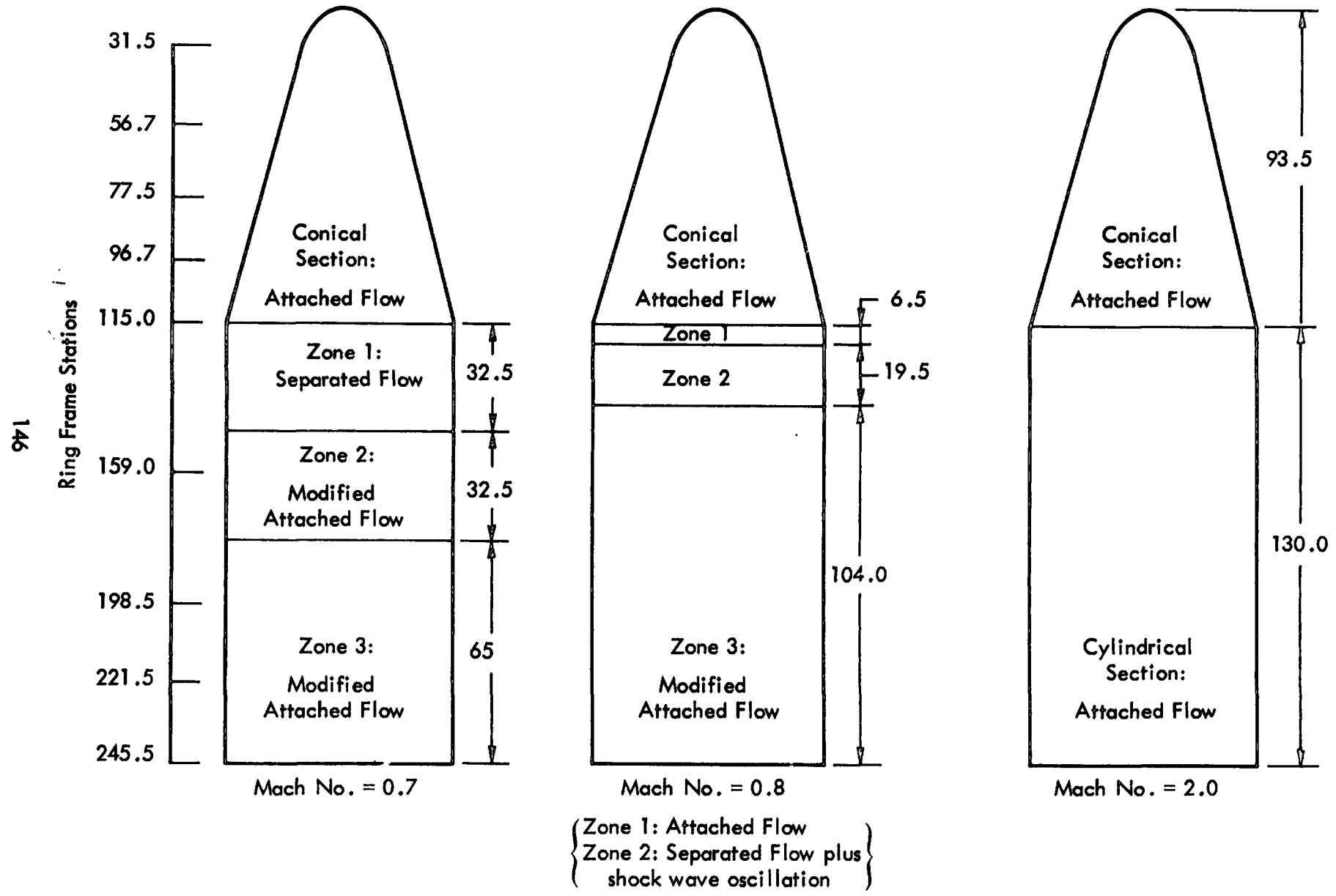
Figure 24. Characteristics of the Aerodynamic Fluctuating Pressure Environments for the Nimbus Shroud (15-degree Cone-Cylinder Body)
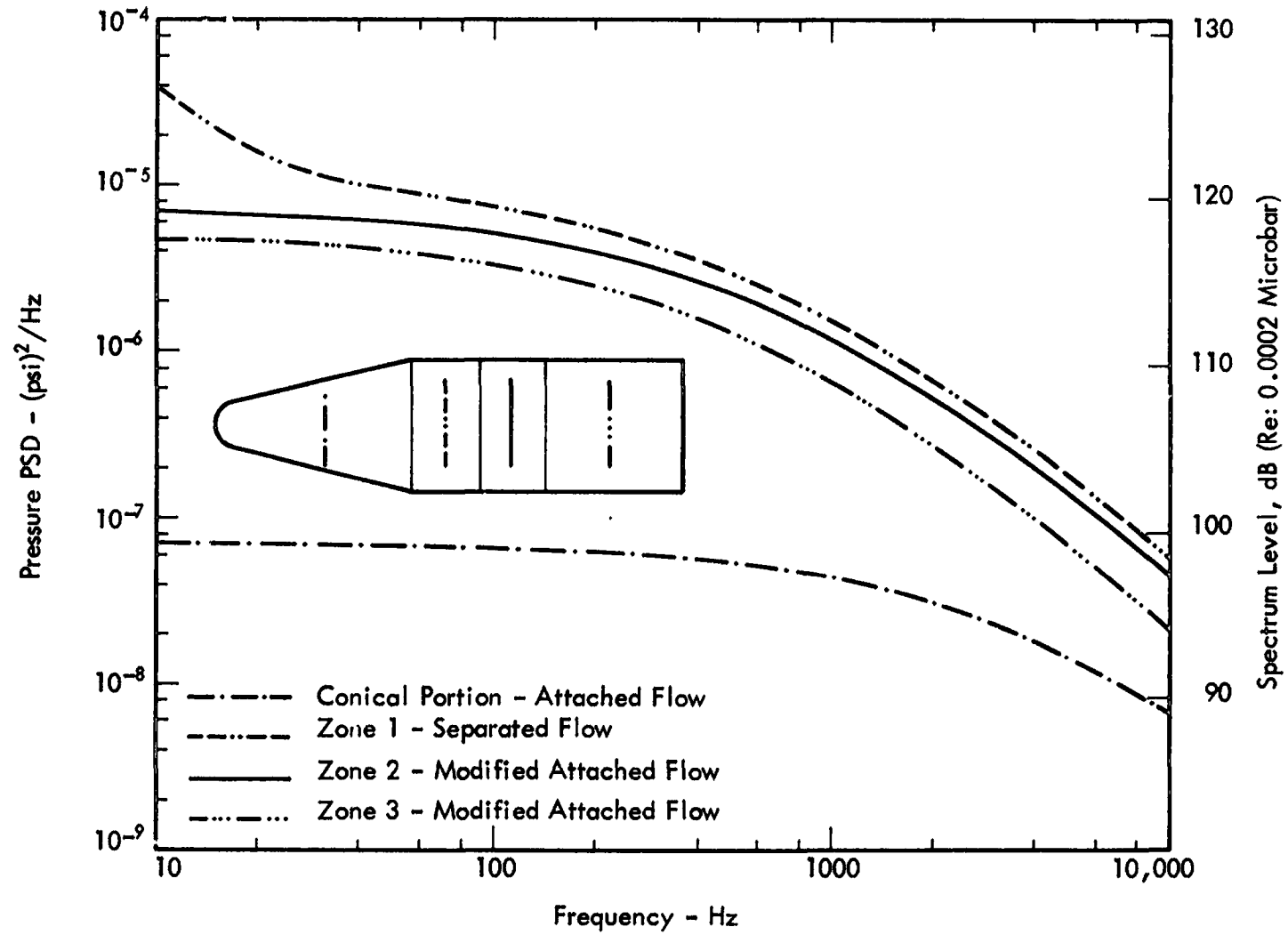
Figure 25. Spectra of Fluctuating Pressures over the Nimbus Shroud; Mach 0.7

147
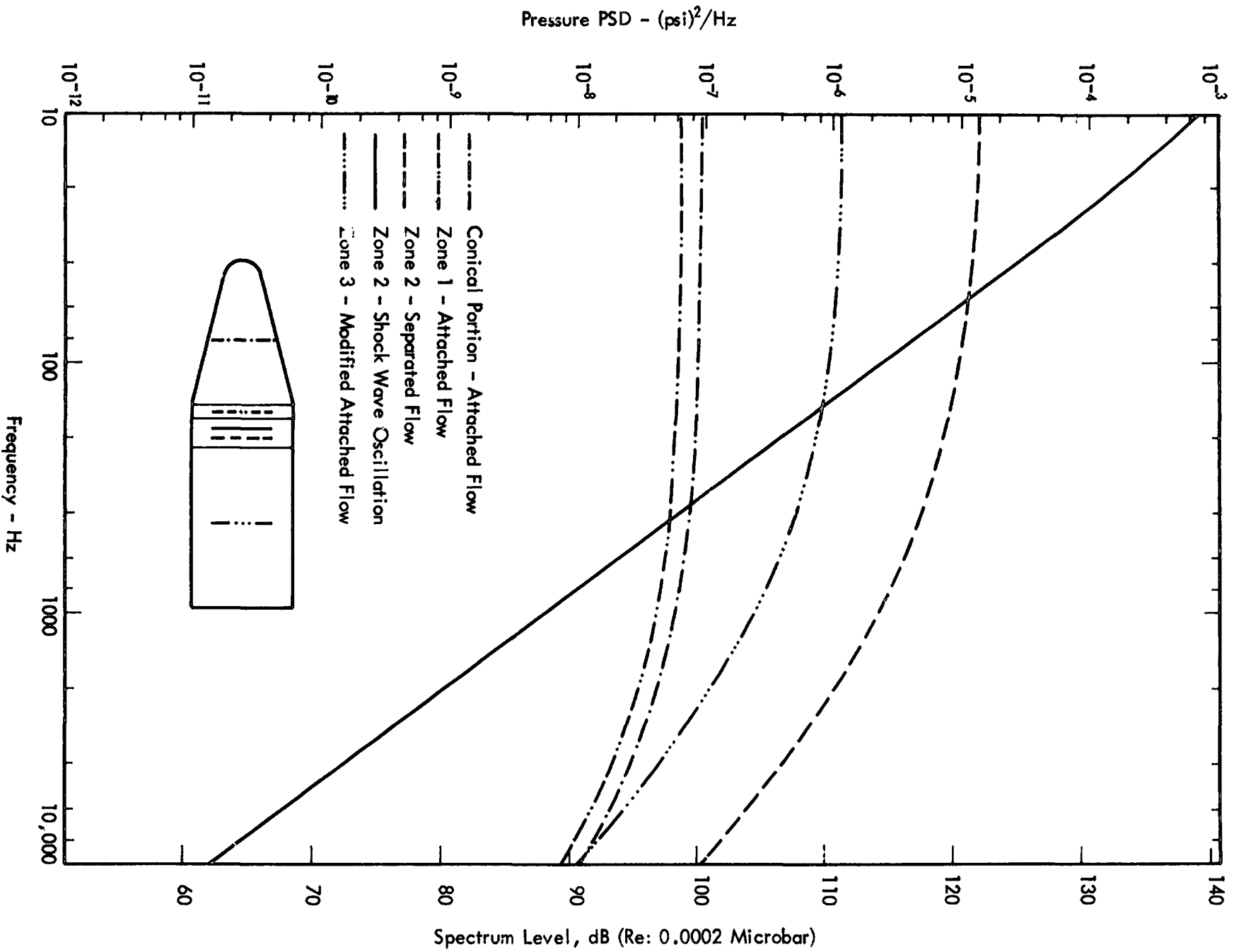
Figure 26. Spectra of Fluctuating Pressure over the Nimbus Shroud; Mach 0.8

Legend:
- Conical Portion – Attached Flow
- Zone 1 – Attached Flow
- Zone 2 – Separated Flow
- Zone 2 – Shock Wave Oscillation
- Zone 3 – Modified Attached Flow

Pressure PSD – (psi)²/Hz

Frequency – Hz

Spectrum Level, dB (Re: 0.0002 Microbar)

148
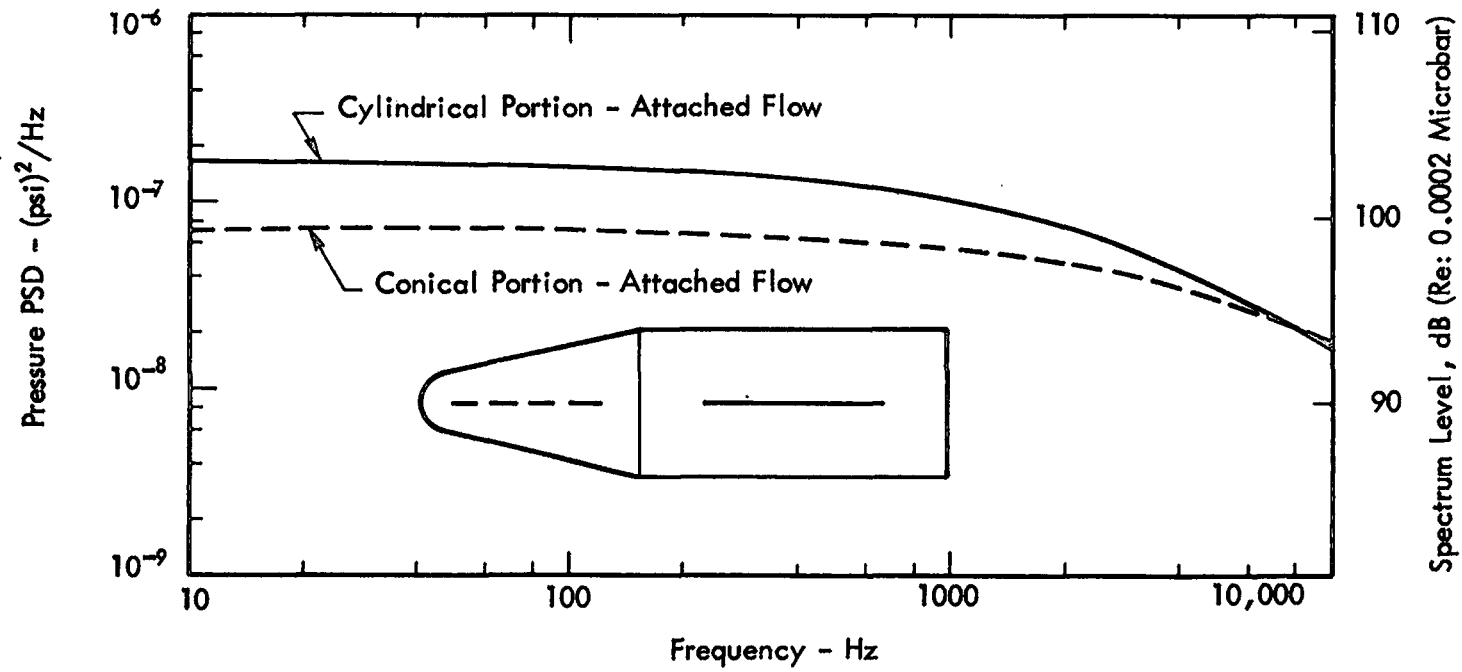
Figure 27. Spectra of Fluctuating Pressures over the Nimbus Shroud; Mach 2.0
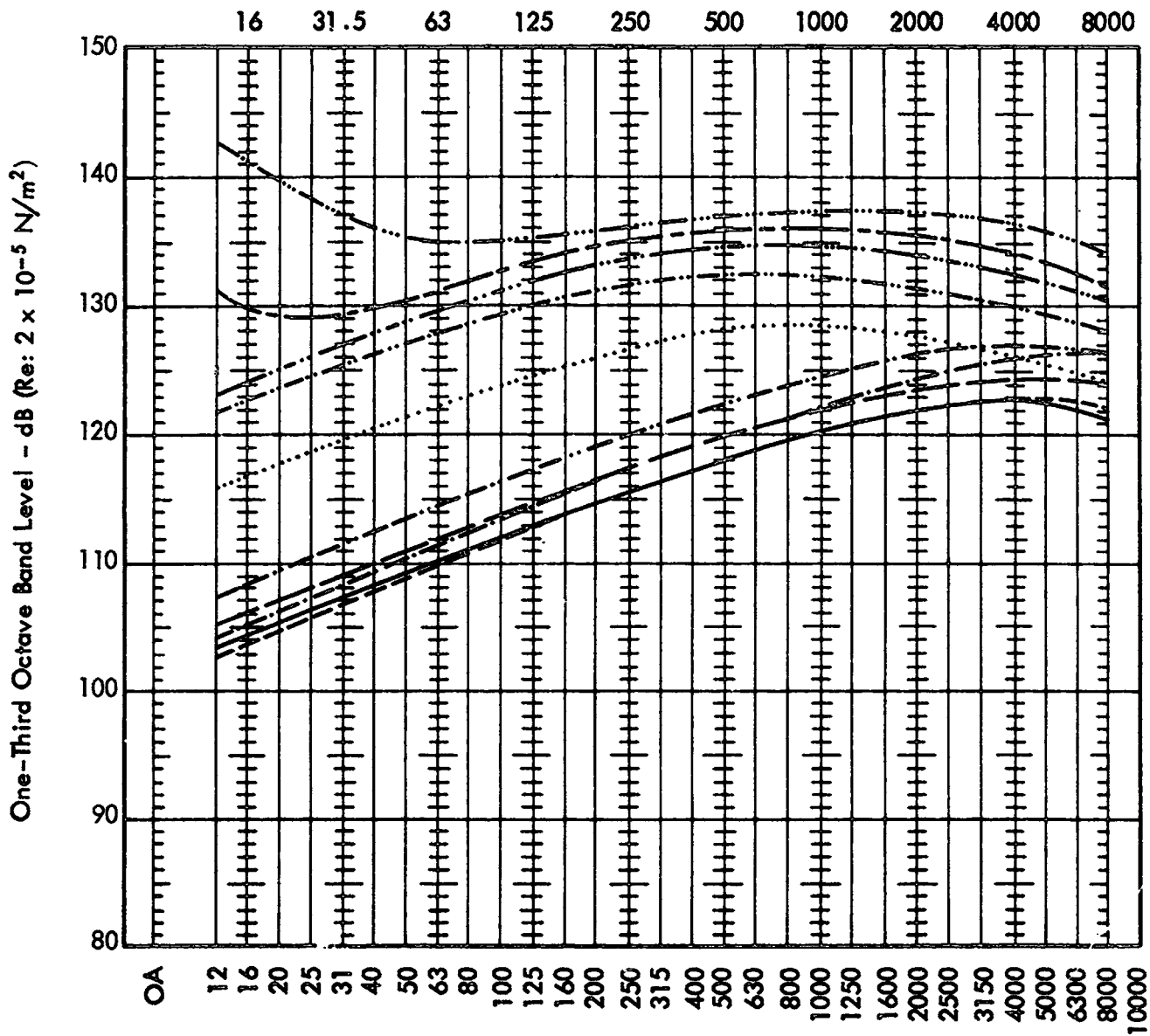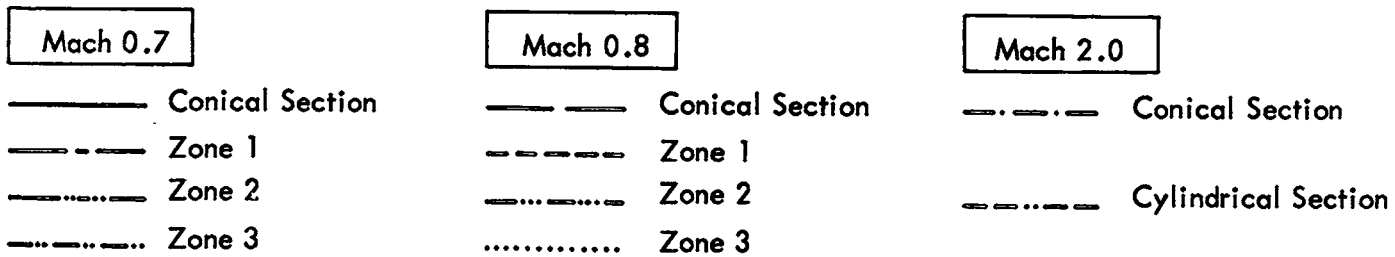
Figure 28. Calculated One-Third Octave Band Sound Pressure Levels at Surface of Nimbus Shroud during Flight; Mach Numbers M = 0.7, M = 0.8, and M = 2.0

150

Octave Band Center Frequencies
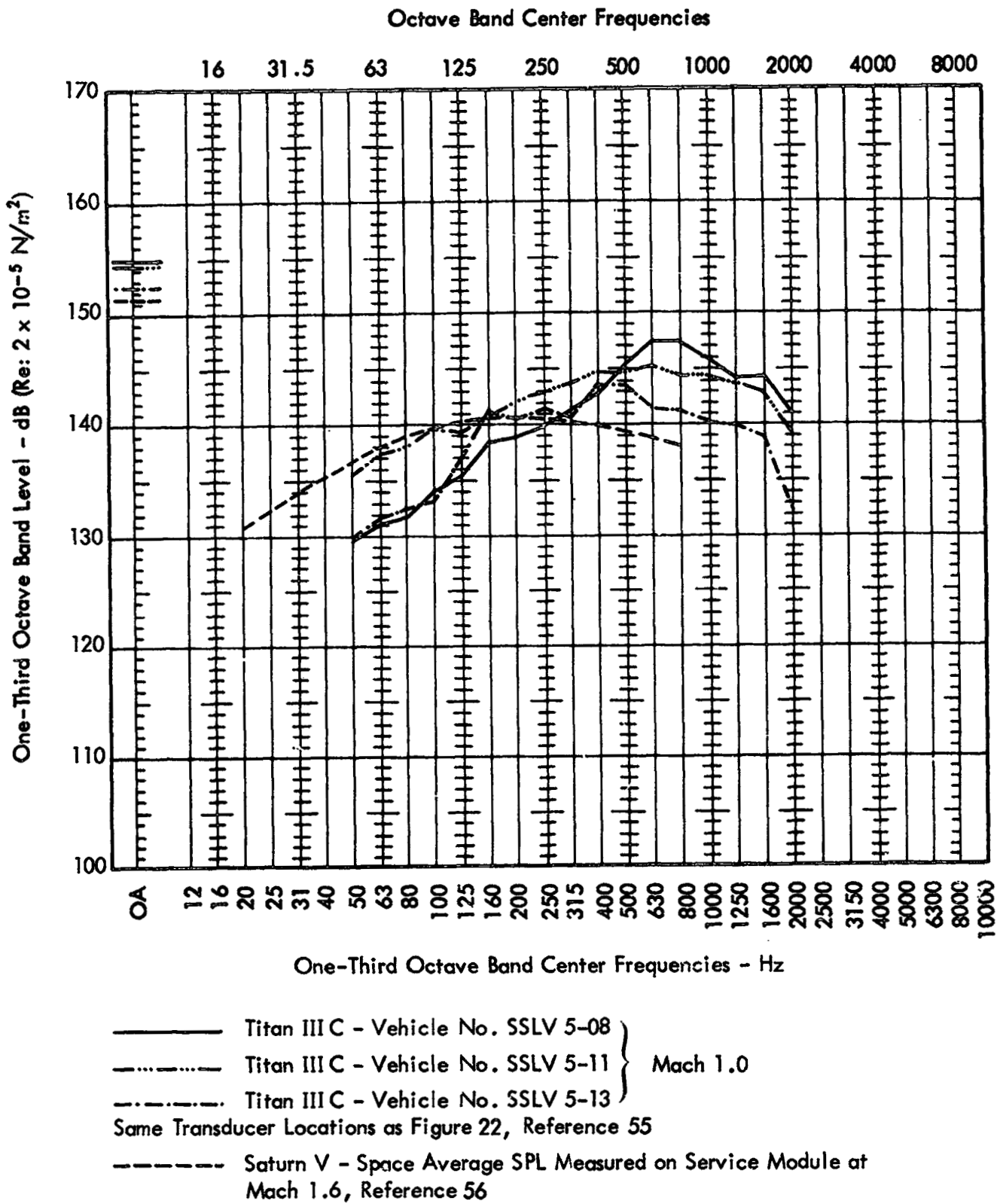
Figure 29. One-Third Octave Band Sound Pressure Levels Measured at the Payload Surface during Flight; Titan III C and Saturn Vehicles

Legend:

———————— Titan III C – Vehicle No. SSLV 5–08 ⎫
—···—···— Titan III C – Vehicle No. SSLV 5–11 ⎬ Mach 1.0
—·—··—·—· Titan III C – Vehicle No. SSLV 5–13 ⎭
Same Transducer Locations as Figure 22, Reference 55

———————— Saturn V – Space Average SPL Measured on Service Module at Mach 1.6, Reference 56

151
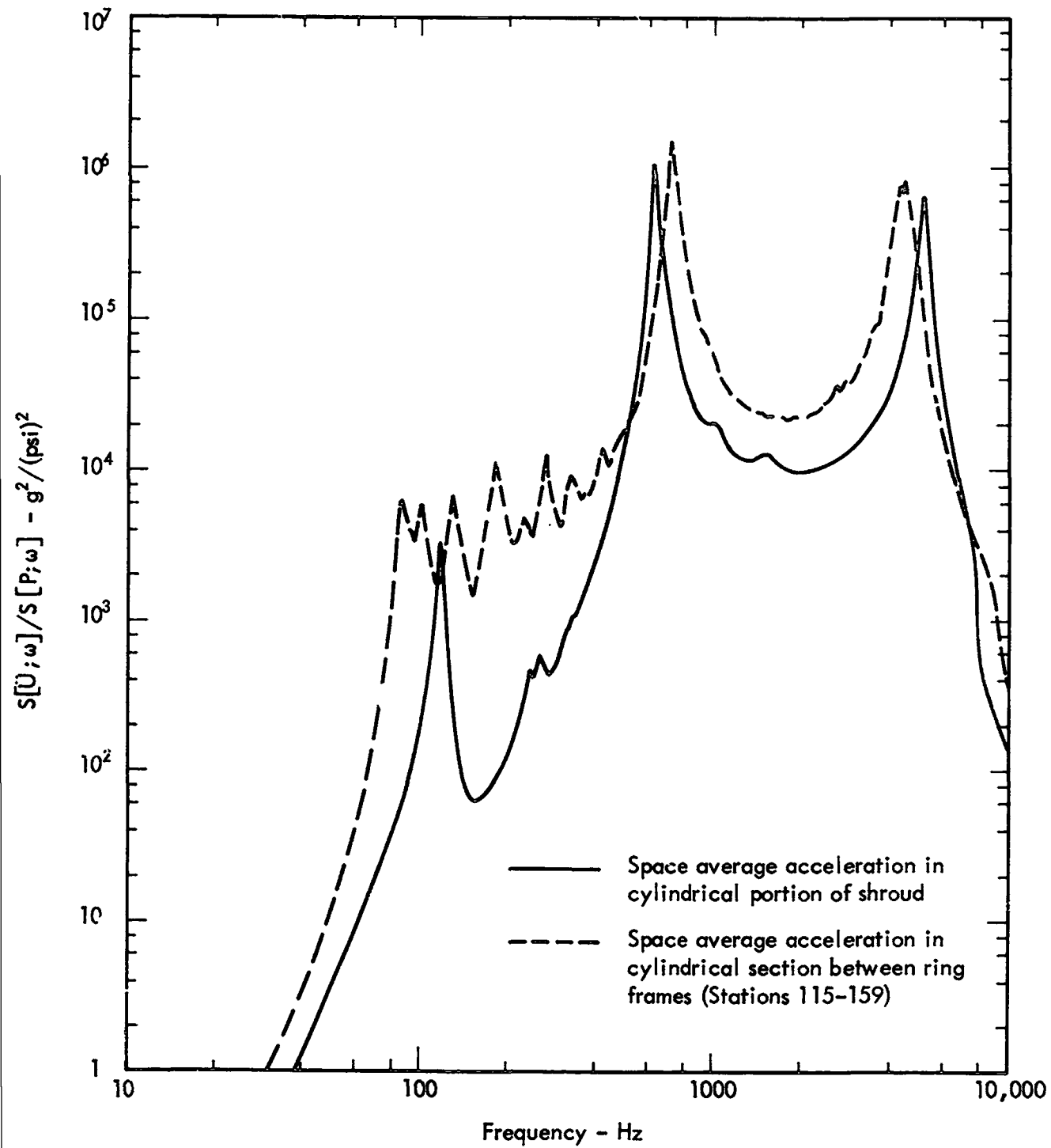
NOTE: For Conversion of Acceleration PSD to Acceleration Spectrum Level;
        [AL–SPL] – dB (Re 1 g and 2.10^{-5} N/m^2) = $\left\{10 \log_{10} (g^2/(psi)^2) - 170.75\right\}$ – dB

Figure 30. Acceleration Spectra of Cylindrical Portion of Nimbus Shroud;
            Lift–Off Acoustic Environment

152
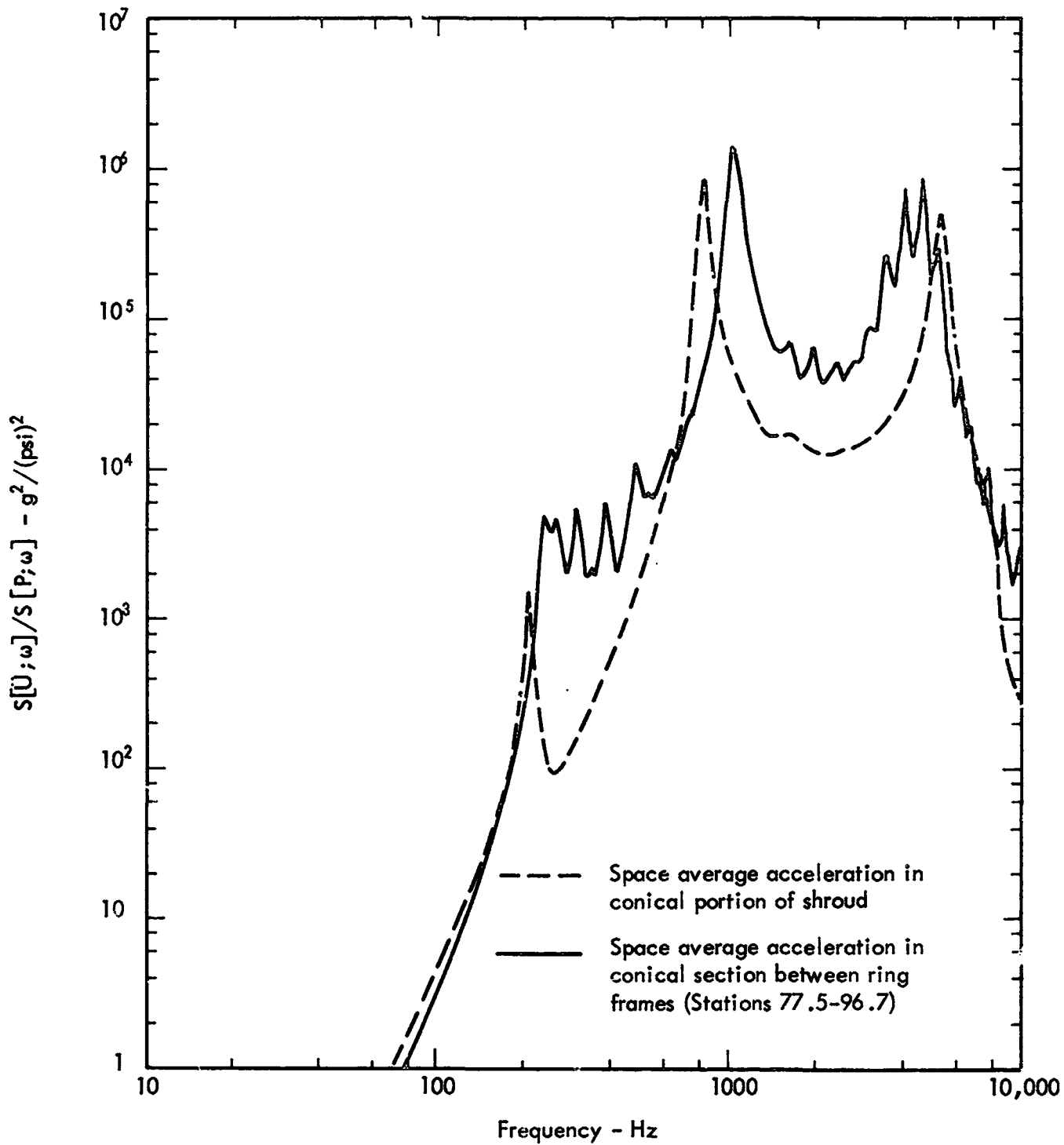
Figure 31. Acceleration Spectra of Conical Portion of Nimbus Shroud; Lift-Off Acoustic Environment

153
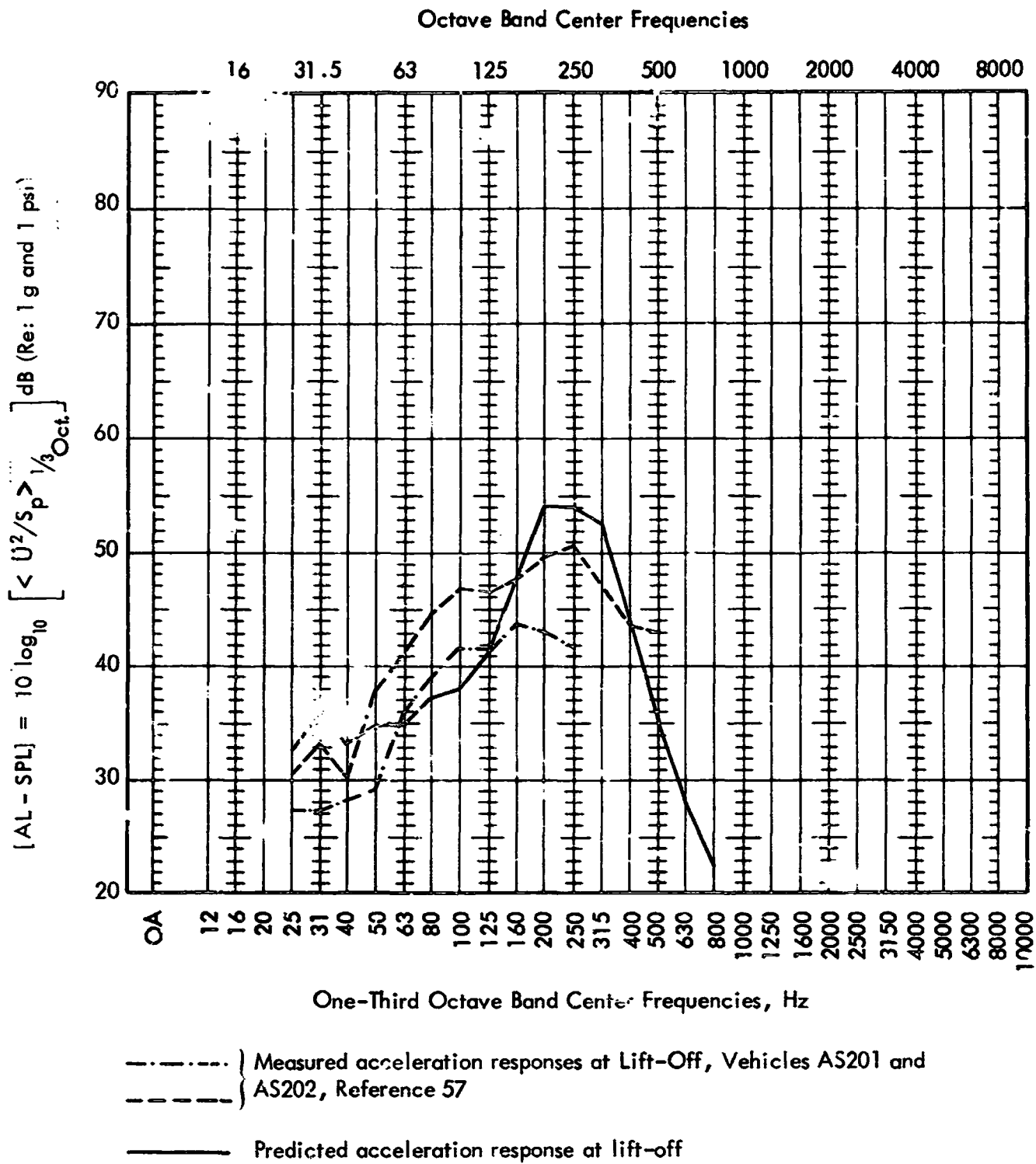
Figure 32. One-Third Octave Band Normalized Acceleration Response of the SLA during Lift-Off

154
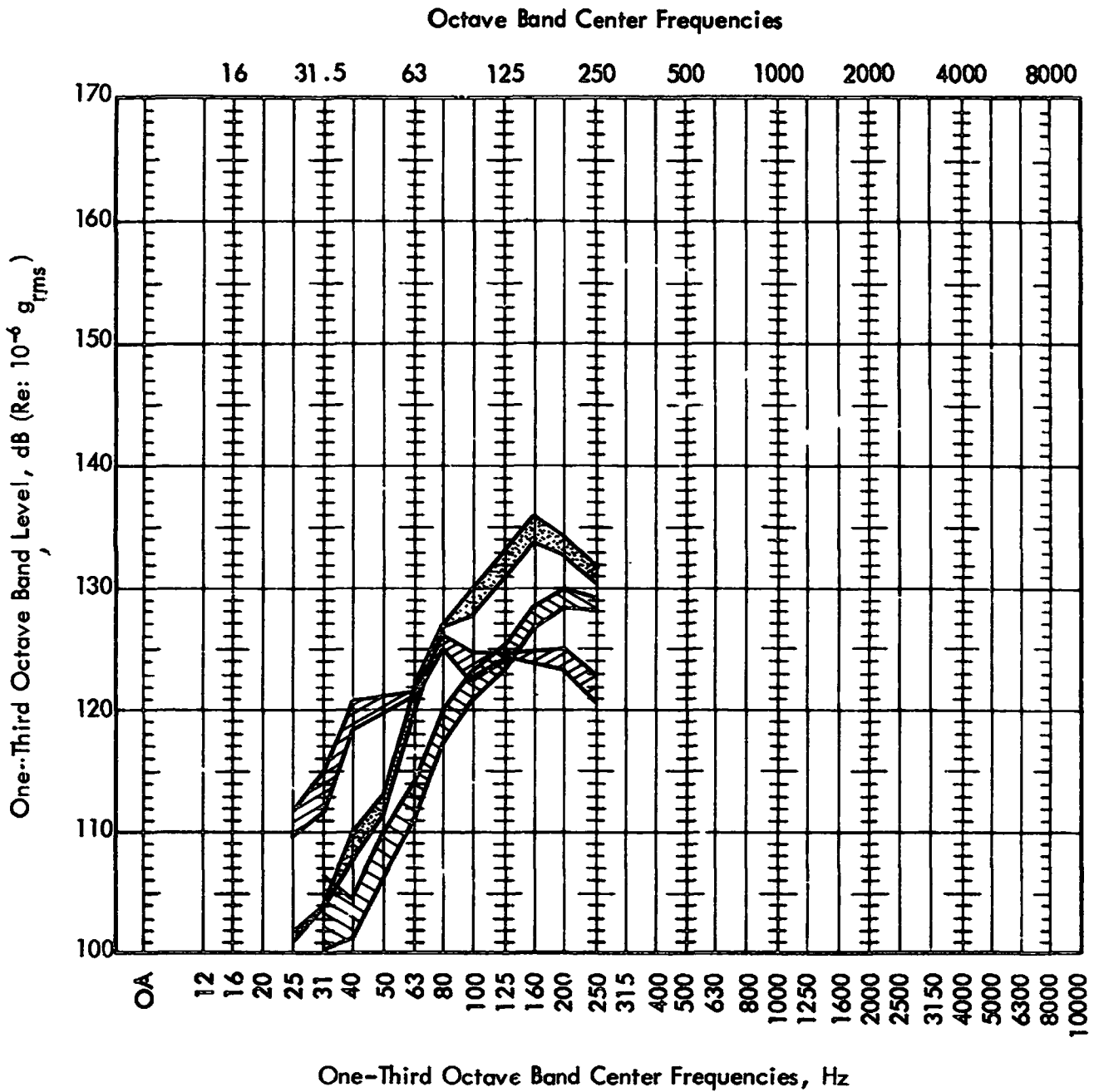
Figure 33. One-Third Octave Band Acceleration Levels of the SLA Structure during Lift-Off, Transonic Flight and Supersonic Flight (Data from Reference 57)
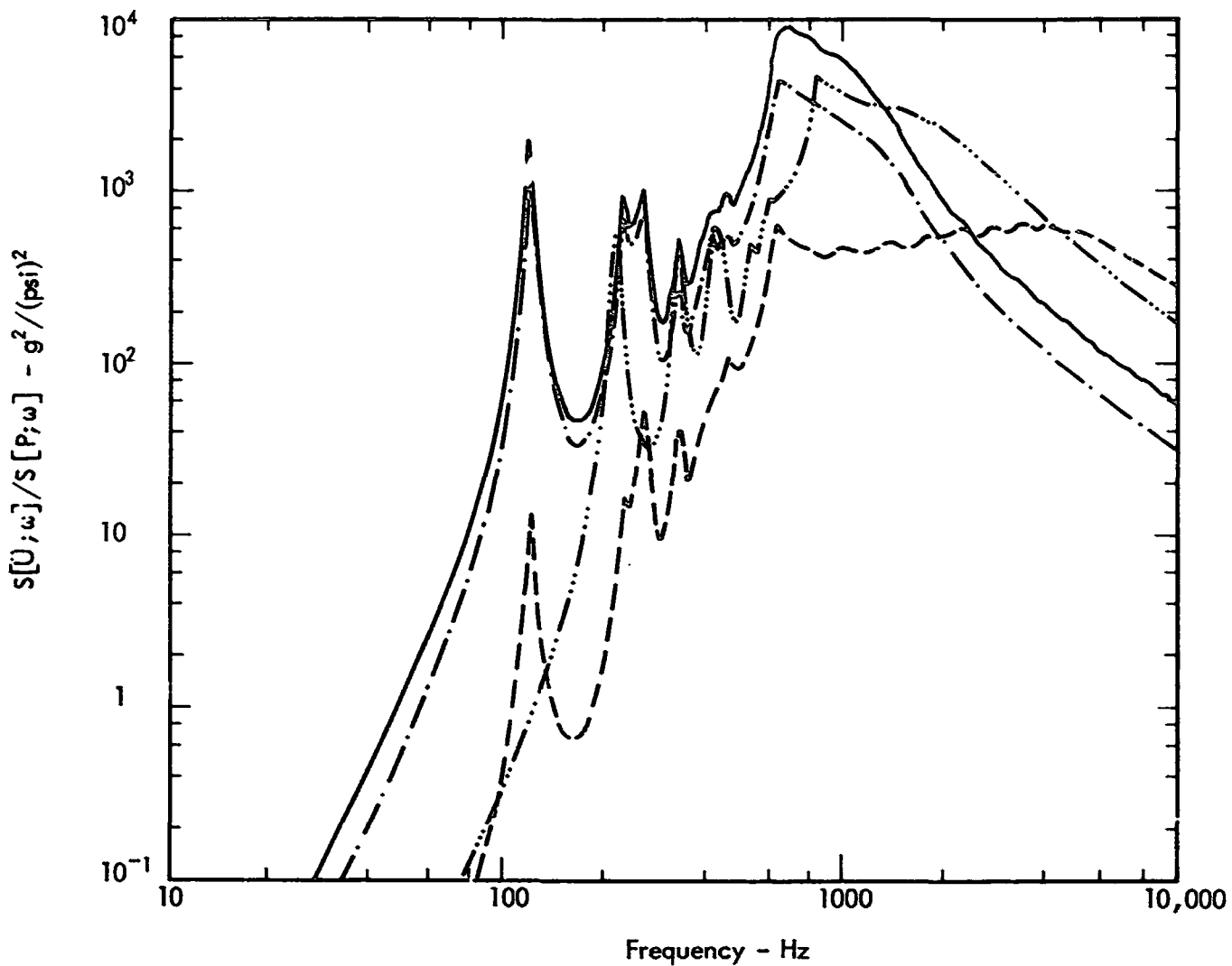
155

10^4

10^3

10^2

10

1

10^{-1}

$S[\ddot{U};\omega]/S[P;\omega] - g^2/(psi)^2$

10   100   1000   10,000

Frequency – Hz

— — — —   Space average acceleration in cylindrical portion of shroud
                due to separated flow concentrated over Zone 1

— · — · —   Space average acceleration in cylindrical portion of shroud
                due to modified attached flow concentrated over Zone 2

———————   Space average acceleration in cylindrical portion of shroud
                due to modified attached flow concentrated over Zone 3

— ··· — ···   Space average acceleration in conical portion of shroud due
                to attached flow over entire conical surface

Figure 34. Acceleration Spectra of Nimbus Shroud; Mach 0.7

156
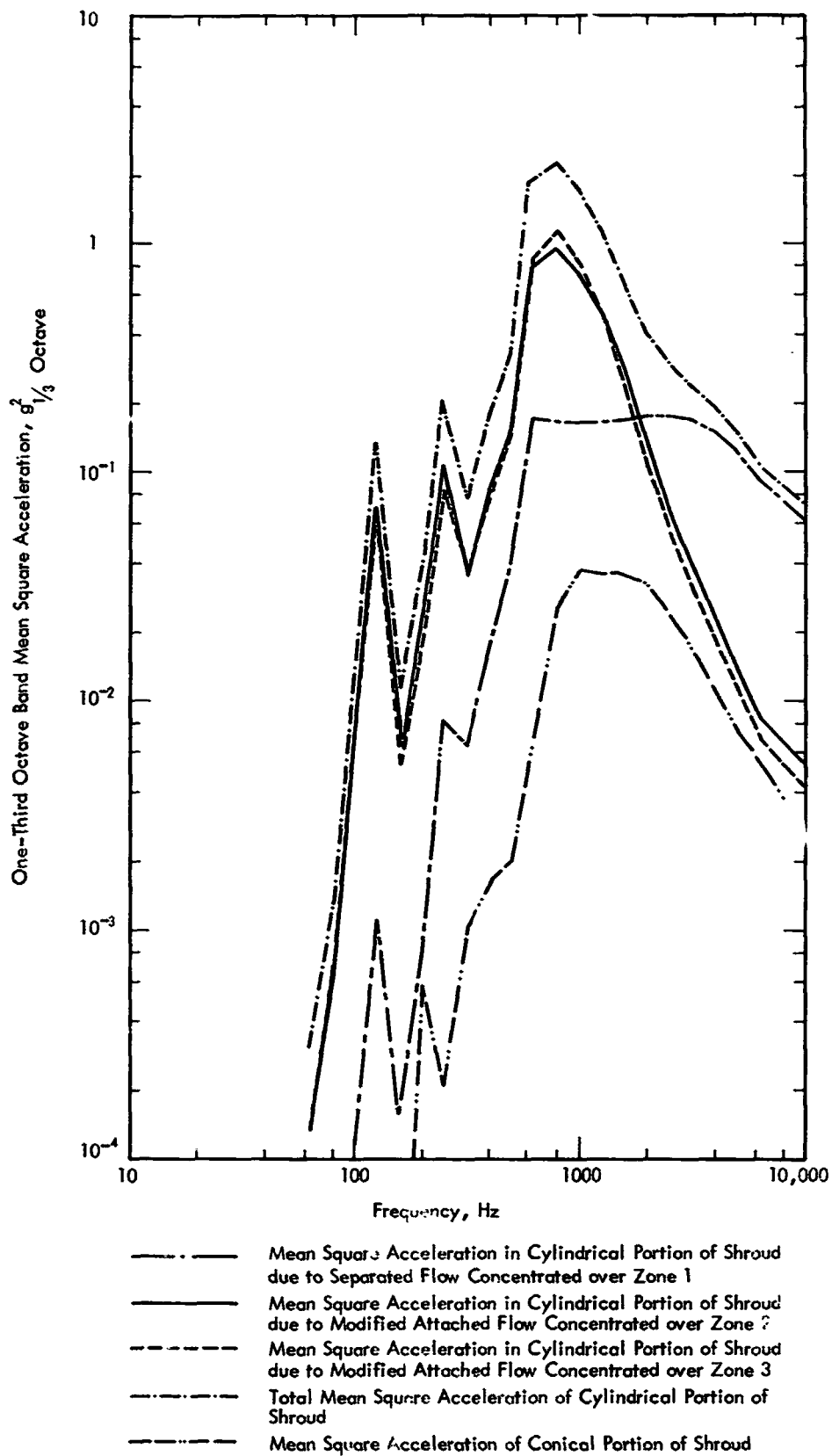
Figure 35. Mean Square Acceleration of Nimbus Shroud; Mach 0.7

The legend of the figure reads:

— · — Mean Square Acceleration in Cylindrical Portion of Shroud due to Separated Flow Concentrated over Zone 1

——— Mean Square Acceleration in Cylindrical Portion of Shroud due to Modified Attached Flow Concentrated over Zone 2

— — — Mean Square Acceleration in Cylindrical Portion of Shroud due to Modified Attached Flow Concentrated over Zone 3

— · · — Total Mean Square Acceleration of Cylindrical Portion of Shroud

— — · · — Mean Square Acceleration of Conical Portion of Shroud

The vertical axis reads: One–Third Octave Band Mean Square Acceleration, $g^2_{1/3}$ Octave

The horizontal axis reads: Frequency, Hz

157

Figure 36. Acceleration Spectra of Local Sections of the Nimbus Shroud; Mach 0.7
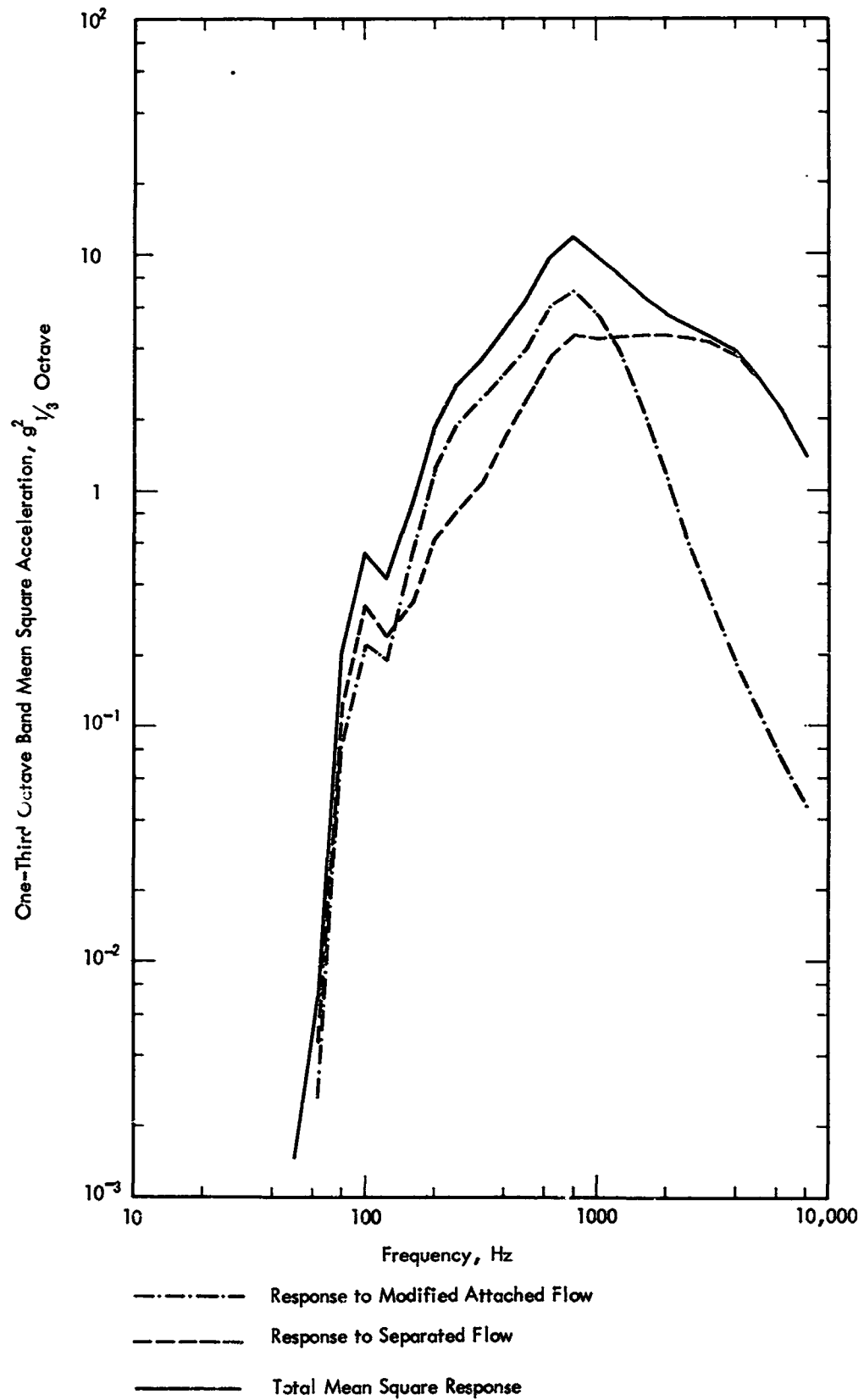
Figure 37. Mean Square Acceleration of Segment Between Ring Frame
Stations 115 and 159; Nimbus Shroud, Mach 0.7

159
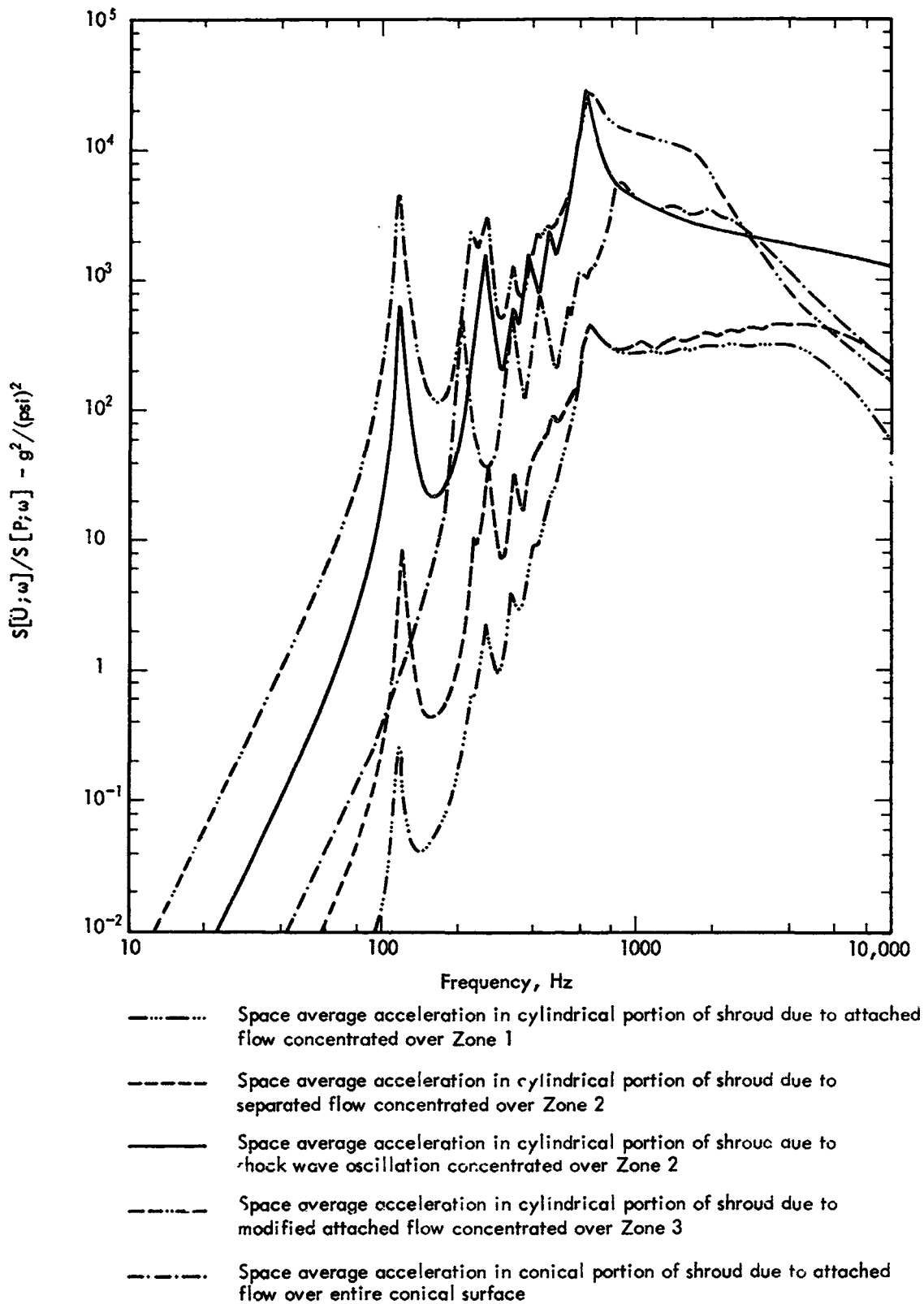
Figure 38. Acceleration Spectra of Nimbus Shroud; Mach 0.8

The y-axis is labeled $s[U;\omega]/s[P;\omega] - g^2/(psi)^2$ and the x-axis is labeled Frequency, Hz.

Legend:

—···—··· Space average acceleration in cylindrical portion of shroud due to attached flow concentrated over Zone 1

————— Space average acceleration in cylindrical portion of shroud due to separated flow concentrated over Zone 2

————— Space average acceleration in cylindrical portion of shroud due to shock wave oscillation concentrated over Zone 2

—··—··— Space average acceleration in cylindrical portion of shroud due to modified attached flow concentrated over Zone 3

—·—·—· Space average acceleration in conical portion of shroud due to attached flow over entire conical surface

160

Figure 39. Mean Square Acceleration of Nimbus Shroud; Mach 0.8

161
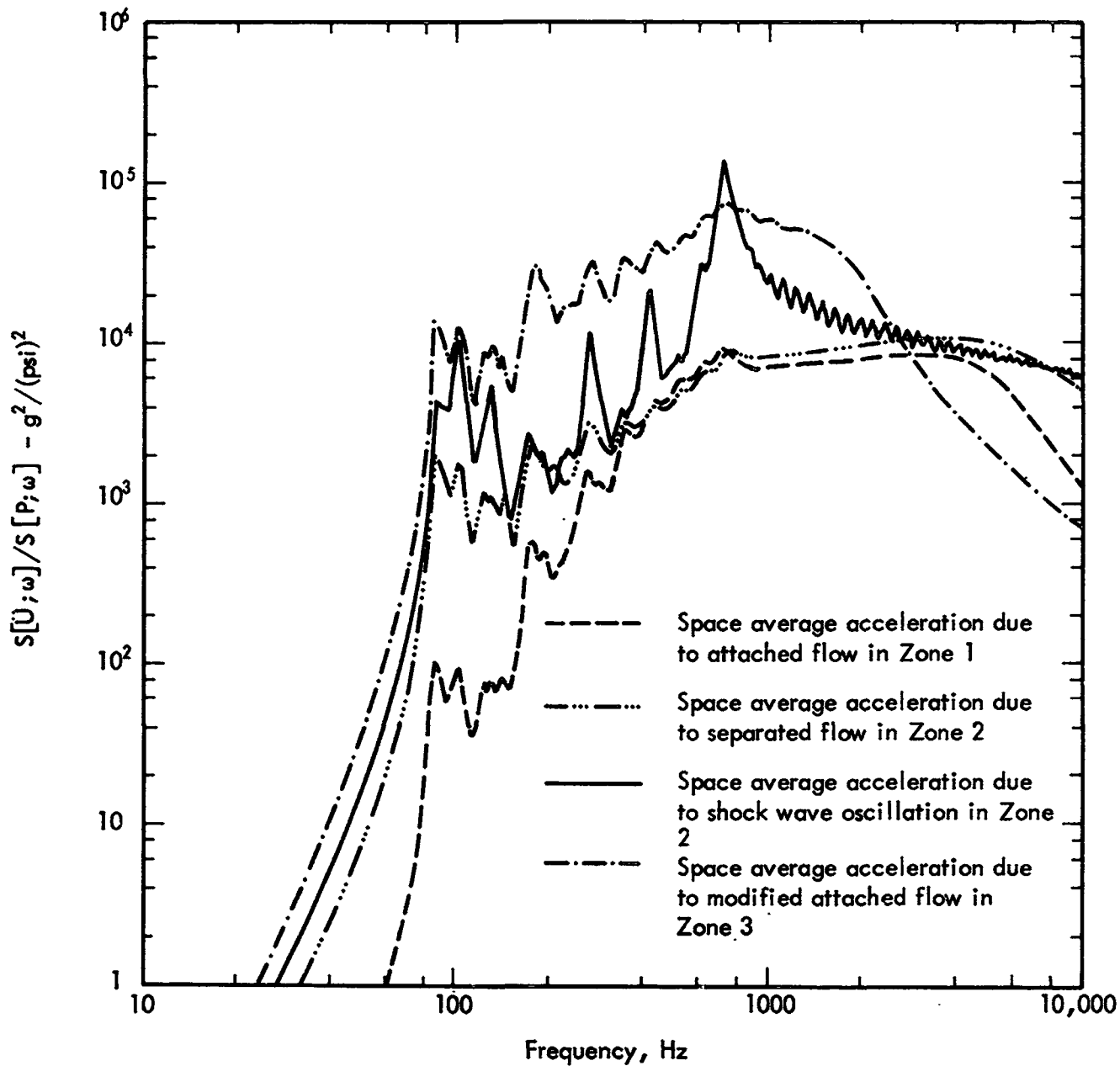
Figure 40. Acceleration Spectra of Structural Section Between Ring Frame Stations 115 and 159; Nimbus Shroud – Mach 0.8
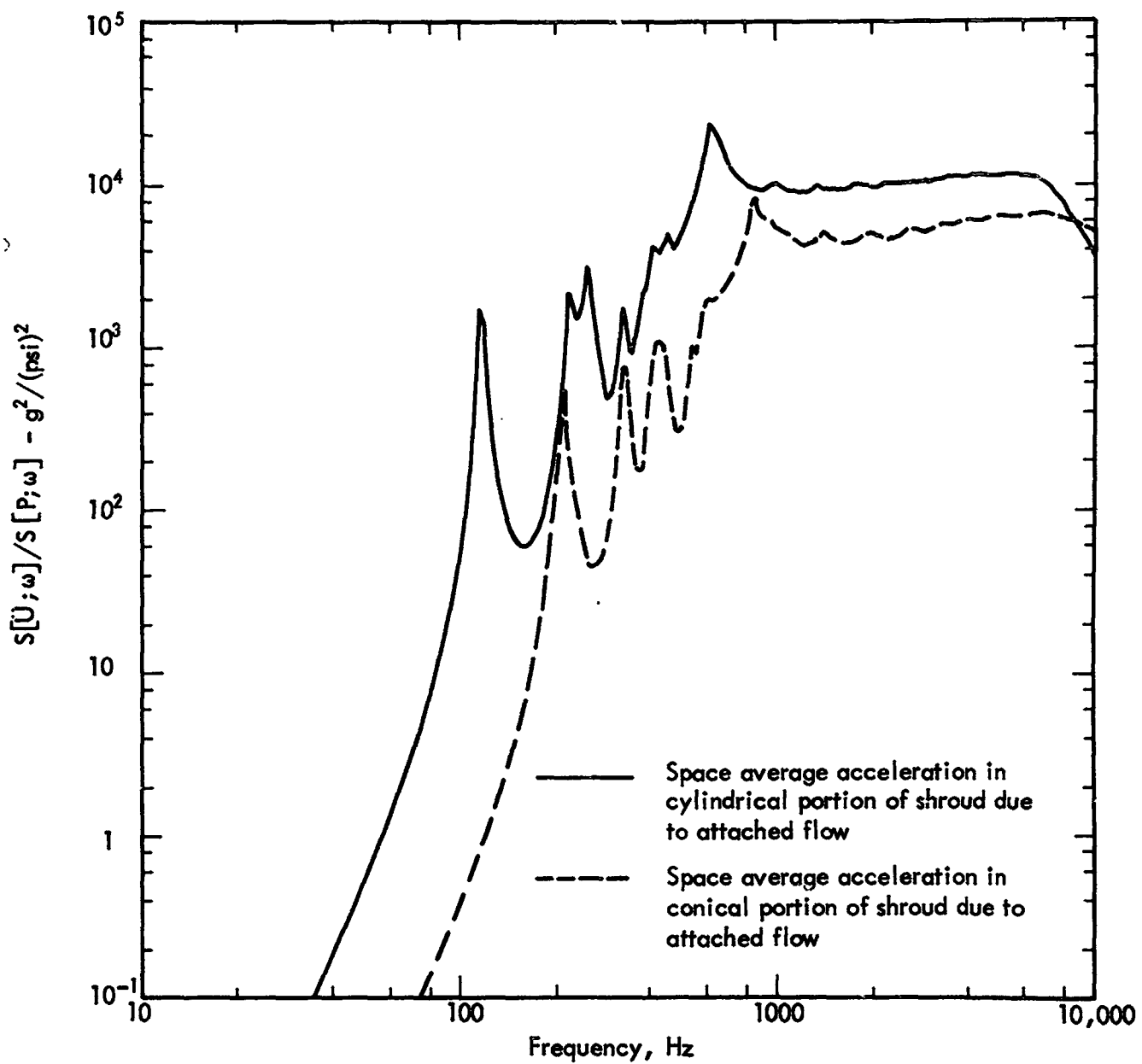
Figure 41. Acceleration Spectra of Nimbus Shroud; Mach 2.0 (approximately Max q)
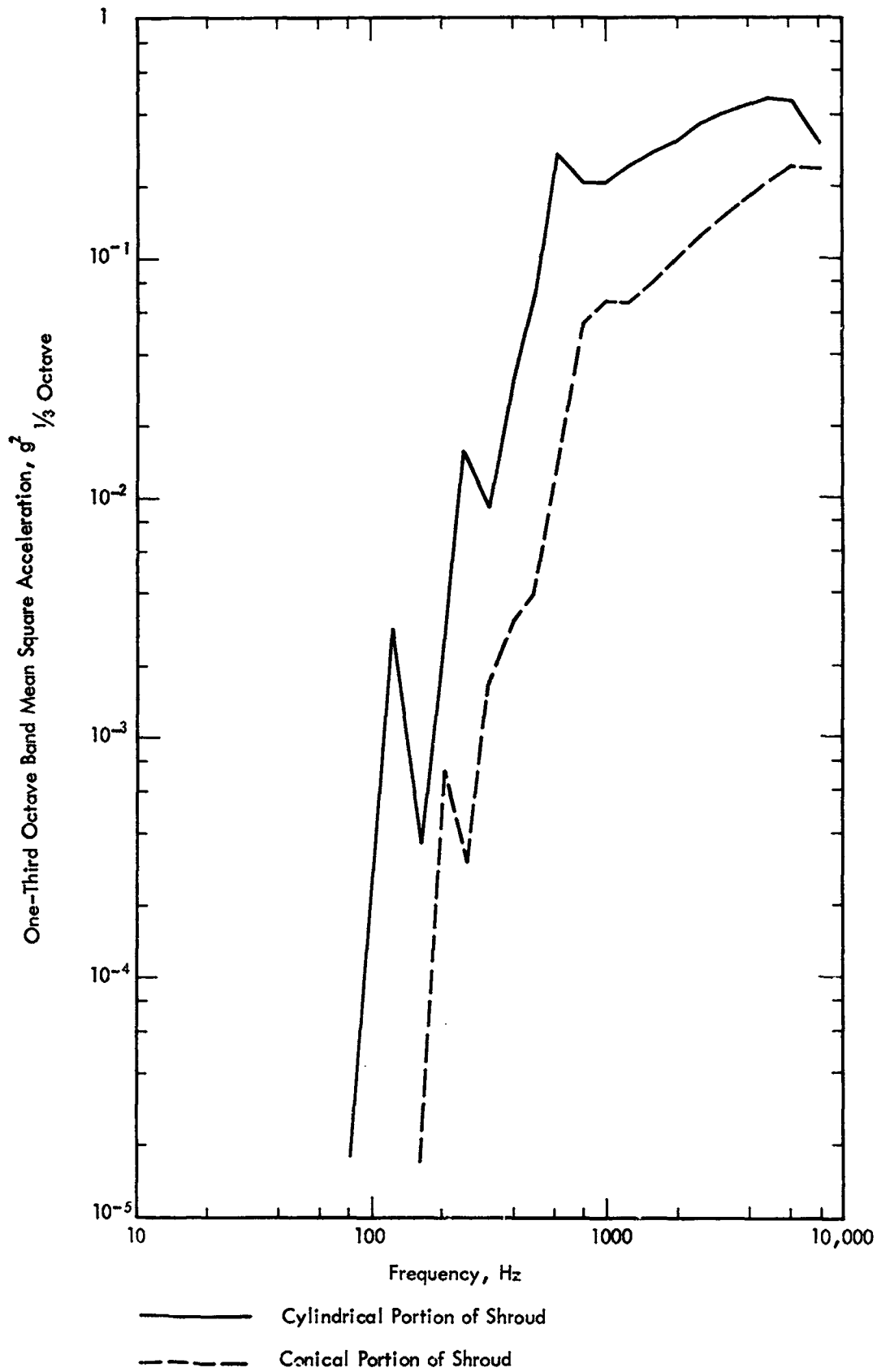
Figure 42. Mean Square Acceleration of Nimbus Shroud; Mach 2.0

164
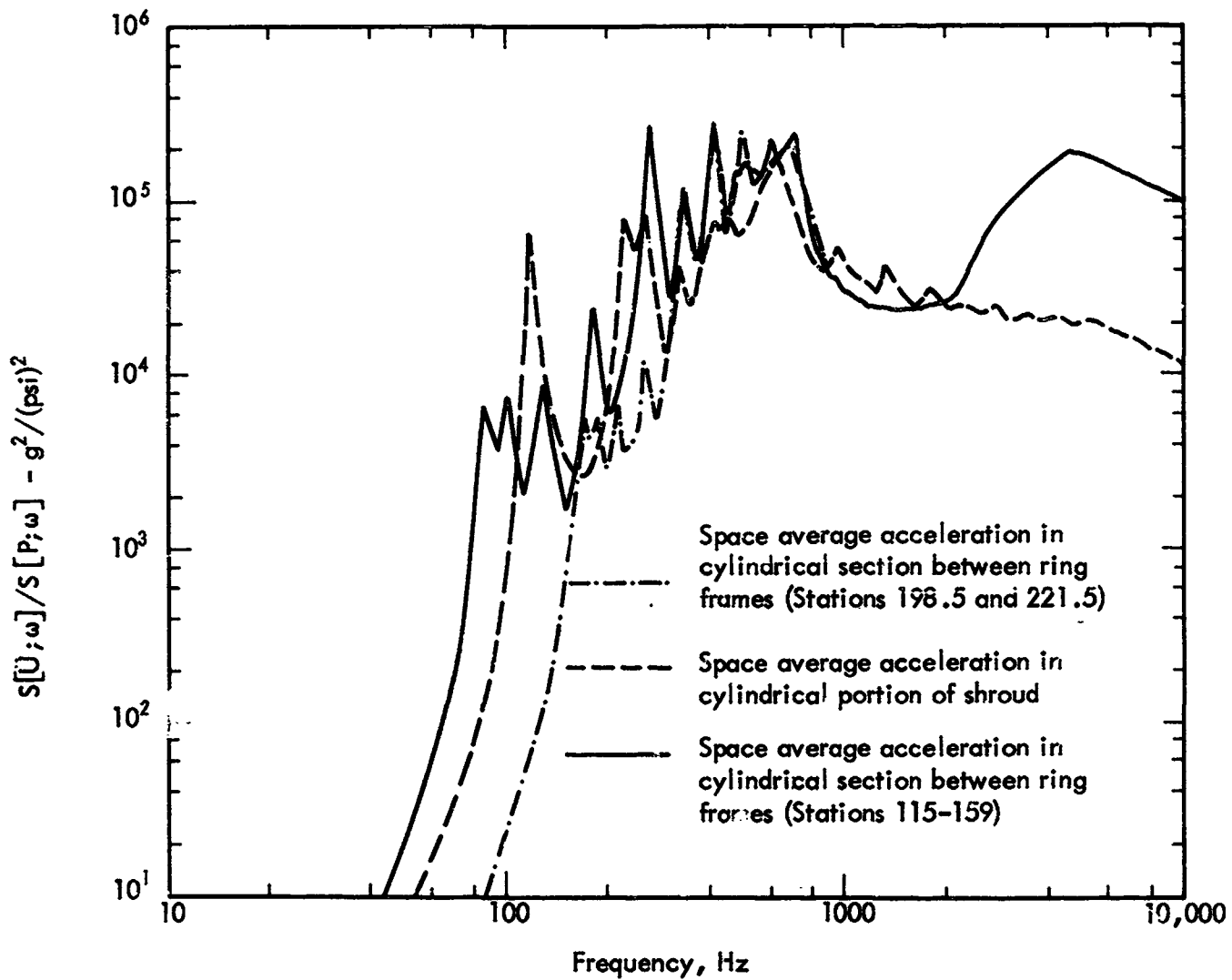
Figure 43. Acceleration Spectra of Cylindrical Portion of Nimbus Shroud; Reverberant Acoustic Field

165

C.4
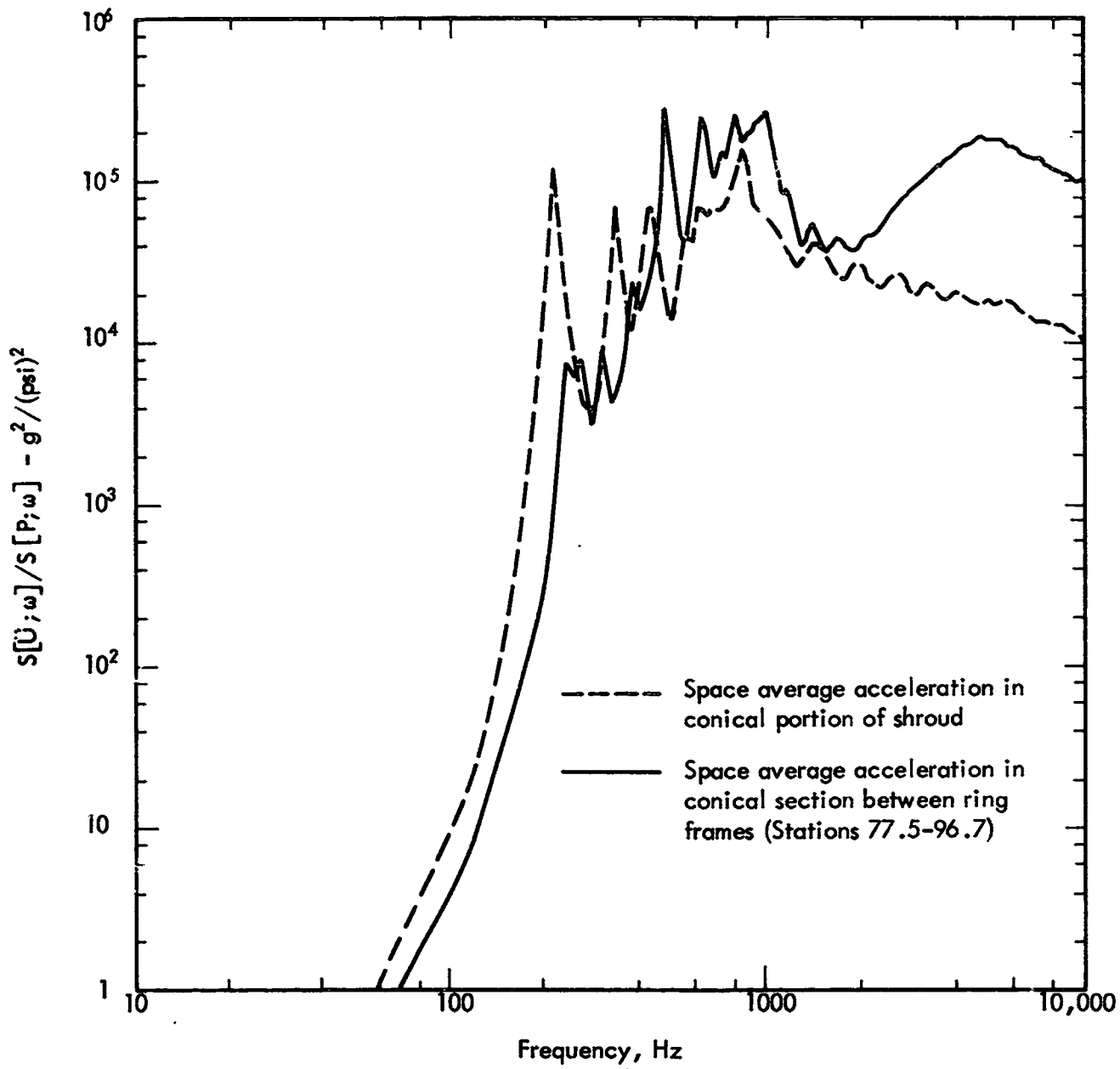
Figure 44. Acceleration Spectra of Conical Portion of Nimbus Shroud; Reverberant Acoustic Field
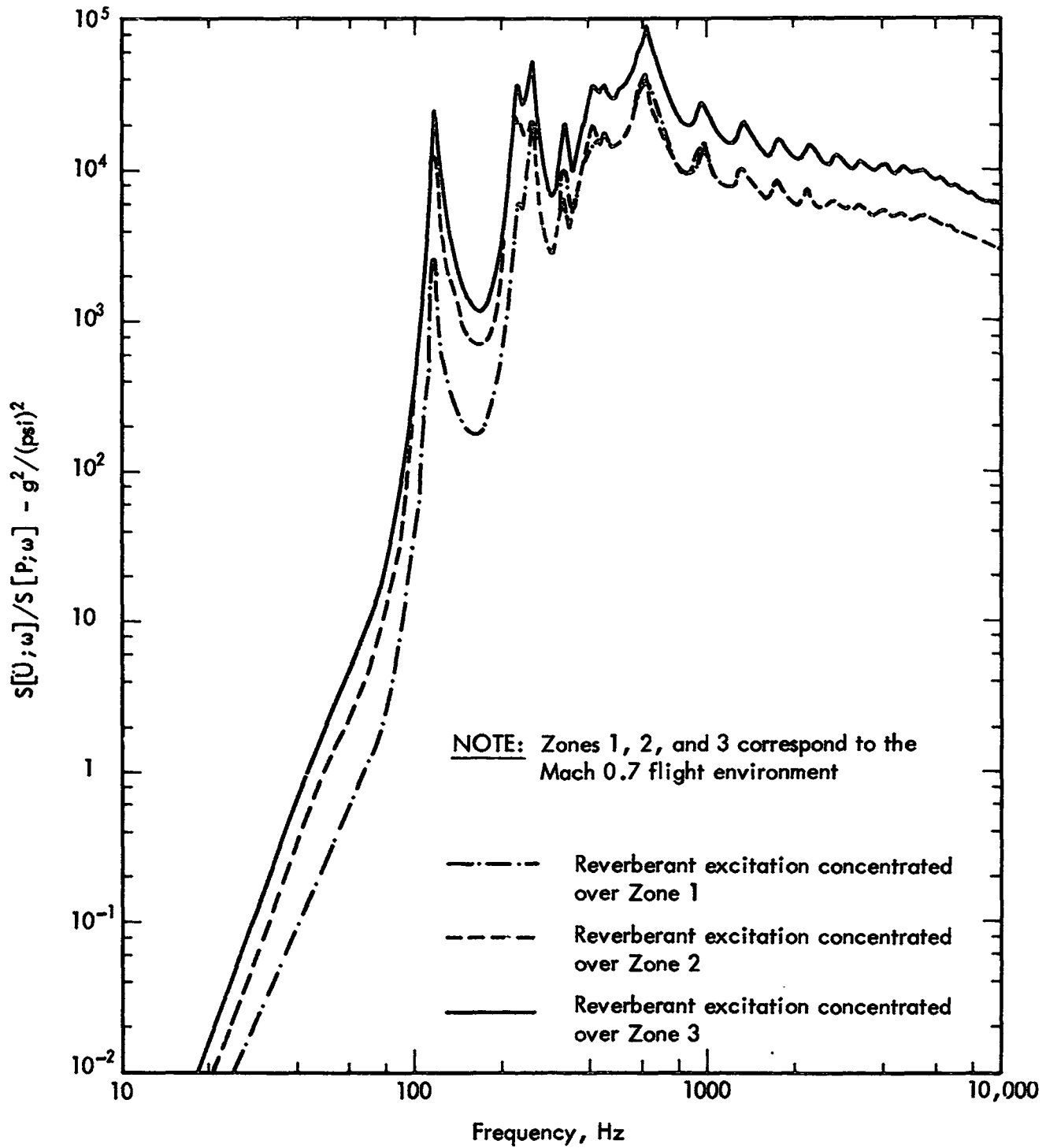
Figure 45. Acceleration Spectra of Cylindrical Portion of Nimbus Shroud; Localized Reverberant Acoustic Fields
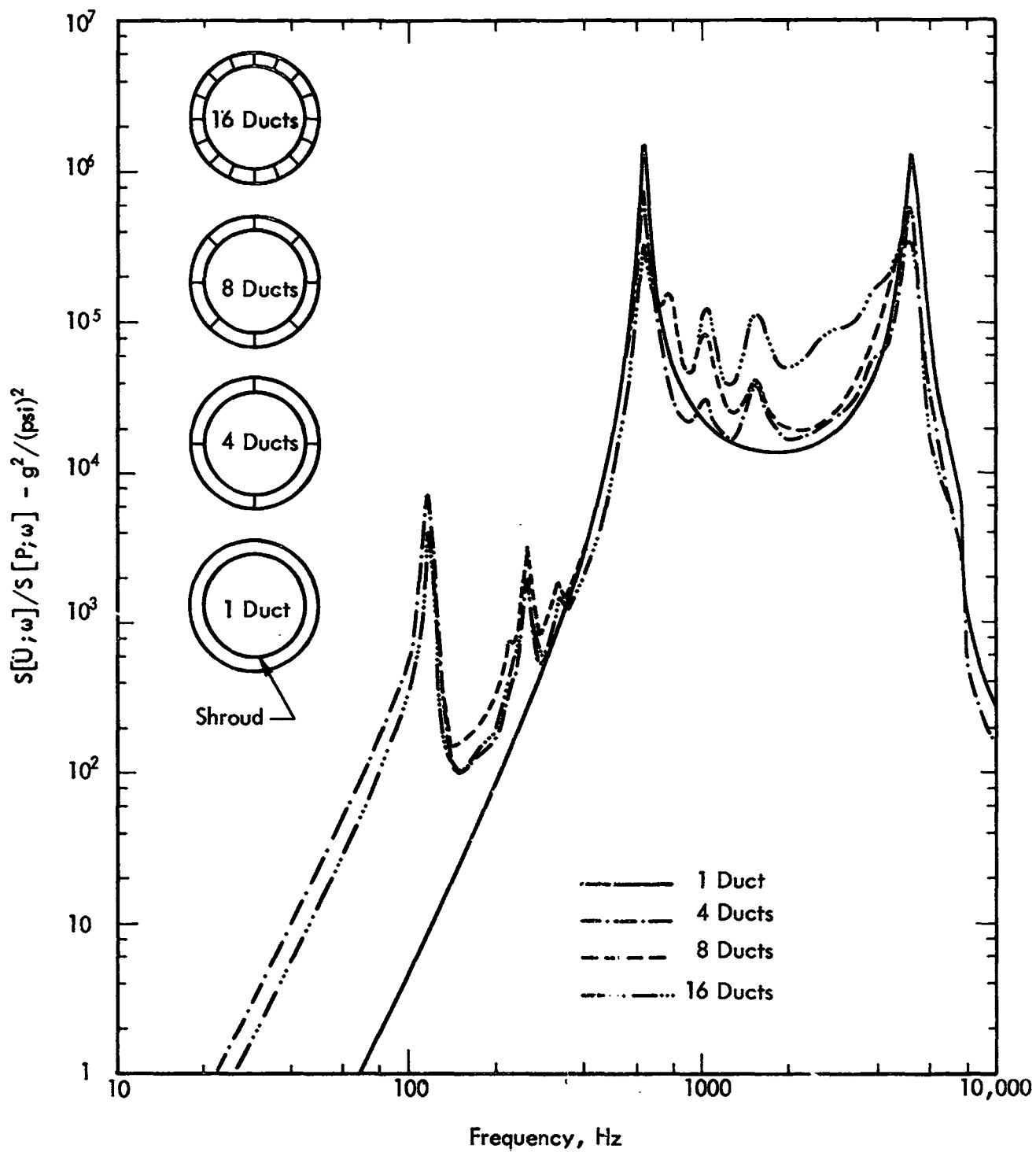
Figure 46. Acceleration Spectra of Cylindrical Portion of Nimbus Shroud;
Progressive Wave Axial Ducts

168
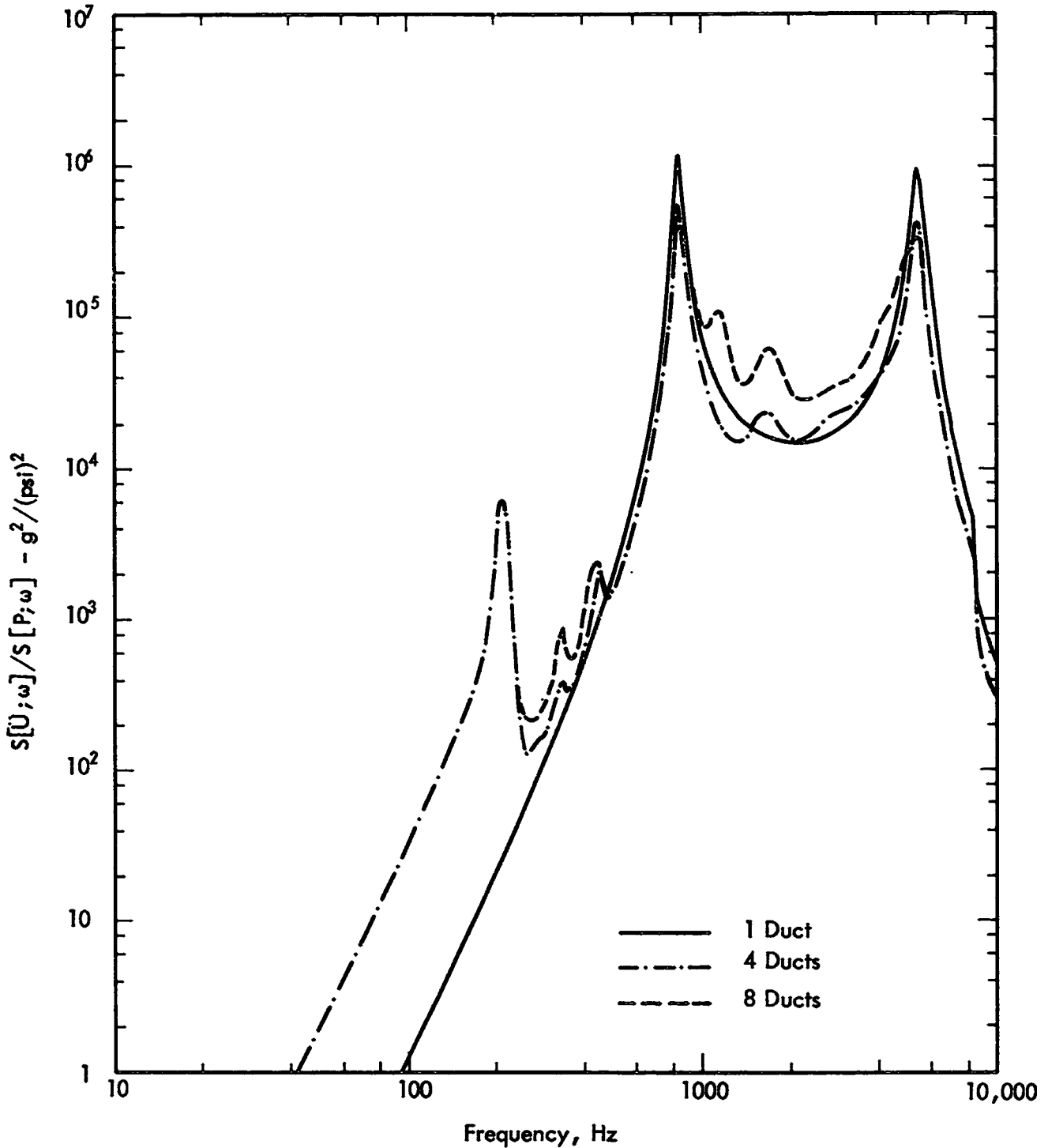
Figure 47. Acceleration Spectra of Conical Portion of Nimbus Shroud; Progressive Wave Axial Ducts

Octave Band Center Frequencies

One-Third Octave Band Center Frequencies, Hz
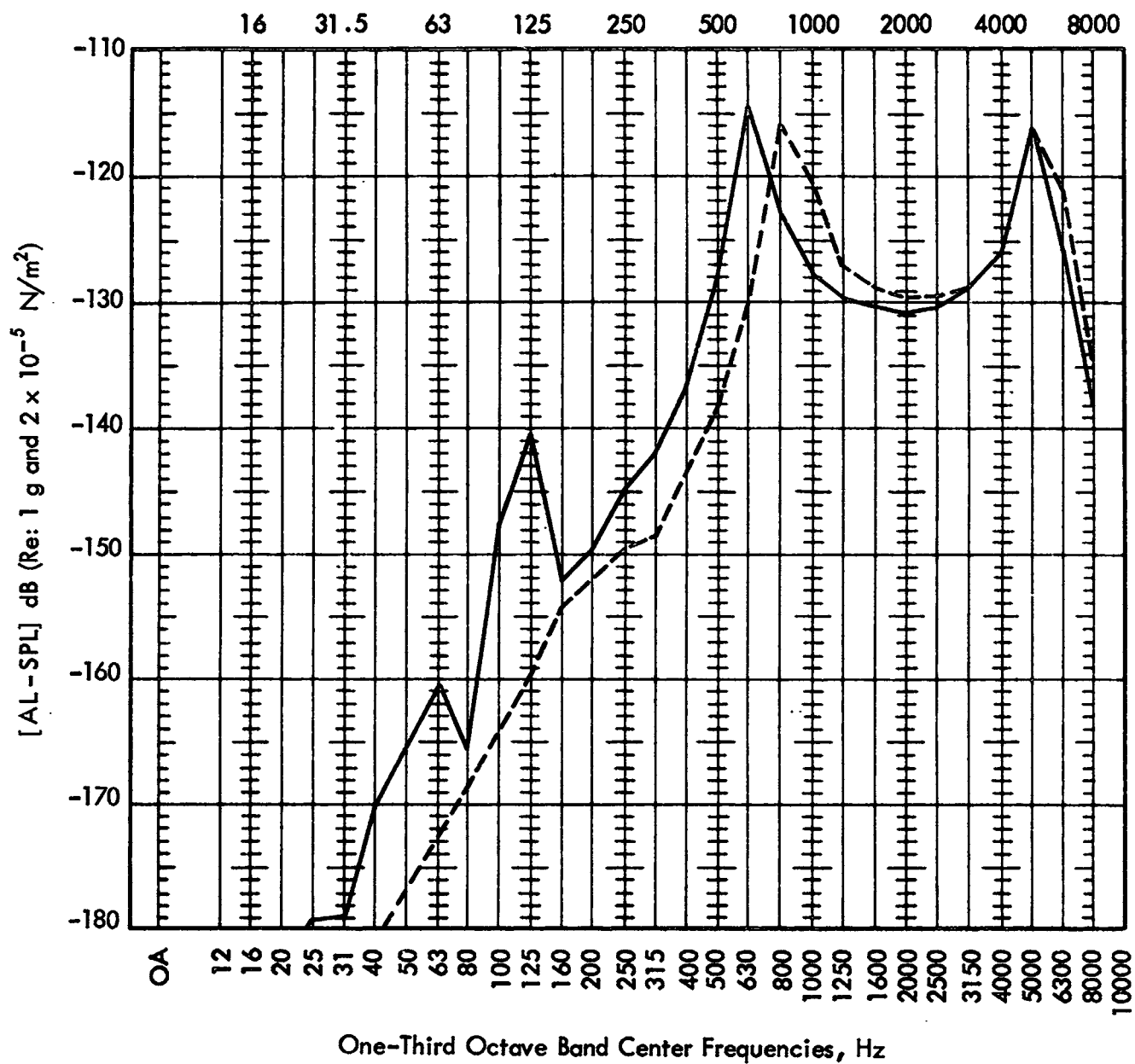
——————— { Cylindrical Section

— — — — — { Conical Section

(a) Lift-Off Acoustic Environment

Figure 48. One-Third Octave Band Normalized Acceleration Responses of the Nimbus Shroud

170

Octave Band Center Frequencies

One-Third Octave Band Center Frequencies, Hz

———————— { Cylindrical Section
— — — — — { Conical Section
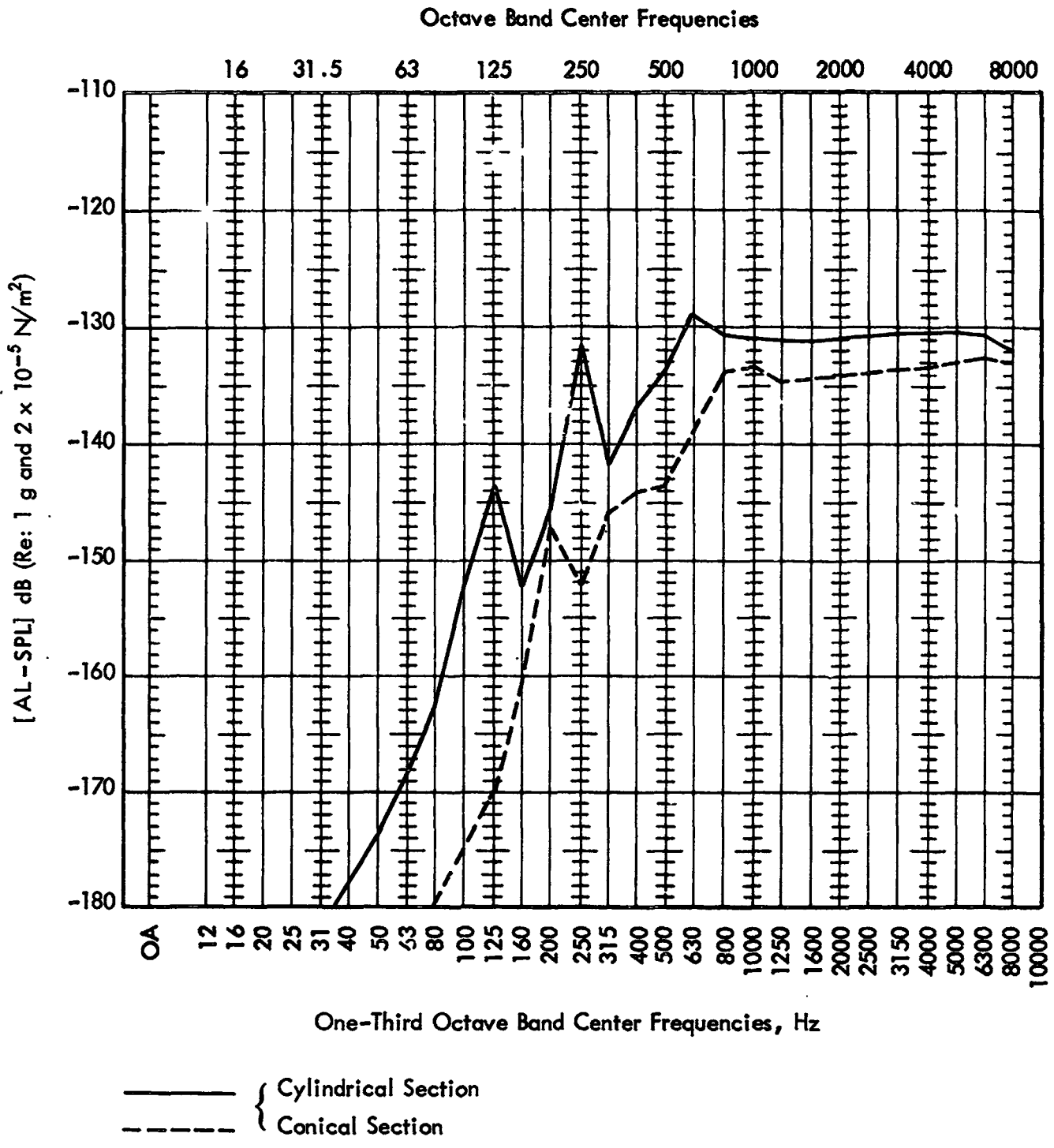
(b) Aerodynamic Environment at Mach 2.0

Figure 48. Continued

171

Octave Band Center Frequencies
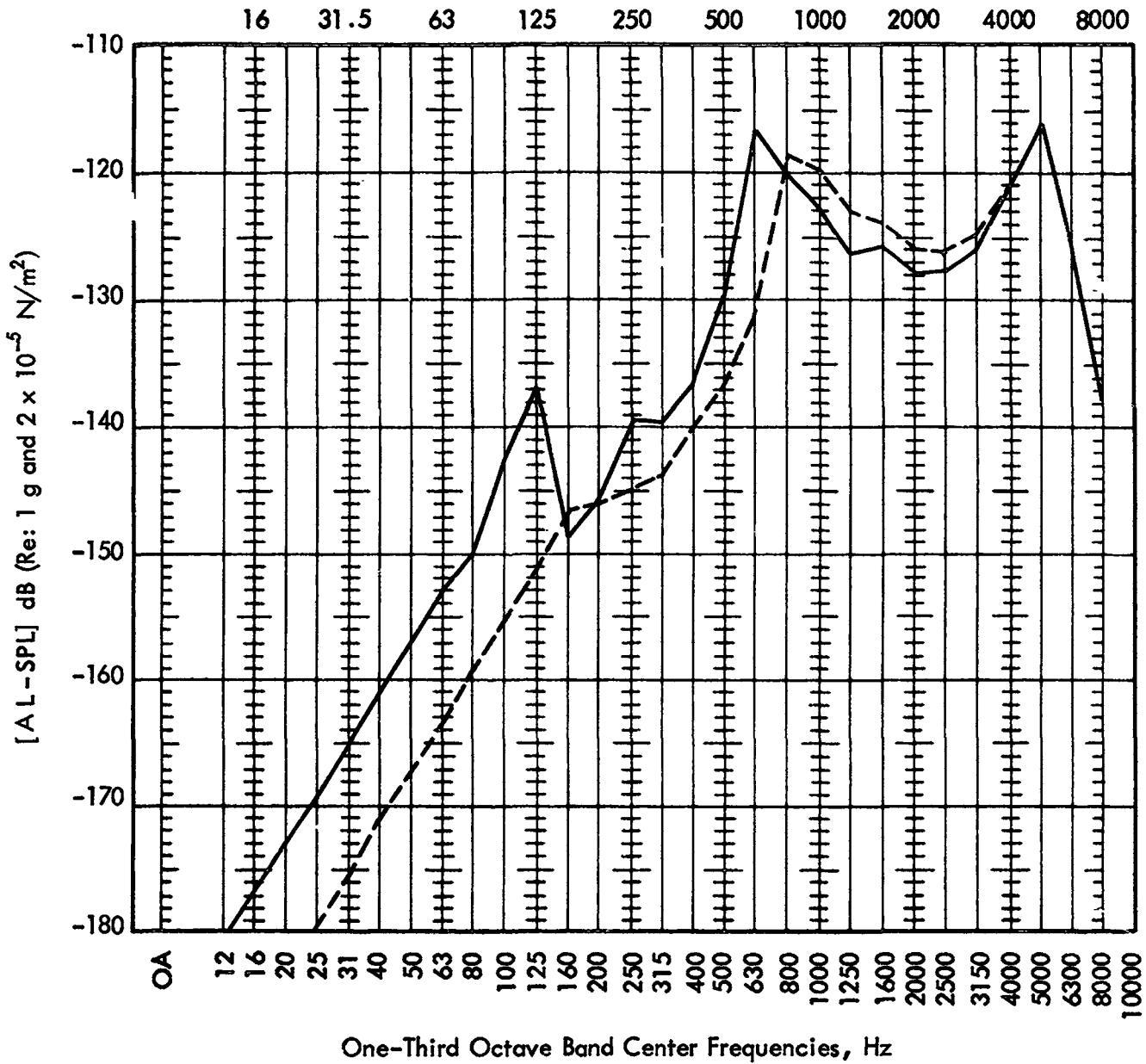
Cylindrical Section

Conical Section

(c) 8 - Progressive Wave Ducts

Figure 48. Continued

172

Octave Band Center Frequencies

One-Third Octave Band Center Frequencies, Hz

———— { Cylindrical Section

————— { Conical Section
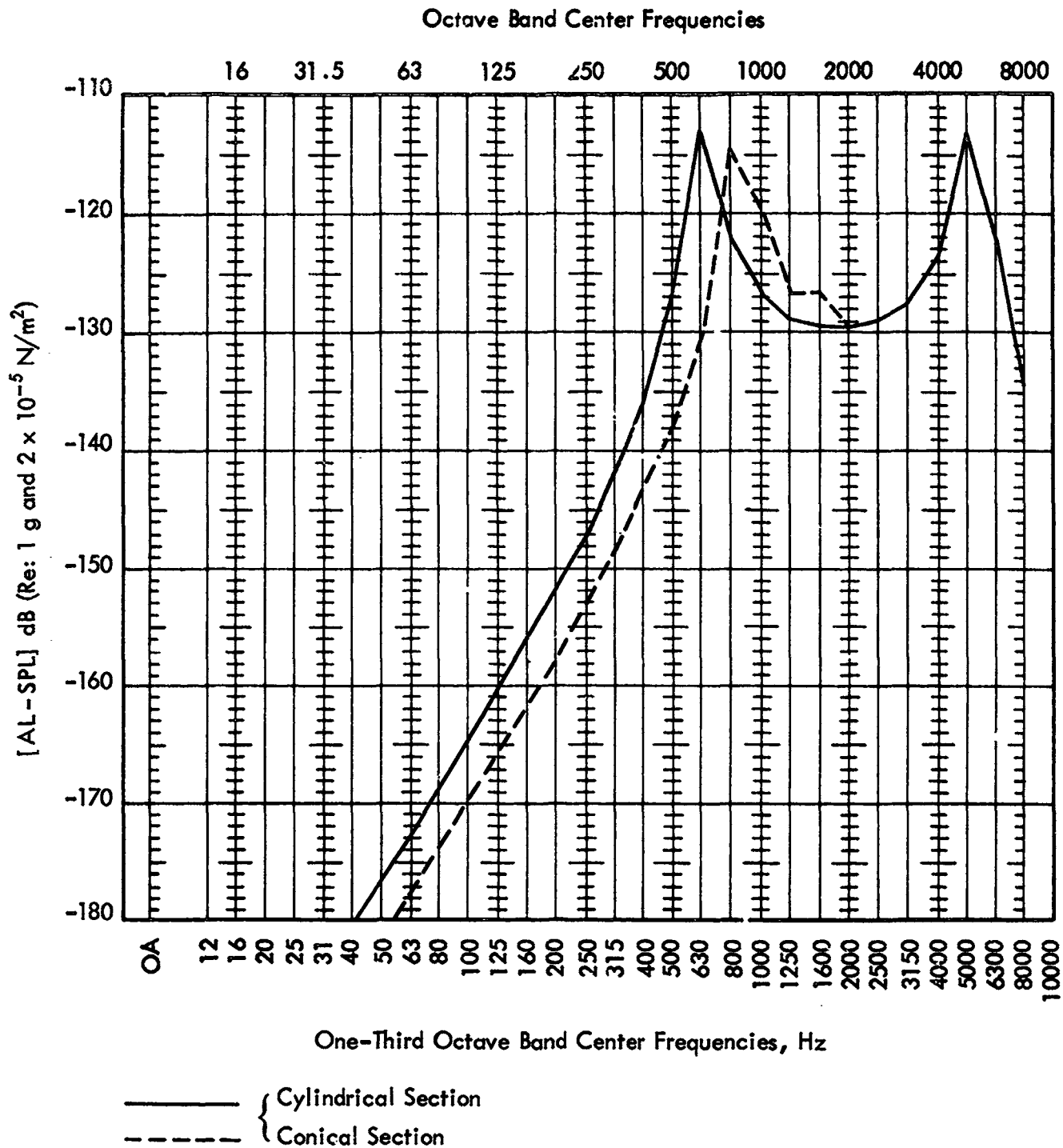
(d) 1 - Progressive Wave Duct

Figure 48. Continued

173

Octave Band Center Frequencies

One-Third Octave Band Center Frequencies, Hz.

——————— { Cylindrical Section
– – – – – { Conical Section
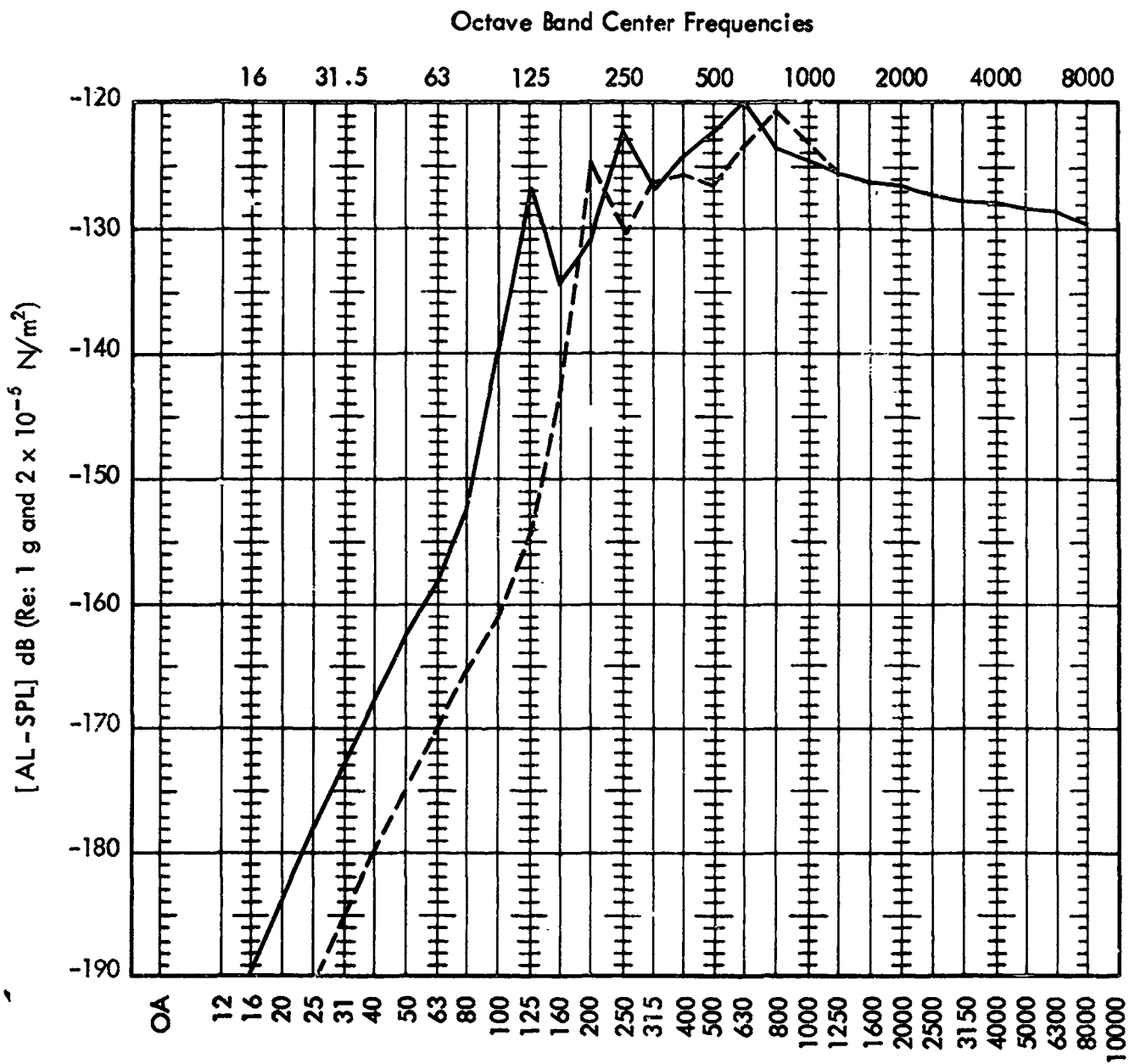
(e) Reverberant Acoustic Field

Figure 48. Concluded

174
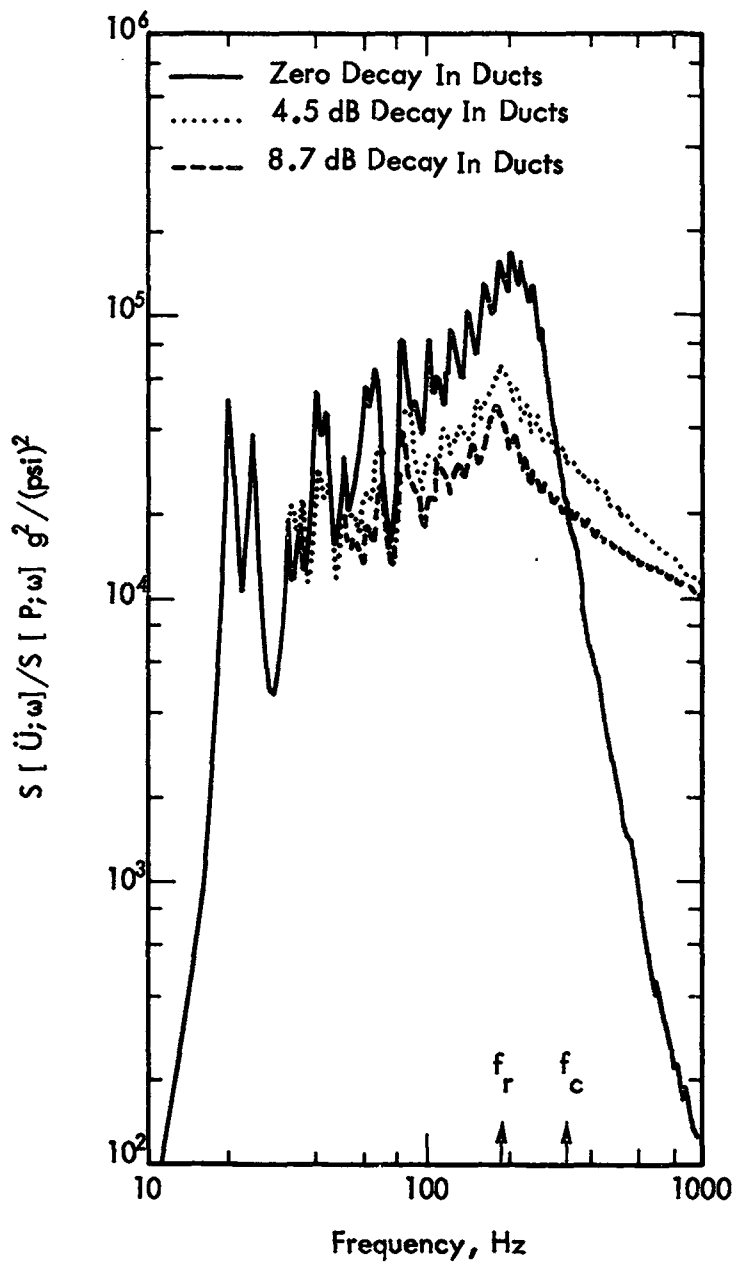
Figure 49. Response of SLA Structure to 16-Duct Progressive Wave Excitation; Effects of Exponential Decay in Sound Pressure Level along the Duct (results from Reference 14)

175
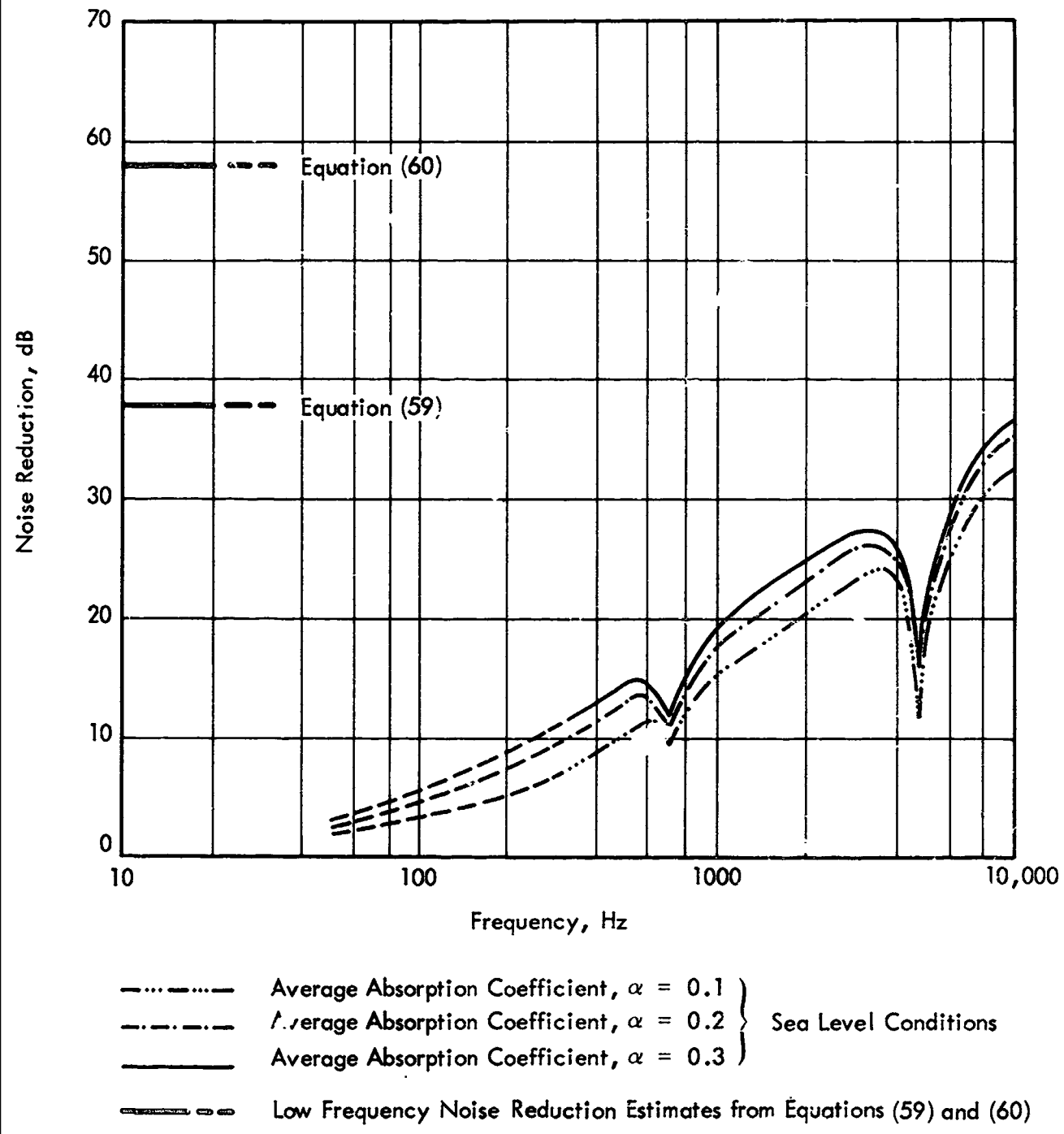
Figure 50. Noise Reduction of Cylindrical Portion of Nimbus Shroud; Effect of Varying the Average Absorption Coefficient
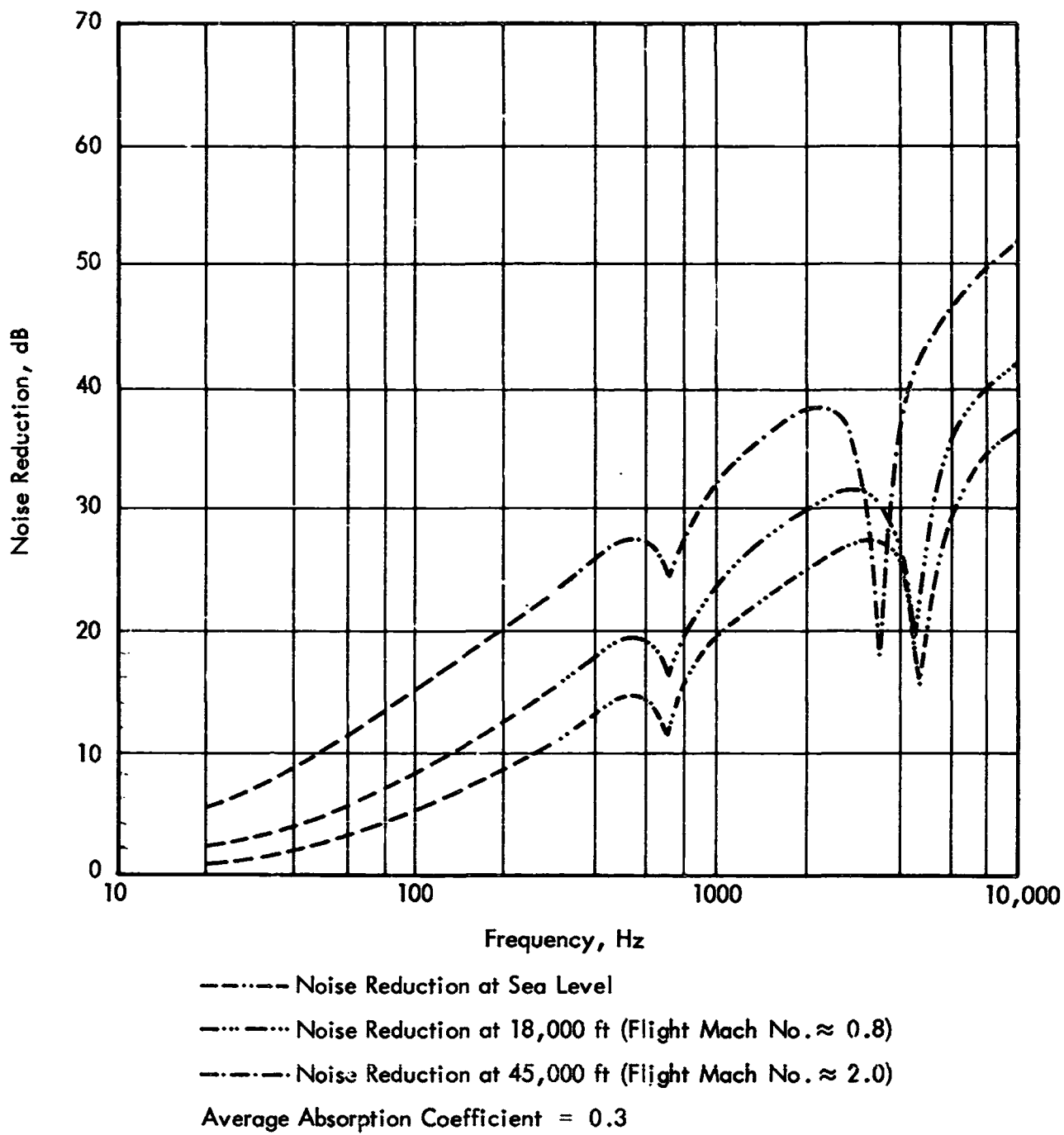
Figure 51. Noise Reduction of Cylindrical Portion of Nimbus Shroud; Effect of Altitude

The figure is a graph with the following elements:

- Y-axis: Noise Reduction, dB (0 to 70)
- X-axis: Frequency, Hz (10 to 10,000)
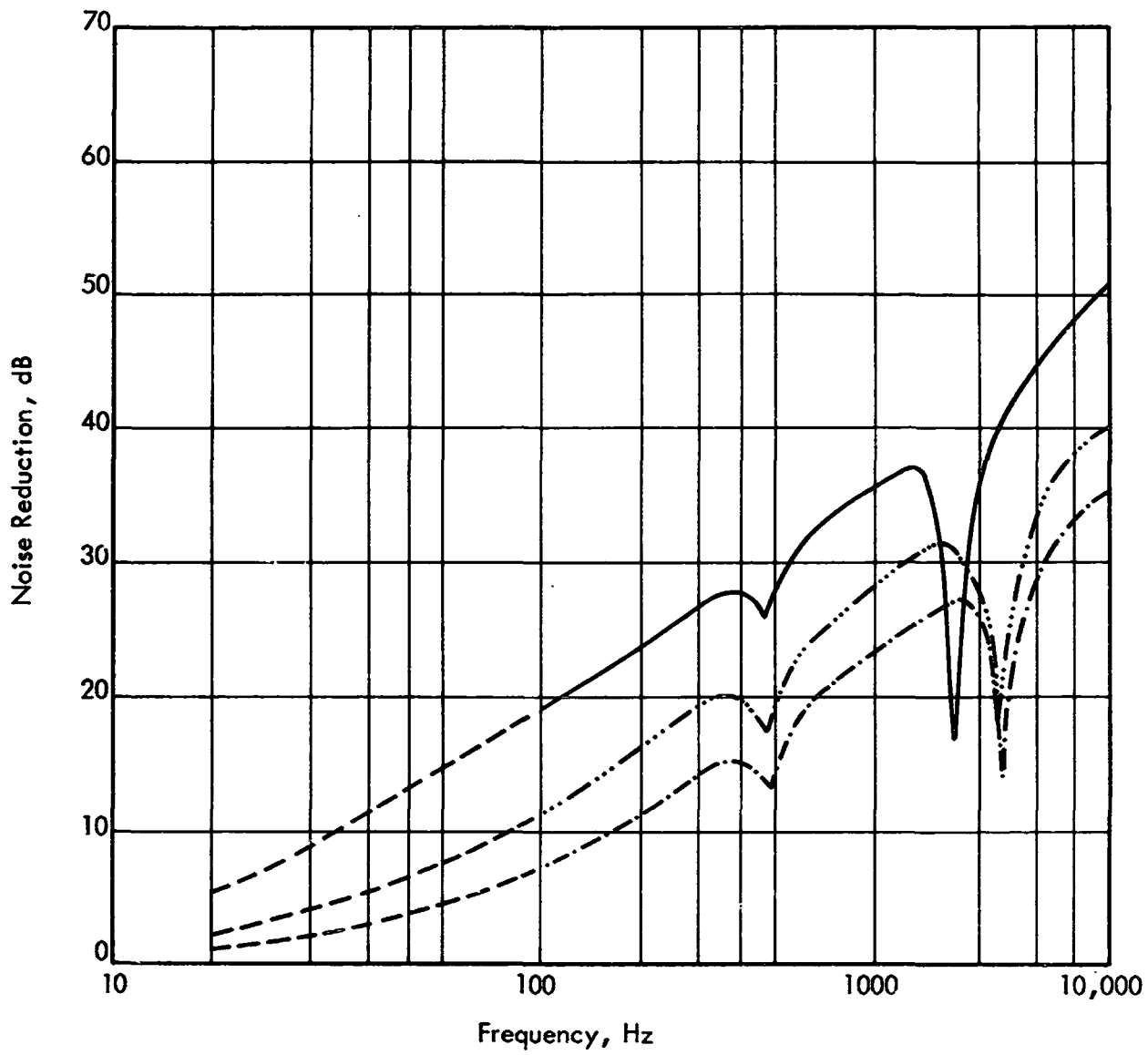
Legend:
— — ··· — Noise Reduction at Sea Level
— ··· — ··· Noise Reduction at 18,000 ft (Flight Mach No. ≈ 0.8)
— · — · — · Noise Reduction at 45,000 ft (Flight Mach No. ≈ 2.0)
Average Absorption Coefficient = 0.3

Figure 52. Noise Reduction of Conical Portion of Nimbus Shroud; Effect of Altitude
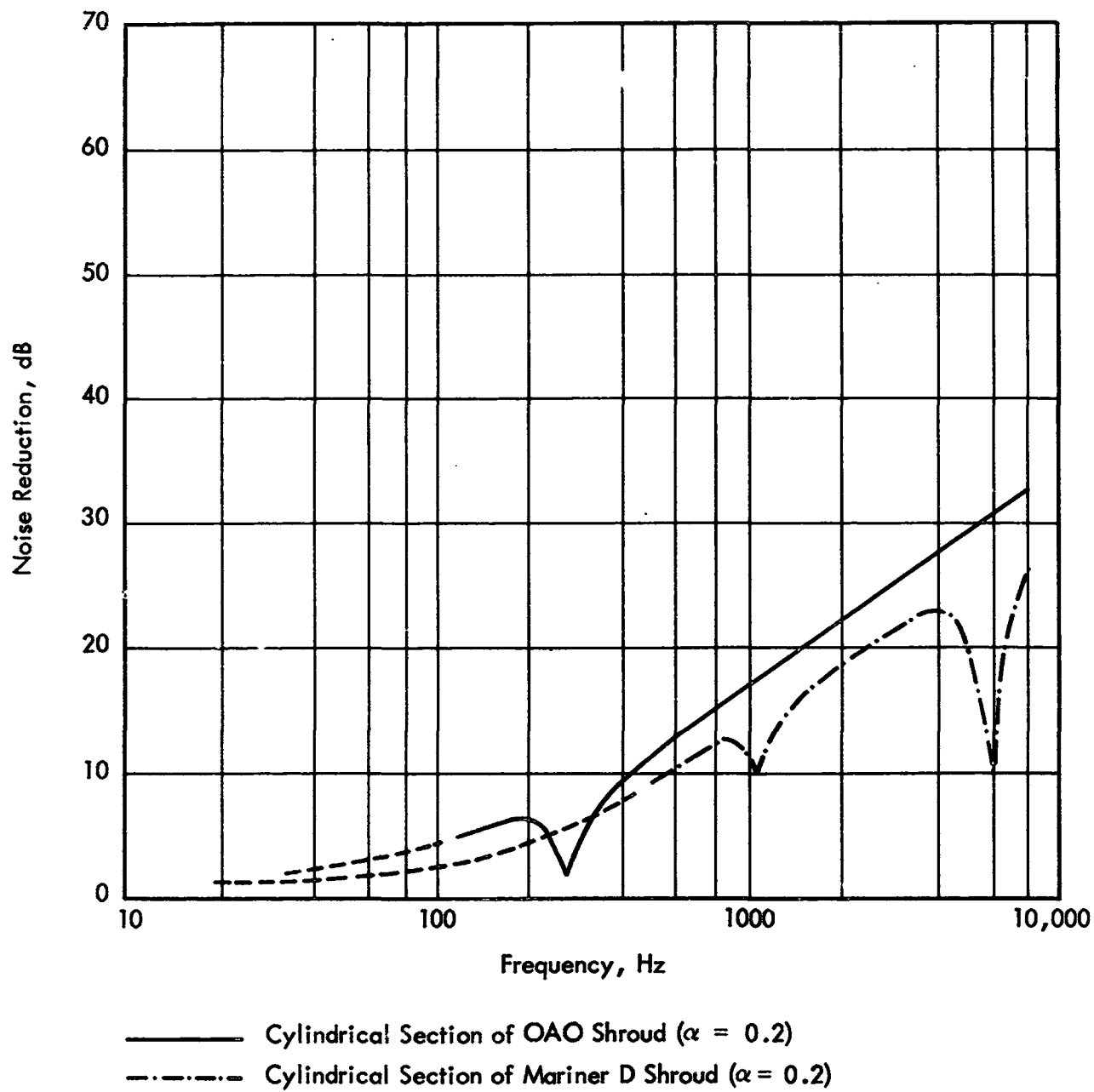
Figure 53. Noise Reduction of OAO and Mariner D Shrouds

179
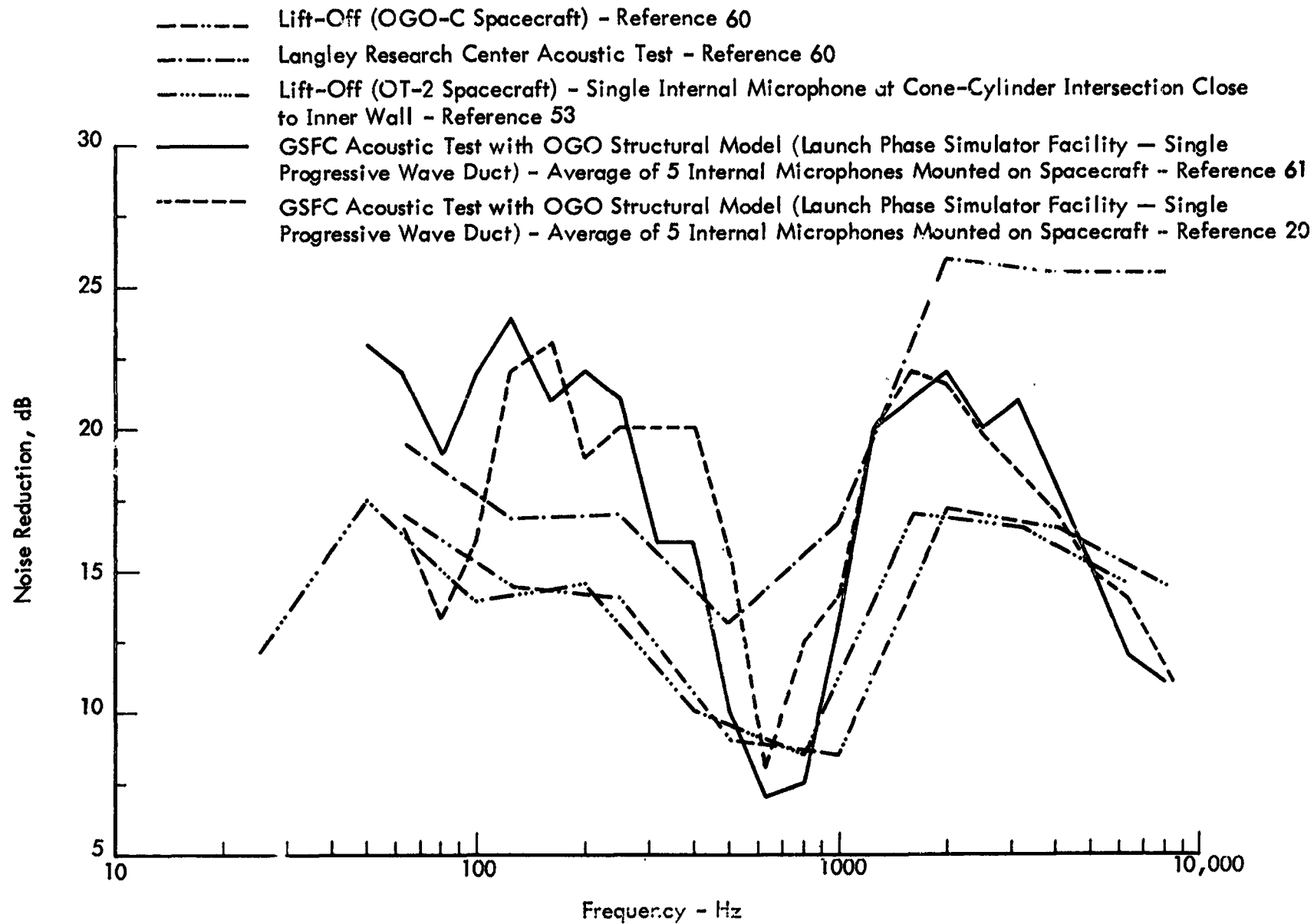
Figure 54. Comparison Between Flight and Laboratory Noise Reduction Data for the Nimbus Shroud
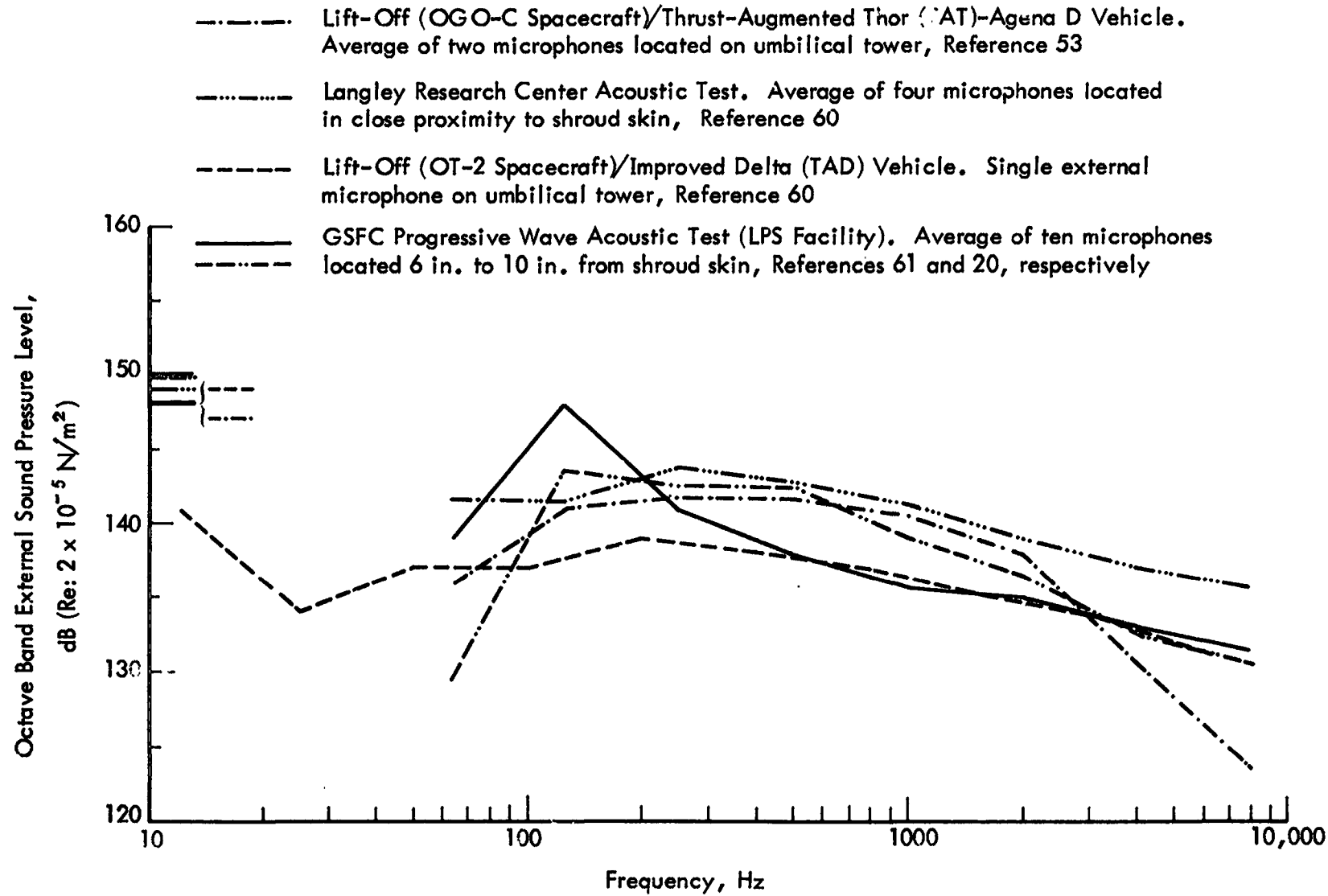
Figure 55. Range of External Sound Pressure Levels Corresponding to the In-Flight and Laboratory Noise Reductions shown in Figure 54 for the Nimbus Shroud
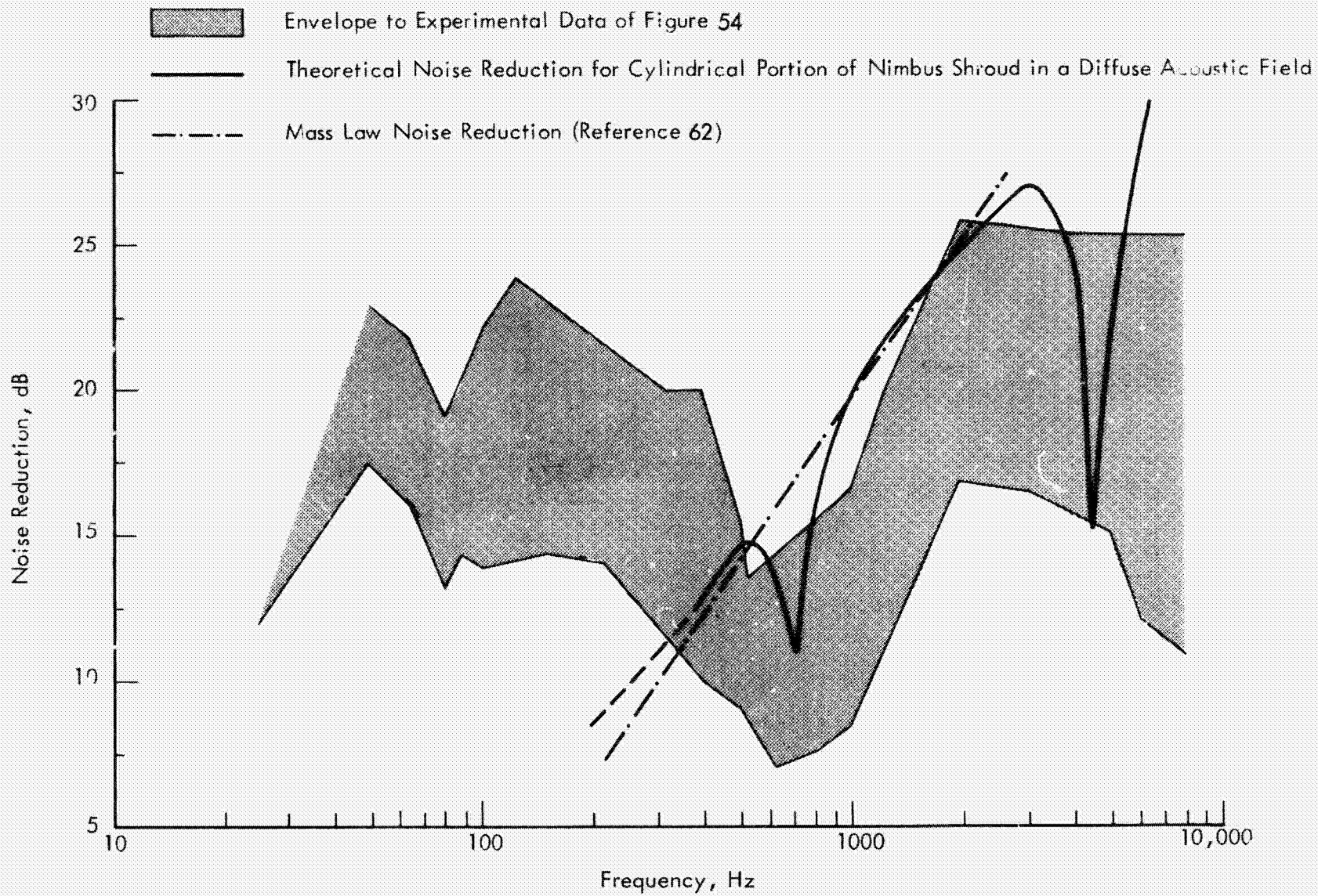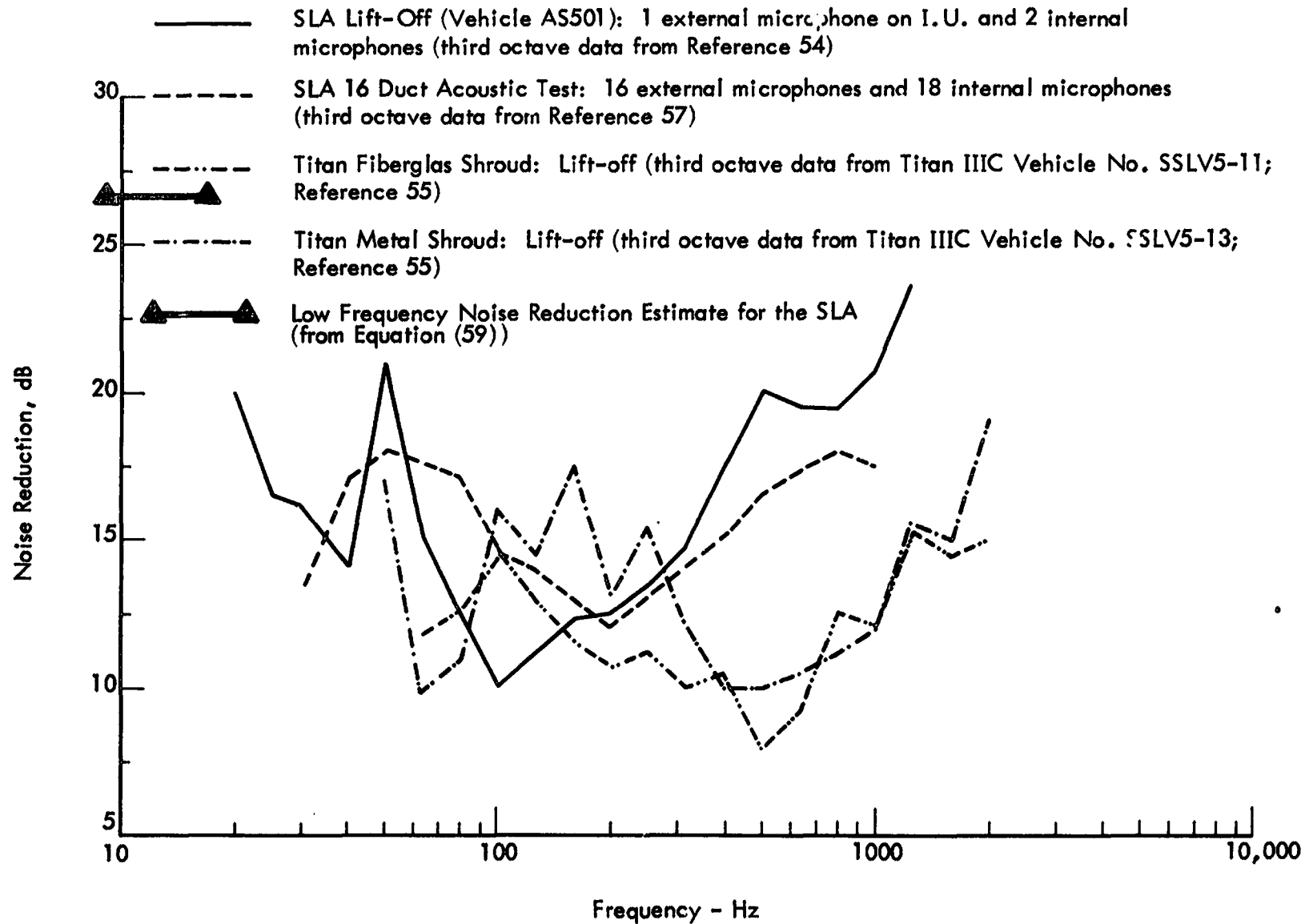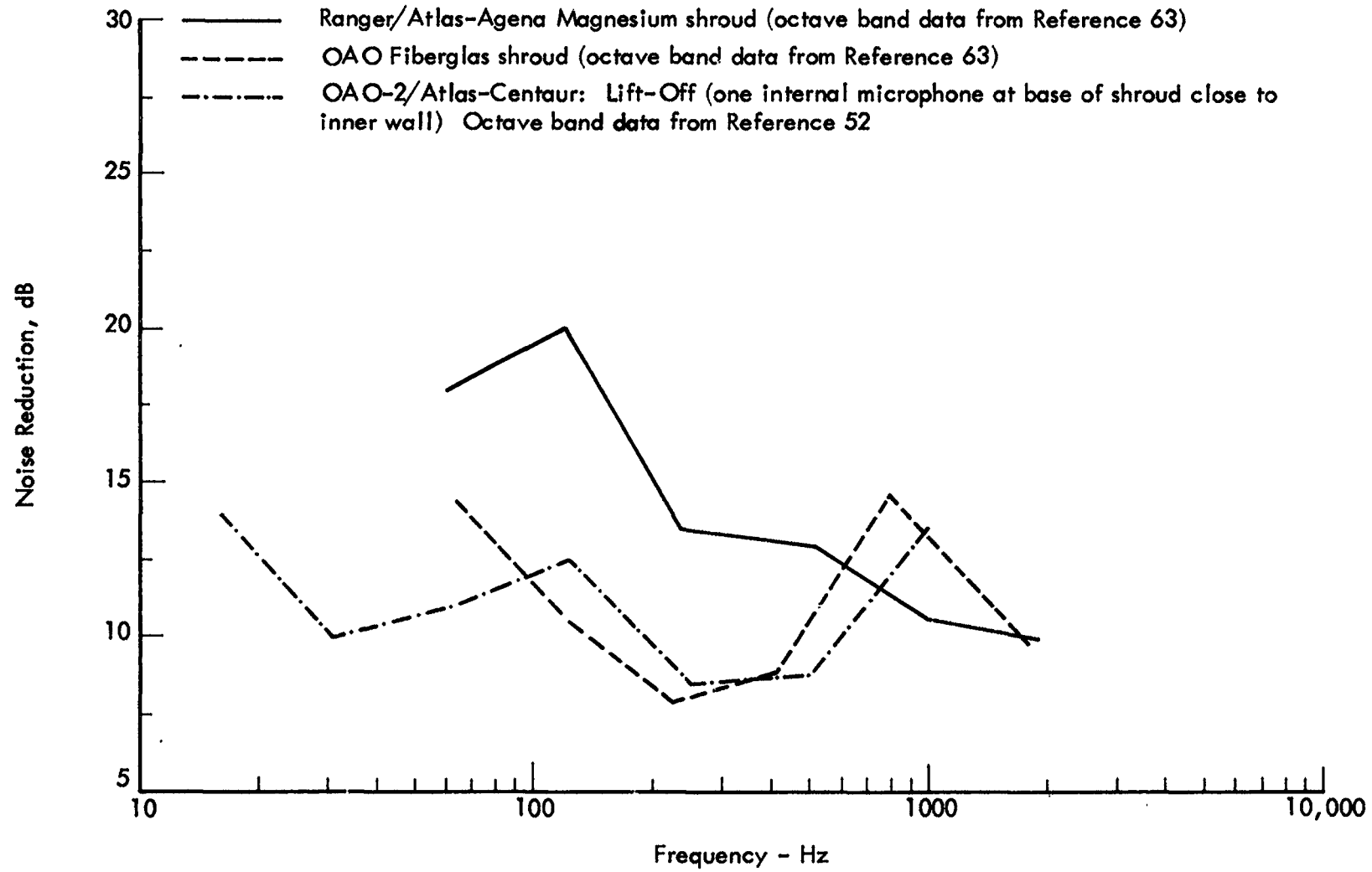
Figure 56. Noise Reduction of Nimbus Shroud; Comparison Between Measured Data and Prediction

Figure 57. Range of Noise Reduction Data for the SLA, Ranger, OAO, and Titan Shrouds

Ranger/Atlas-Agena Magnesium shroud (octave band data from Reference 63)

OAO Fiberglas shroud (octave band data from Reference 63)

OAO-2/Atlas-Centaur: Lift-Off (one internal microphone at base of shroud close to inner wall) Octave band data from Reference 52
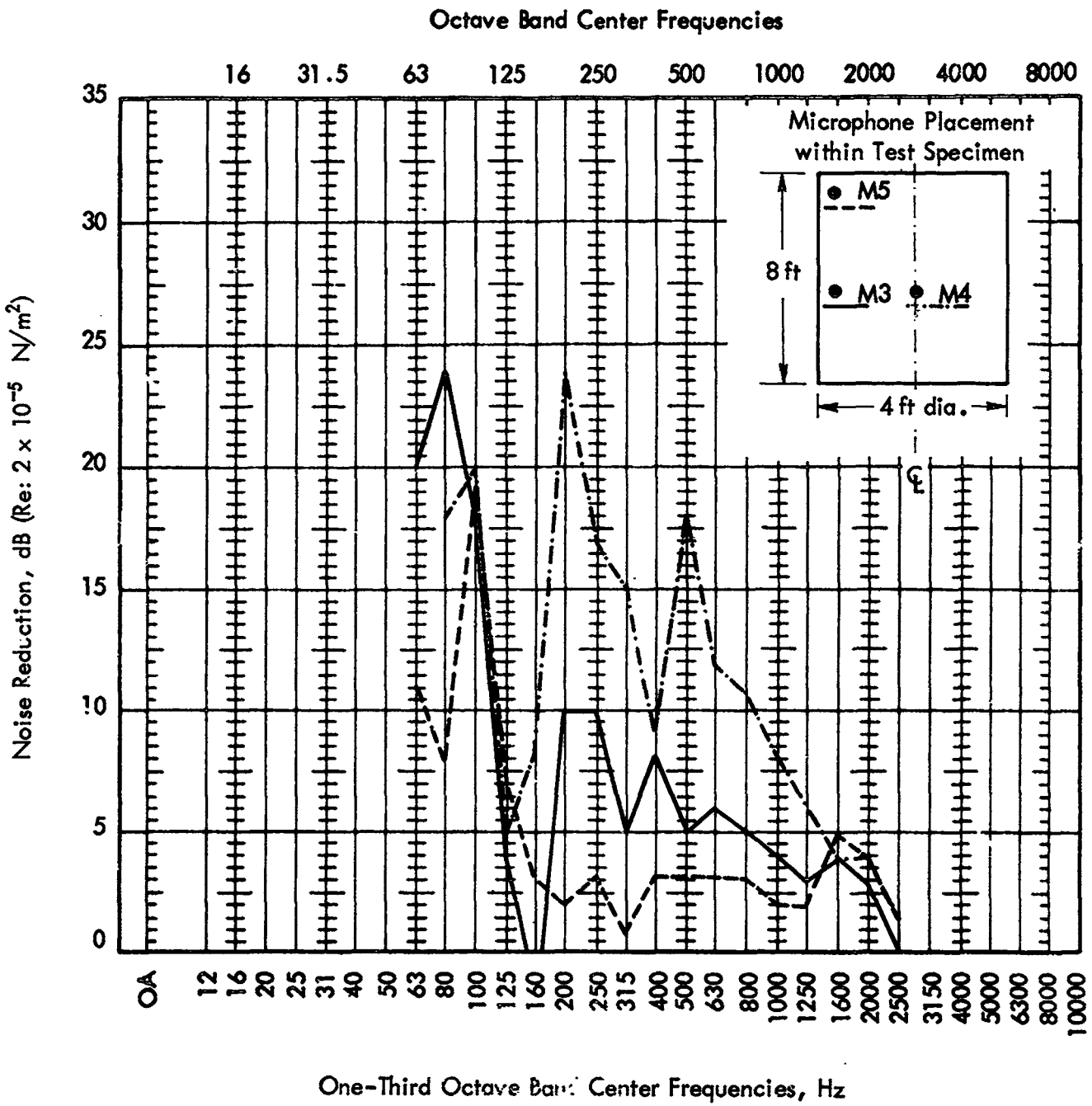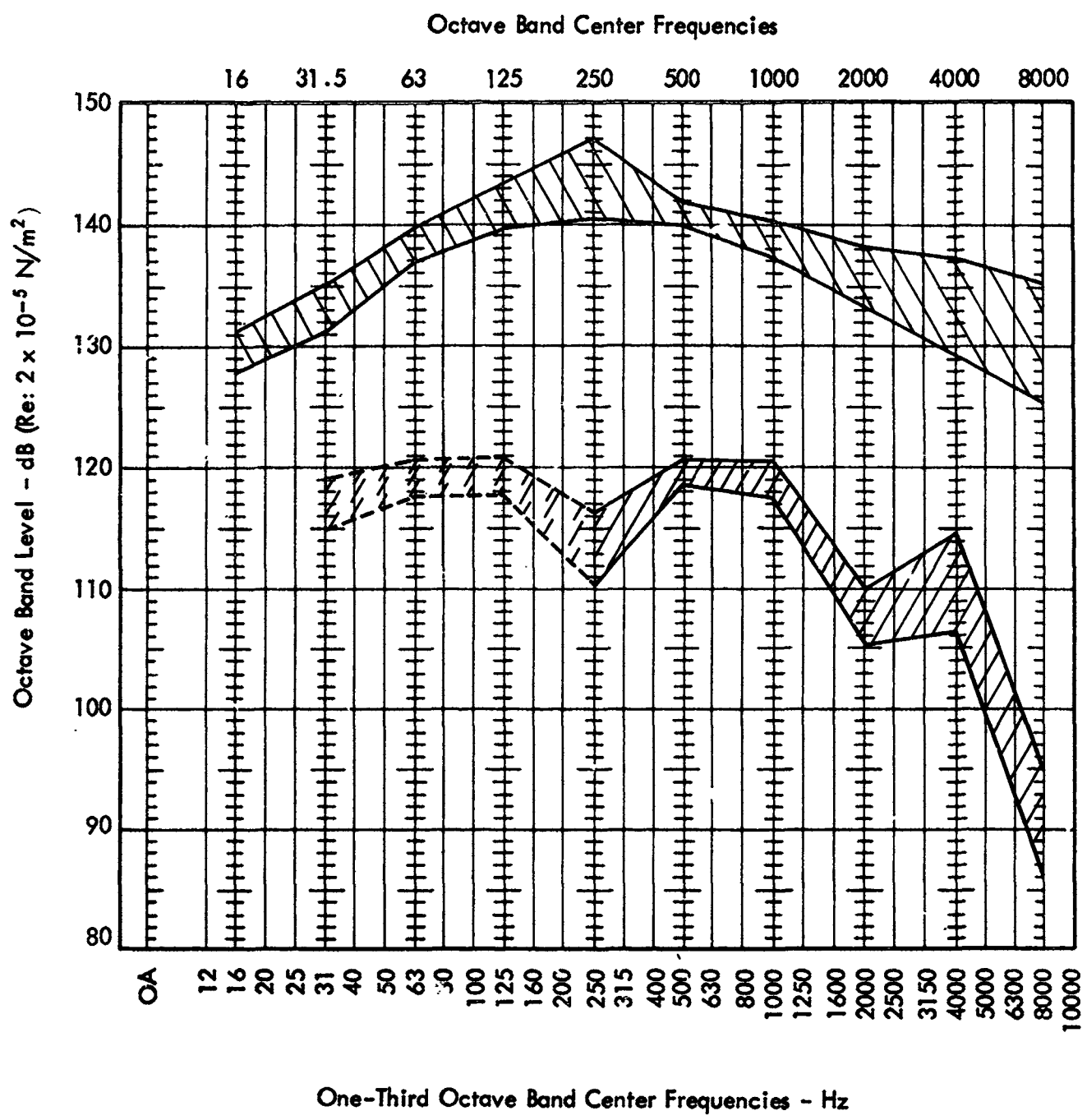
(b) Ranger and OAO Shrouds

Figure 57. Concluded

184

Figure 58. Noise Reduction Determined at Different Locations inside a Ring-Frame and Stringer Stiffened Cylinder (4 ft diameter by 8 ft long), Reference 31

Octave Band Center Frequencies

One-Third Octave Band Center Frequencies – Hz

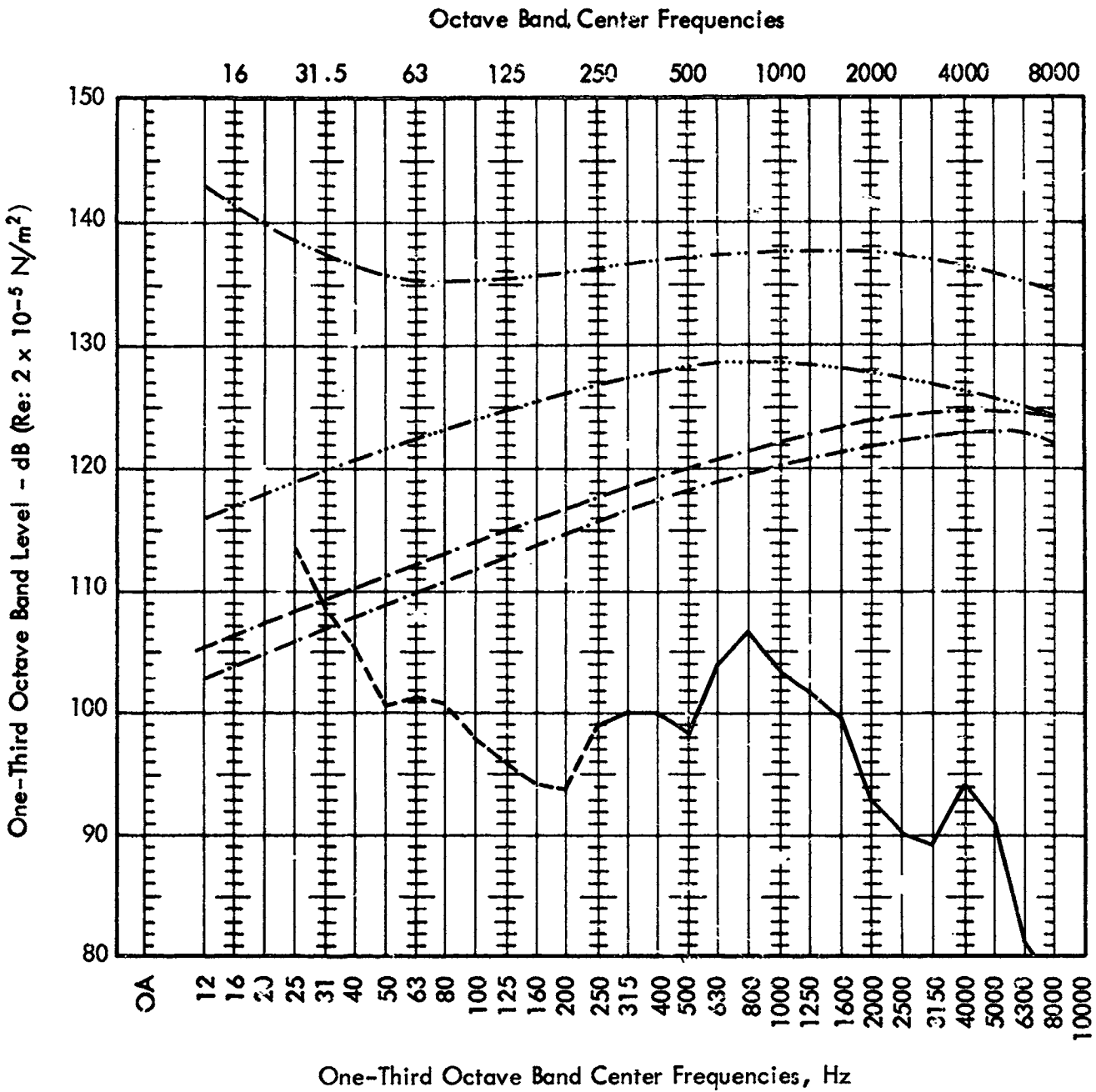Range of External SPL from Figure 19

Internal Sound Pressure Levels at these Frequencies based upon
Lower Envelope to Measured Noise Reductions shown in Figure 54

Figure 59. Predicted Space–Average Internal Sound Pressure Levels at Lift–Off
for the Nimbus Shroud

186

Octave Band Center Frequencies

One-Third Octave Band Center Frequencies, Hz
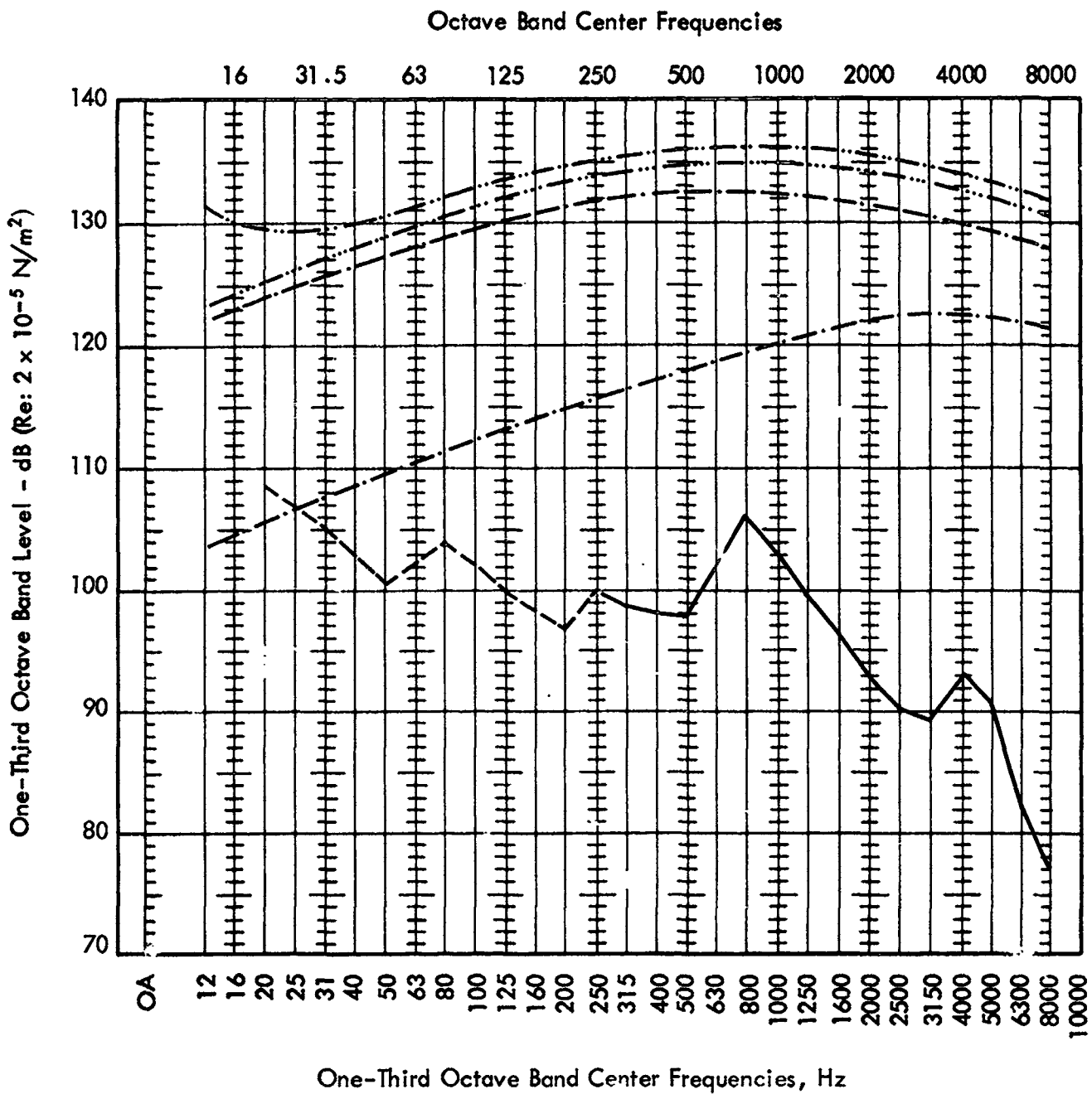
——..——..—— Cylinder, Zone 1 ⎫
——...——...—— Cylinder, Zone 2 ⎬ External SPL's (From Figure 28)
——.——.——. Cylinder, Zone 3 ⎭
——.——.——.. Cone
———————— Internal Sound Pressure Levels at these Frequencies based upon Measured Noise Reductions shown in Figure 54

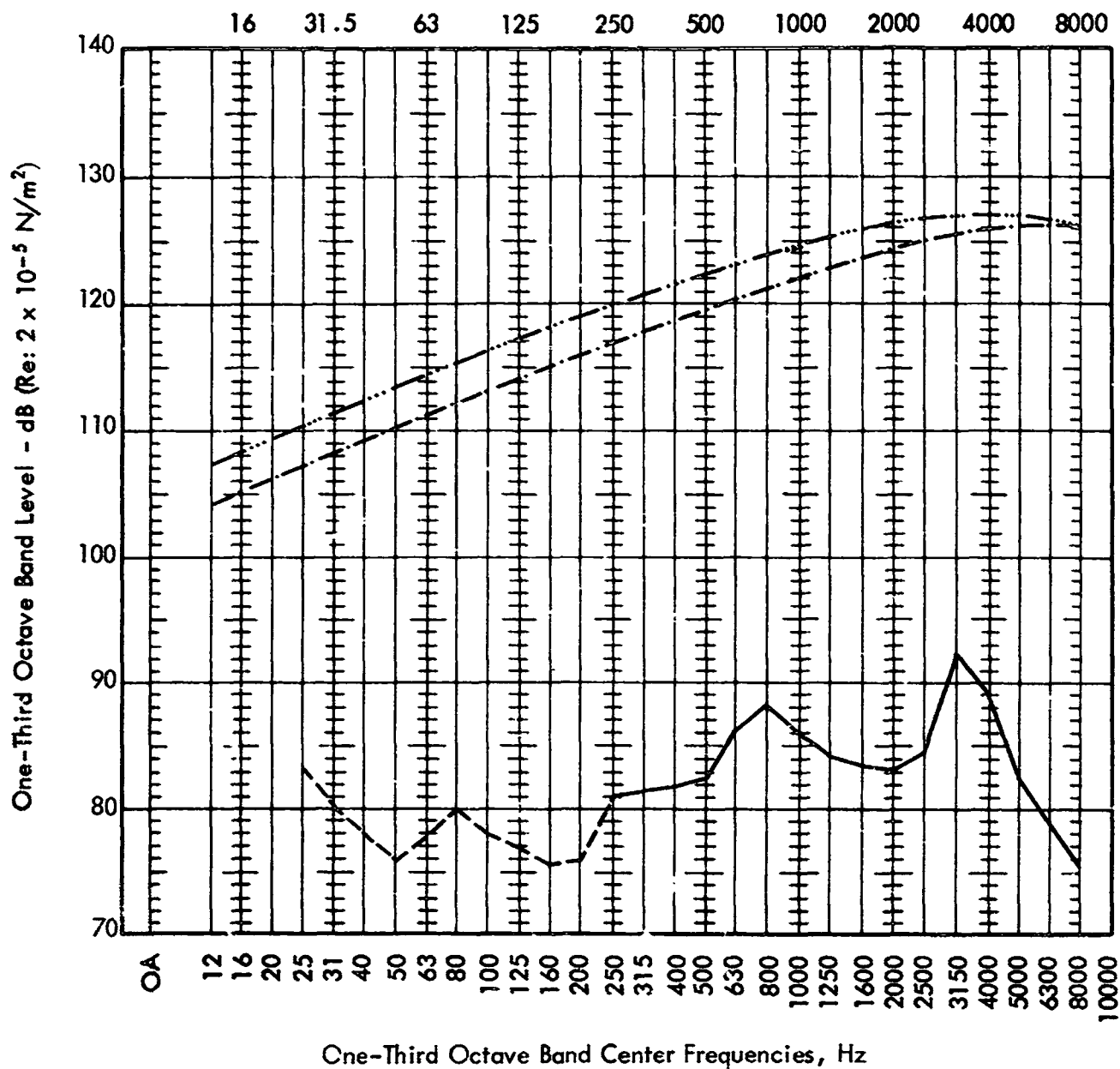Figure 60.   Predicted Space-Average Internal Sound Pressure Levels at Mach 0.7 for the Nimbus Shroud

Octave Band Center Frequencies

One-Third Octave Band Center Frequencies, Hz

—..—..— Cylinder, Zone 2
—...—.... Cylinder, Zone 3   } External Sound Pressure Levels (From Figure 28)
—.—..—. Cone
—.—.—.— Cylinder, Zone 1

— — — — Internal Sound Pressure Levels at these Frequencies based upon
Measured Noise Reductions shown in Figure 54

Figure 61. Predicted Space-Average Internal Sound Pressure Levels at Mach 0.8 for
the Nimbus Shroud

188

Figure 62. Predicted Space-Average Internal Sound Pressure Levels at Mach 2.0 for the Nimbus Shroud

189

Octave Band Center Frequencies

One-Third Octave Band Center Frequencies, Hz

— — — — — Lift-Off

—·—·—·— Transonic

—···—···— Max Q

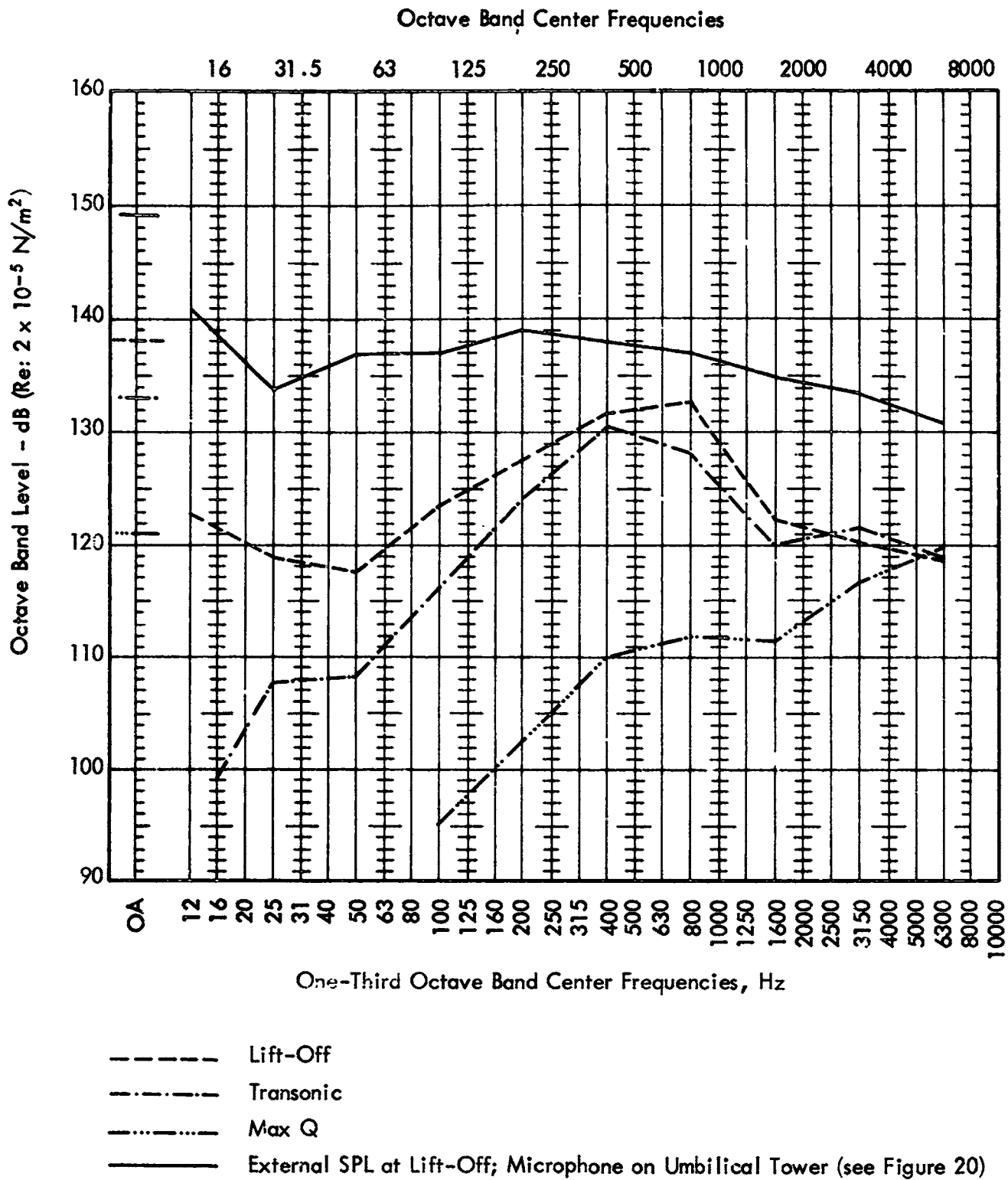————— External SPL at Lift-Off; Microphone on Umbilical Tower (see Figure 20)

Figure 62. Measured Internal Sound Pressure Levels during Launch and Flight of the
OT-2 Spacecraft/Improved Delta (TAD) Vehicle; Nimbus Shroud (Ref. 53)
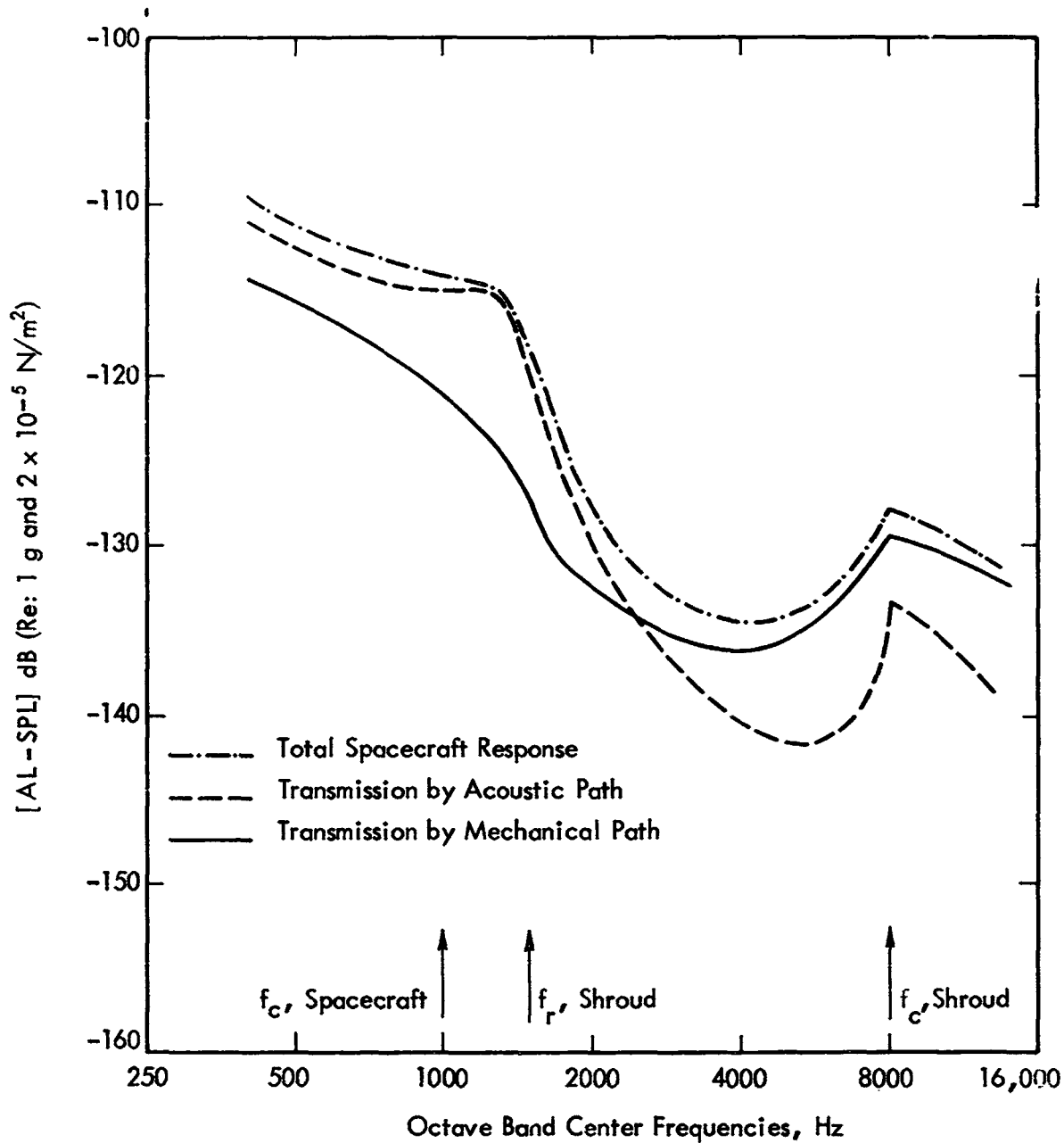
Figure 64. Predicted One-Third Octave Band Spacecraft Responses to Vibration
Transmitted by the Different Paths; One-Half Scale Model of the
Spacecraft-Shroud System from Reference 65

Figure 65. Measured One-Third Octave Band Spacecraft Responses to Vibration Transmitted by the Different Paths; One-Half Scale Model of the Spacecraft-Shroud System from Reference 65
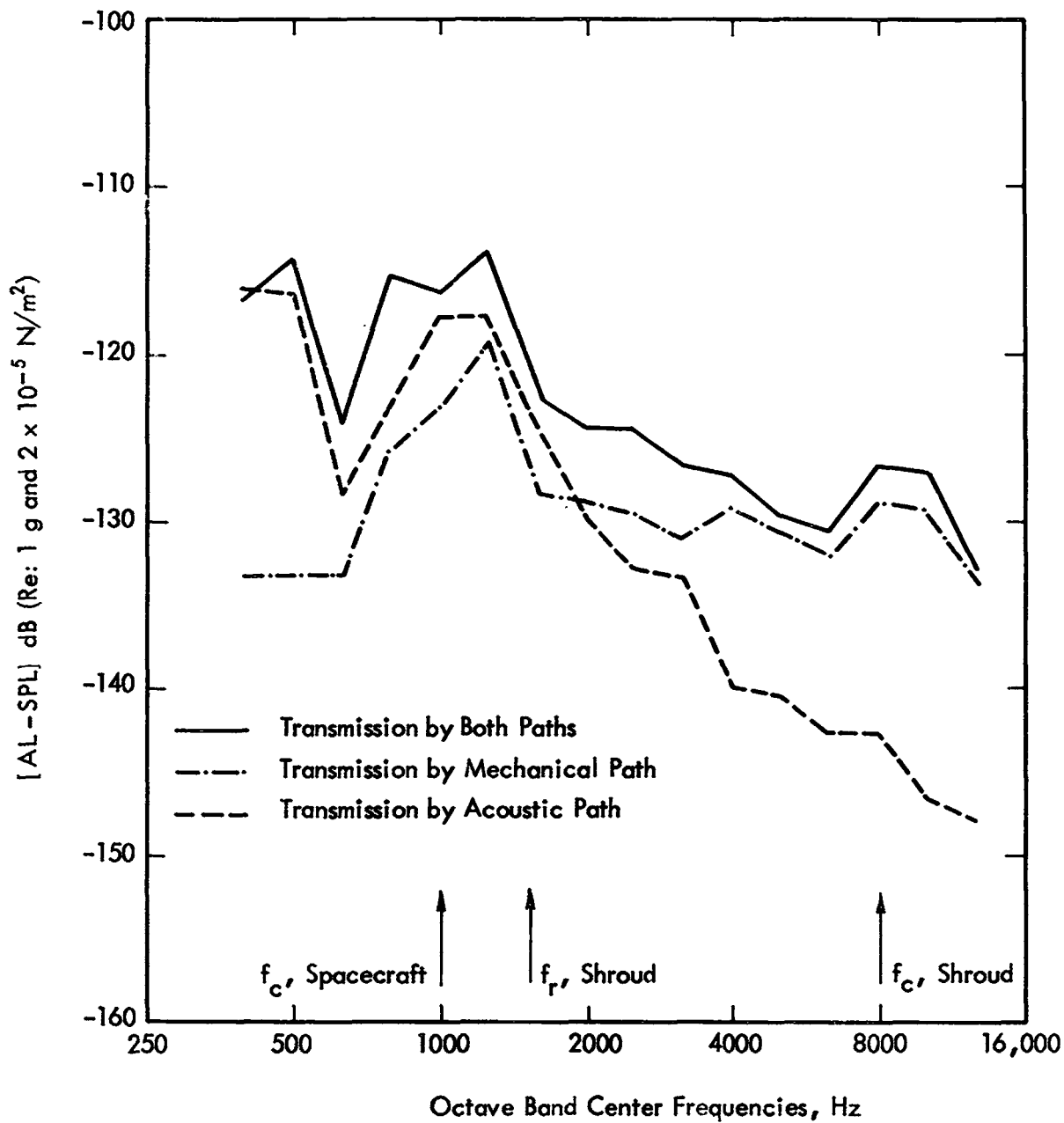
192
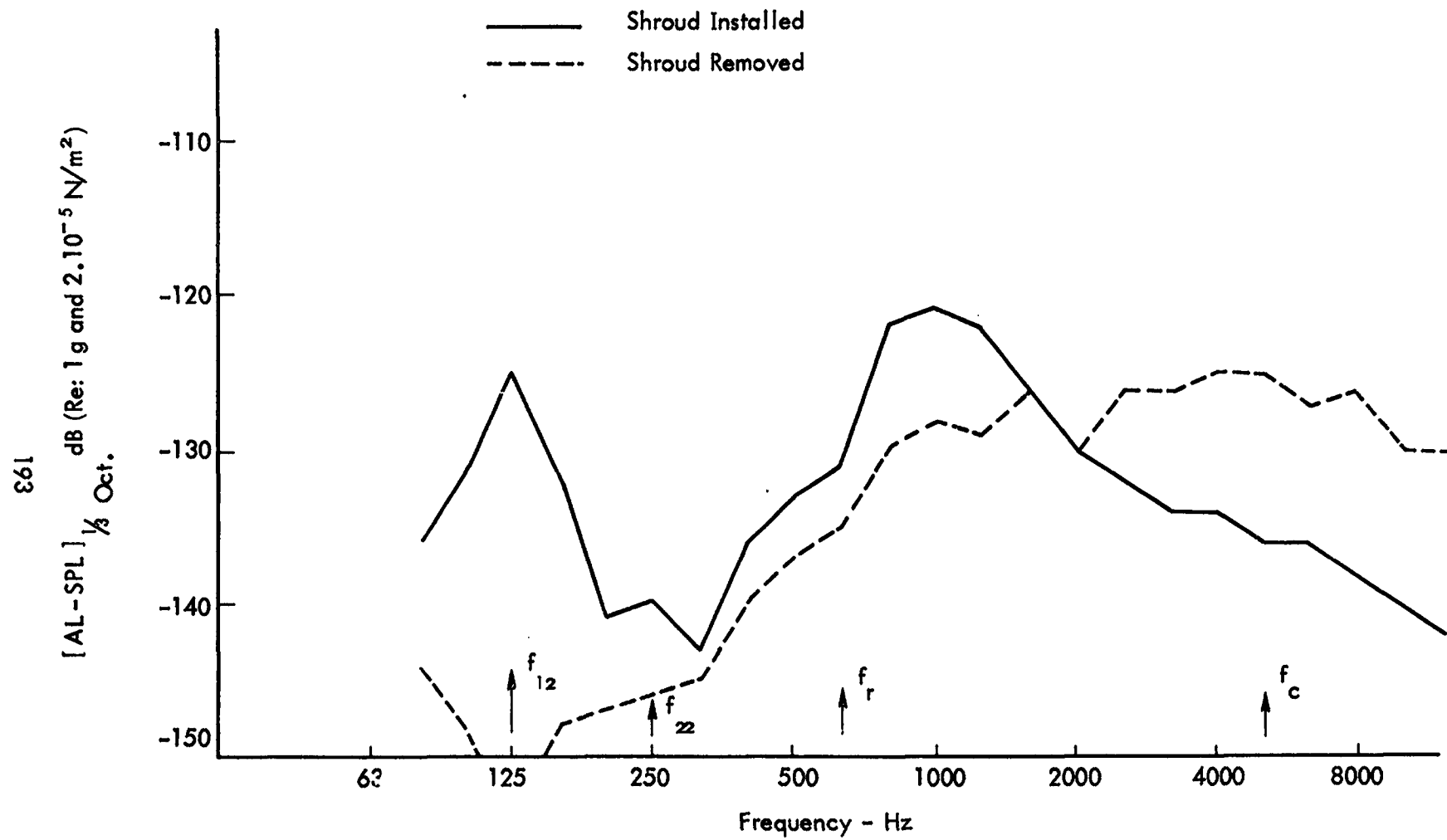
(a) Average Acceleration at Base of Adapter Truss

Figure 66. Measured Acceleration Responses of the OGO Spacecraft during Progressive Wave Testing with and without the Nimbus Shroud Installed, from Reference 61
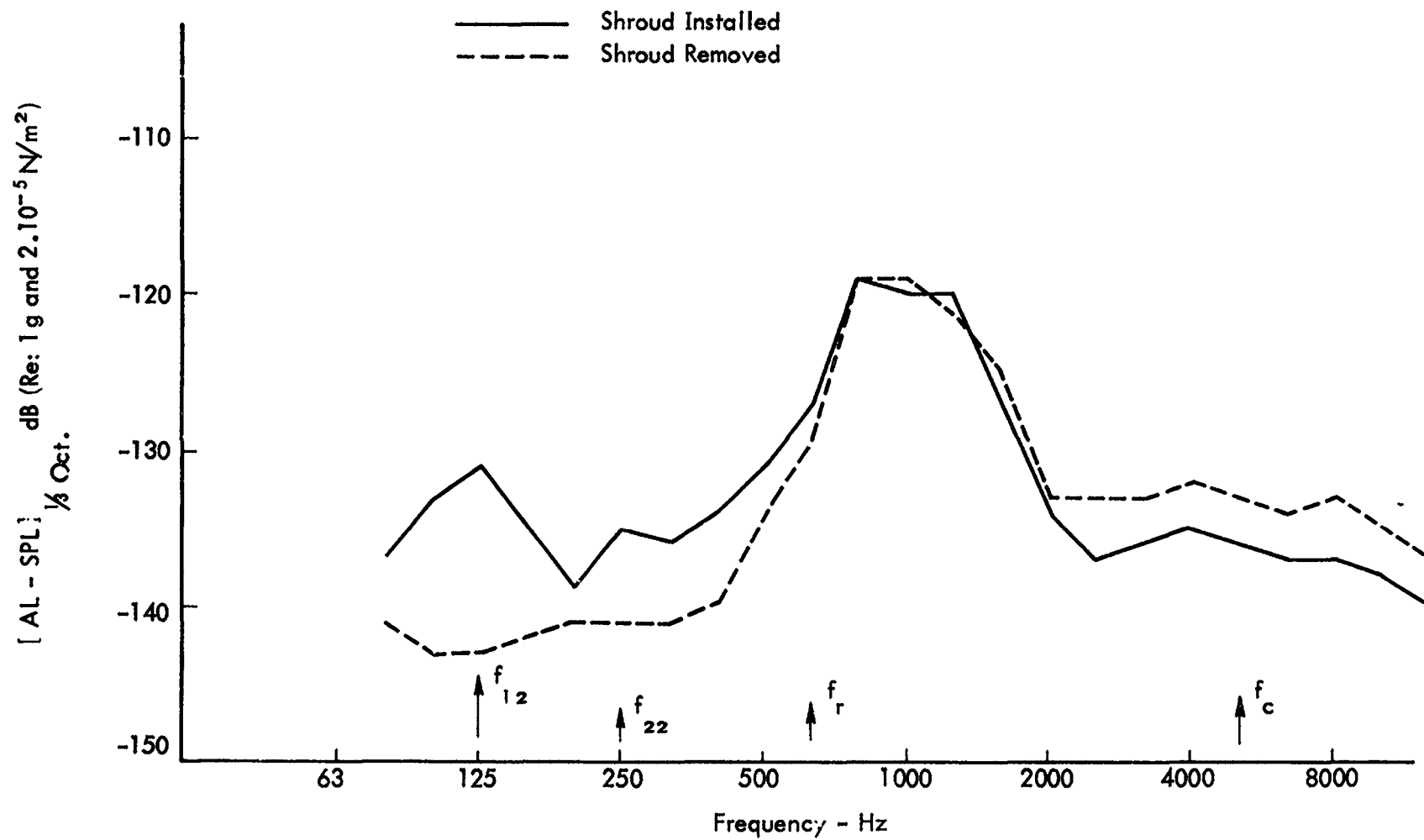
(b) Average Acceleration at Top of OGO Spacecraft

Figure 66. Concluded

Figure 67. Normalized Space Average Radial Accelerations of Simulated Payload for Air and Helium within the Shroud (from Reference 66)
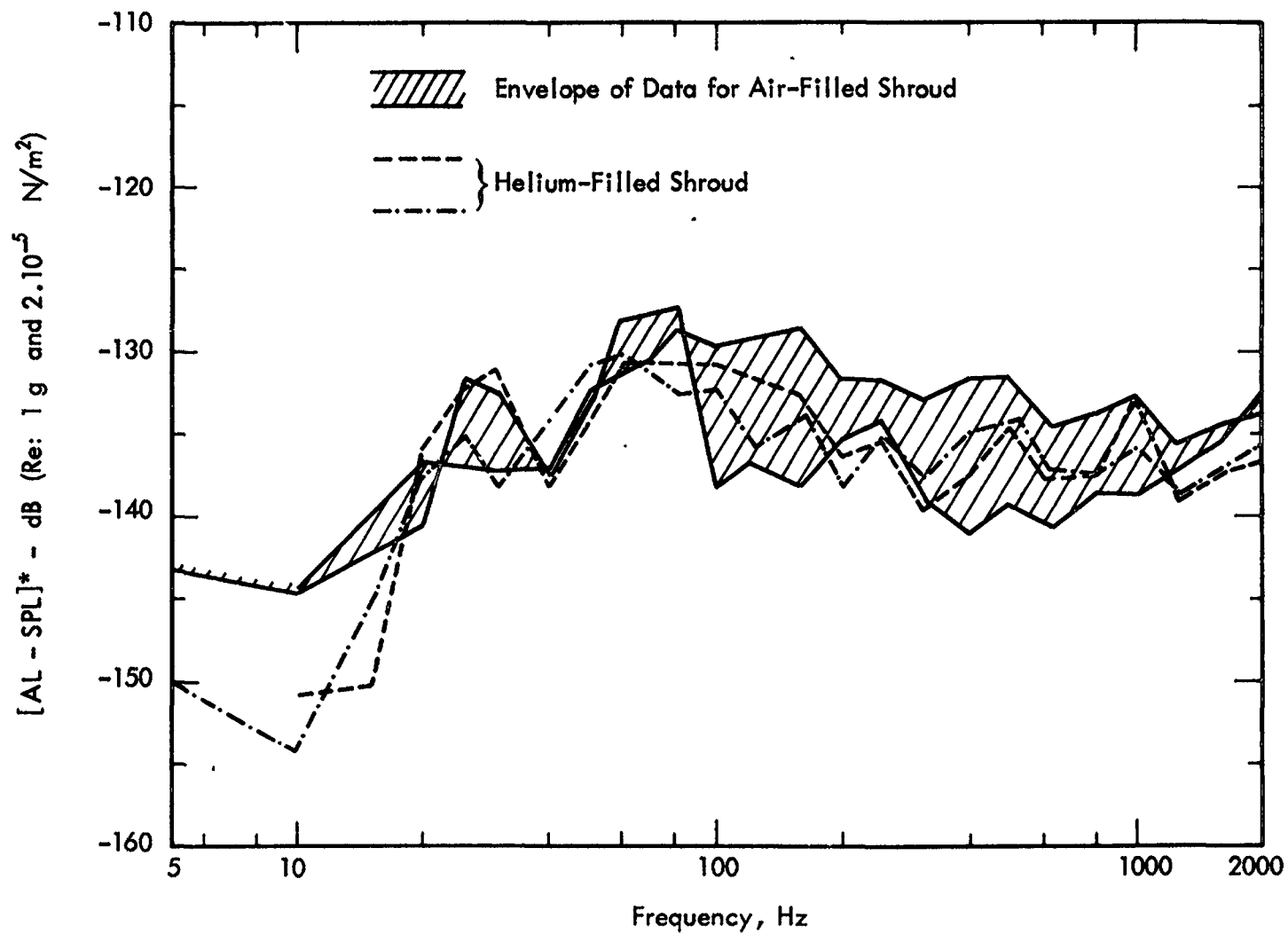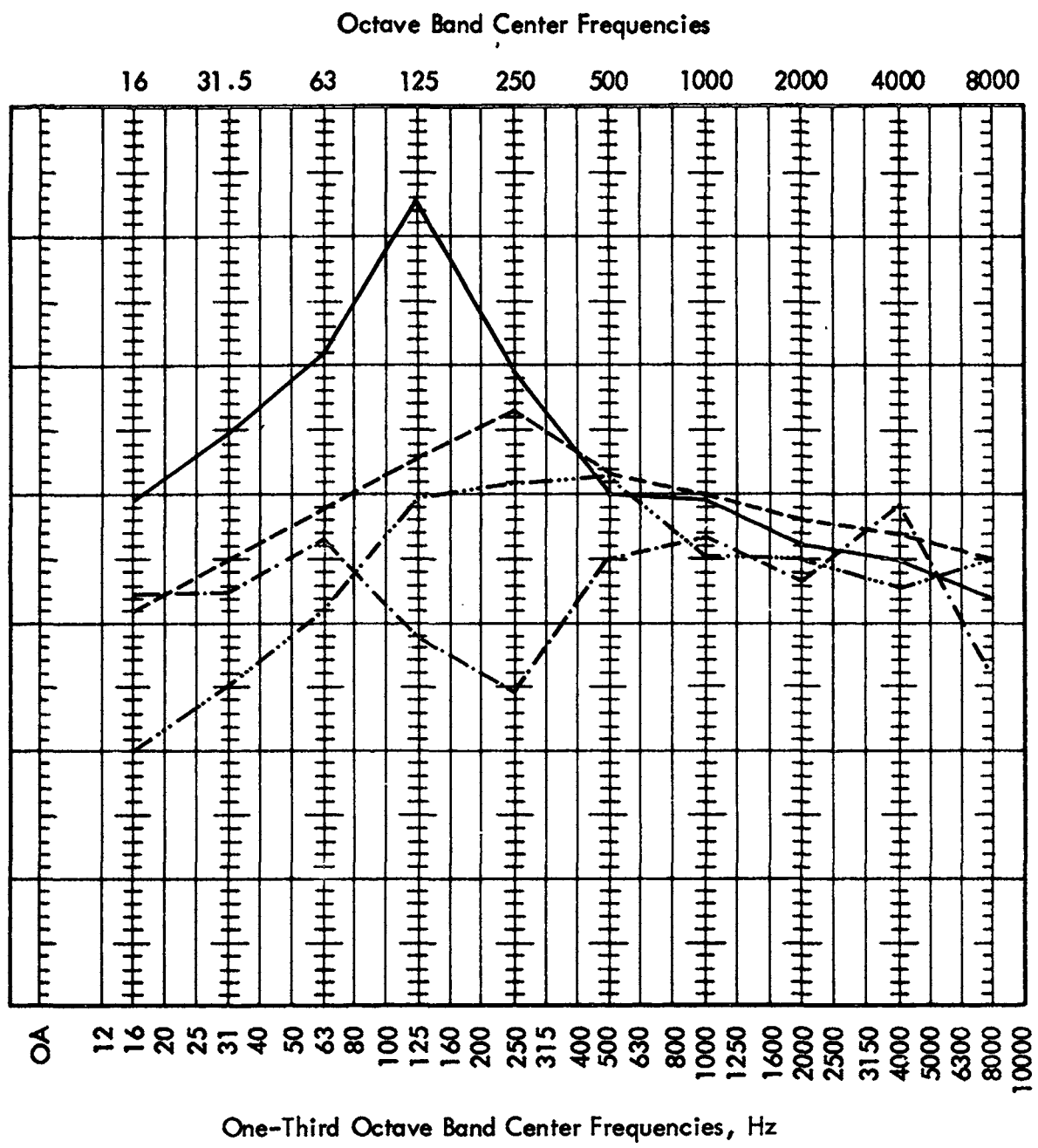
* Note: SPL = Space Average Sound Pressure Level at External Surface of Shroud

Octave Band Center Frequencies

One-Third Octave Band Center Frequencies, Hz

Octave Band Level – dB (Re: 2×10^{-5} N/m^2)

- – – – – – Upper Envelope to Lift–Off Spectra Shown in Figure 19
- – ·– ·–·– Reverberant Acoustic Field
- ————— Single Progressive Wave Axial Duct
- – ···– ···– Eight Progressive Wave Axial Ducts

(a) Cylindrical Section of the Nimbus Shroud

Figure 68. Equivalent Acoustic Environments to Simulate the Structural Response of the Nimbus Shroud at Lift–Off

Octave Band Center Frequencies
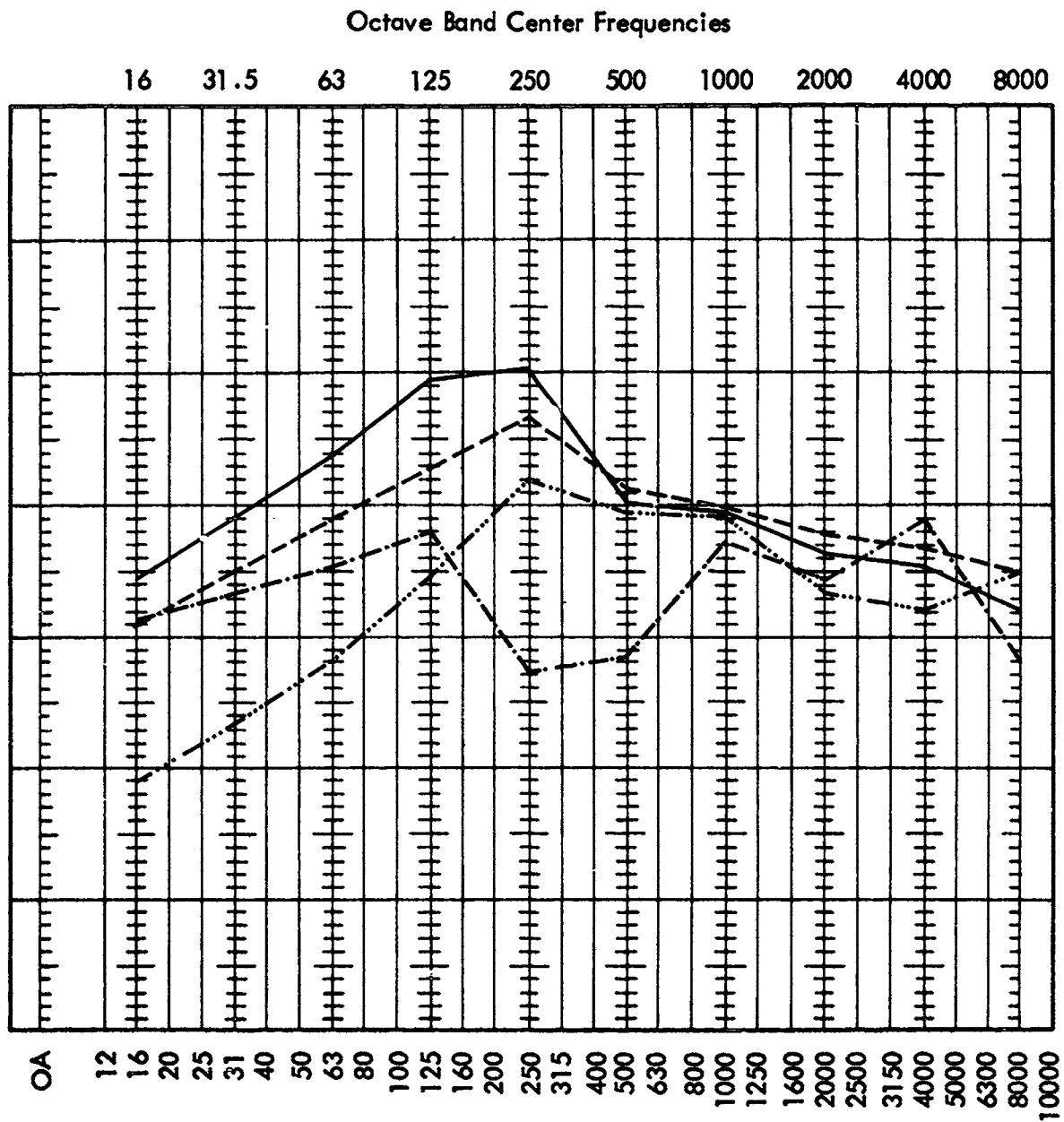
One-Third Octave Band Center Frequencies, Hz

———— Upper Envelope to Lift-Off Spectra Shown in Figure 19

—·—·—·— Reverberant Acoustic Field

——————— Single Progressive Wave Axial Duct

—···—···— Eight Progressive Wave Axial Ducts

(b) Conical Section of the Nimbus Shroud

Figure 68. Concluded
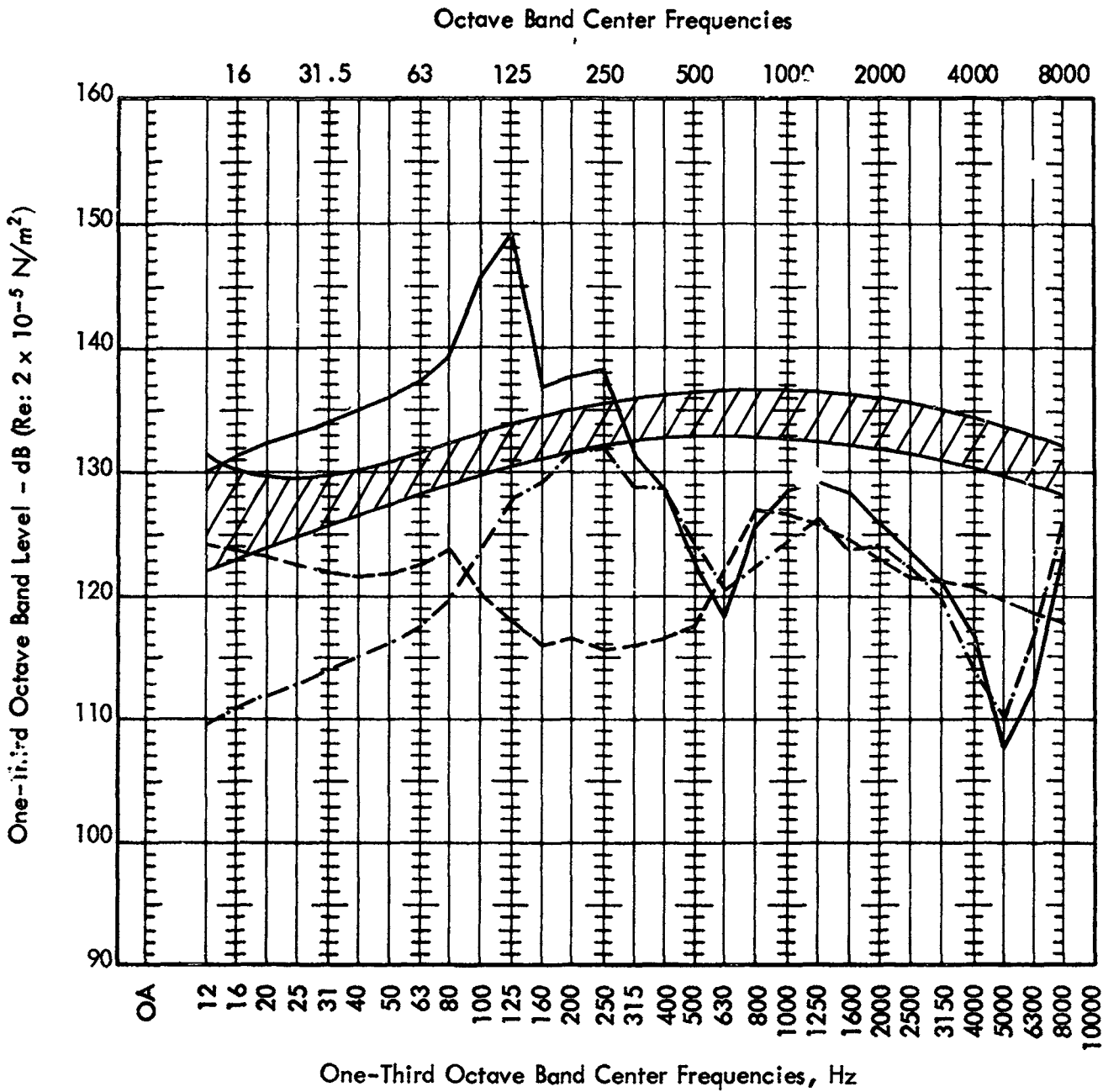
197

Figure 69. Equivalent Acoustic Environments to Simulate the Structural Response of the Nimbus Shroud at Mach 0.7

198

Figure 69. Concluded

(b) Conical Section of the Nimbus Shroud

Legend:

—···—···— External Sound Pressure Levels over the Conical Section of Mach 0.7 (data from Figure 28)

— — —~— — Reverberant Acoustic Field

——————— Single Progressive Wave Axial Duct

—·—·—·— Eight Progressive Wave Axial Ducts

Octave Band Center Frequencies

16 31.5 63 125 250 500 1000 2000 4000 8000

One-Third Octave Band Level – dB (Re: 2 × 10⁻⁵ N/m²)

One-Third Octave Band Center Frequencies, Hz

———·····—— External Sound Pressure Level over Zone 2 of Cylindrical Section at
Mach 0.8 (data from Figure 28)

—··—··— External Sound Pressure Level over Zone 3 of Cylindrical Section at
Mach 0.8 (data from Figure 28)

—··—··— Reverberant Acoustic Field

———————— Single Progressive Wave Axial Duct

— — — — — Eight Progressive Wave Axial Ducts

(a) Cylindrical Section of the Nimbus Shroud

Figure 70. Equivalent Acoustic Environments to Simulate the Structural Response of
the Nimbus Shroud at Mach 0.8

200

Octave Band Center Frequencies

One-Third Octave Band Center Frequencies, Hz

—···——···— External Sound Pressure Level over the Conical Section at Mach 0.8
(data from Figure 28)
—·——·——·— Reverberant Acoustic Field
——————— Single Progressive Wave Axial Duct
— — — — — Eight Progressive Wave Axial Ducts
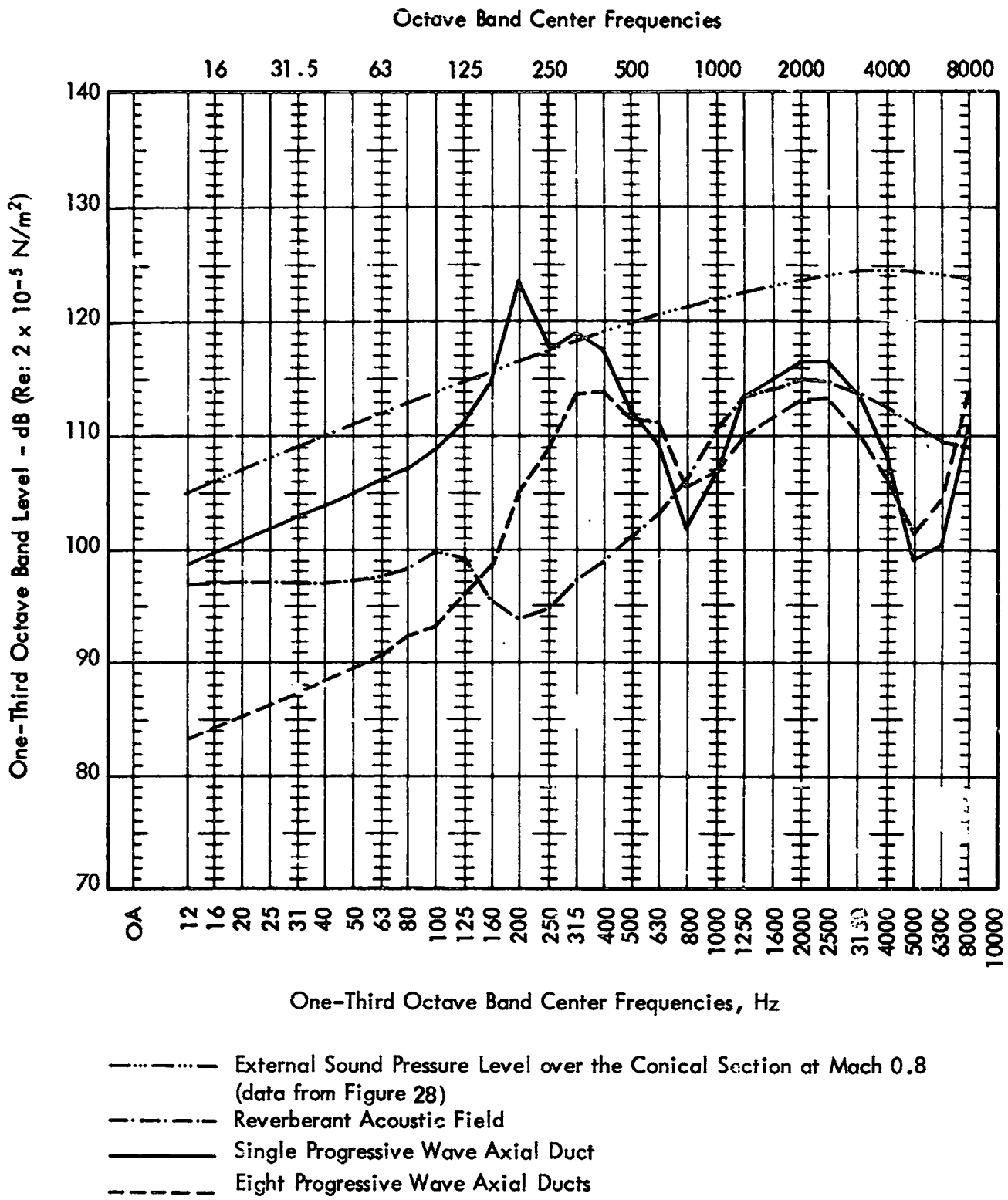
(b) Conical Section of the Nimbus Shroud

Figure 70. Concluded

Octave Band Center Frequencies

One-Third Octave Band Center Frequencies, Hz
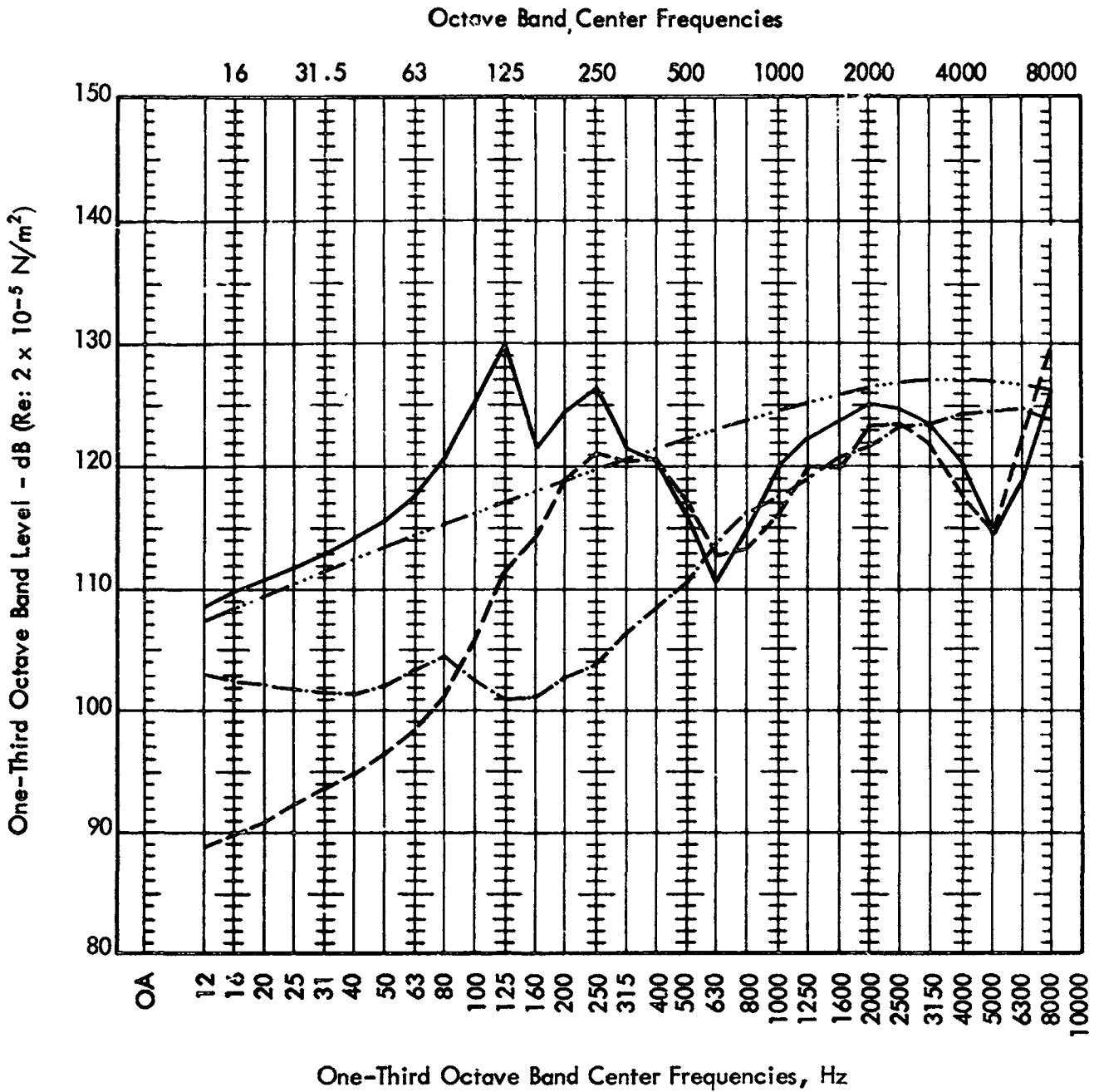
— · · · — · · — · · ·   External Sound Pressure Level over the Cylindrical Section at Mach 2.0
(data from Figure 28)
— · — · — · —   Reverberant Acoustic Field
————————   Single Progressive Wave Axial Duct
— — — — —   Eight Progressive Wave Axial Ducts

(a) Cylindrical Section of the Nimbus Shroud

Figure 71. Equivalent Acoustic Environments to Simulate the Structural Response of
the Nimbus Shroud at Mach 2.0

202

Octave Band Center Frequencies

One-Third Octave Band Center Frequencies, Hz

—⸱⸱⸱—⸱⸱⸱— External Sound Pressure Level over the Conical Section of Mach 2.0
(data from Figure 28)

—⸱—⸱—⸱— Reverberant Acoustic Field

————— Single Progressive Wave Axial Duct

— — — — Eight Progressive Wave Axial Ducts
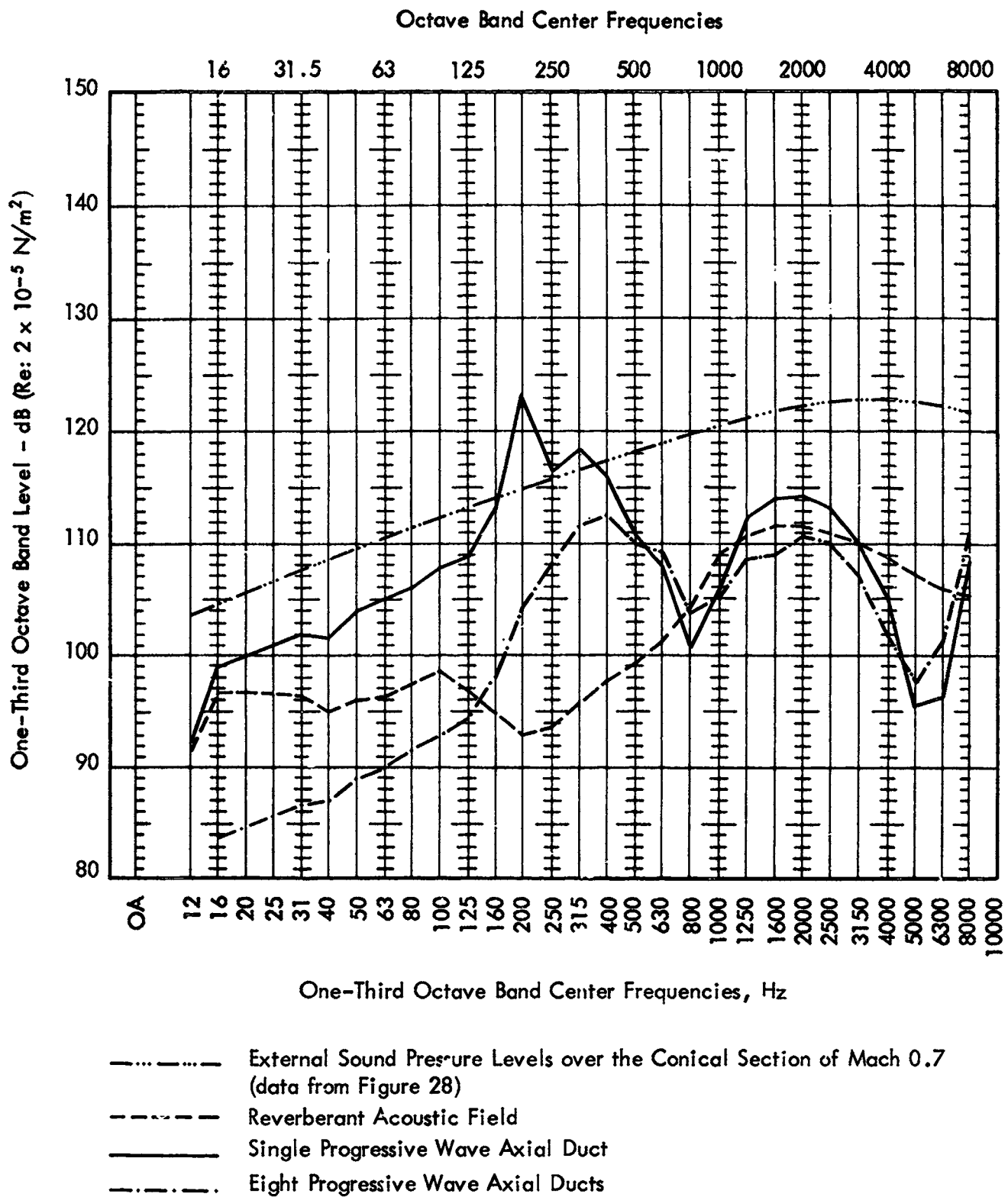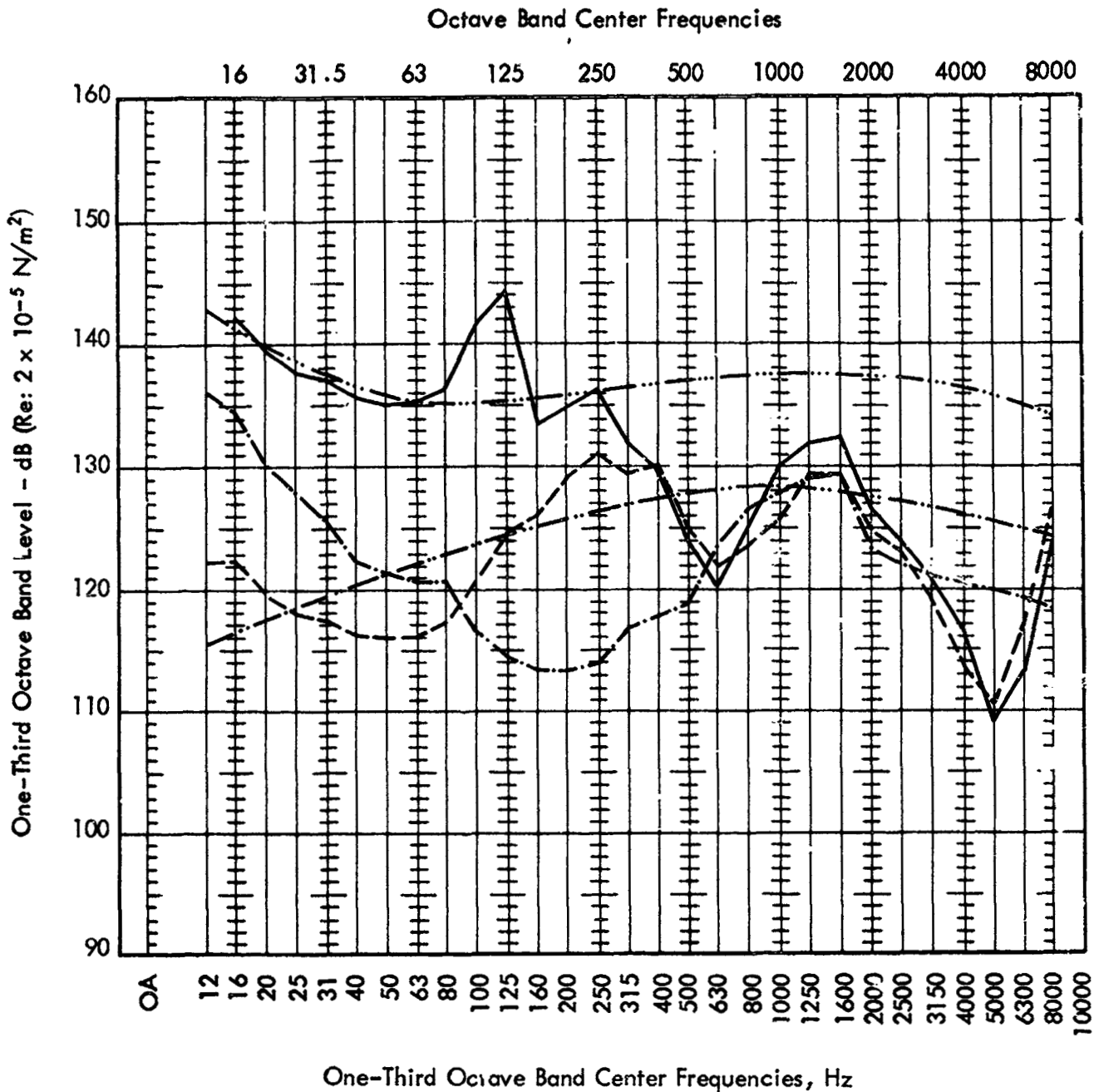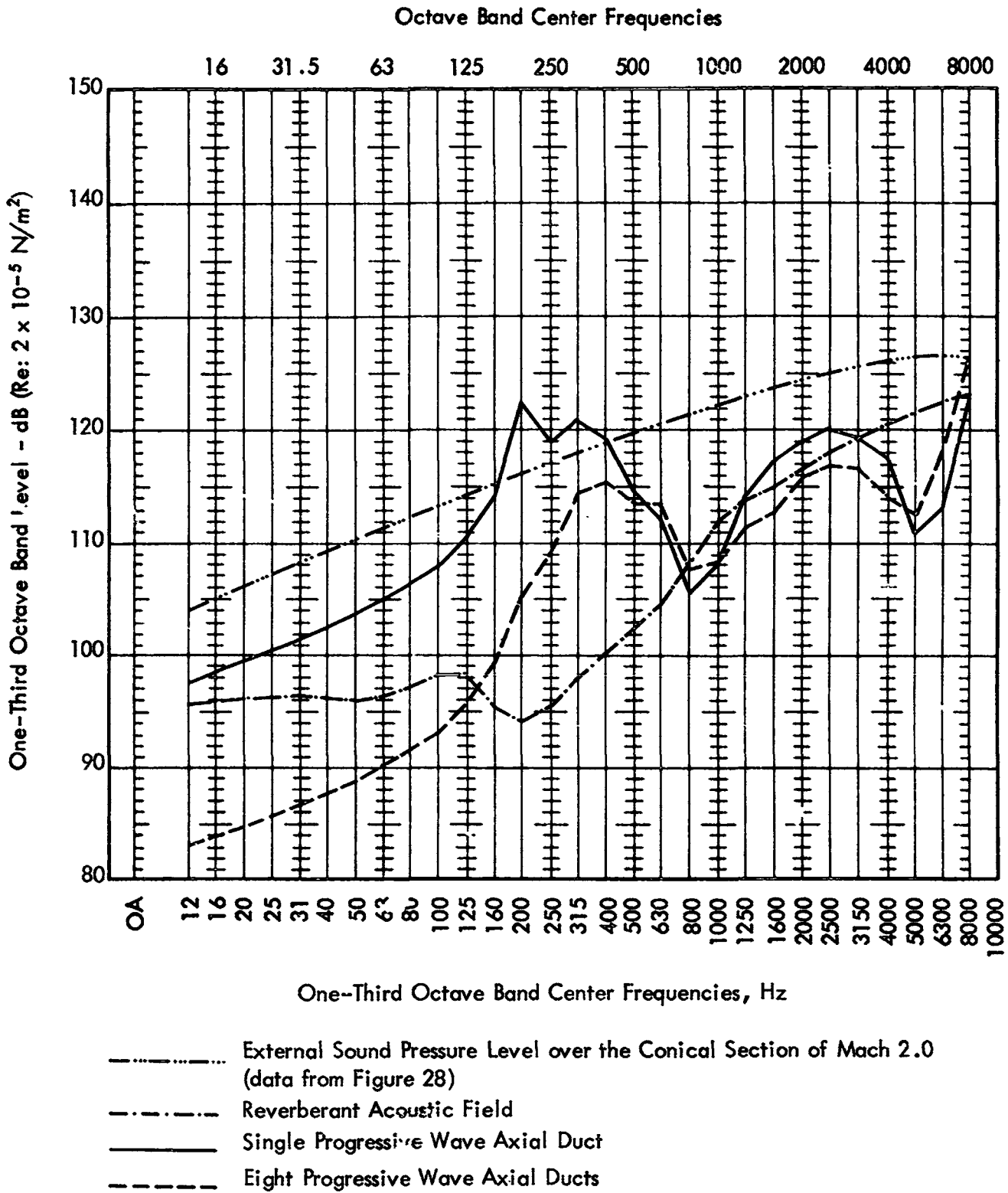
(b) Conical Section of the Nimbus Shroud

Figure 71. Concluded

Figure 72. Equivalent Local Reverberant Acoustic Field to Simulate the Structural Response of the Nimbus Shroud Section Between Ring Frame Stations 115.0 and 159.0 at Mach 0.7
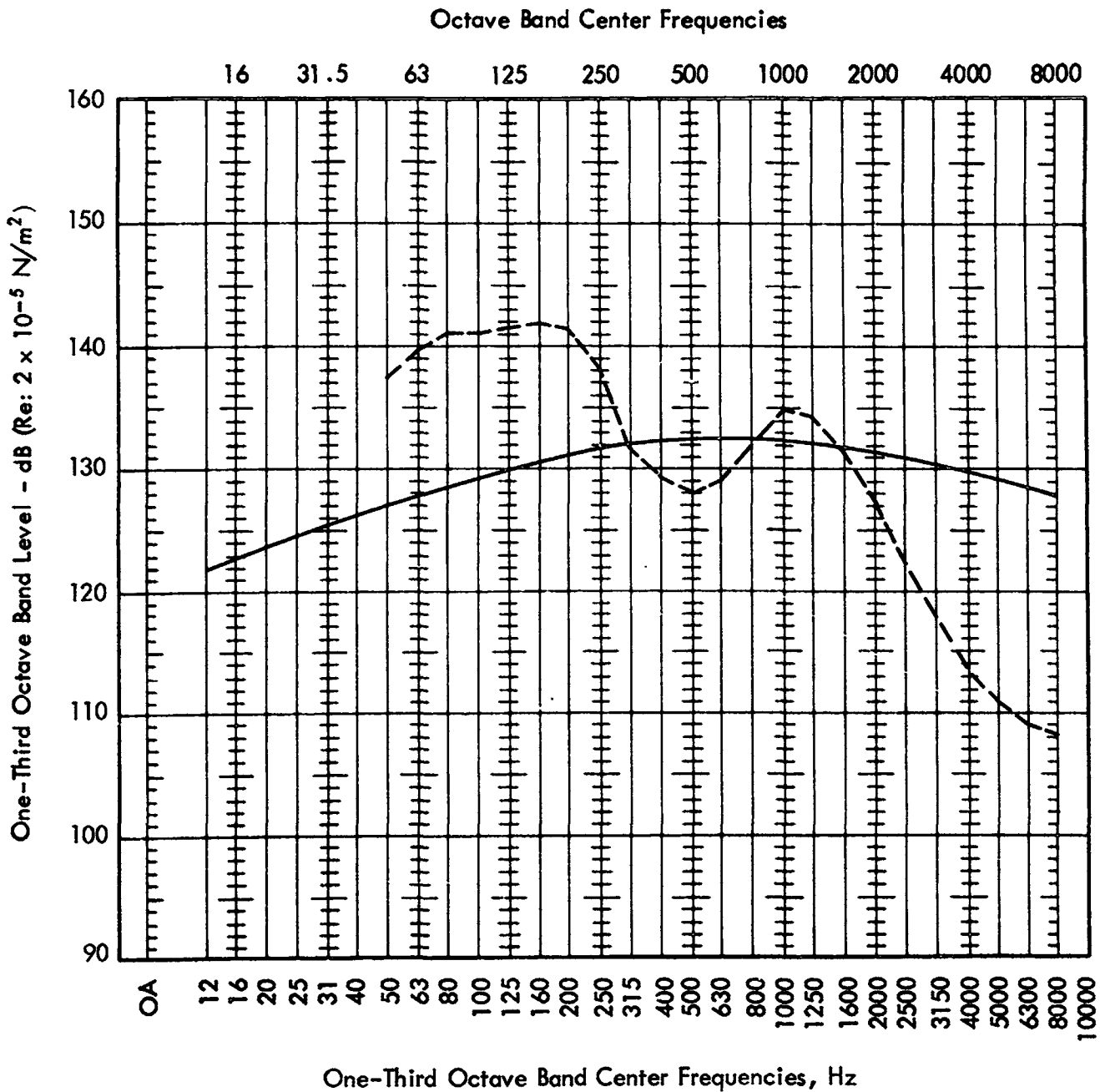
Figure 73. Equivalent Reverberant Acoustic Field to Simulate the Structural Response of the Nimbus Shroud Section between Stations 198.5 and 221.5 at Mach 0.7

205
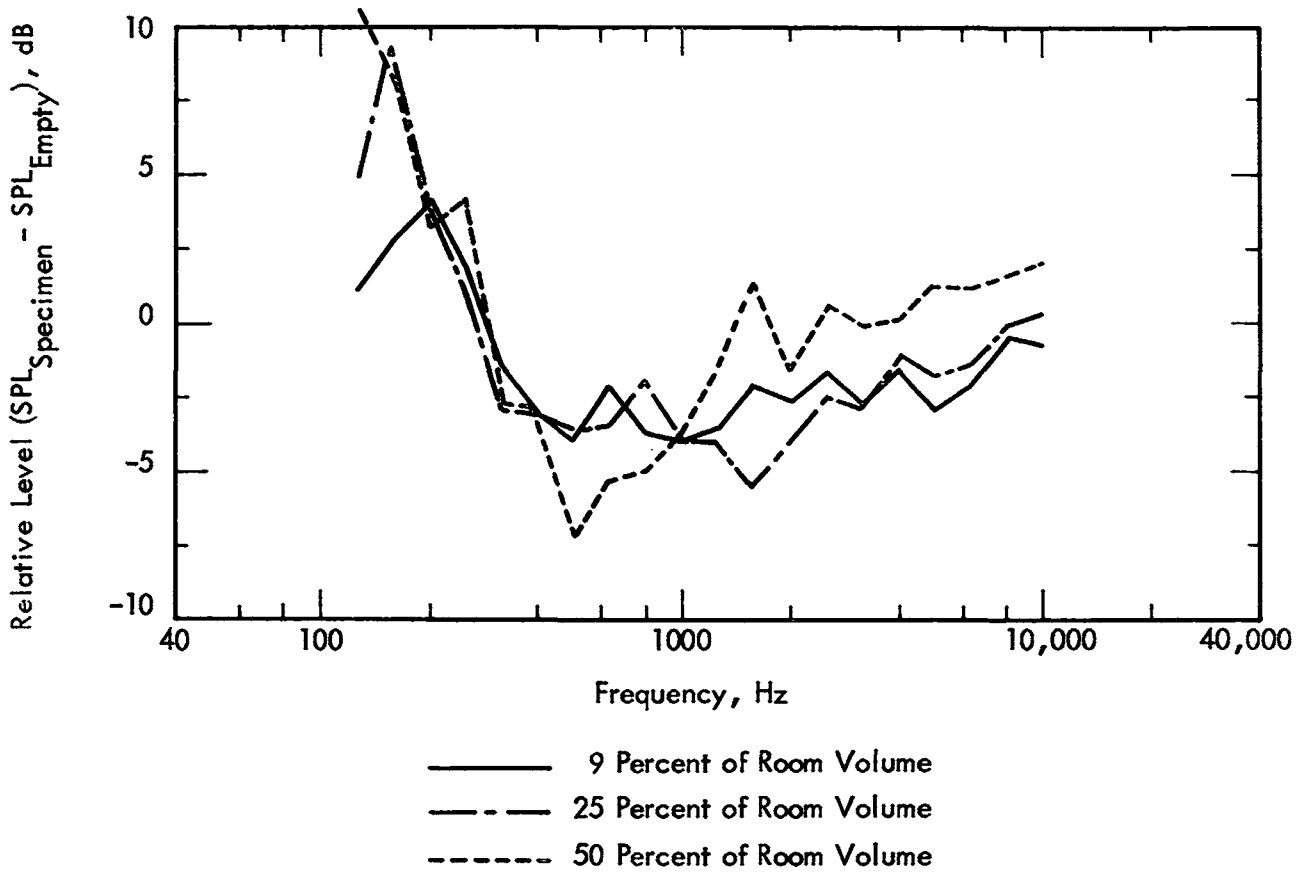
Figure 74. Sound Pressure Levels Measured in a Reverberation Room with Various Specimen Sizes Relative to Sound Pressure Levels Measured in the Empty Room

206
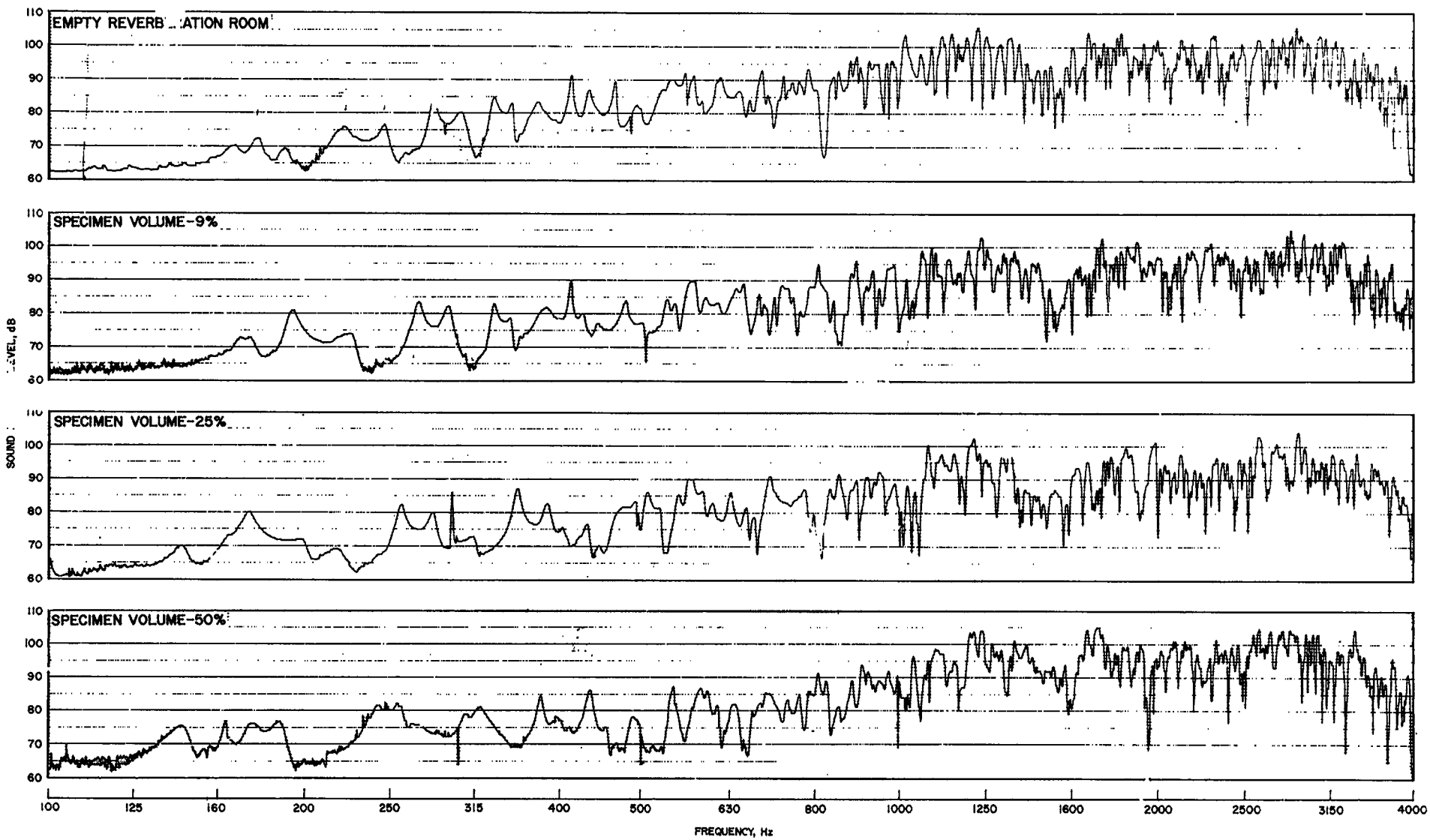
Figure 75. Expanded Scale Sine Sweep Showing Differences in Reverberation
Room Response for Various Test Specimen Volumes

$$f_0 V^{1/3} \approx c \sqrt[3]{\frac{N(f)Q}{4\pi}} \qquad \text{(See Equation (66))}$$
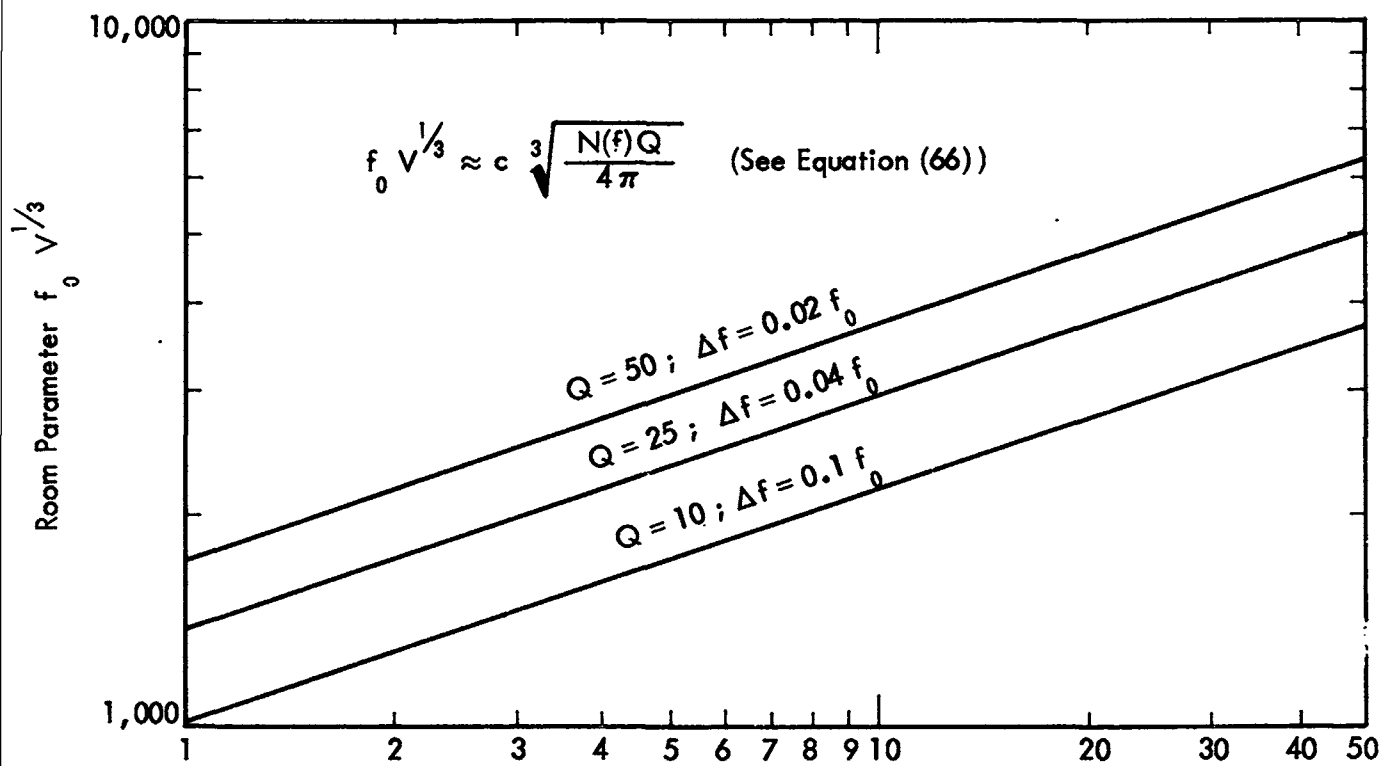
Average Number of Modes, N(f), within the Bandwidth, Δf, of a Structural Mode

Figure 76. Number of Acoustic Modes in a Reverberation Room within a Bandwidth, Δf, of a Single Structure Mode
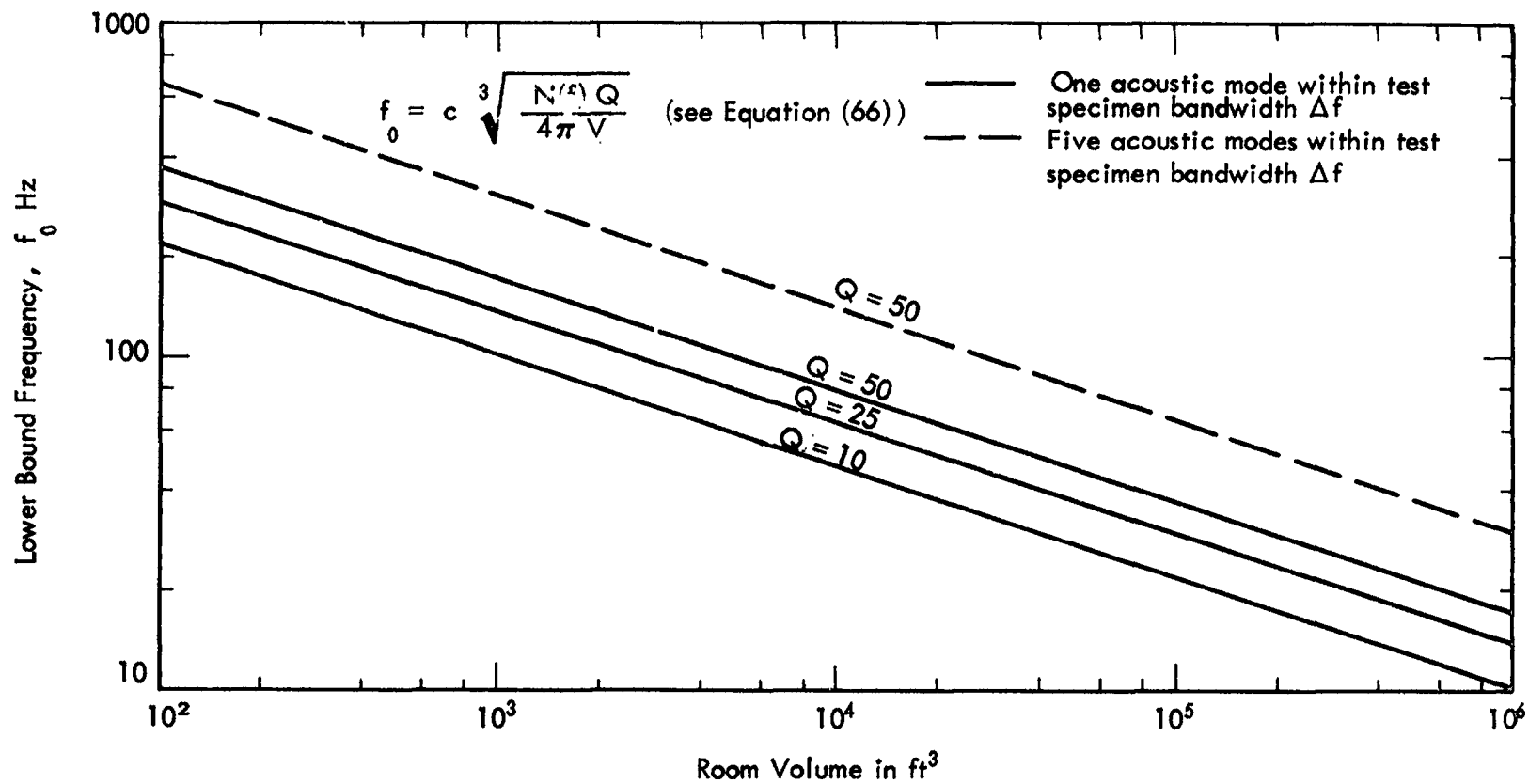
Figure 77. Comparison of Reverberant Room Volume and Lower Bound Frequency for Two Values of Average Number of Acoustic Modes within Test Specimen Bandwidth Δf
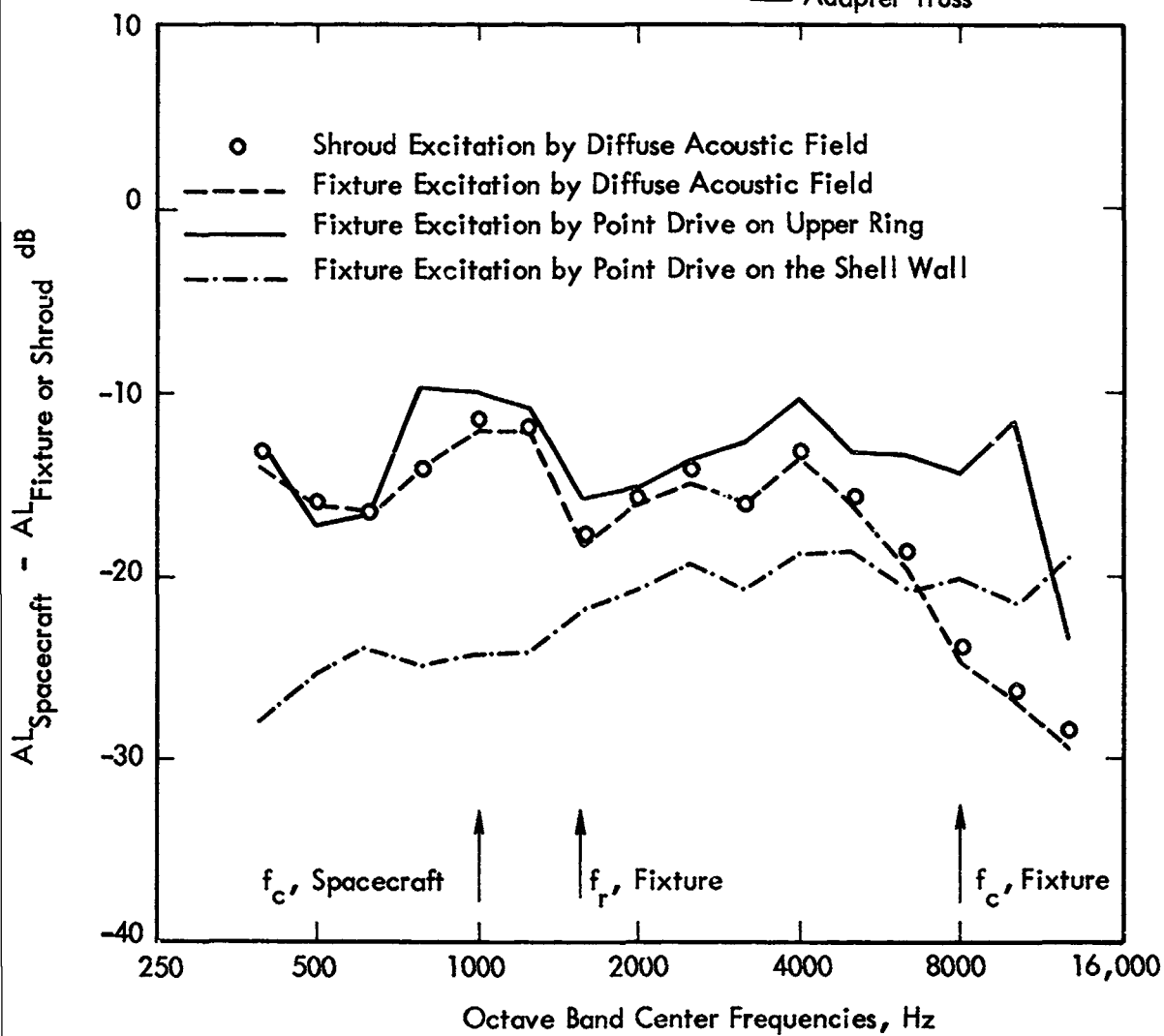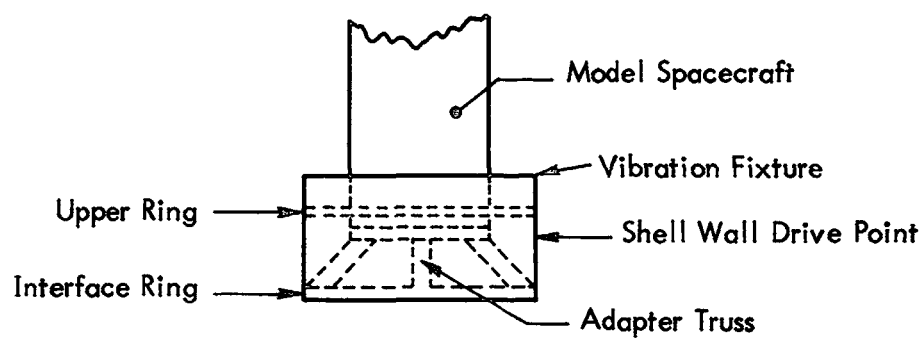
Figure 78. Vibration Transmission to the Spacecraft via the Mechanical Path; One-Third Octave Band Normalized Response Levels for Different Types of Excitation, from Reference 65

210

APPENDIX A

ROCKET NOISE ENVIRONMENTS FOR
SHROUD/SPACECRAFT SYSTEMS

1.0 INTRODUCTION

For large contemporary rocket powered vehicles, the rocket noise is an important part of the overall environment experienced by the vehicle and its payload. Since many of these vehicles can produce over 100 million watts of acoustic power at launch, it is necessary to accurately specify the noise environments when designing such vehicles or their payload and shroud systems.

The primary concern in this Appendix is the specification of noise environments for the payload and shroud region of the vehicle. A typical rocket exhaust noise field can be divided into three regions:

- Near-Field — This region is immediately outside of the rocket exhaust flow itself. The sound pressure level is very high in the near-field such that finite amplitude effects should be considered. The pressure fluctuation field contains a component which is out of phase with the particle velocity. In specifying the acoustic environments in this region, the effect of sound source location must be taken in to account. The end of the near-field is generally defined as five wavelengths away from the noise source.

- Mid-Field — This region is located immediately outside of the near-field. In this region, the pressure fluctuations are in phase with the particle velocity. The apparent noise source location remains an important parameter for the specification of noise environments in the mid-field.

- Far-Field — This region occupies all the space beyond the mid-field. The rocket exhaust can be regarded as a single point source where noise of all frequencies is emitted. In order to define the acoustic environments in this region, the atmospheric and ground attenuation effects must be considered.

The payload and shroud system on a launch vehicle can be considered to be located in the acoustic mid-field of the rocket exhaust. For the rocket noise environment, the most severe acoustic loading on the launch vehicle occurs during lift-off. Therefore, the configuration of the first stage boosters as well as the deflector geometry are important parameters to be considered in determining the overall acoustic environment.

Several precise methods of rocket noise prediction will be discussed in Section 2.0. Each of these methods has its own merit with respect to specific ranges of application. The influence of the deflector configuration on the noise environment and a few other special problems will be discussed in Section 3.0. Finally, the spatial correlation characteristics of the noise field around the launch vehicle will be discussed in Section 4.0.

2.0 METHODS OF PREDICTION OF ROCKET NOISE

In spite of the wide variations in size, design, and propellant requirements in rocket engines, the exhaust flows are generally dynamically similar. For existing large launch vehicles, the rocket exhaust flow velocity ranges generally from 7500 to 9000 ft/sec, with a typical Mach number of approximately 3.5. The expansion ratio of the rocket exhaust is nearly constant for optimum rocket nozzle performance along the flight trajectory in the atmosphere.

Various methods are available for rocket noise predictions. However, due to the semi-empirical nature of these methods, none of them are general enough to cover all situations. Each of them, however, has its own merit for its relevance to certain special conditions. Four different methods for rocket noise predictions will be discussed in this Section. The first is a method introduced by Cole, et al., (Reference 1). This is one of the earliest methods which can provide a precise definition of rocket noise environments, and is based on a series of rocket engine tests with thrusts ranging from 1000 lbs to 130,000 lbs. The second method was developed by the Wyle Laboratories research staff through a series of rocket noise studies. In this approach, the rocket exhaust flow is divided into segments of apparent noise sources and the acoustic pressure fluctuations at various points on the vehicle can be computed by summing the contributions from these source segments. The apparent source location and the strength of the sources are derived from experimental data, and presented in terms of normalized parameters. The third method follows a different approach and was developed by Franken and Wiener in 1963 (Reference 2). Acoustic measurements of launch noise environments on vehicles such as the Titan and Jupiter, were synthe-sized into a set of three normalized curves. These curves represent approximately the top, mid-section and bottom section of the launch vehicles. A correction factor is available to take into account the variations in thrust for individual launch vehicles. This method has been shown to be accurate for predictions of the noise environments for large launch vehicles. Finally, a fourth method which deals with very large boosters was introduced by Wilhold, et al., (References 3 and 4). This method takes into ac-count the importance of noise source distribution and the deflected geometry of the rocket exhaust. The basic non-dimensional spectrum is compiled from data obtained during launch and static testing of large booster engines. This method which provides the flexibility of dealing with advanced strap-on launch vehicles such as Titan III C, or projected post-Saturn launch vehicles has been shown to be very accurate.

214

The detailed procedure for each method, as well as its range of application, will be discussed below. For launch vehicles with simple geometry, the noise environment can us   e predicted by using one of these four methods. For strap-on launch vehic.., ..wever, two different   rhods may be required to handle the main rocket booster and the strap-on rockets separately.

It should be emphasized that each of these methods predicts the free-field sound pressure levels in the absence of the structure. To obtain the actual surface sound pressure levels, a correction of 3 dB should be added to the free-field levels for frequencies equal to or greater than $c_0/2\pi R$, where c_0 is the speed of sound in air, and R is the radius of the payload shroud. This 3 dB correction represents an average increase in sound pressure level around the circumference of the shroud due to the impingement of random phase acoustic waves.

The Method of Cole, et al.

This method of prediction was developed from a series of rocket noise measurements undertaken by Cole, et al., (Reference 1) at the Air Force Wright Air Development Center. Both rockets with liquid propellant, and rockets with solid propellant were included, and most of these had standard conical nozzles. The thrust of these rockets ranged from 1000 lbs to 130,000 lbs. Near field and far field levels from eleven static fired and three vertically launched rockets were measured under free-field conditions. No exhaust blast deflectors were utilized for the static firings. Full details of this re   rch program are reported in Reference 1.

Essentially, this method predicts the overall sound power of a given rocket by using an empirical formula. The spectrum and the directivity index of the noise field are given in non-dime onal graphs. The prediction procedure is given as follows:

Notation

SPL	=	Sound Pressure Level
PWL	=	Sound Power Level
OA	=	Overall
OB	=	Octave Band
W_M	=	Total Mechanical Power of Rocket in Watts
t	=	Thrust, lbs
g	=	Gravitational Acceleration = 32.2 ft/sec^2
w	=	Weight Flow, lbs/sec

$$d \quad = \quad \text{Exit Diameter of Rocket Exhaust, ft}$$

$$f \quad = \quad \text{Geometric Mean Frequency of Octave Band}$$

$$v \quad = \quad \text{Gas Velocity at Nozzle Exit, ft/sec}$$

Procedure

1. Determine the overall sound power level using Figure 1

$$\text{OAPWL} = 78 + 13.5 \log_{10} W_M \cdot \text{ dB, re: } 10^{-13} \text{ watts}$$

where

$$W_M = 0.676 \, tv = 0.676 \, \frac{t^2 g}{w} \text{ watts}$$

2. Determine octave band power spectrum of the source as follows:

   a) Compute the Strouhal numbers fd/V for the center frequencies of the octave bands.

   b) Determine the power spectrum level re: zero reference at each Strouhal number from the empirical curve shown in Figure 2.

   c) Determine the power spectrum level re: 10^{-13} watts by computing zero reference level which equals OAPWL − 10 $\log_{10} v/d$ and algebraically adding this reference level to each power spectrum level determined in the previous step.

   d) Convert these power spectrum levels at the geometric mean frequencies to octave band power levels by adding the appropriate 10 $\log_{10} \Delta f$ correction factors on Figure 2 to each power spectrum level.

3. Determine AO and OB space average SPL's at 100 ft from the formula:

   $$\text{Space Average SPL} = \text{PWL} - 43 \text{ dB}$$

4. Correct these space average SPL's at 100 ft to those free-field levels at any distance R by employing the corrections on Figure 3a or 3b.

5. Algebraically add the appropriate generalized directivity indice of Figure 4a or 4b to the computed space average free field SPL (R, f) to determine SPL (R, f, θ).

Although this method was originally intended for noise predictions in the far-field, it is safe to extend the application into the mid-field for small launch vehicles. In this case, the correction factor is Step 4 can be obtained simply by using the inverse square spreading rule. The deflection of the rocket exhaust flow should be considered in Step 5.

Cole's method of prediction has been found to be accurate for rockets with total mechanical power of less than 10^9 watts.

During a second measurement program (Reference 5) Cole investigated the noise radiation characteristics of nine different types of vehicle during launch. These launchings included Titan, Atlas, Saturn 1B, Thor, and Jupiter vehicles. However, no refinements to the generalized power spectrum shown in Figure 2 were attempted. Peverley and Smith (Reference 6) have reduced a portion of this Titan data together with Saturn data from References 7, 8 and 9 and compared these results with Cole's generalized power spectrum. The results obtained by Peverley and Smith are shown in Figure 2. Except for the Titan data at low Strouhal numbers, the results are in good agreement with Cole's empirical curve.

Method Developed by Wyle Laboratories

It is known from previous experimental work by Dyer (Reference 10) and others (References 11, 12 and 13) that each segment of the jet exhaust flow apparently produces noise mainly in a characteristic frequency band, with the lower frequencies being further away from the rocket nozzle exit plane. Since the effective noise producing region of the rocket exhaust is at least as long as the rocket vehicle itself, it is important to know the apparent noise source location for an accurate estimate of the near-field and mid-field environments. For predictions of the rocket noise environment on the launch vehicle, a method which took into account the effect of source location was first introduced by Dyer (Reference 14). A later study by Potter and Crocker (Reference 15) has added a significant number of refinements to Dyer's method, and has resulted in two accurate source allocation methods for predicting rocket noise environments. These methods are more appropriate for predicting the noise environments produced by rocket vehicles of moderate size.

In the first method, a non-dimensional octave band spectral function (Figure 5) is assumed to represent the quality of the overall noise field. Two curves are shown in Figure 5, one derived from Cole's spectral function shown in Figure 2, and the other derived from experimental data reported by Morgan and Young (Reference 11), Tedrick (Reference 16) and Mayes, et al. (Reference 17). It can be seen that for Strouhal numbers greater than about 0.02, the octave band spectrum derived from Cole's curve fits this data reasonably well. It is recommended that for Strouhal numbers less than 0.02, the upper curve should be used. It was found during studies of near-field characteristics that the source location

is a function of Mach number. A detailed discussion of the jet flow structure can be found in Reference 18 by Eldred, et al.

The simpler source allocation method of prediction has been presented in Reference 19; however, the procedure is described here in detail, as follows:

Step 1 — Obtain necessary geometry and rocket performance data including the surface position of interest, P, nozzle exit conditions, (mass flow, velocity etc., sufficient to calculate total mechanical power), deflector position, if any, and flow turning angle (Figure 6), number of nozzles n, nozzle diameter D_e, jet exit Mach number M_j (ratio of exhaust velocity to speed of sound in the flow, typically equal to 3.5).

Step 2 — Calculate the Strouhal numbers $(f D_e/V)_i$ for the octave band center frequencies of interest. For multiple nozzles, use the equivalent diameter

$$D_e^* = \sqrt{n} \ D_e$$

Step 3 — Calculate the overall acoustic power generated by the exhaust

$$OAPWL = 130 + 10 \log_{10} \eta W \qquad dB \ re \ 10^{-13} \ watts$$

where η is the acoustic efficiency (~ 0.003) and W is the mechanical power of the exhaust flow in watts.

Step 4 — Read the relative octave band power levels, $\Delta OBPWL_i$ from Figure 5 for each non-dimensional frequency $(f D_e/V)_i$.

Step 5 — Look up the downstream source location X/D_e for each frequency in Figure 7. (The solid curve for the open scoop deflector is normally the preferred curve for determining the apparent source locations.) Correct to actual distance X (multiplying by D_e) and identify distance R_i (between source and P), and θ_i, the angle between P and the positive flow direction ($\simeq$ 180 if the flow is undeflected or if the apparent source position is upstream of the deflector – see Figure 6).

Step 6 — Compute octave band free-field sound pressure levels at the point P according to:

218

$$OBSPL_i = OAPWL + \Delta OBPWL_i - 20 \log_{10} R_i + DI(\theta)_i - 10.5$$

$$\left[10 \log_{10} \frac{P}{P_0} \left(\frac{T_0}{T} \right)^{1/2} + 20 \log (1 - M_F) \right] \text{if in flight}$$

where P and T are the ambient pressure and absolute temperature (subscript 0 for sea level conditions). $DI(\theta)_i$ is the directivity index obtained from Figure 8; the directivity curves shown in this figure are essentially those presented in Reference 19, and are based upon previous experimental measurements (References 1, 11, 15 and 17). It is emphasized however, that these curves represent far-field directivity, whereas shroud/spacecraft systems are located in the acoustic mid-field. It is therefore recommended that a directivity index of 0 dB is assumed for radiation directions between 90 degrees, and 135 degrees to the exhaust flow. For radiation directions between 135 degrees and 180 degrees it is recommended that the directivity index be varied from 0 dB to -5 dB. Previous comparisons between predicted and measured rocket noise spectra at the vehicle have shown these assumed directivity indices to be satisfactory.

The second source al' :r*ion prediction method is based upon the fact that at any location in the exhaust '!·· .c :trum of noise is generated rather than noise at a discrete frequency as ·w ₁.. in the previous source allocation method. This source allocation technique is ιc.y more complex than the previous method and involves a significant amount of c·· .ation ro arrive at the free-field sound pressure levels. However, this method is especially suitable when shielding occurs between the point of interest on the vehicle and the apparent sources in the flow. This technique was first presented by Eldred, et al. (Reference 18) and later refined by Potter and Crocker (Reference 15). The procedure is as follows:

<u>Step 1</u> — Same as previous source allocation method.

<u>Step 2</u> — Calculate the length of the laminar flow core, x_t, from the relation:

$$x_t = 3.45 D_e (1 + 0.38 M_e)^2$$

For multiple nozzles, use the equivalent diameter

$$D_e^* = \sqrt{n} \, D_e$$

<u>Step 3</u> — Calculate the overall acoustic power generated by the exhaust:

$$OAPWL = 130 + 10 \log_{10} \eta W \quad dB \text{ re } 10^{-13} \text{ watts}$$

219

where $W = 0.676\, n\, t\, V_e$,watts

η = acoustic efficiency (≈ 0.003)

n = number of nozzles

t = thrust per nozzle, lbs

V_e = exit velocity, ft/sec

Step 4 — Divide the rocket exhaust flow into a number of segments of length, δ_x . It is recommended that the laminar flow core be divided into at least 3 segments.

Step 5 — Determine the normalized acoustic power per unit core length from Figure 9 for each segment:

i.e. $[\,PWL - OAPWL\,] - dB$

where   PWL = Acoustic Power per unit core length

Step 6 — Compute the acoustic power for each segment of the rocket exhaust flow as follows:

$$(PWL)_i = [PWL - OAPWL] + OAPWL + 10 \log_{10} \delta_x/x_t \; dB \; re \; 10^{-13} \; watts$$

where i denotes the i-th segment, and

δ_x = length of segment (ft).

Step 7 — Using the normalized power spectrum shown in Figure 10, compute the acoustic power in a given bandwidth for each segment as follows:

$$(PWL)_{ik} = 10 \log_{10} \left[\frac{W_{fx}}{W_x} \cdot \frac{V_e\, a_0}{x a_e} \right] + (PWL)_i - 10 \log_{10} \frac{V_e\, a_0}{x a_e}$$

$$+ \; 10 \log_{10} \Delta f_k \hspace{2cm} dB \quad re \; 10^{-13} \; watts$$

where W_{fx} = Sound Power per Hz per unit axial length at distance x from the nozzle exit plane (watts/Hz/ft)

W_x = Sound Power per unit axial length at distance x from the nozzle exit plane (watts/ft)

x = Distance from the nozzle exit plane to the center of the i-th segment (ft)

k = Center frequency of the appropriate band (i.e., $\Delta f_k = 0.707 \, f_k$ for the octave band centered at f_k)

a_0 = Ambient speed of sound (ft/sec)

a_e = Exit speed of sound (ft/sec)

Step 8 — For the point of interest on the vehicle, P, compute the free-field sound pressure level in each frequency band contributed by each segment as follows:

$$(SPL)_{ik} = (PWL)_{ik} - 20 \log_{10} R_i - 10.5 + DI \, (\theta)_i$$

where R_i = Distance from center of i-th segment to the point of interest P.

Step 9 — Sum the contribution (in a given frequency band) from all segments in the exhaust flow from the relation:

$$(SPL)_k = 10 \log_{10} \sum_i \text{Antilog} \frac{(SPL)_{ik}}{10} \, , \; dB \; re \; 2.10^{-5} \; N/m^2$$

The Franken and Wiener Method

This prediction method was compiled from actual noise measurements obtained on several large rocket-powered systems including Jupiter, Atlas, Titan, and Saturn. The firing configu...ion considered here involves the rocket firing vertically downward, with an exhaust deflector turning the stream into one or more horizontal paths. This prediction method has been found to be accurate for the class of rocket launch vehicles described above and the procedure is relatively simple. However, it is difficult to apply this method to predict the noise environment of special vehicle configurations which do not

conform with the restrictions imposing during the compilation of this method. These restrictions include the ratio of the total vehicle length to rocket nozzle diameter and the deflector configuration.

The prediction procedure is straightforward as follows (Reference 2):

1) Determine the total system thrust F in pounds and the effective nozzle diameter D_{eff} in inches from the relation

$$D_{eff} = \sqrt{n}\ D$$

2) Obtain the octave band sound pressure level estimates from Figures 11-13 for typical thrust conditions. Replot the abscissas of these curves in terms of frequency, using the appropriate value of the effective nozzle diameter D_{eff}.

3) Determine the typical thrust from Figure 14

4) Calculate the quantity

$$10 \log_{10} \frac{\text{total thrust}}{\text{typical thrust}}$$

and add this quantity to the levels obtained in Step 2.

5) For deflector configurations in which the spacing between the rocket exhaust nozzle and the impingement point on the deflector exceeds about three times D_{eff}, make the appropriate level correction in each band as indicated in Figures 11-13.

The level estimates obtained by this procedure represent the maximum octave band sound pressure levels to be expected, since the levels in the vicinity of the vehicle generally decrease after lift-off. Shielding effects, if present, will reduce the maximum levels below the estimates obtained by this procedure. It should be emphasized that these sound pressure levels are those existing near the surface of the vehicle and are not true surface pressures.

The Prediction Method Developed by Wilhold, et al.

This method represents the state-of-the-art of noise environment predictions for large rocket boosters. Due to the extremely large thrust and power of rockets such as Saturn, the deflector and the deflected exhaust stream provide a very complex environment for the near-field, mid-field, and far-field. The more advanced post-Saturn rocket configurations further complicate the problem. Therefore, separate methods of prediction

have been developed for the near-field, mid-field, and far-field by Wilhold, et al., (References 3 and 4). Only the mid-field prediction method, which is relevant to payload/shroud systems, is presented here. The prediction method is as follows:

Notation

OB SPL	$=$	octave band sound pressure level in dB, re: 2×10^{-5} newton/m^2
DSF	$=$	the dimensionless spectrum function which is a term proportional to acoustic power radiated toward the vehicle for a given Strouhal number, the dimensionless frequency term, fD/V_e
V_e	$=$	effective nozzle exit velocity (ft/sec)
$\dot{\omega}$	$=$	weight flow rate (lbs/sec) per nozzle
P_0	$=$	ambient atmospheric density (lb-sec^2/ft^4)
C_0	$=$	ambient sound velocity in the atmosphere (ft/sec)
D	$=$	diameter of the nozzle exit (ft)
D_e	$=$	effective diameter of the nozzle exit $= \sqrt{N}\, D$
T	$=$	thrust per engine (lbs)
g	$=$	gravitational constant (ft/sec^2)
N	$=$	number of engines
f	$=$	frequency (Hz)
f_c	$=$	center frequency of the octave band of interest (Hz)
$X_0\,(f)$	$=$	apparent source distance (from Figure 16), (ft)
X	$=$	is the distance between the engine nozzle plane and the vehicle position of interest (ft)
$R(f) = \sqrt{X_0^2\,(f) + X^2}$		distance from the source of a given frequency to the vehicle station (ft)

Procedure

The octave band sound pressure level near the vehicle can be obtained by using the following equation:

$$\text{OB SPL} = 10 \log_{10} (\text{DSF}) - 10 \log_{10} \left[\frac{2V_e \dot{\omega}}{\rho_0 C_0 DT^2 gN} \right]$$

$$- 20 \log_{10} R(f) + 10 \log_{10} f_c + 126 \quad (dB)$$

where the dime. ·nless spectral function (DSF) is given in Figure 15, and the distance function R (f) can be determined from Figure 16.

The curves given with this prediction technique are usable only for deflected supersonic flows, i.e., while the vehicle is on-pad or being statically fired. This restriction is chosen because it represents the most severe rocket noise environment as far as the vehicle is concerned. For the special case of strap-on rockets, the acoustic output of the strap-on rockets should be estimated separately, and then be added to the noise field produced by the main booster stage.

3.0 SPECIAL EFFECTS

Deflector Geometry

One of the most significant characteristics of rocket noise radiation is its directivity pattern. For an undeflected rocket exhaust flow, the maximum acoustic radiation is in a direction between 50 to 60 degrees from the downstream flow direction. The acoustic intensity remains relatively high up towards 90°, and then decreases significantly as the direction progresses from 90° towards 180°, the direction of flight. This effect is responsible mainly for the remarkable sound intensity profile at launch.

The sound pressure level on the vehicle begins to build up rapidly after ignition. Within a few seconds after liftoff, the overall sound pressure level reaches a peak and then starts to decline sharply. It has been observed that the overall SPL on the vehicle drop; is much as 25 dB in 9 to 10 seconds (Reference 4). The physical explanation is relatively simple. After ignition, the rocket engine rapidly reaches full power, therefore, the noise level begins to build up. When the launch vehicle is on the launch pad, or shortly after lift off, the jet exhaust flow is deflected to a direction parallel to or inclined above the ground plane. The launch vehicle thus receives a significant amount of acoustic power from the exhaust. Within a few seconds after liftoff, the rocket nozzle exit plane draws away from the deflector. Thus, most of the noise returns to the vehicle at a 180° directivity instead of less than 90°, and the SPL at the vehicle drops sharply from its peak value. It is, therefore, the deflector geometry which has a first order effect on the rocket exhaust noise environment surrounding the vehicle. The deflector geometry also has a secondary eff· t on the rocket noise environment. After the exhaust is deflected by a deflector,

the mixing process of the exhaust flow is somewhat modified. According to a scale model study of the deflector geometry effect by Cole, et al. (Reference 20), it was found that deflectors which diffuse the flow rapidly also produce lower power levels, with a conical deflector showing the lowest PWL. Some of these results are shown in Figure 17. It was found also that the near field sound pressure levels are increased by about 5 dB if the nozzle exit plane is within three nozzle exit diameters from the deflectors. These conclusions have been confirmed by measurements taken during Saturn static tests and launches (References 6 and 21).

If the rocket exhaust were divided into two streams by a wedge, or four streams by a spike, an estimate of the sound field environment produced by each of these streams should be made separately and then combined to give the total sound field. The overall sound power spectrum is not affected significantly by the splitting, however, the directivity pattern and local spectrum in various regions in the far field may be very complex. Fortunately, this directional effect does not have very much influence on the mid-field environment surrounding the vehicle itself. This effect is, thus, of little significance for payload/shroud systems.

Effects of Coolant Water

Theoretically, the rocket exhaust noise can be reduced by 15 dB or 20 dB by injecting a large amount of water at the launch pad to quench the exhaust flow. However, a water mass flow rate of more than ten times the propellant flow rate is required to achieve significant reductions. The existing water spray arrangements at the launch pads are primarily for cooling purposes only and have a negligible effect on the acoustic environment.

Launch Acoustic Measurements

It was emphasized at the beginning of this section that the directivity of the rocket exhaust noise has a dominant effect on the noise profile around the launch vehicle. Thus, caution must be exercised in the interpretation of acoustic measurements obtained from microphones which are not located on the vehicle structure. A specific case in point is acoustic data obtained from measurements on the launch umbilical tower. The time history of the noise environment recorded by a microphone on the umbilical tower may differ drastically from those recorded by microphones on the launch vehicle. However, if a microphone on the tower were located near the shroud, its measurements of noise environment before lift off and one or two seconds after liftoff would resemble closely the acoustic environment experienced by the shroud itself. Thus, these tower microphone measurements should be used only with caution and the conditions under which measurements were taken must be carefully evaluated.

4.0 SURFACE PRESSURE CORRELATIONS

A necessary preliminary to any study of structural response of a vehicle to a random pressure field is the calculation of the surface pressure correlation function or its Fourier transform. It is known that, for a three-dimensional diffuse field without the structure present, the pressure correlation function is of the form $\sin kr/kr$, where r is the spatial separation, and k is 2π divided by the wave length. For a plane wave, the correlation function is simply $\cos k(x - x')$, where x is in the direction of wave propagation. However, the pressure correlation function will be changed in the presence of the vehicle due to diffraction effects.

Dyer discussed in Reference 14 some pressure correlation results determined from measurements along a missile surface. The longitudinal and angular correlations are shown in Figures 8 and 9 in the main body of the report. Dyer found that the longitudinal correlation agreed very well with $\cos k(x - x')$, the correlation function for a plane wave, for small non-dimensional separation distances. The angular correlation function shown in Figure 9 is plotted versus $ka(\phi - \phi')$. Since the structural radius is a, then $a(\phi - \phi')$ is the circumferential separation on the missile surface. Thus it can be seen that for a given separation, angular correlation is equal to or greater than the longitudinal correlation. Dyer interpreted this result as follows; consider the largest separation possible in the circumferential direction, to be $a\pi$, i.e., observation points on opposite sides of the missile. At low frequencies, the sound source is centered relatively far down stream of the nozzle, consequently the noise reaching the missile appears to originate from a single source point, rather than from the volume distribution of the source. Thus the pressure signals separated by $a\pi$ are still correlated. At high frequencies, the sound source is centered relatively close to the nozzle. Thus the noise propagating along opposite sides of the missile originates from different portions of the noise source, and because the high frequency noise follows essentially straight-line paths, the signals are uncorrelated.

The surface pressure correlation for a cylinder in a three-dimensional diffuse sound field has been computed theoretically by Wenzel in Reference 22. It was found that the longitudinal correlation function shown in Figure 18 follows closely the function $\sin kr/kr$ as expected from a diffuse field in the absence of a cylinder. However, the circumferential correlation, also shown in Figure 18 falls considerably below the free field correlation function, especially at low frequencies.

In the mid-field, the peak octave band sound pressure level occurs near a Strouhal number of 0.1. By considering that the shroud diameter is approximately the same as the effective diameter of the first stage rocket engines, the peak wavelength will be about twice the shroud diameter. Hence, most of the acoustic pressure functions are well correlated. Although the rocket exhaust flow may be deflected with respect to the ground plane, the directional effect in the low frequency range is not significant. On the other hand, if the acoustic environment of the shroud were simulated by a diffuse field, then, by comparing the results of Dyer and Wenzel, the simulated correlation length may be smaller than the actual correlation occurring in the launch environments. The effect of correlation length on the structural response can be verified by experiment

or structural analysis. For rockets having strap-on configurations, such as the Titan IIIC, the rocket nozzles are widely separated. Each exhaust flow produces its sound field independently. According to the method of computing the effective diameter, it is found immediately that the peak frequency is at least half an octave higher than a rocket with a clustered set of engines producing the same thrust and mechanical power. The sound source region is also more diverse. Qualitatively, the correlation function may resemble the correlation function for a diffuse sound field.

The mid-field pressure correlation function on a vehicle for a given launching configuration has been predicted by Potter (Reference 23). In this method, the noise for a given frequency is assumed to originate from an apparent source location in the exhaust stream. The wave front spreads out spherically and when it arrives at the vehicle, it is practically a plane wave with a definite angle of incidence. According to the classical theories of diffraction around a cylinder, a correlation function for this particular wave length can be computed. The details of this computation have been reported in Reference 23. An approximate procedure for estimating the narrow band space-correlation coefficients, based upon the work reported in Reference 23 is discussed in greater detail in Section 3.2.1 in the main body of the report.

REFERENCES

1. Cole, J.N., et al., "Noise Radiation from Fourteen Types of Rockets in the 1000 to 130,000 Pound-Thrust Range," WADC TR 57-354 (Dec. 1957).

2. Franken, P.A., and Wiener, F.M., "Estimation of Noise Levels at the Surface of a Rocket-Powered Vehicle," Shock and Vibration Bull. No. 31, Pt. 3, pp. 27-31, 1963.

3. Wilhold, G.A., et al., "A Technique for Predicting for Field Acoustic Environments Due to a Moving Rocket Sound Source," NASA TN D-1832, 1963.

4. Wilhold, G.A., et al., Private Communication, 1970.

5. Cole, J.N., et al., "Acoustic Noise and Vibration Studies at Cape Canaveral Missile Test Annex, Atlantic Missile Range," WPAFB ASD Tech Report TR 61-608, December 1962.

6. Peverley, R. W. and Smith E. B., "A Practical Method of Predicting the Acoustical Dynamic Environment for Large Booster Launch Facilities," Shock and Vibration Bull. No. 33, Pt. 2, pp. 89-101, 1964.

7. Dorland, W. D. and Tedrick, R. N., "Results of Acoustical Survey of SA-1 Launch," MTP- Test - 62-2, March 1962.

8. Dorland, W. D. and Tedrick, R. N., "Results of Acoustic Survey of SA-2 Launch," MTP - Test - 62-5, August 1962.

9. Cummings, N., et al., "Results of Acoustical Survey of SA-3 Launch," MTP - Test - 63-2, February 1963.

10. Dyer, I., "Distribution of Sound Sources in a Jet Stream," J. Acoust. Soc. Am. 31, 1016-1021, 1959.

11. Morgan, W.V., and Young, K.J., "Studies of Rocket Noise Simulation with Substitute Gas Jets, and the Effects of Vehicle Motion on Jet Noise," Wright Patterson Air Force Base, ASD-TDR-62-787, 1962.

12. Mull, H.R., and Erickson, J.C. Jr., "Survey of the Acoustic Near Field of Three Nozzles at a Pressure Ratio of 30," NACA-TN-3978, 1957.

13. Howes, W.L. and Mull, H.R., "Near Noise Field of a Jet Engine Exhaust, I - Sound Pressures," NACA TN 3763, 1956.

14. Dyer, I., "Estimation of Sound Induced Missile Vibration," Ch.9, - "Random Vibration," ed. S.H. Crandall, MIT Press, 1958.

15. Potter, R. C. and Crocker, M. J., "Acoustic Prediction Methods for Rocket Engines, Including the Effects of Clustered Engines and Deflected Exhaust Flow," NASA CR-566, 1966.

16. Tedrick, R. N., "Acoustic Measurements of Static Tests of Clustered and Single-Nozzled Rocket Engines," JASA, Vol. 36, No. 11, November 1964.

17. Mayes, W. H., et al., "Near Field and Far-Field Noise Surveys of Solid Fuel Rocket Engines for a Range of Nozzle Exit Pressures," NASA TN-D-21, 1959.

18. Eldred, K.M., et al., "Suppression of Jet Noise, with Emphasis on the Near Field," Wright Patterson Air Force Base, ASD-TDR-62-578, 1963.

19. Sutherland, L.C., ed. "Sonic and Vibration Environments for Ground Facilities - A Design Manual," Wyle Laboratories Research Staff Report WR 68-2, 1968.

20. Cole, J.N., et al., "Effect of Various Exhaust Blast Deflectors on the Acoustic Noise Characteristics of 1000 Pound Thrust Rockets," Wright Patterson Air Force Base, WADD-TR-60-6, 1960.

21. Wiener, F.M., "Rocket Noise of Large Space Vehicles," the Fourth International Contress on Acoustics, Congress Report II, pp. 209-230, 1962.

22. Wenzel, A.R., "Pressure Correlation for a Cylinder in a Diffused Sound Field," J. Acoust. Soc. Am. Vol. 41, pp. 1459-1466, 1967.

23. Potter, R.C., "Correlation Patterns of the Acoustic Pressure Fluctuations on the S-IC Vehicle Due to the Exhaust Noise at the Test and Launch Hand," Wyle Research Report WR 66-15, 1966.

24. Franken, P. A. "Methods of Space Vehicle Noise Prediction," WADC Tech. Report 58-343, Vol. 2, September 1960.

25. Smith, E. B. and Brown, W.L., "Acoustic Scale-Model Tests of High-Speed Flows," Phase II Final Report, Martin-Marietta Corporation Report CR-66-75, 1966.
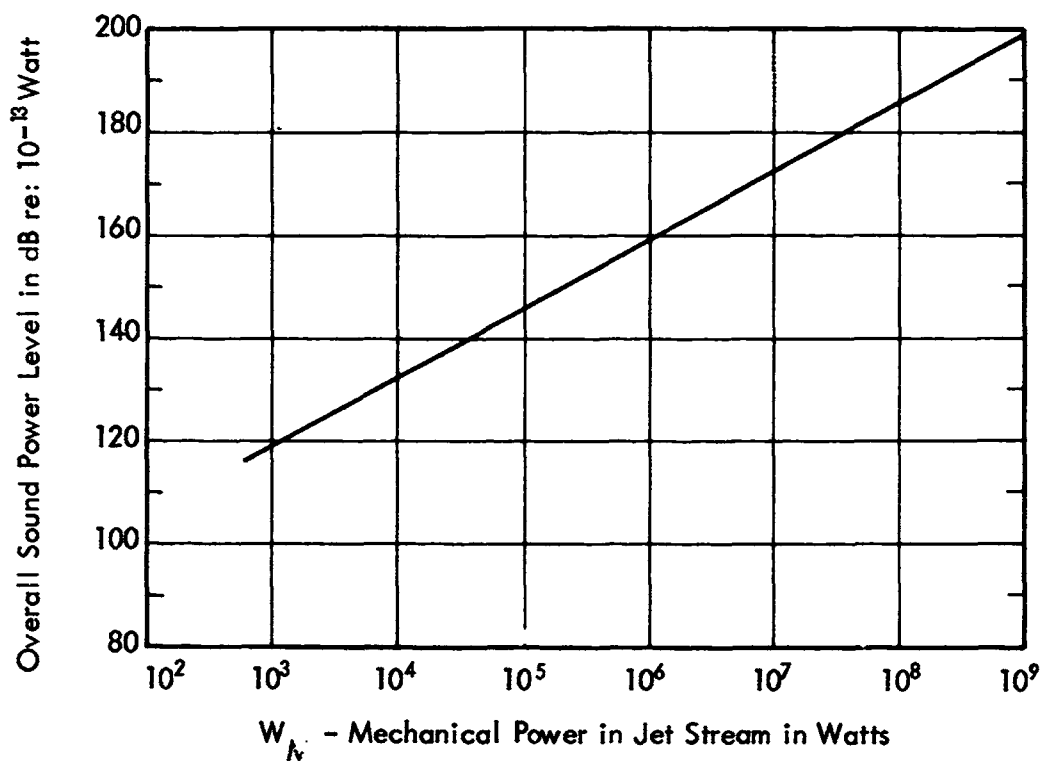
Figure 1. Correlation of Overall Acoustic Power Level to Mechanical
Power in the Jet Stream (Reference 1)

230
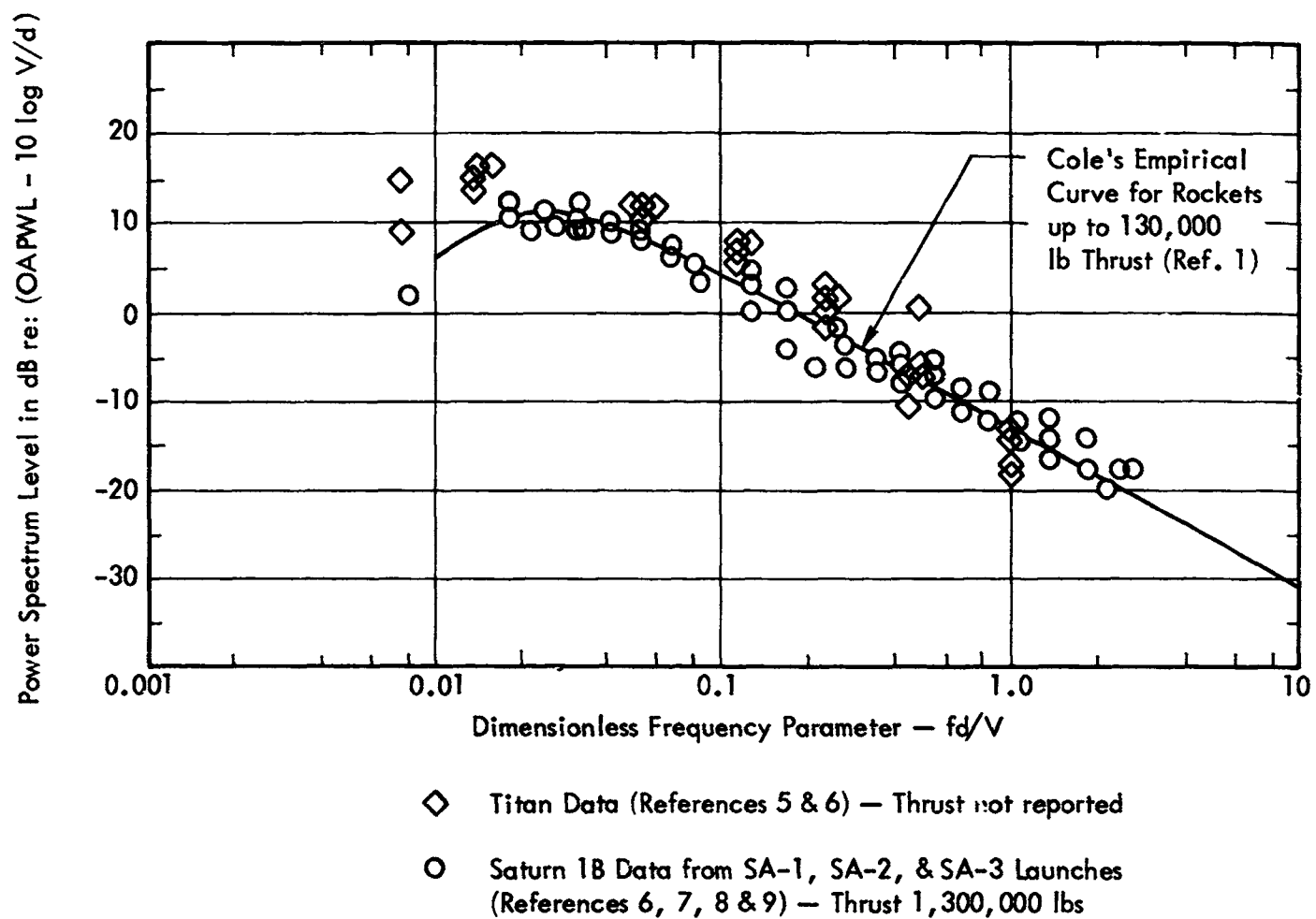
Figure 2. Generalized Constant Bandwidth Power Spectrum of Rocket Noise
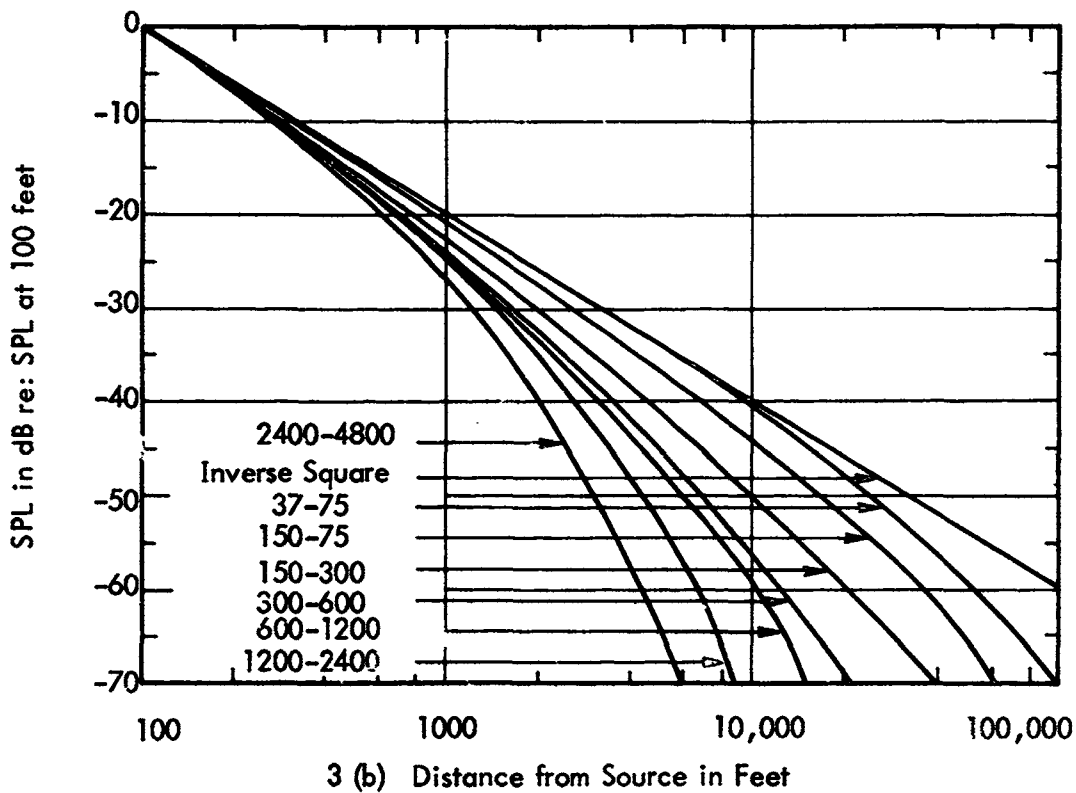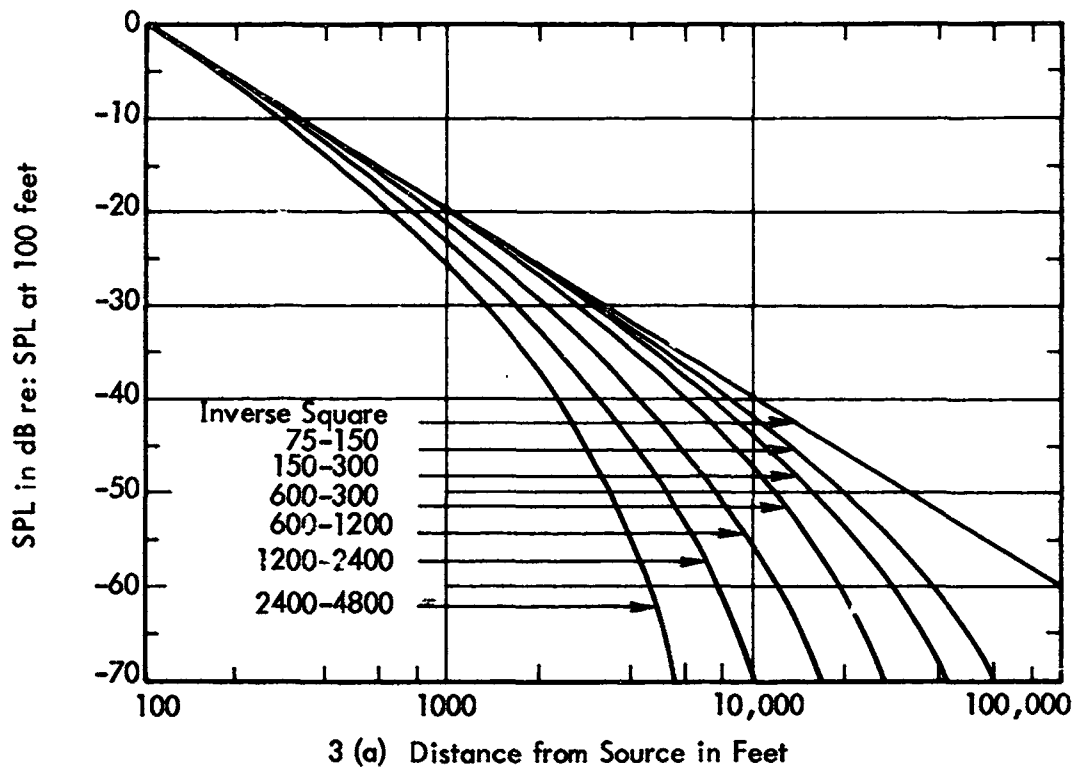
Figure 3. Reduction of Sound Pressure Level with Distance for (a) Air to Ground Propagated Sound and (b) Ground to Ground Propagated Sound (Reference 1)

232
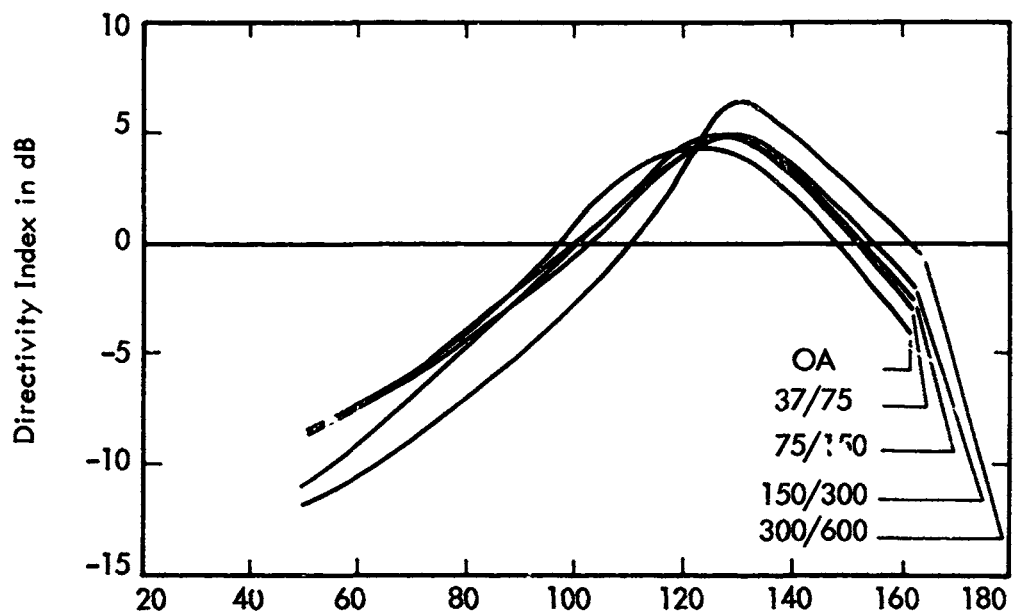
4(a) Angle θ in Degrees from Forward End of Rocket
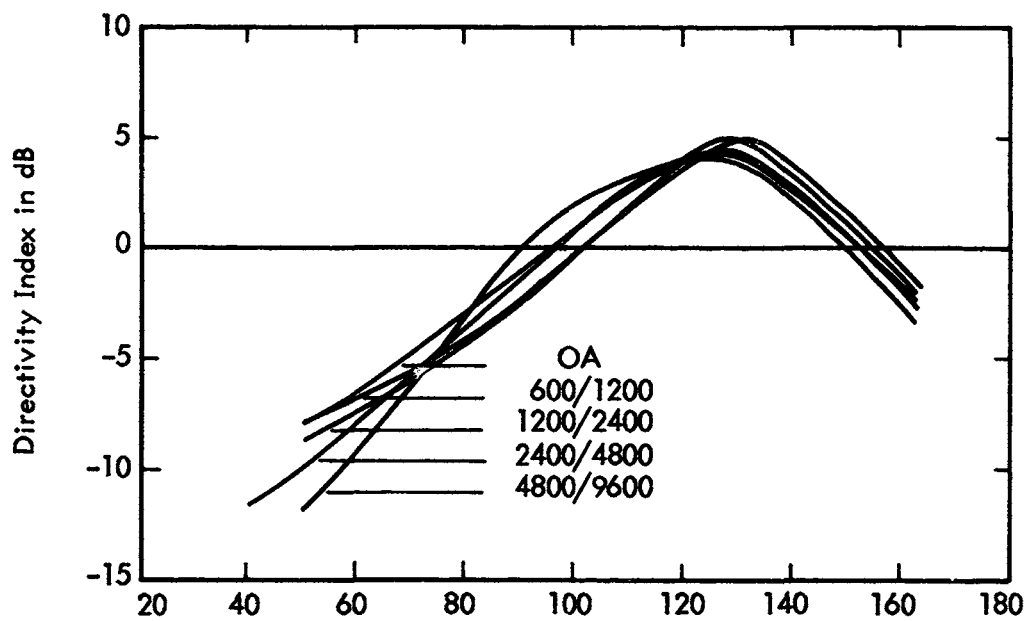
4(b) Angle θ in Degrees from Forward End of Rocket

Figure 4. Generalized Directivity Indices (Reference 1)

233
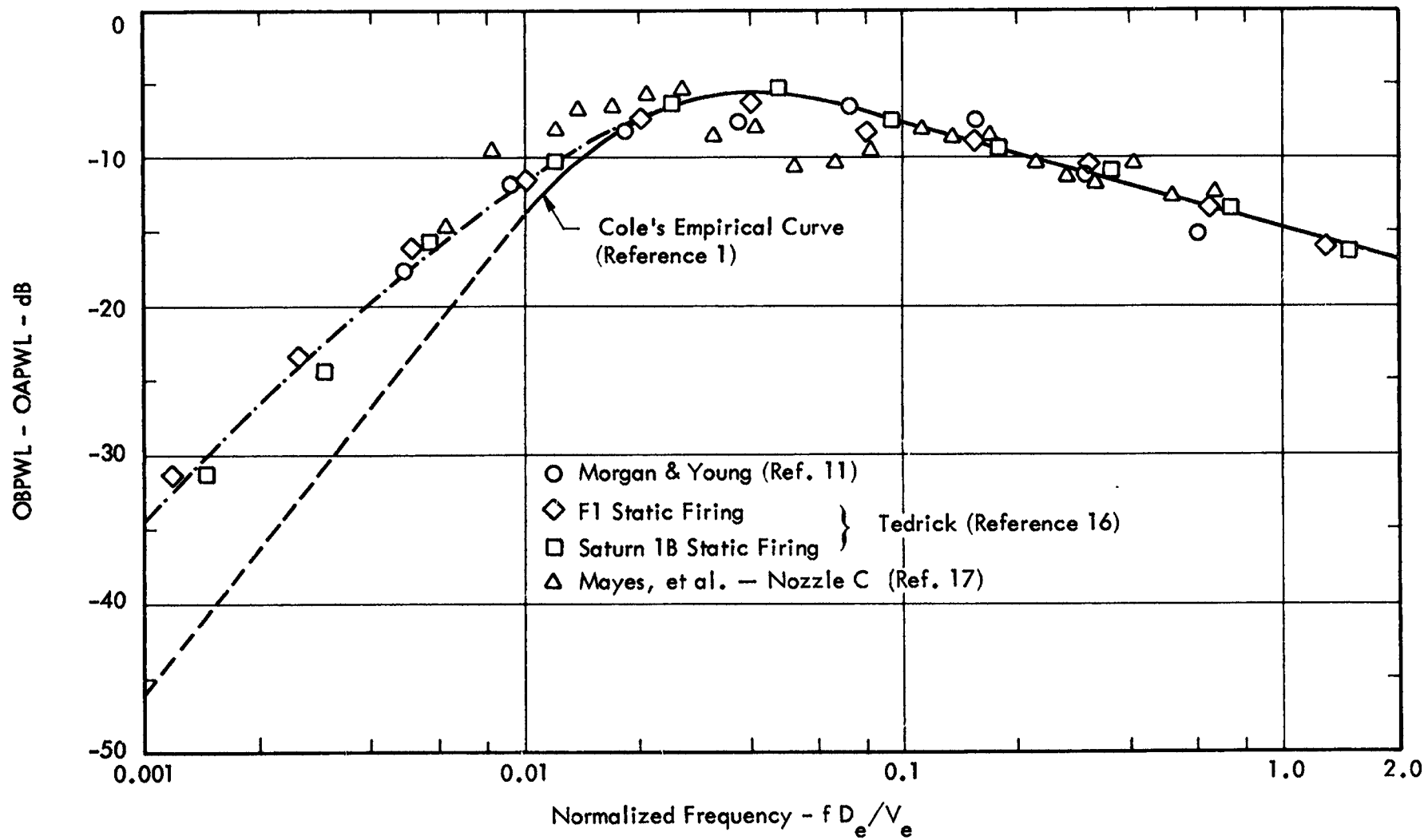
Figure 5. Normalized Octave Band Spectrum of Acoustic Power
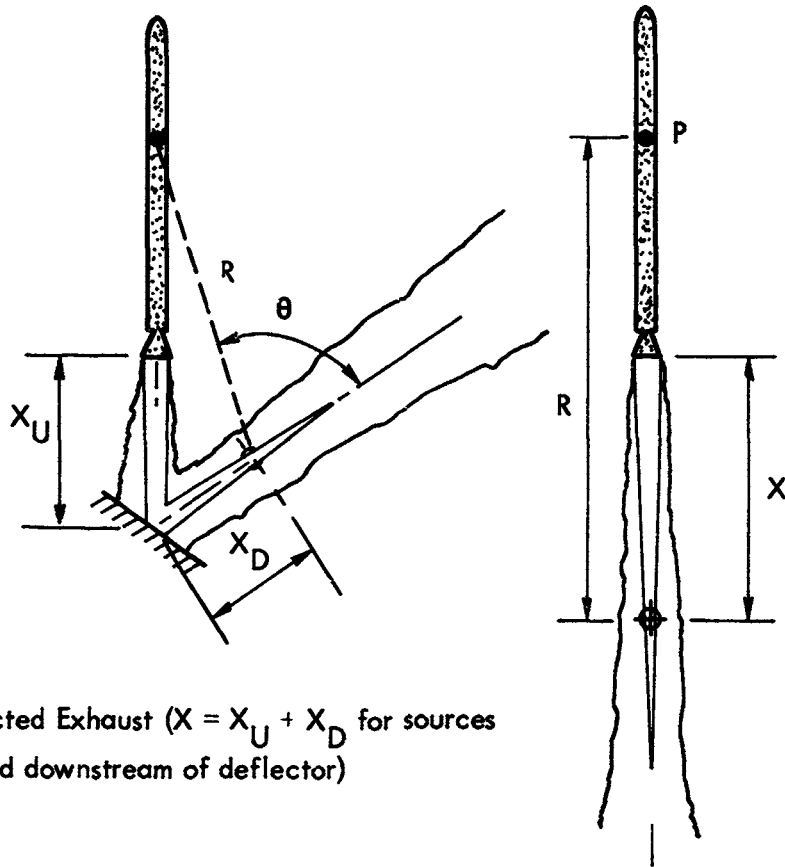
a). Deflected Exhaust ($X = X_U + X_D$ for sources located downstream of deflector)

b) Undelfected Exhaust ($\theta \simeq 180$)

Figure 6. Noise Source Location Geometry

235
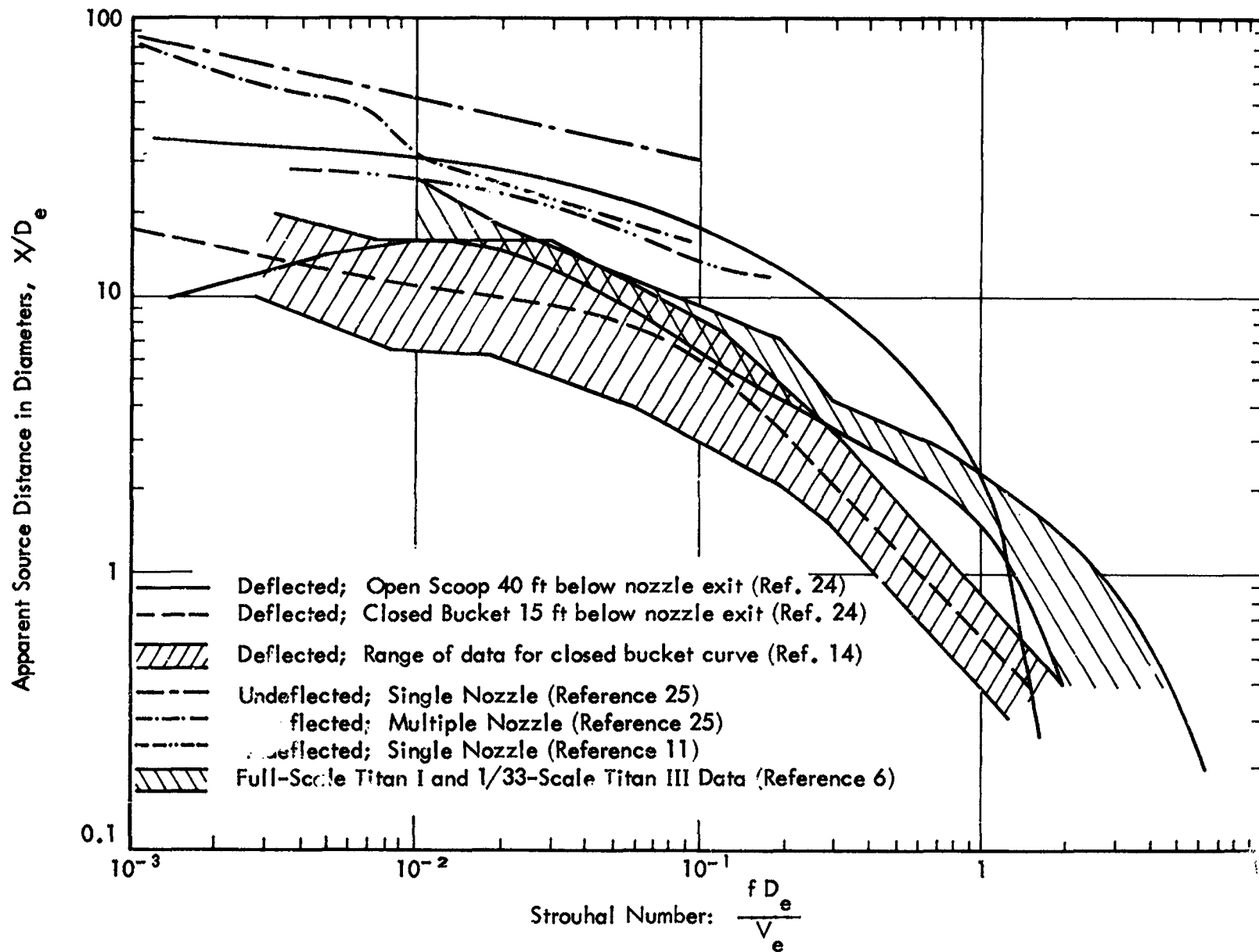
Figure 7. Apparent Source Distribution in a Rocket Exhaust Flow

The chart contains the following axes and legend:

Y-axis: Apparent Source Distance in Diameters, X/D_e

X-axis: Strouhal Number: $\dfrac{f D_e}{V_e}$

Legend:
- Deflected; Open Scoop 40 ft below nozzle exit (Ref. 24)
- Deflected; Closed Bucket 15 ft below nozzle exit (Ref. 24)
- Deflected; Range of data for closed bucket curve (Ref. 14)
- Undeflected; Single Nozzle (Reference 25)
- flected; Multiple Nozzle (Reference 25)
- eflected; Single Nozzle (Reference 11)
- Full-Scale Titan I and 1/33-Scale Titan III Data (Reference 6)

Figure 8. Directivity Curves

Curve Number	1	2	3	4	5	6	7	8	9	10	11
Octave Band Center Frequency Hz.	2	4	8	16	32	64	125	250	500	1,000	2,000
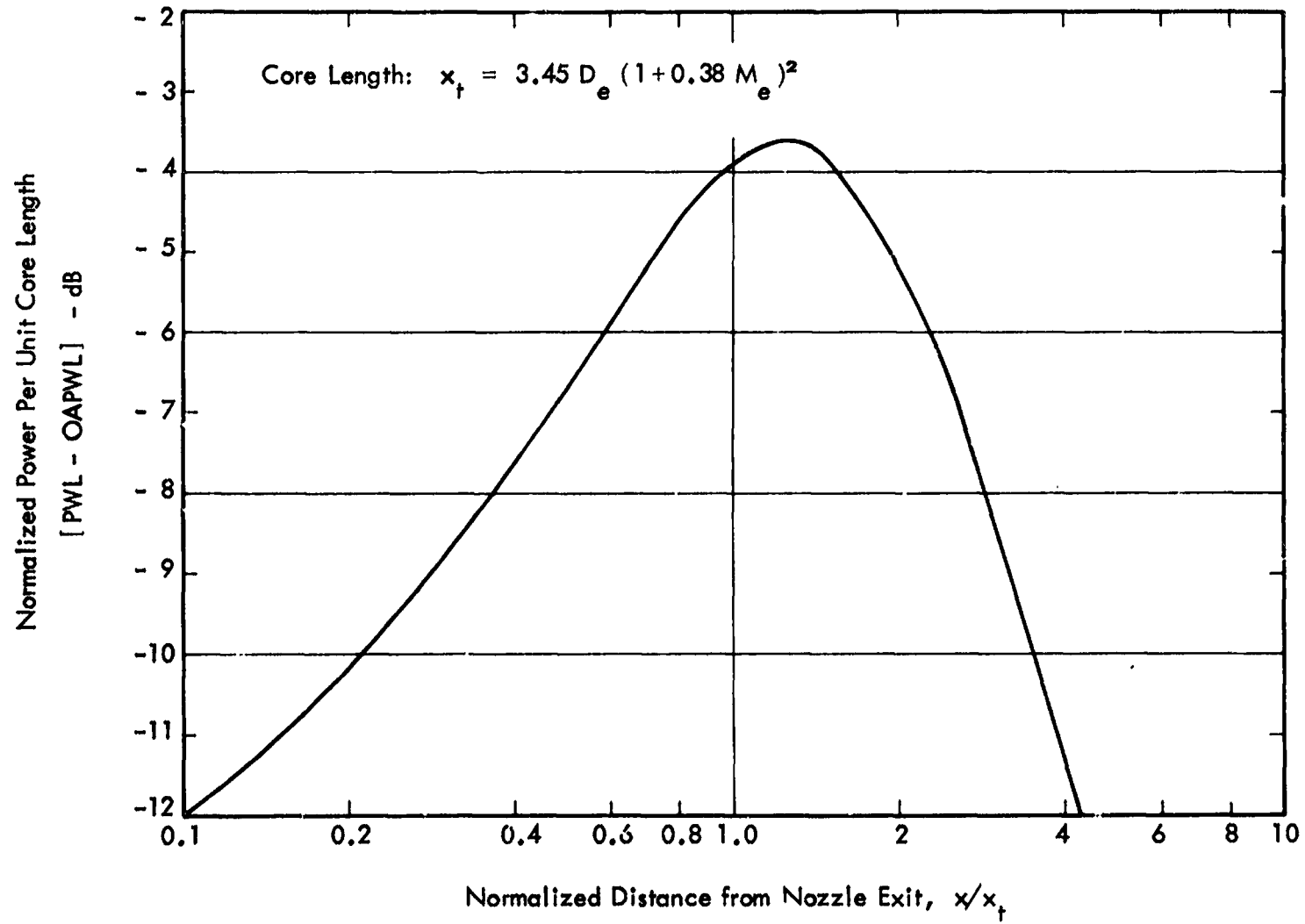
Figure 9. Acoustic Power Produced Per Unit Core Length (from Reference 23)
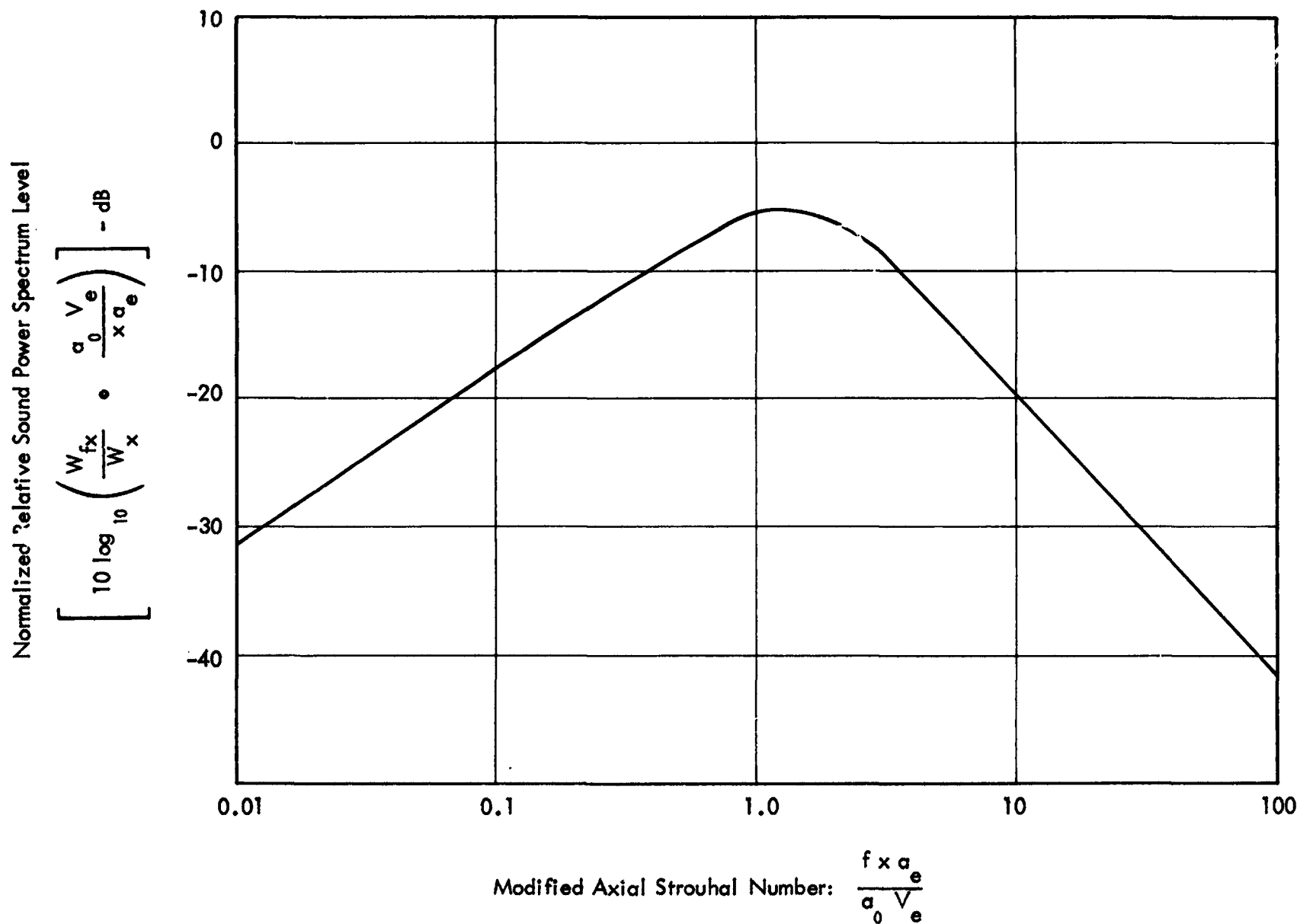
Figure 10: Normalized Power Spectrum with Distance Downstream; from Reference 15

The y-axis is labeled: Normalized Relative Sound Power Spectrum Level $\left[10 \log_{10} \left(\dfrac{W_{fx}}{W_x} \cdot \dfrac{a_0 \, V_e}{x \, a_e} \right) \right] - dB$

The x-axis is labeled: Modified Axial Strouhal Number: $\dfrac{f \times a_e}{a_0 \, V_e}$
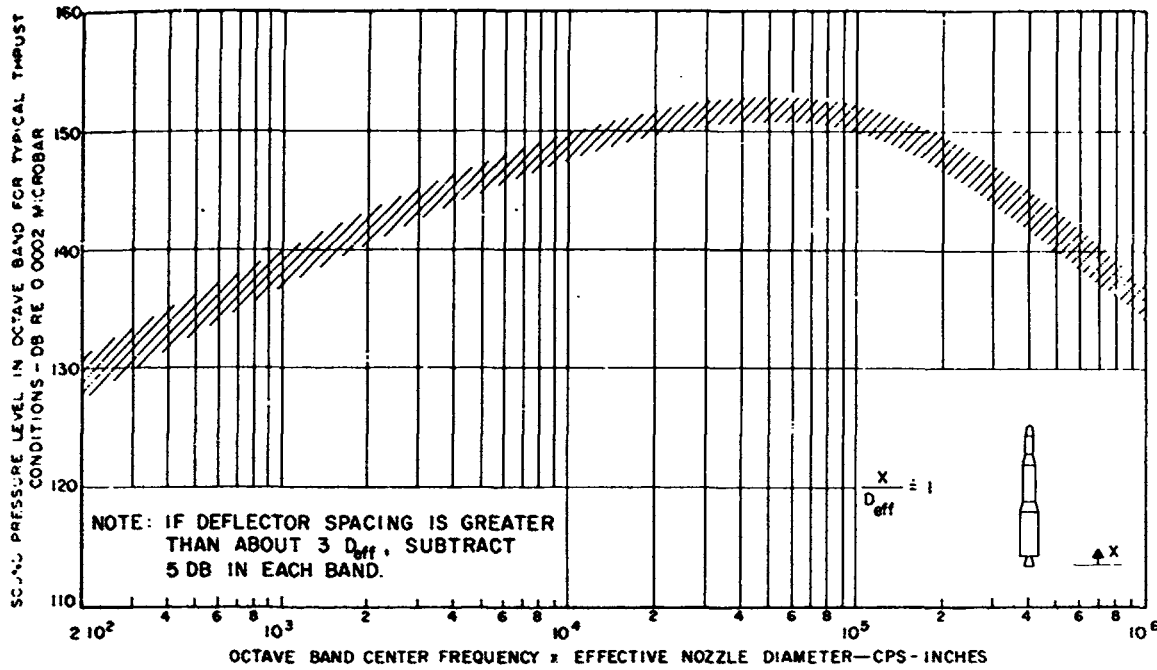
Figure 11. Sound Pressure Levels Near Tail Section of Space
Vehicle-Static Test or Before Lift-off (Reference 2)
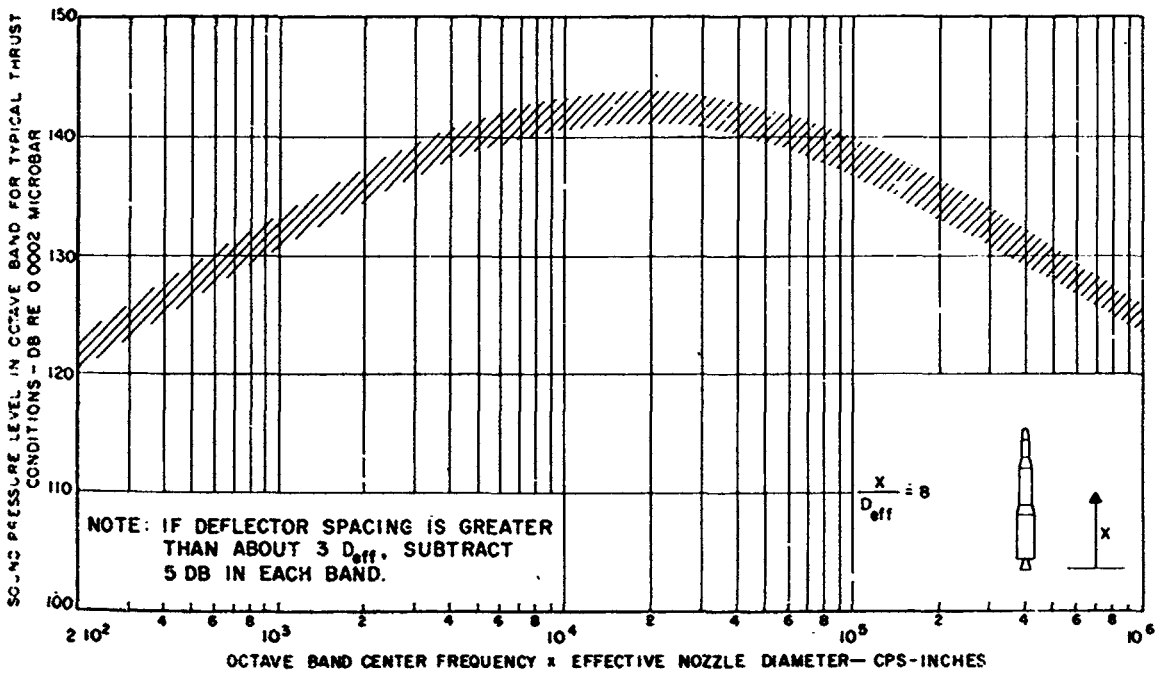
Figure 12. Sound Pressure Levels Halfway Along Length of Space
Vehicle-Static Test or Before Lift-off (Reference 2)

240
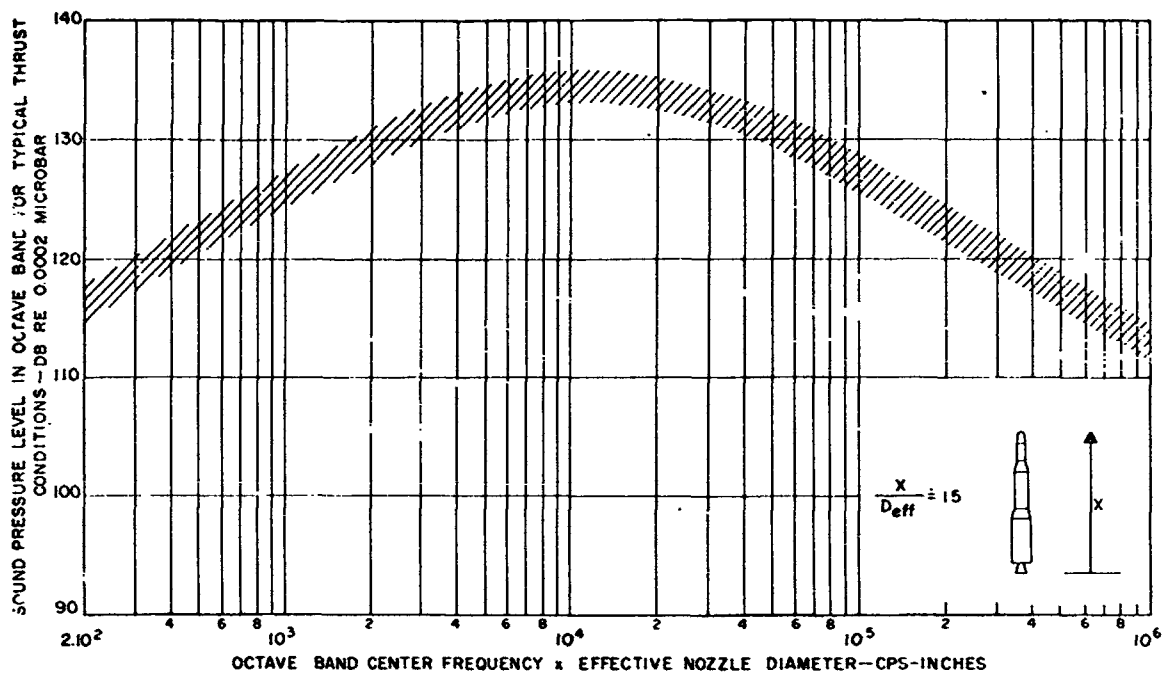
Figure 13. Sound Pressure Levels Near Nose of Space Vehicle-Static
Test or Before Lift-off (Reference 2)

241
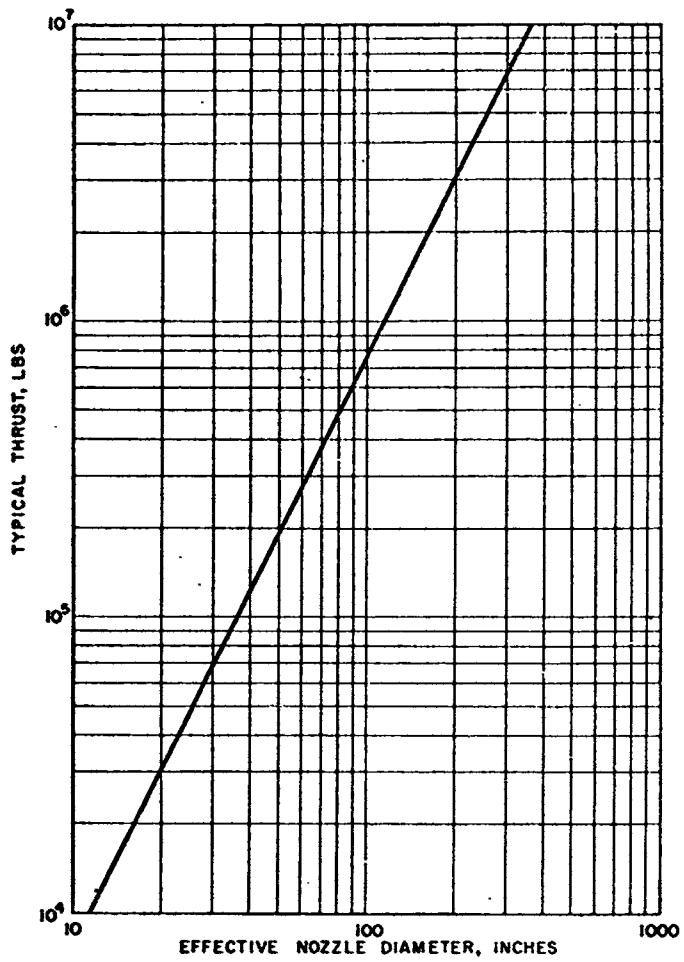
Figure 14. Relationship Between Typical Thrust and
Effective Nozzle Diameter (Reference 2)
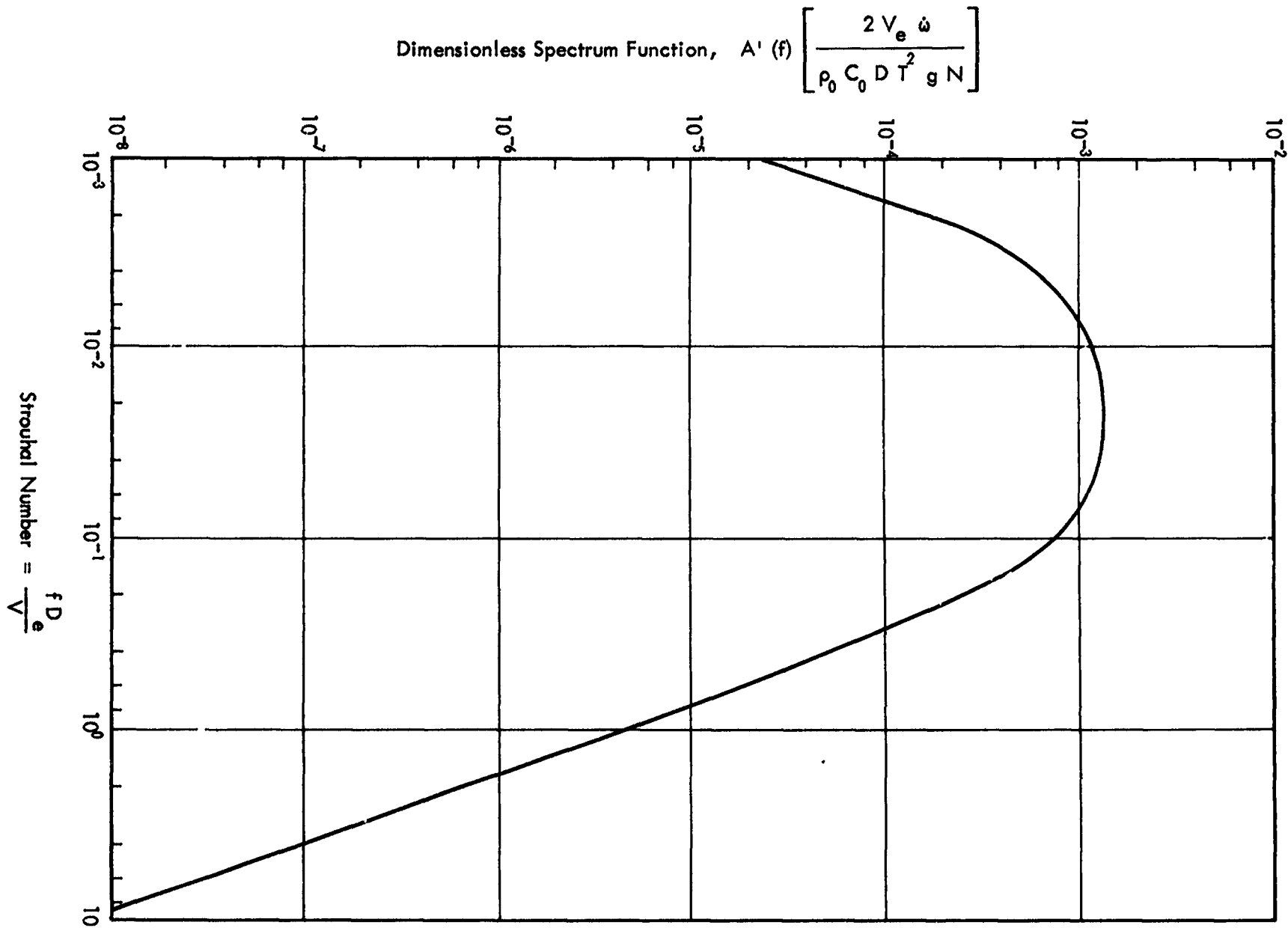
Figure 15. Non-Dimensional Spectrum Function Versus Strouhal Number (References 3 and 4)

243
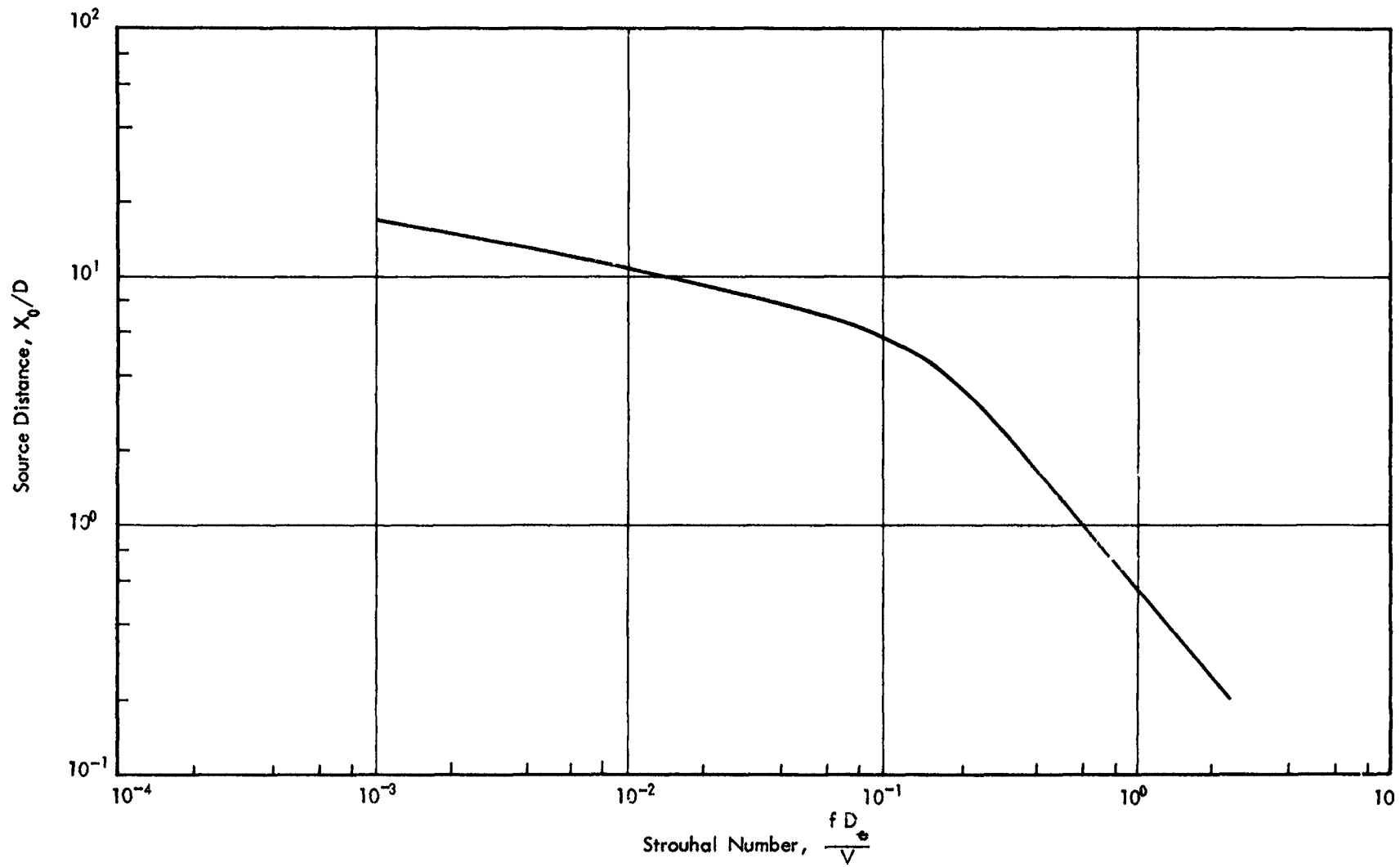
Figure 16. Non-Dimensional Apparent Source Distance Versus Strouhal Number (References 3 and 4)
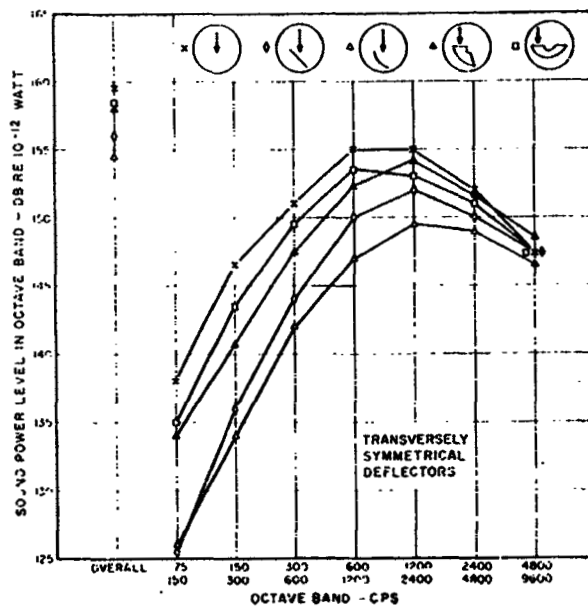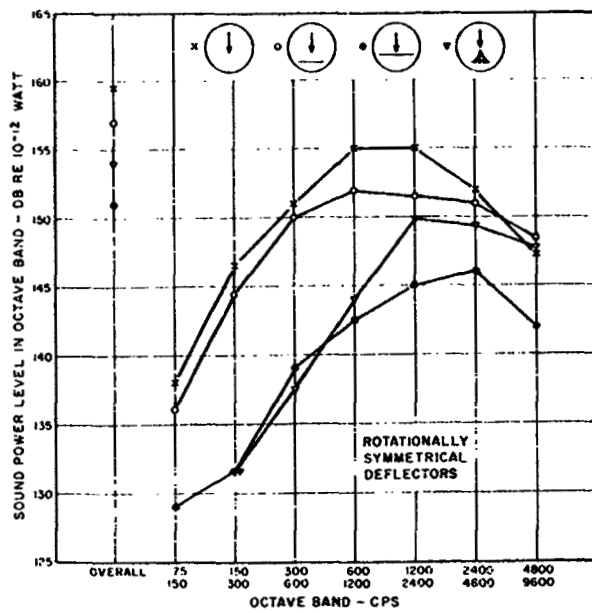
Figure 17. Experimental Results Showing the Effect of Various Exhaust Deflectors on the Sound Power Radiated by a Small (1000 lb thrust) Rocket Engine (Reference 20)

245
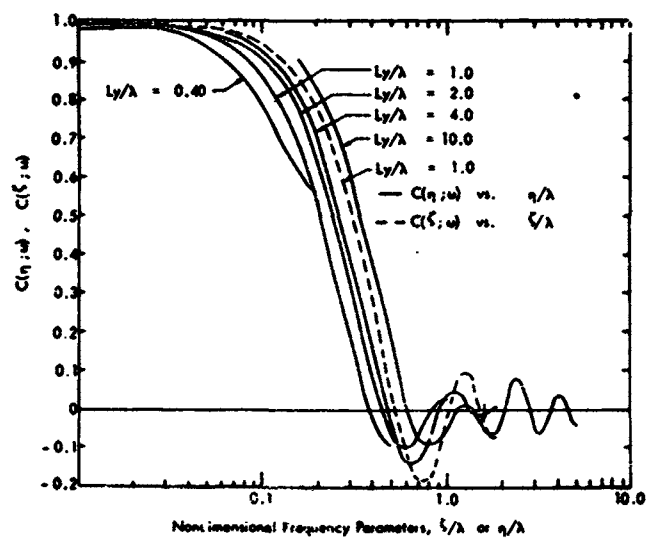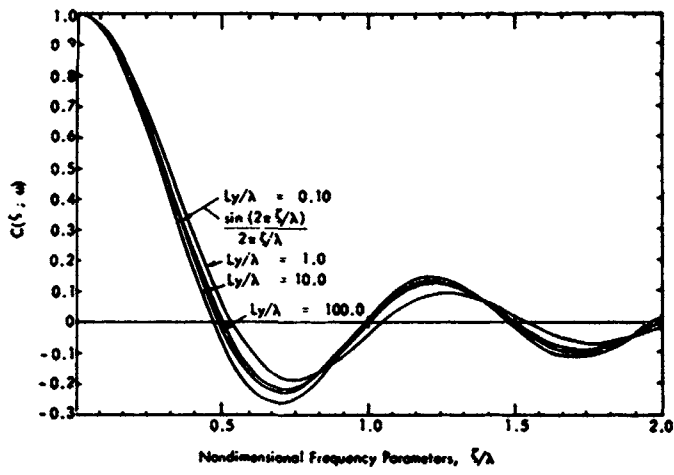
Figure 18. Narrow-Band Longitudinal and Lateral Space Correlation Coefficient
on Surface of a Cylinder Immersed in a Reverberant Acoustic Field
(Reference 22)

246

APPENDIX B

PREDICTION OF IN-FLIGHT FLUCTUATING PRESSURE ENVIRONMENTS

1.0 INTRODUCTION

When a vehicle moves through air there are two basic means by which it can produce noise: (1) by its propulsion mechanism (motor-jet, rocket, etc.,) and (2) by its interaction with its surroundings. At low speeds, for example, during and immediately after lift-off, the first of these is by far the dominant one while near or above the speed of sound, mechanism (2) becomes most important.

During any flight cycle for an aerospace vehicle, there are three important phases of the flight which should be investigated in order to assess the structural loading due to fluctuating pressures. These are listed in the chronological order in which they occur.

- Lift-off phase during which acoustic excitation results from the rocket exhaust noise.

- Launch flight to orbit phase, during which rocket exhaust noise diminishes and aerodynamic fluctuating pressures (pseudo-sound) starts to dominate. From an aerodynamic noise viewpoint, this phase becomes most critical at transonic Mach numbers $(0.60 \leq M \leq 1.6)$

- Re-entry phase during which only aerodynamic fluctuating pressures are present.

This Appendix is devoted to the specification of surface fluctuating pressures resulting from unsteady aerodynamic phenomena during the launch phase of flight. Aerodynamic fluctuating pressures (pseudo-sound) are zero at launch and increase to peak values as the vehicle passes through the transonic Mach number range. Previous wind tunnel and flight data show that fluctuating pressures are proportional to free-stream dynamic pressure q_∞ $(= \gamma P_\infty M_\infty^2 / 2$, where γ is the ratio of specific heats, P_∞ is the free-stream static pressure, and M_∞ is the free-stream Mach number) for a given unsteady flow phenomenon. However, peak fluctuating pressures do not necessarily occur at maximum q_∞ for certain regions of a vehicle due to the non-homogeneous nature of the flow field. For example, regions of the vehicle exposed to separated flow and the impingement of oscillating shock waves will experience fluctuating pressures at least an

order of magnitude greater than regions exposed to attached flow. Thus, if separated flow and oscillating shock waves are present, say at Mach numbers other than the range of maximum q_∞, then peak fluctuating pressures will also be encountered at conditions other than at maximum q_∞. Thus, it is easily seen that vehicle configuration is very important in the specification of fluctuating pressure levels since the source phenomena are highly configuration dependent in addition to varying with Mach number and angle of attack.

In light of the foregoing discussion, one general statement can be made in regard to aerodynamic fluctuating pressures. Regions exposed to the same unsteady phenomenon will experience fluctuating pressure levels which are proportional to free-stream dynamic pressure. Thus, it can be readily seen that a fundamental parameter in the specification of the surface excitation is free-stream dynamic pressure and its variation with Mach number. For a given configuration, Mach number and angle of attack define the phenomena, and dynamic pressure defines the fluctuating pressure levels associated with the phenomena.

Unsteady aerodynamic flow and the attendant fluctuating pressures experienced by aerospace vehicles naturally depend on the flight environments and the geometry of the vehicle. There are an infinite number of possible configurations and any discussion of their fluctuating pressure environment must be general. Practically all experimental data for unsteady aerodynamic flow have been acquired for bodies of revolution which are typical of missile configurations. As a result of these studies, it is well known that certain basic unsteady flow conditions will occur regardless of the detailed geometry of the vehicle. The occurrence of these basic fluctuating pressure phenomena and their statistical properties can be predicted quite accurately. It is convenient to discuss these basic flow conditions for bodies of revolution; however, this is certainly no restriction on either the feasibility or the practicality of predicting their occurrence on more complicated configurations. Thus, in the following paragraphs, general features of typical bodies of revolution are defined and the unsteady flow fields which they encounter are discussed. Furthermore, aerospace vehicles may have a number of protuberances projecting from their surface in which case the flow field is complicated

by the super-position of the protuberance flow field onto the flow field of the basi.
structure. Most protuberances are three-dimensional projections and general charac-
teristics of these flows should be considered as separate and unique problems.

2.0 BASIC FLUCTUATING PRESS RE PHENOMENA

Examples of several bodies of revolution are shown in Figure 1. For the purpose of
the present discussion, three basic configurations will be considered as specified
below:

- Cone-cylinder shroud
- Cone-cylinder-flare shroud
- Cone-cylinder-boattail shroud

Virtually all axisymmetric vehicles fall into one of these categories although numerous
modifications to the basic geometry have been employed in the past.

Several fluctuating pressure environments having different statistical properties may
exist over a vehicle at any given instant in the flight trajectory. It is convenient to
consider three separate Mach number ranges — subsonic, transonic, and supersonic —
for each of the three basic shroud configurations. Further, the flow fields will depend
on the angle of attack of the vehicle which causes nonsymmetrical loading (both
statically and dynamically); however, for the purpose of this discussion, non metri-
cal loading will not be discussed.

Schematics of subsonic, transonic and supersonic flow fields for the basic configurations
are shown in Figure 1. At subsonic speeds, all three configurations experience regions
of attached flow and separated flow. The cone-cylinder portion of each configuration
induces separated flow immediately aft of the cone cylinder juncture for cones having
half-angles greater than approximately 15 degrees. Re-attachment occurs within
approximately one diameter aft of the shoulder (depending on cone angle) for the cone-
cylinder and boattail configurations, whereas for the flare body, separation may con-
tinue over the flare. Both the flare and boattail induce separation for typical config-
urations. At high transonic speeds, the flow negotiates the shoulder of a cone-cylinder

251

body without separating, reaches supersonic speed immediately aft of the shoulder and produces a near-normal, terminal, shock wave a short distance aft of the shoulder. The boundary layer immediately aft of the shock may or may not separate depending on the strength of the shock wave. At transonic speeds, the boattail and flare region produce separated flow which may be accompanied by weak shock waves in the vicinity of the separation and reattachment points. At supersonic speeds, the cone-cylinder configurations produce regions of attached flow. For the flare configuration, the separated flow is bounded by shock waves at the separation and reattachment points, whereas for the boattail configuration, separation occurs at the shoulder of the boat-tail (expansion region) and is bounded at the reattachment point by a shock wave.

It is evident that even simple vehicle shapes, such as cone-cylinders, produce complex and highly nonhomogeneous flow fields at certain Mach numbers — particularly at subsonic and transonic speeds. The unsteady flow phenomena are of particular importance at transonic speeds, since in this range, fluctuating pressures reach maximum values due to their proportionality to dynamic pressure. In order to assess the fluctuating pressure environment of a vehicle of any arbitrary geometry, it is convenient to discuss the statistical properties of the fluctuating pressures for each of the basic types of unsteady flow condition. From Figure 1 it will be noted that the following flow conditions may occur for various regions of a vehicle.

- Attached flow
- Separated flow
- Shock-boundary layer interaction

Each of the above flow conditions exhibits different statistical characteristics. Attached flow pressure fluctuations result from the disturbances within turbulent boundary layers. Separated flow pressure fluctuations result from disturbances within the separated shear layer and instabilities associated with the separation and reattachment points. Pressure fluctuations for shock-boundary layer interaction result from the movement of the shock wave and the static pressure discontinuity associated with the shock wave. The statistical characteristics of each fluctuating pressure environment

252

that are important in the analysis of structural response may be classified under three parameters:

- The overall level
- The power spectrum
- The cross-power spectrum (or narrow band cross correlation)

Each unsteady flow condition with general statistical characteristics will be discussed separately in the following subsections.

2.1 Attached Turbulent Boundary Layers

The surface fluctuating pressures beneath attached turbulent boundary layers have been the subject of both theoretical and experimental study for a number of years. The turbulent boundary layer extends over a considerable portion of the surface of vehicles in flight and, thus, it is considered to be one of the principle sources of aero-acoustic excitation to the vehicle structure. Several years ago, workers such as Kraichman, Lilley, and Hodgson developed theoretical formulations for the fluctuating pressures under turbulent boundary layers and, more recently, several carefully planned experiments have provided additional information on the statistical characteristics of the pertubations. Lowson, Reference 1, presents a good summary of the results of studies on this subject, with the exception of some recent measurements by NASA-Ames. In Lowson's report, the basic mechanism underlying the production of the surface pressure fluctuations beneath turbulent boundary layers is discussed, together with a presentation of empirical and semi-empirical prediction techniques. This section of the present discussion is a brief overview of Lowson's prediction formulae with the exception of the power spectra, which has been modified to be more consistent with the power spectra at low Strouhal numbers. The following discussion presents a review of the experimental results and prediction formulae in terms of the most important statistical parameters.

253

Overall Level

The correct method of presenting overall fluctuating pressure levels for surfaces beneath the convected turbulence in boundary layers is in terms of the root-mean-square fluctuating pressure level, $\sqrt{\overline{p^2}}$. Free-stream dynamic pressure, q_∞, local dynamic pressure, q_ℓ, and wall shear stress, τ_ω, have been used to normalize $\sqrt{\overline{p^2}}$ so that meaningful data collapse can be realized throughout Mach number range. The most generally accepted normalizing parameter is q_∞ and hus, will be used in the current expressions.

The effects of free-stream Mach number, M_∞, on the normalized RMS intensities of the fluctuating pressures in attached flows are shown in Figure 2. There is significant scatter in the data which may be attributed to several factors: 1) background noise and free-stream turbulence in the testing medium, 2) instrumentation quality and the precision of the experimental technique, 3) data acquisition and reduction techniques, etc. For the range of Mach numbers covered in the data of Figure 2, the normalized RMS value of the fluctuating pressure varies from $\sqrt{\overline{p^2}}/q_\infty \approx 0.006$ at subsonic Mach numbers to 0.002 at supersonic Mach numbers. Lowson, Reference 1, proposed the following semi-empirical prediction formula which appears to agree with the general trend in the data:

$$\sqrt{\overline{p^2}}\Big/q_\infty = 0.006/(1 + 0.14 M_\infty^2) \tag{1}$$

It is important to note that this formula has some theoretical basis and is not strictly an empirical approximation of measured results (see Reference 1). The use of this formula at high supersonic and hypersonic Mach numbers should be done so with the understanding that it has not been verified in this Mach number range and may lead to significant error. However, in the Mach number range up to, say $M_\infty = 3.0$, it is in good agreement with experimental results.

254

It should be noted that the results presented in Figure 2 , particularly the wind tunnel results, were obtained for both homogeneous and stationary flows at free-stream conditions and in the absence of external pressure gradients. Consideration should be given to local conditions which deviate from free-stream conditions.

Power Spectra

Power spectra represent the distributions of the mean square fluctuating pressure with frequency. Power spectra for attached turbulent boundary layers are found to scale on a Strouhal number basis; that is, the frequency is normalized by multiplying by a typical length and dividing by a typical velocity. The advantages of using normalized spectra are obvious since it enables similar, homogeneous, flows to be represented by a single spectrum regardless of the scale of the flow field or the free-stream velocity.

Numerous studies have been conducted to determine the proper parameters to be used to nondimensionalize the spectra for various aero-acoustic environments. Unfortunately, the choice of parameters which best collapses the data appear to be dependent on the nature of the fluctuating pressure environment. In general, free-stream velocity is used as the normalizing velocity parameter, although a typical eddy convection velocity (itself a function of frequency) has been used occasionally. The local convection velocity appears to correspond more closely with the physical situation for fluctuating pressures due to turbulent eddies. Selection of a typical length is more difficult. Boundary layer thickness (δ_b), displacement thickness (δ^*), wall shear stress (τ_ω) and momentum thickness (θ) have all been used by various investigators. The most generally used typical lengths are δ_b and δ^*.

Lowson, Reference 1 , proposed an empirical formula for the power spectrum for attached turbulent boundary layers based, primarily, on the experimental results of Speaker and Ailman. In comparing this formula with other data, and in particular, with recent measurements at supersonic speeds by NASA-Ames, the Lowson prediction appears to underestimate the spectral levels at low Strouhal numbers and also gives too large a roll-off at high Strouhal numbers. Therefore, a new formula is presented

which appears to be more representative of experimental findings throughout the Mach number range. In this formula, it will be noted that δ^* and U_∞ (the free-stream velocity) have been used as normalizing parameters. The power spectral density, $\Phi(\omega)$ is given by the relation:

$$\frac{\Phi(\omega) U_\infty}{q_\infty^2 \delta^*} = \frac{(\overline{P^2}/q_\infty^2)}{\frac{\omega_0 \delta^*}{U_\infty} \left\{ 1 + (\omega/\omega_0)^{0.9} \right\}^{2.0}} \tag{2}$$

where
$$\omega_0 = 0.5 \frac{U_\infty}{\delta^*}$$

$$\overline{P^2}/q_\infty^2 = \frac{(0.006)^2}{(1 + 0.14 M_\infty^2)^2}$$

$$\delta^* = \delta_b/8 \quad \text{for } M < 1.0$$

$$\delta^* = \frac{(1.3 + 0.43 M_\infty^2)\, \delta_b}{10.4 + 0.5 M_\infty^2 \left[1 + 2.10^{-8}\, R_e \right]^{1/3}} \quad \text{for } M > 1.0$$

$$\delta_b = x \left[0.37\, R_e^{-0.2} \left\{ 1 + \left(\frac{R_e}{6.9 \cdot 10^7} \right)^2 \right\}^{0.1} \right]$$

x = Downstream distance from the leading edge

R_e = Reynolds number = $U_\infty\, x/\nu$

ν = Kinematic viscosity

256

A comparison of the predicted power spectrum with experimental spectra is presented in Figure 3.

Cross-Power Spectra

The final requirement in determining the characteristics of the fluctuating pressure field of the turbulent boundary layer is to define the narrow band, space correlation function or co-power spectral density. This parameter is the key function needed to describe an impinging pressure field on a structure in order to calculate the induced mean-square response of the structure (see, for example, Reference 17 for the structural response computational technique). The spatial correlation properties of a fluctuating pressure field can be obtained only from a careful and detailed examination of the field at a large number of points. Measurements by several investigators have shown that the co-power spectral density of turbulent boundary layer pressure fluctuations in the direction of the flow can be approximated by an exponentially damped cosine function, and the lateral co-spectral density can be approximated by an exponential function. The general form of the cross-power spectral density is:

$$S_{pp}(\zeta, \eta, \omega) = \phi(\omega) A(\zeta, \eta, \omega) \cos\left(\frac{\omega \zeta}{U_c}\right) \tag{3}$$

where $A(\zeta, \eta, \omega)$ is the modulus of the cross-power spectral density, and $\phi(\omega)$ is the power spectral density of the homogeneous field.

Here, it is assumed that the pressure field is homogeneous, in the sense that the cross-power spectral density is a function only of the separation distances (ζ in the longitudinal direction and η in the lateral direction) so that it is independent of the actual positions (say x and $x + \zeta$ longitudinally and y and $y + \eta$ laterally). Further, ω and U_c are the circular frequency and convection velocity, respectively. Assuming that $A(\zeta, \eta, \omega)$ is separable into its longitudinal and lateral components, and normalizing by the power spectral density of the homogenous field gives (Reference 1):

257

$$G_{pp}(\zeta, \eta, \omega) = G_\zeta(\zeta, \omega) \, G_\eta(\eta, \omega) = \left\{ A_\zeta(\zeta, \omega) \cdot \cos\left(\frac{\omega \zeta}{U_c}\right) \right\} \cdot A_\eta(\eta, \omega)$$

$$= C(\zeta, \omega) \cdot C(\eta, \omega) \tag{4}$$

where $C(\zeta, \omega)$ and $C(\eta, \omega)$ are the correlation coefficients in the longitudinal and lateral directions, respectively. The assumed separable form leads to the prediction that the magnitude of C is constant along straight lines on the surface, forming a diamond pattern surrounding the origin. This characteristic is somewhat physically unreasonable (see Reference 2); however, for purposes of calculating the induced structural response the assumption of separability greatly simplifies the mathematics and, hence, it is generally accepted. However, Lowson (Reference 1) notes that a more likely form for the lines of constant amplitude would be elliptic, suggesting that the usual separable solution underestimates the correlation area by $\pi/2$. Thus, integration of formula containing the cross-spectral density function should be multiplied by a factor of $\pi/2$ to allow for its probable underestimate of the correlation area at any frequency.

Measurements of the correlation coefficients have been made by Bull and others (see Reference 1) and the results are presented in Figures 4a and 4b. It is seen that the data in Figures 4a and 4b have been collapsed based on Strouhal numbers $\dfrac{\zeta\omega}{U_c}$ and $\dfrac{\eta\omega}{U_c}$. From these data, the following empirical expressions were derived for the correlation coefficients:

$$C(\zeta, \omega) = \exp\left(-0.10 \left| \zeta \right| \omega/U_c\right) \cdot \cos\left(\frac{\omega \zeta}{U_c}\right) \tag{5}$$

$$C(\eta, \omega) = \exp\left(-0.715 \left| \eta \right| \omega/U_c\right) \tag{6}$$

258

These correlation curves have been inserted in Figures 4a and 4b for comparison.
Typical values of the convection velocity (itself a function of frequency) for subsonic
flow are $U_c = 0.6 U_\infty$ for the small scale eddies near the wall and $U_c = 0.9 U_\infty$
for the large scale eddies near the outer edge of the boundary layer.

The accuracy of Equations (5) and (6) break down at small values of $\dfrac{\omega \zeta}{U_c}$;
however, in Reference 3, Bull presents measured asymptotic values of the
correlation coefficients for small values of $\dfrac{\omega \zeta}{U_c}$ and $\dfrac{\eta \zeta}{U_c}$. Based on these data,
the Equations (5) and (6) may be corrected to include the lower frequencies, and
the resulting expressions are:

$$C(\zeta, \omega) = \exp\left(-0.10 \left|\zeta\right| \omega/U_c\right) \cdot \exp\left(-0.27 \left|\zeta\right| \Big/ \delta_b\right) \cdot \cos\left(\frac{\omega \zeta}{U_c}\right) \quad (7)$$

$$C(\eta, \omega) = \exp\left(-0.72 \left|\eta\right| \omega/U_c\right) \cdot \exp\left(-2.0 \left|\eta\right| \Big/ \delta_b\right) \quad (8)$$

These expressions appear to be valid at both subsonic and supersonic speeds.

2.2   Separated Flow

Separated flows as induced by steps, wedges, flares and other, basically two-dimensional geometric changes have undergone considerable study only in recent years. Considerably less data is available on the fluctuating pressure environments within separated flow regions than is the case with attached turbulent boundary layers. Furthermore, there are various types of separated flows and little is known of the similarities and differences of their statistical properties. Example separated flow environments are listed below:

- Blunt body-induced separation (as occur at cone-cylinder and flare-cylinder expansion corners at subsonic Mach numbers)

- Flare-induced, step induced, and wedge-induced separation (as occur in compression corners)

- Shock-induced separation (as occur on cylinders, airfoils, etc., beneath terminal shock waves at transonic speeds and due to shock wave impingement at supersonic speeds)

- Boattail-induced and rearward facing-step-induced separation (such as occur in the base region of launch vehicles).

All of the foregoing environments differ to some degree in their aerodynamic structure. However, some basic comments can be made in regard to their fluctuating pressure characteristics. First, all of these environments may be regarded as two-dimensional type separated flows having mean separation and reattachment lines which are normal to the free-stream. Second, a general characteristic is that if the flow separates from an expansion corner, the separation line is quite stable in that oscillations which produce fluctuating pressures are not generated. However, if separation occurs, say, on the cylindrical portion of a payload shroud (flare induced separation) the separation point is unstable and may produce significant fluctuating pressures, particularly at supersonic speeds where the separation is accompanied by an oblique shock wave.

260

Third, the reattachment point of the separated flow field produces rather large fluctuating pressure levels for virtually all types of separated flow fields. The region within the separated flow field (between the separation and reattachment points) is a fairly homogeneous environment which is characterized by fluctuating pressure levels greater than those for attached flow but less than those encountered at the separation and reattachment points. Example data for various separated flow fields are presented in the following sections.

Overall Level

A typical example of the fluctuating pressures resulting from blunt-body separation is shown in Figure 5 (results taken from Reference 18). These data were obtained at high subsonic Mach numbers for a 25-degree cone-cylinder configuration. The axial distribution of $\sqrt{\overline{P^2}}/q_\infty$ shows a relatively nonhomogeneous environment with a peak level which moves aft with increasing Mach number. The peak in $\sqrt{\overline{P^2}}/q_\infty$ results from the reattachment of the separated flow from the shoulder. Thus, the extent of the separated region increases with increasing Mach number. Peak levels of rms fluctuating pressure reach 11 percent of free-stream dynamic pressure at a free-stream Mach number of 0.70, and results from the instability of the reattachment point. It will be noted that the fluctuating pressure levels near the shoulder ($X/D = 0$) are relatively low (same order of magnitude as generally found within the homogeneous region of two-dimensional separated flows and typical of the environment for separated shear layers) thus indicating that the separation point which occurs at the shoulder is relatively stable. Separated flow over the boattail region of a bulbous vehicle may be expected to exhibit fluctuating pressure characteristics very similar to the cone-cylinder; however, the blunt-body separation on a cone-cylinder body is limited to the subsonic speed range, whereas, the boattail configuration may induce separation at all Mach numbers.

Typical fluctuating pressure data for flare-induced separation are presented in Figure 6 (results taken from Reference 14). These data clearly show the region of homogeneous separated flow, bounded on the upstream by the oscillating shock wave (forward peak in $\sqrt{\overline{P^2}}/q_\infty$), and on the downstream by the reattachment perturbations (aft peak in $\sqrt{\overline{P^2}}/q_\infty$). Surface fluctuating pressures for the separated flow region range from 1.5 to 2.7 percent of the free stream dynamic pressure. Levels associated with the upstream shock wave generally range from 4 to 8 percent of the free-stream dynamic pressure (see Reference 14); whereas, levels in the region of reattachment may range from 6 to 12 percent of q_∞ and agree reasonably well with the reattachment levels for blur body separation. Further discussion of shock-wave oscillation data is presented in a later section.

The variation of fluctuating pressure level, normalized by free-stream dynamic pressure, with local Mach number (M_ℓ) for various separated flow environments downstream of expansion corners is presented in Figure 7. The regions aft of cone-cylinder junctures and rearward-facing steps, and in the near wake of boattail configurations are represented by the data presented in Figure 7. These environments will be referred to as expansion induced separated flows and it will be noted that the attendant fluctuating pressures exhibit the same general trend with local Mach number. The largest levels occured at low Mach numbers and decreased as local Mach numbers increased. These data represent the region of plateau static pressure and the tolerance brackets on the data represent the variations due to non-homogeneous flow within the region of constant static pressure rather than scatter in the measurements. A good empirical approximation to these experimental measurements is:

Expansion Induced Separated Flow:

$$\sqrt{\overline{P^2}}/q_\infty = \frac{0.045}{1 + M_\ell^2} \tag{9}$$

262

This equation is similar in form to that previously proposed for attached turbulent boundary layers.

Fluctuating pressure measurements for the region of plateau static pressure upstream of compression corners are presented in Figure 8. The regions immediately upstream of forward-facing steps, wedges, and flares are represented by the data presented in Figure 8. Also, the previous fluctuating pressure data for expansion induced separated flow, shown in Figure 7, are presented in this figure for comparison. In general, the compression corner data show an increase in fluctuating pressure level with increasing free-stream Mach number in the range, $1.0 \leq M_\infty \leq 2.0$ — reaching a constant level at Mach numbers above 2.0. Free-stream Mach number is used here because adequate data is not available for determining the local Mach number in the vicinity of the compression induced separated flow region. Derivation of an empirical prediction formula for the fluctuating pressure level within compression induced separated flows has not been attempted at this time.

Power Spectra

The most comprehensive available data for power spectra of the fluctuating pressure within separated flows was obtained for the homogeneous region of compression corners at supersonic Mach numbers (References 14, 19, 20 and 21). These data, presented in Figure 9, were obtained for forward facing steps, wedges and conical frustums. All data, represented by the cross-hatched band, showed a distinct similarity in spectral characteristics when compared using normalized spectral level and frequency expressed as functions of local velocity, free-stream dynamic pressure, and local boundary layer thickness. A number of velocity, length and pressure parameters were used to collapse the data; however, local velocity (U_ℓ), local boundary layer thickness (δ_ℓ) and free-stream dynamic pressure appeared to be adequately representative of the parameter dependence of the fluctuating pressures for the configurations studied. Power spectra of the fluctuating pressures within the homogeneous region of separated flows may be represented by the following empirical formula:

$$\frac{\phi(f)\, U_\ell}{q_\infty^2\, \delta_\ell} = \frac{\overline{P^2}/q_\infty^2}{\dfrac{f_0\, \delta_\ell}{U_\ell}\left\{1 + \left(f/f_0\right)^{0.83}\right\}^{2.15}} \tag{10}$$

where $\qquad f_0 \qquad = 0.17\, \dfrac{U_\ell}{\delta_\ell}$

$$\overline{P^2}/q_\infty^2 = \frac{0.045}{1+M_\ell^2} \qquad \text{, Figure 7, for expansion induced separated flows.}$$

$$\overline{P^2}/q_\infty^2 = \text{the results as determined in Figure 8 for compression induced separated flows.}$$

and the subscripts ℓ and ∞ refer to local and free-stream conditions respectively.

It is anticipated that Equation 10 can be used with good accuracy to predict the power spectra for fluctuating pressures within the homogeneous region of expansion induced separated flows although it was derived ⊦ sed on data taken in compression corners.

Cross-Power Spectra

Typical cross-power spectra for the homogeneous region of two-dimensional separated flows are presented in Figure 10. Again, noting that the co-spectral density is the same as the narrow-band spatial correlation, it is seen that the separated flow exhibits spatial coherence very similar to that of attached turbulent boundary layers. The damping of the sinusoidal cross spectra for separated flow is exponential at high values of $\omega\zeta/U_c$ as is the case for attached flow. Thus as a first approximation, the normalized longitudinal co-spectra may be represented by:

$$C(\zeta, f) = e^{-a\omega\zeta/U_c} \cos\frac{\omega\zeta}{U_c} \tag{11}$$

264

The damping coefficient, a, is dependent on free-stream Mach number according to the results presented in Reference 14. The Chyu and Hanely results show damping coefficients ranging from approximately 0.13 at $M_\infty = 2.5$ to a value of 0.33 at $M_\infty = 1.6$. This suggests that the turbulence structure in separated flows decays somewhat more rapidly than for attached flow which has a coefficient of exponential decay of 0.10. It should be noted that the exponential decays represent the envelope of the cross-spectra for various spatial distances, ζ. For a given value of ζ, the cross-spectra can be represented by the exponential envelope only at high frequencies, the lower limits of which increase with increasing distance between measurement points.

The loss of coherence at low frequencies precludes a general collapse of the data using a constant damping coefficient. This problem was overcome by Coe and Rechtien, Reference 20, by introducing an attenuation coefficient which is related to the normalized modulus of the cross-power spectral density by

$$\left| G\left(\zeta, \frac{f\,\delta_\ell}{U_\ell}\right) \right|_{norm} = e^{-\alpha\zeta} \tag{12}$$

The normalized modulii for available or selected transducer spacings, ζ, were curve-fitted by an exponential function using the method of least squares to obtain a non-dimensional attenuation-coefficient function $\alpha\left(\zeta, f\,\delta_\ell / U_\ell\right) \cdot h$ in References 19-21. The parameter h is the height of the protuberances used to generate the separated flow field. Empirical approximations of the attenuation coefficient, based on the experimental results of Coe and Rechtien, are:

$$\alpha\left(\zeta, \frac{f\,\delta_\ell}{U_\ell}\right) = 0.75/\text{in.} \quad , \quad \frac{f\,\delta_\ell}{U_\ell} < 6 \times 10^{-3} \tag{13}$$

$$\alpha\left(\zeta, \frac{f\delta_\ell}{U_\ell}\right) = 0.75 \left[\frac{f\delta_\ell/U_\ell}{\left(f\delta_\ell/U_\ell\right)_0}\right] ,$$ (14)

$$6 \times 10^{-3} \leq \frac{f\delta_\ell}{U_\ell} \leq 6 \times 10^{-2}$$

where $$\left(\frac{f\delta_\ell}{U_\ell}\right)_0 = 6 \times 10^{-3}$$

$$\alpha\left(\zeta, \frac{f\delta_\ell}{U_\ell}\right) = 1.5 / \text{in.} \quad , \quad \frac{f\delta_\ell}{U_\ell} > 6 \times 10^{-2}$$ (15)

Lateral Direction

$$\alpha\left(\eta, \frac{f\delta_\ell}{U_\ell}\right) = 0.75 / \text{in.} \quad , \quad \frac{f\delta_\ell}{U_\ell} < 6 \times 10^{-3}$$ (16)

$$\alpha\left(\eta, \frac{f\delta_\ell}{U_\ell}\right) = 0.75 / \text{in.} \left[\frac{f\delta_\ell/U_\ell}{\left(f\delta_\ell/U_\ell\right)_0}\right]^{0.3} \quad , \quad \frac{f\delta_\ell}{U_\ell} \geq 6 \times 10^{-3}$$ (17)

where $$\left(\frac{f\delta_\ell}{U_\ell}\right)_0 = 6 \times 10^{-3}$$

It will be noted that the longitudinal and lateral attenuation coefficients are the same at Strouhal numbers, $f\delta_\ell/U_\ell < 6 \times 10^{-2}$ and that the lateral attenuation coefficient becomes larger than the longitudinal value at $f\delta_\ell/U_\ell \geq 6 \times 10^{-2}$. It was pointed out in Reference 19 that this spatial characteristic indicates that the predominant turbulence is nonconvective at the lower frequencies and that contours of equal

266

correlation would be circular; whereas, at $f\delta_\ell / U_\ell > 6 \times 10^{-2}$ the divergence of the longitudina and lateral attenuation coefficients indicate a progressively extended correlation pattern in the direction of the free-stream with increasing frequency. This statement is not entirely true since the usual separable form of the cross-power spectral density leads to the prediction that the magnitude of the normalized modulus is constant along straight lines on the surface, forming a diamond pattern surrounding the origin rather than a circular or elliptic pattern. Under the assumption of separability of the longitudinal and lateral cross-power spectra, the following equations (which employ the attenuation coefficient) may be used as prediction formula for the normalized longitudinal and lateral co-spectra.

Longitudinal Co-Spectra

$$C\left(\zeta, \frac{f\delta_\ell}{U_\ell}\right) = e^{-\alpha_\zeta \zeta} \cos \frac{\omega \zeta}{U_c} \tag{18}$$

Lateral Co-Spectra

$$C\left(\eta, \frac{f\delta_\ell}{U_\ell}\right) = e^{-\alpha_\eta \eta} \tag{19}$$

where $\quad \alpha_\zeta = \alpha\left(\zeta, \frac{f\delta_\ell}{U_\ell}\right)$ as defined in Equations 13, 14 and 15.

$$\alpha_\eta = \alpha\left(\eta, \frac{f\delta_\ell}{U_\ell}\right) \quad \text{as defined in Equations 16 and 17.}$$

267

2.3 Shock-Wave Oscillation

Generally, shock wave oscillation produces the most intense fluctuating pressure levels
that are usually encountered by a vehicle. As for the case of separated flow, there
are many types of shock-wave oscillation and little is known in regard to the similarities
and differences of their statistical parameters. Typical shock waves encountered by
vehicles are:

- Terminal shock waves for regions of transonic flow

- Displaced oblique shock waves as induced by the separated flow
  in compression corners at local supersonic speeds

- Reattachment shock waves in the vicinity of the reattachment
  point for separated flows generated by both compression and
  expansion corners.

- Impingement shock waves as caused by local bodies such as
  strap-on rockets.

All shock waves may be expected to produce similar fluctuating pressure environments
since the movement of the shock wave results from the interaction with the separated

flow at the foot of the shock wave (see Reference 19) and the fluctuating pressure is
the result of the modulation of the pressure gradient through the shock wave. A
special case of shock wave oscillation is referred to as an alternating flow condition,
whereby, the flow at an expansion corner intermittently fluctuates between a
separated and attached condition. This environment is illustrated schematically in
Figure 11 for a 25 degree cone angle together with the more common terminal shock—
wave oscillation case. Example data for various shock wave oscillation environments
are presented in the following sections.

Overall Level

The axial distribution of rms fluctuating pressure resulting from terminal shock wave oscillation is shown in Figure 11 (from Reference 18). A special case of terminal shock wave oscillation results when the terminal shock wave moves forward to the expansion shoulder of a cone-cylinder. For this case, the flow intermittently fluctuates between the blunt-body separated flow condition and the attached flow condition at high subsonic (low transonic) Mach numbers. This condition represents an alternating unbalance between the large pressure rise through the shock wave that exceeds the values required to separate the flow and the small pressure rise that is too small to maintain fully separated conditions.

Extremely large fluctuating pressures result from this condition; however, it should be noted that this phenomenon occurs over a small Mach number range and generally is of very low frequency. Thus for large Mach number transients, this phenomenon may not occur. On the other hand, some experimental studies using aeroelastic wind tunnel models indicate that this phenomenon may become coupled with the vibrational response of vehicles such that flutter in the lower order bending modes would result for certain configurations — particularly for bulbous shaped payloads on rather slender launch vehicles.

As Mach number is increased above the range of alternating flow, the localized oscillation of the shock wave produces intense fluctuating pressures for the region in close proximity to the shock wave as shown in Figure 11. The shock wave moves aft with diminishing strength with increasing Mach number such that the rms fluctuating presssure levels also decreases. In addition to the results presented in Figure 11, the fluctuating pressures which occur at the separation and reattachment points for separated flow over compression corners (Figure 6) are fairly complete examples of shock-wave oscillation data.

269

Power Spectra

Only recently has comprehensive data been presented on the spectral characteristics
of shock-wave oscillation. Much of the previous data were presented in linear—
linear graphical form rather than using log—log scales. As a result, much resolution
was lost at the high frequencies. Recent experimental data by Coe and Richtien
(Reference 20) gives a clearly defined spectrum for shock wave oscillation at $M_\infty = 2.0$;
however, data at other Mach numbers have not been published. Data obtained for
three-dimensional protuberance flows do agree with the Coe and Richtien data and
thus substantiates their limited published results. The normalized power spectra for
shock-wave oscillation for both two- and three-dimensional protuberances (References
18 and 19) are presented in Figure 12. The power spectrum shows a relatively steep
roll-off starting at a Strouhal frequency $(f \delta_0 / U_0)$ of 1×10^{-2}, where the subscript
0 denotes local velocity and boundary layer thickness upstream of the shock wave. The
roll-off is 8 dB per octave for the range $1 \times 10^{-2} \leq f \delta_0 / U_0 \leq 2 \times 10^{-1}$ and above
this range the roll-off changes suddenly to 4 dB per octave. These unique spectral
characteristics of shock-wave induced fluctuating pressures are explained by the
physical behavior of the shock-wave oscillation and the resulting pressure time history.
The shock wave is basically a pressure discontinuity which becomes slightly distorted
by the boundary layer such that a finite gradient through the shock wave is observed
at the surface. Oscillation of the shock wave produces a wave form which approaches
a random-rectangular wave as the displacement of the oscillation increases. Superim-
posed upon this signal is the low amplitude, high frequency disturbance associated
with the attached boundary layer (for that portion of the signal when the shock wave
is aft of the measurement point) and the moderate amplitude and frequency disturbances
associated with separated flow (for that portion of the signal when the shock wave is
forward of the measurement point). The roll-off rate of the power spectrum for a ran-
dom-rectangular wave form is 6 dB per octave which is 2 dB lower than the experi-
mentally observed value. Above $f \delta_0 / U_0 = 2 \times 10^{-1}$, the power spectral density

for the random modulation of the shock wave diminishes below the power spectral density for the turbulence portion of the signal. Thus, the roll-off rate changes to a value roughly equal to that for separated flow since this environment is the larger of the two turbulence generating mechanisms (the other being attached flow).

Noting that the power spectra for shock wave oscillation is composed of 1) low frequency spectral energy of the shock wave and 2) high frequency spectral energy of the separated flow and attached boundary layer, the resulting empirical formula for the power spectra may be written as a combination of power spectra of the contributing sources:

$$\left[\phi(f)\right]_{SW}^{H} = \left[\phi(f)\right]_{SW}^{I, H} + k_1 \left[\phi(f)\right]_{S}^{H} + k_2 \left[\phi(f)\right]_{A}^{H} \qquad (20)$$

where the subscripts and superscripts denote the following:

Subscripts: SW - shock wave

   S - separated flow

   A - attached flow

Superscripts: I - absence of viscosity (inviscid)

   H - homogeneous flow

The constants, k_1 and k_2 are weighting functions which account for that portion of the total energy resulting from the presence of viscous flow in the form of separated flow and attached flow respectively. It should be noted that the two secondary environments (separated flow and attached flow) are not simultaneously superimposed on the shock wave signal but rather are time shared. This, together with the fact that these environments may be correlated with the gross motion of the shock wave results in values of k_1 and k_2 less than 1.0. Finally, for peak overall levels of shock wave oscillation (corresponding to a point located at the mean position of the shock wave) the contribution of attached flow is negligible in comparison to that for separated flow. Thus, Equation 20 may be simplified to

271

$$\left[\phi\left(f\right)\right]_{SW}^{H} = \left[\phi\left(f\right)\right]_{SW}^{I,\,H} + k_1 \left[\phi\left(f\right)\right]_{S}^{H} \qquad (21)$$

Based on the experimental data of Reference 19, the power spectra $\left[\phi(f)\right]_{SW}^{I,\,H}$ for shock wave oscillation in the absence of viscous flow normalized by local inflowing boundary layer thickness and velocity and free-stream dynamic pressure is given by:

$$\left[\frac{\phi(f)\,U_0}{q_\infty^2\,\delta_0}\right]_{SW}^{I,\,H} = \frac{\left(\overline{P^2}\big/q_\infty^2\right)_{SW}^{I,\,H}}{\left(\dfrac{f_0\,\delta_0}{U_0}\right)_{SW} \left\{1+\left(f/f_0\right)^{1.55}\right\}^{1.7}} \qquad (22)$$

where:

$$\left[\overline{P^2}\big/q_\infty^2\right]_{SW}^{I,\,H} = \left[\overline{P^2}\big/q_\infty^2\right]_{SW}^{H} - k_1 \left[\overline{P^2}\big/q_\infty^2\right]_{S}^{H}$$

$\left[\overline{P^2}\big/q_\infty^2\right]_{SW}^{H}$ —   overall level of shock oscillation peak corresponding to the mean location of the shock wave.

$\left[\overline{P^2}\big/q_\infty^2\right]_{S}^{H}$ —   overall level of homogeneous separated flow as defined from Figures 7 and 8.

The subscript 0 denotes local velocity and boundary layer thickness upstream of the shock wave.

272

$$\left(\frac{f_0 \, \delta_0}{U_0}\right)_{SW} = 1 \times 10^{-3}$$

$$k_1 = 0.25$$

determined empirically from experimental data of Reference 19

Substitution of Equations 10 and 22 into Equation 21 gives the final expression for the power spectra for shock wave oscillation.

$$\left[\frac{\phi(f)\, U_0}{q_\infty^2 \, \delta_0}\right]_{SW}^{H} = \frac{\left(\overline{P^2} \Big/ q_\infty^2\right)_{SW}^{I,H}}{\left(\frac{f_0 \, \delta_0}{U_0}\right)_{SW}\left\{1 + \left(f/f_0\right)^{1.55}\right\}^{1.7}} +$$

$$0.25 \; \frac{\left(\overline{P^2} \Big/ q_\infty^2\right)_{S}^{H}}{\left(\frac{f_0 \, \delta_0}{U_0}\right)_{S}\left\{1 + \left(f/f_0\right)^{0.83}\right\}^{2.15}} \qquad (23)$$

where $(f_0 \delta_0/U_0)_S$ is now defined for conditions upstream of the shock wave.

A comparison of the predicted power spectra for shock-wave oscillation with experimental measurements is presented in Figure 13. Also shown in the upper right hand corner of this figure is the variation in $\sqrt{\overline{P^2}}/q_\infty$ with distance upstream from the 45 degree wedge. It should be noted that this prediction formula holds true only at a point corresponding to the mean location of the shock wave. On either side of the shock wave, the influence of the shock diminishes rapidly due to its small displacement such that the environment is basically either attached or separated flow with some low frequency intermittency due to the shock wave. It is convenient to refer to these regions as non-homogeneous attached and separated flows and they will be discussed later in Section 2.4.

273

Cross-Power Spectra

Very little data has been published in the form of cross-power spectra of fluctuating pressures beneath oscillating shock waves. Because oscillating shock waves at a given flight condition are confined to relatively small areas of the vehicle surface, it is extremely difficult to define the spatial characteristics of the attendant fluctuating pressures. Fluctuating pressures in the vicinity of the shock wave are highly non-homogeneous; although they do appear to be related in both spectral shape and spatial coherence. The only significant results on the spatial coherence of fluctuating pressures in the vicinity of shock-waves are those by Coe and Rechtien (Reference 20) Their data indicate that the fluctuating pressures generated by the shock wave are related only at frequencies below $f\delta_0 / U_0 = 0.08$ for the region immediately downstream of the mean location of the shock wave (Figure 14). For the region immediately upstream of the shock-wave, a small degree of coherence is also evident in this frequency range as well as at $f\delta_0 / U_0 \geq 0.2$. A comparison of the power spectra and coherence function shows some very interesting characteristics of shock-induced fluctuating pressures. First, the power spectra of fluctuating pressures on each side of the peak level point show large low frequence energy which can be identified as having the same basic characteristics as the shock wave spectrum for $f\delta_0 / U_0 \leq 0.08$. This is confirmed by the coherence of the data over the same frequency range $\left(f\delta_0 / U_0 \leq 0.08 \right)$. For $f\delta_0 / U_0 > 0.08$, power spectra immediately upstream and downstream of the shock wave show spectral characteristics identical to attached turbulent boundary layer and separated flow, respectively. Thus, for $f\delta_0 / U_0 > 0.8$, the spatial correlation of fluctuating pressure immediately upstream of the peak should be characteristic of attached flow; whereas, immediately downstream of the peak they should be characteristic of separated flow. However, when the spatial correlation is normalized by the power spectral densities to obtain the coherence function, this coherence appears to be minimized due to the large spectrum level for the point of peak fluctuating pressure. Further discussion on this

274

characteristic will be given later in the section on non-homogeneous attached and separated flows.

The spatial decay of the low frequency, shock induced fluctuating pressure in the longitudinal direction as shown in Figure 14 may be represented by an exponential coherence function as follows:

$$\gamma\left(\zeta, \frac{f\delta_0}{U_0}\right) = e^{-80 \ f\delta_0/U_0} \tag{24}$$

A comparison of this empirical prediction with experimental ⟨ ⟩ s presented in Figure 14. It should be noted that, as separation distance is increased, the above formula fails to account for the low coherence at low frequencies. However, because the large non-homogeneous effects associated with the flow in close proximity of the shock wave, the application of classical statistical methods to define the spatial characteristics for large separation distances may be questionable. Thus, for regions under the peak, Equation 24 is felt to be an accurate represe.itation of the spatial characteristics of the fluctuating pressures in the longitudinal direction.

The longitudinal co-spectra may be written:

$$C(\zeta, f) = e^{-40 \ f\delta_0/U_0} \cos 2\pi \frac{f\delta_0}{U_0} \tag{25}$$

Published data is not available on the transverse spatial characteristics of shock-induced fluctuating pressures. However, it is anticipated that these disturbances will be reasonably correlated over much larger distances in the transverse direction than in the longitudinal direction because of the continuity of the shock wave in the plane normal to the flow.

275

2.4   Non-Homogeneous Attached and Separated Flows

Non-homogeneous attached and separated flows are defined as environments which are basically attached or separated; however, the statistical properties of their attendant fluctuating pressures vary with spatial location. Examples to be considered herein are attached and separated flows immediately upstream and downstream of oscillating shock waves, respectively. The non-homogeneity may result from intermittency of the shock wave oscillation or from a more basic modification to the turbulence structure of attached and separated flow due to the motion of the shock wave. The variations in both the overall level and power spectra with position relative to the shock wave are evident in Figure 13. These data are shown in comparison with homogeneous attached and separated flow data to illustrate the presence of low frequency energy due to the shock wave. Again, basic characteristics of the overall levels, power spectra, and cross-power spectra will be discussed for the purpose of defining empirical prediction techniques for the non-homogeneous attached and separated flows.

Overall Level

The overall fluctuating pressure levels for attached and separated flow in close proximity to an oscillating shock wave are bounded on the low side by the levels of fluctuating pressures corresponding to homogeneous environments and are bounded on the high side by the peak fluctuating pressures corresponding to shock wave oscillation. In essence, this means that the differences between the homogeneous and non-homogeneous fluctuating pressure levels may be attributed directly to fluctuating pressures induced by the oscillating shock wave for the case considered here. Thus, normalized fluctuating pressure levels for non-homogeneous flows may be defined as:

$$\left(\frac{\sqrt{\overline{P^2}}}{q_\infty}\right)^H_A \leq \left(\frac{\sqrt{\overline{P^2}}}{q_\infty}\right)^{NH}_A \leq \left(\frac{\sqrt{\overline{P^2}}}{q_\infty}\right)^H_{SW} \tag{26}$$

$$\left(\frac{\sqrt{\overline{P^2}}}{q_\infty} \right)^H_S \leq \left(\frac{\sqrt{\overline{P^2}}}{q_\infty} \right)^{NH}_S \leq \left(\frac{\sqrt{\overline{P^2}}}{q_\infty} \right)^H_{SW} \tag{27}$$

where the subscripts and superscripts are defined as follows:

Subscripts   A - attached flow

                  S - separated flow

                  SW - shock wave

Superscripts   H - homogeneous conditior

                  NH - non-homogeneous condition

Under the assumption of statistical independence between the various sources, i.e., attached flow, separated flow and shock wave oscillation, the fluctuating pressure levels may be expressed as:

$$\left(\frac{\sqrt{\overline{P^2}}}{q_\infty} \right)^{NA}_A = \sqrt{ \left[\left(\frac{\sqrt{\overline{P^2}}}{q_\infty} \right)^H_A \right]^2 + c_1 \left[\left(\frac{\sqrt{\overline{P^2}}}{q_\infty} \right)^H_{SW} \right]^2 } \tag{28}$$

$$\left(\frac{\sqrt{\overline{P^2}}}{q_\infty} \right)^{NH}_S = \sqrt{ \left[\left(\frac{\sqrt{\overline{P^2}}}{q_\infty} \right)^H_S \right]^2 + c_2 \left[\left(\frac{\sqrt{\overline{P^2}}}{q_\infty} \right)^H_{SW} \right]^2 } \tag{29}$$

where c_1 and c_2 are weighting functions less than 1.0, which represent the contribution of the shock wave to the overall fluctuating pressure level. The values of c_1 and c_2 vary with spatial location relative to the shock wave and therefore, are difficult to predict. However, the above method of representation is useful in the prediction of power spectra for non-homogeneous flows as will be shown in the next section.

Power-Spectra

To predict the power spectra for non-homogeneous flows, a prior knowledge of the overall fluctuating pressure levels is required. Under the assumption of statistical independence ,etween the various contributing sources, the power spectra for non—homogeneous environments may be written as the summation of power spectra of the contributing sources. Using the same symbolic representation as for the overall level, the power spectra for non-homogeneous environments may be written as:

$$\left[\phi(f) \right]_A^{NH} = \left[\phi(f) \right]_A^H + c_1 \left[\phi(f) \right]_{SW}^{I, H} \tag{30}$$

$$\left[\phi(f) \right]_A^{NH} = \left[\phi(f) \right]_A^H + c_2 \left[\phi(f) \right]_{SW}^{I, H} \tag{31}$$

From Equations 30 and 31 , c_1 and c_2 are given as

$$c_1 = \frac{\left(\dfrac{\overline{p^2}}{q_\infty^2} \right)_A^{NH} - \left(\dfrac{\overline{p^2}}{q_\infty^2} \right)_A^H}{\left(\dfrac{\overline{p^2}}{q_\infty^2} \right)_{SW}^{I, H}} \tag{32}$$

278

$$c_2 = \frac{\left(\dfrac{\overline{p^2}}{q_\infty^2}\right)_S^{NH} - \left(\dfrac{\overline{p^2}}{q_\infty^2}\right)_A^{H}}{\left(\dfrac{\overline{p^2}}{q_\infty^2}\right)_{SW}^{I,H}} \tag{33}$$

To determine the power spectra for non-homogeneous attached flow as caused by shock wave oscillction in the vicinity of the attached flow region, Equations 2, 22, and 32 are substituted into Equation 30, which gives a form normalized by local conditions upstream of the shock wave:

$$\left[\frac{\phi(f)\,U_0}{q_\infty^2\,\delta_0}\right]_A^{NH} = \frac{\left(\dfrac{\overline{p^2}}{q_\infty^2}\right)_A^{H}}{\left(\dfrac{f_0\,\delta_0}{U_0}\right)_A \left\{1 + \left(f/f_0\right)^{0.9}\right\}^2} +$$

$$\frac{\left(\dfrac{\overline{p^2}}{q_\infty^2}\right)_A^{NH} - \left(\dfrac{\overline{p^2}}{q_\infty^2}\right)_A^{H}}{\left(\dfrac{f_0\,\delta_0}{U_0}\right)_{SW} \left\{1 + \left(f/f_0\right)^{1.55}\right\}^{1.7}} \tag{34}$$

Similarly, substitution of Equations 10, 22, and 33 into Equation 31, leads to the following expression for non-homogeneous separated flow:

$$
\left[\frac{\phi(f) \, U_0}{q_\infty^2 \, \delta_0} \right]_S^{NH} = \frac{\left(\dfrac{\overline{p^2}}{q_\infty^2} \right)_S^{H}}{\left(\dfrac{f_0 \, \delta_0}{U_0} \right)_S \left\{ 1 + \left(f/f_0 \right)^{0.83} \right\}^{2.15}} +
$$

$$
\frac{\left(\dfrac{\overline{p^2}}{q_\infty^2} \right)_S^{NH} - \left(\dfrac{\overline{p^2}}{q_\infty^2} \right)_S^{H}}{\left(\dfrac{f_0 \, \delta_0}{U_0} \right)_{SW} \left\{ 1 + \left(f/f_0 \right)^{1.55} \right\}^{1.7}} \qquad (35)
$$

Comparison of these predictions with experimental measurements are shown in Figure 13.

APPENDIX – REFERENCES

1. Lowson, M. V., "Prediction of Boundary Layer Pressure Fluctuations," Wyle Laboratories Research Staff Report WR 67-15, October 1967.

2. Speaker, W. V. and Ailman, C. M., "Spectra and Space-Time Correlations of the Fluctuating Pressures at a Wall Beneath a Supersonic Turbulent Boundary Layer Perturbed by Steps and Shock Waves," NASA CR-486, May 1966.

3. Bull, M. K., "Properties of the Fluctuating Wall Pressure Field of a Turbulent Boundary Layer," AGARD Report 455, April 1963.

4. Bull, M. K., et al., "Wall Pressure Fluctuations in Boundary Layer Flow and Response of Simple Structure to Random Pressure Fields," University of Southampton, AASU Report 243, 1963.

5. Kistler, A. L. and Chen, W. S., "The Fluctuating Pressure Field in a Supersonic Turbulent Boundary Layer," Jet Propulsion Laboratory Technical Report No. 32-277, August 1962.

6. Belcher, P. M., "Predictions of Boundary Layer Turbulence Spectra and Correlations for Supersonic Flight," Presented at the 5th International Acoustic Congress, Liege, Belgium, September 1965.

7. Serafini, J. S., "Wall Pressure Fluctuations and Pressure Velocity Correlations in a Turbulent Boundary Layer," NASA TR R-165, December 1963.

8. Bakewell, H. P. Jr., et al., "Wall Pressure Correlation in Turbulent Pipe Flow," U. S. Navy Sound Laboratory Report No. 559, August 1962.

9. Shattuck, R. D., "Sound Pressures and Correlations of Noise on the Fuselage of a Jet Aircraft in Flight," NASA TN-D-1086, August 1961.

10. Willmarth, W. W. and Roos, F. W., "Resolution and Structure of the Wall Pressure Field Beneath a Turbulent Boundary Layer," J. Fluid Mech., Vol. 22, Part 1, pp. 81-94, 1965.

11. Maestrello, L., "Measurement of Noise Radiated by Boundary Layer Excited Panels," J. Sound Vib., 2 (2), 1965.

12. Hilton, D. A., "In-Flight Aerodynamic Noise Measurements on a Scout Launch Vehicle," NASA TN D-1818, July 1963.

13. Williams, D. J. M., "Measurements of the Surface Pressure Fluctuations in a Turbulent Boundary Layer in Air at Supersonic Speeds," University of Southampton, AASU Report No. 162, Department of Aeronautics and Astronautics, December 1960.

14. Chyu, W. J. and Hanly, R. D., "Power and Cross-Spectra and Space Time Correlation of Surface Fluctuating Pressures at Mach Numbers Between 1.6 and 2.5," AIAA Preprint No. 68-77, January 1968.

15. Maestrello, L., "Measurement and Analysis of the Response Field of Turbulent Boundary Layer Excited Panels," J. Sound and Vib., 2, No. 3, July 1965.

16. Wi'lmarth, W. W. and Woolridge, C. E., "Measurements of the Fluctuation Pressure at the Wall Beneath a Thick Turbulent Boundary Layer," J. Fluid Mech., Vol. 14, pp. 187-210, 1962.

17. Bozich, D. J. and White, R. W., "Study of the Vibration Responses of Shells and Plates to Fluctuating Pressure Environments," Wyle Laboratories Research Staff Report WR 69-19, September 1969.

18. Robertson, J.E., "Wind Tunnel Investigation of the Effects of Reynolds Number and Model Size on the Steady and Fluctuating Pressures Experienced by Cone Cylinder Missile Configurations at Transonic Speeds," AEDC-TR-66-266, March 1967.

19. Coe, Charles F., "Surface Pressure Fluctuations Associated with Aerodynamic Noise," Basic Aerodynamic Noise Research Conference Proceedings, NASA SP-207.

20. Coe, Charles F., and Rechtien, R. D., "Scaling and Spatial Correlation of Surface Pressure Fluctuations in Separated Flow at Supersonic Mach Numbers," Paper presented at the AIAA Structural Dynamics and Aeroelasticity Specialist Conference, New Orleans, La., April 16-17, 1969.

21. Rechtien, Richard D., "A Study of the Fluctuating Pressure Field in Regions of Induced Flow Separation at Supersonic Speeds," University of Missouri - Rolla UMR Research Report, May 1970.
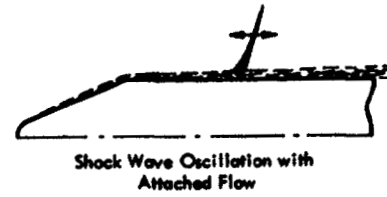
Basic Vehicle Geometry

Mach Number Range

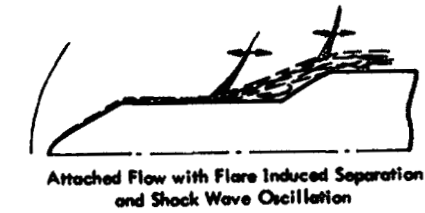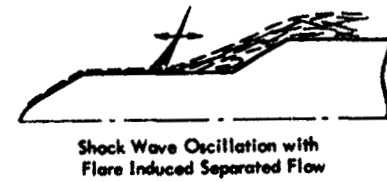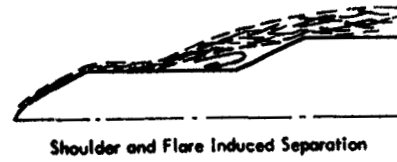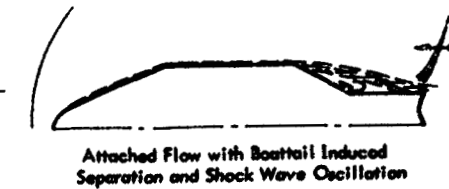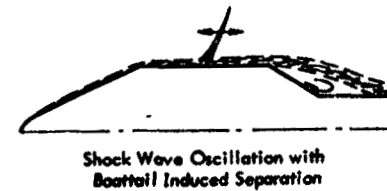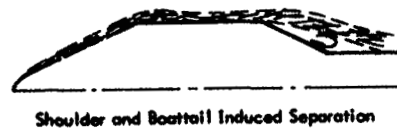Figure 1.   Subsonic, Transonic, and Supersonic Flow Fields for Basic Vehicle Configurations
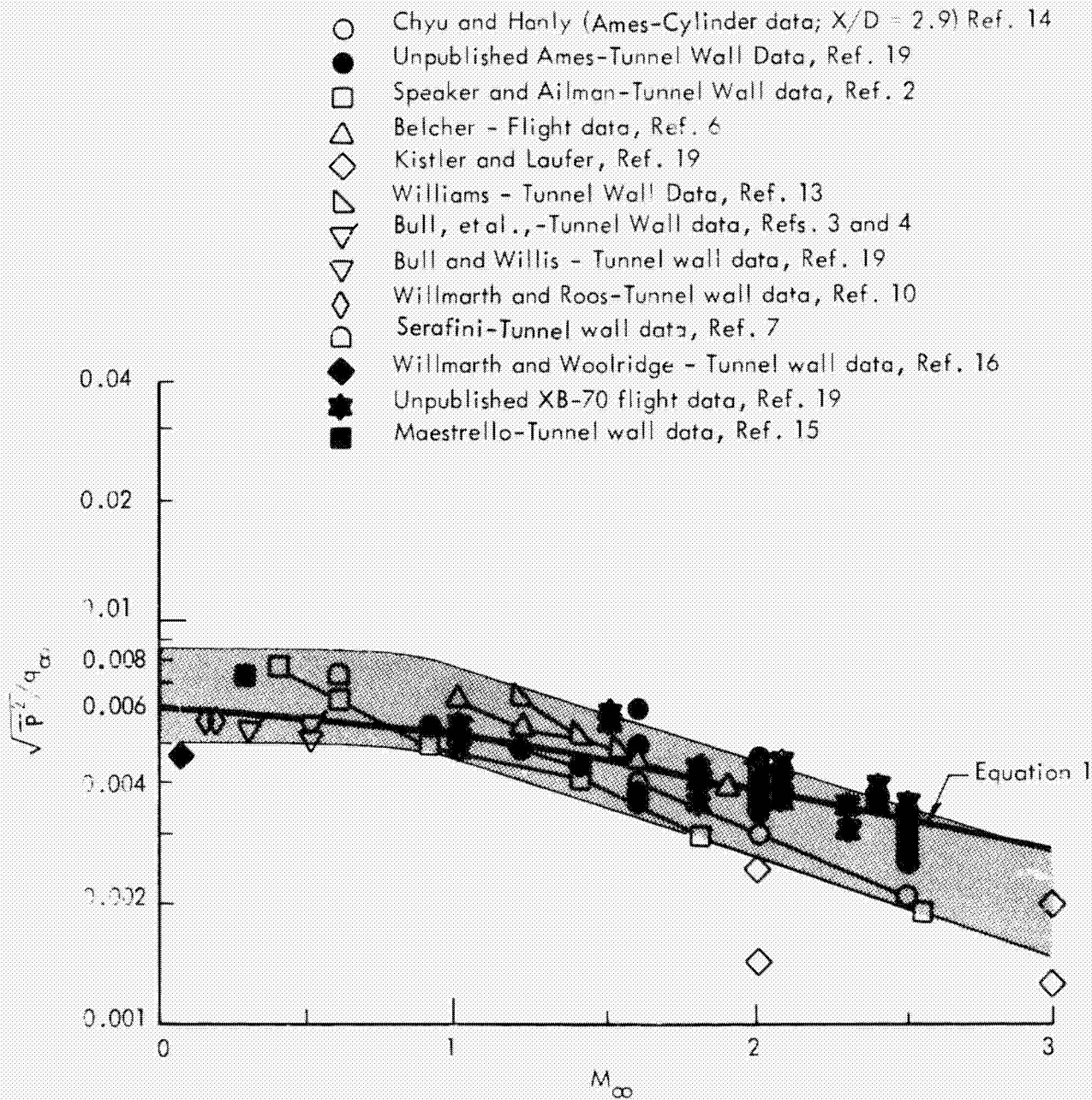
283

Figure 2. Comparison of Pressure Fluctuation Measurements beneath Attached Flows by Various Investigators

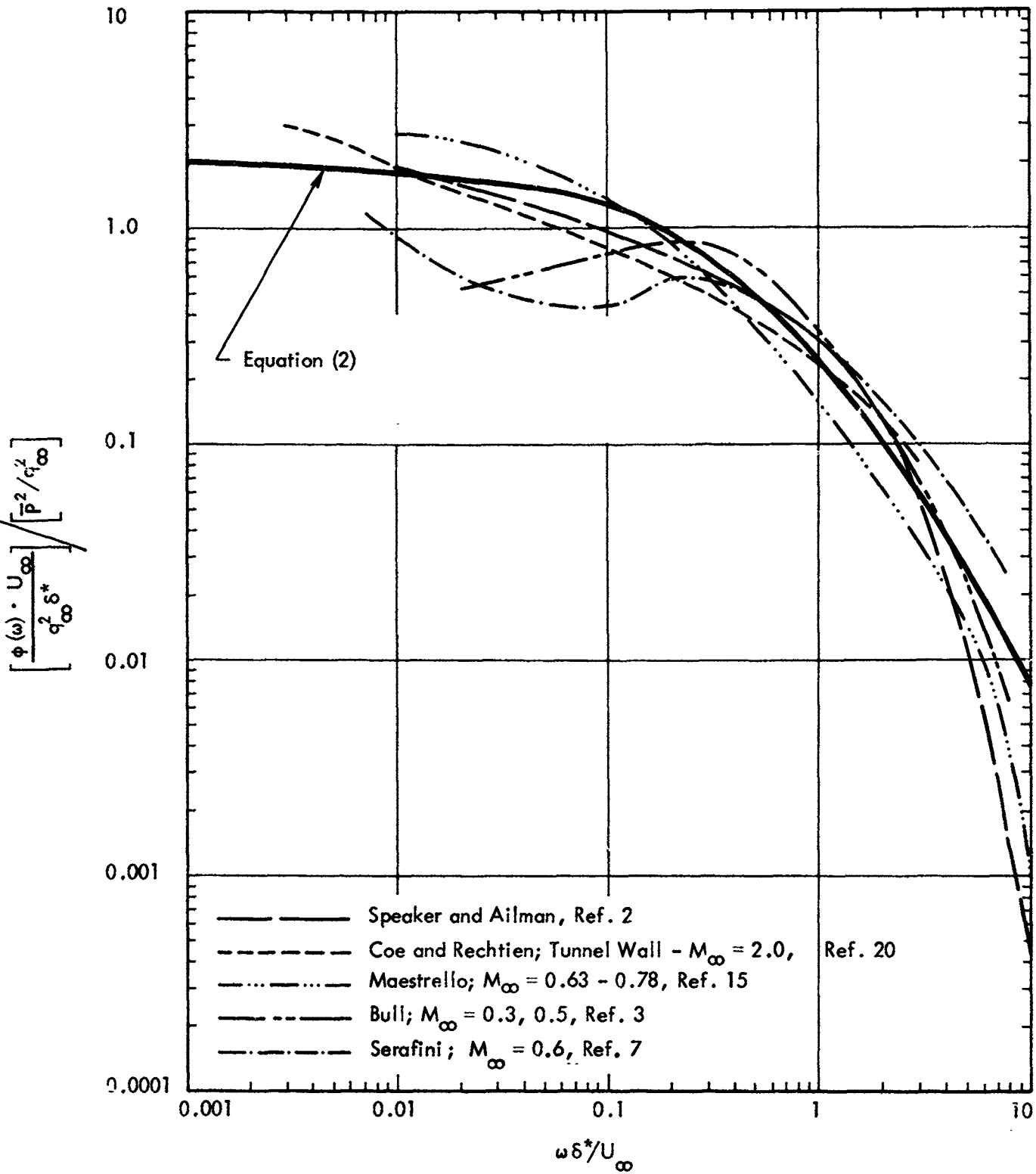Figure 3. Power Spectra for Turbulent Boundary Layer Fluctuating Pressures
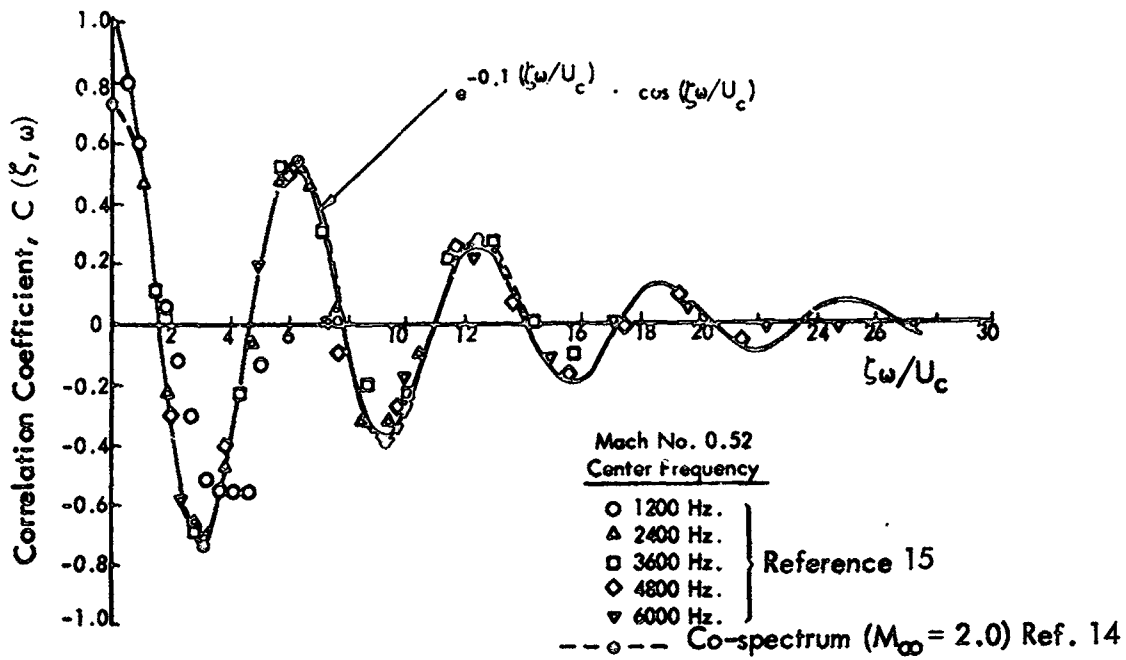
285

Figure 4a. Narrow Band Longitudinal Space Correlation Coefficient for Boundary Layer Fluctuating Pressures
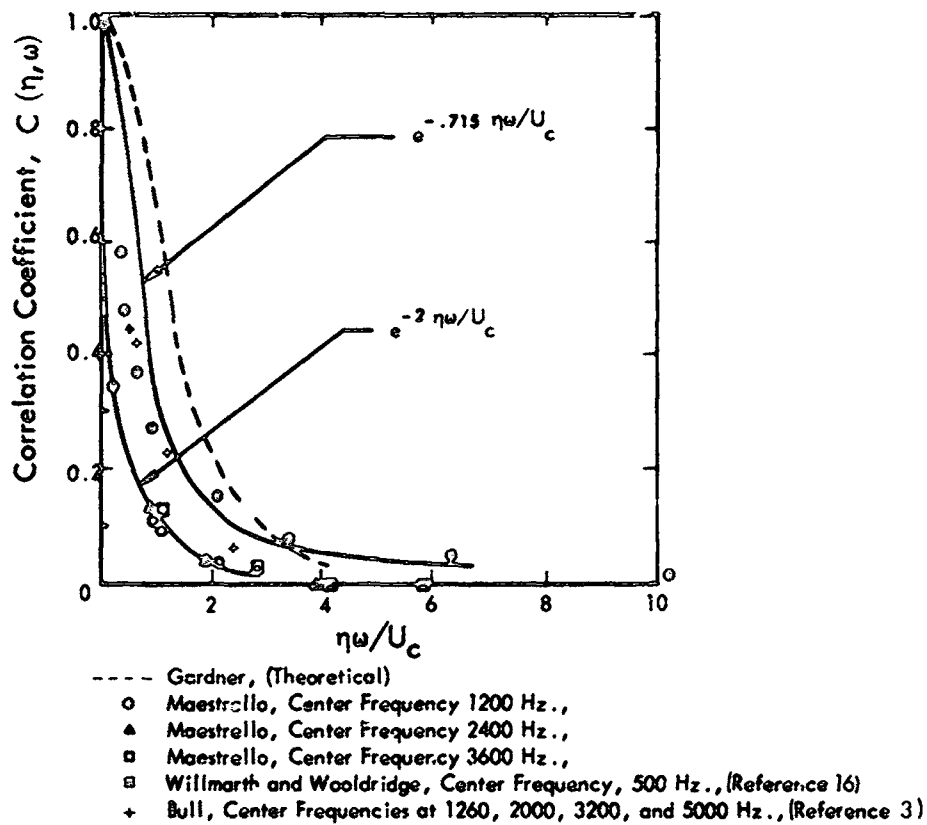
Figure 4b. Narrow Band Lateral Space Correlation Coefficient for Boundary Layer Fluctuating Pressures
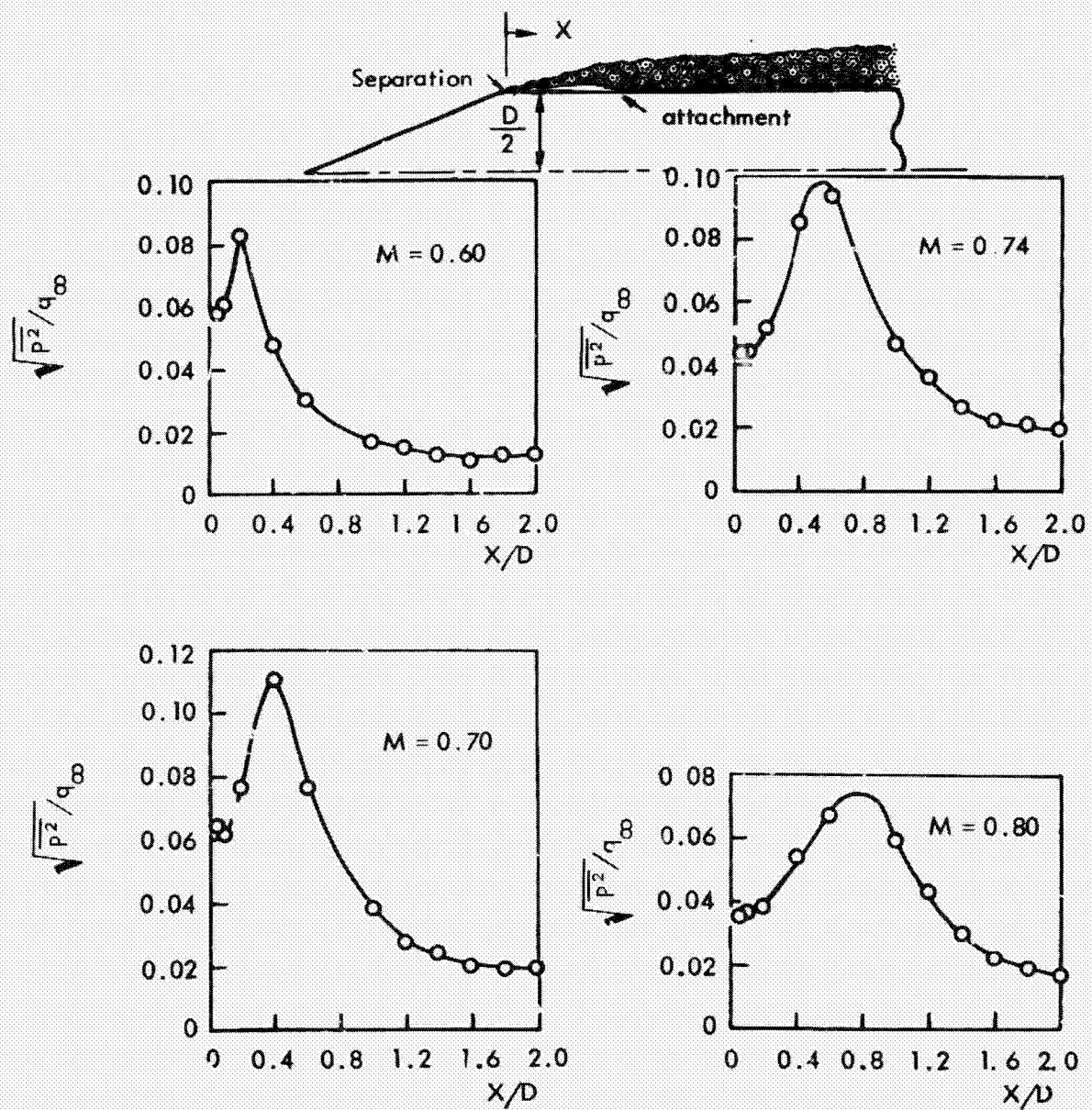
Figure 5. Axial Distribution of Fluctuating Pressures for Blunt Body Separated Flow; 25 Degree Cone-Cylinder (Reference 18)

$$* \text{ NOTE: } C_p = \frac{P_{\ell s} - P_\infty}{q_\infty}$$

$$= \frac{\text{(local static pressure)} - \text{(free-stream static pressure)}}{\text{free-stream dynamic pressure}}$$
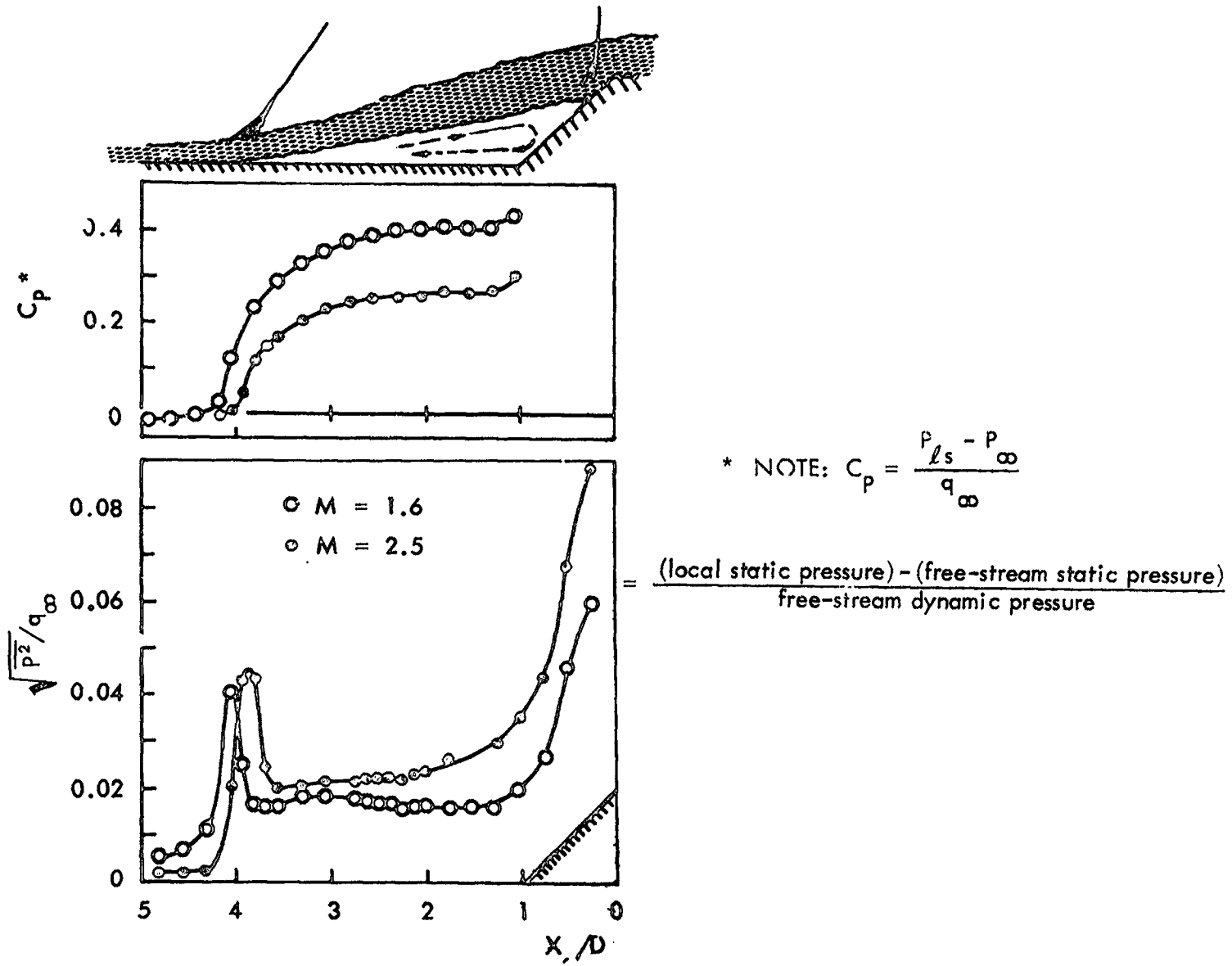
Figure 6. Axial Distributions of Static and Fluctuating Pressures for 45 Degree Flare Induced Separation (Ref. 14)
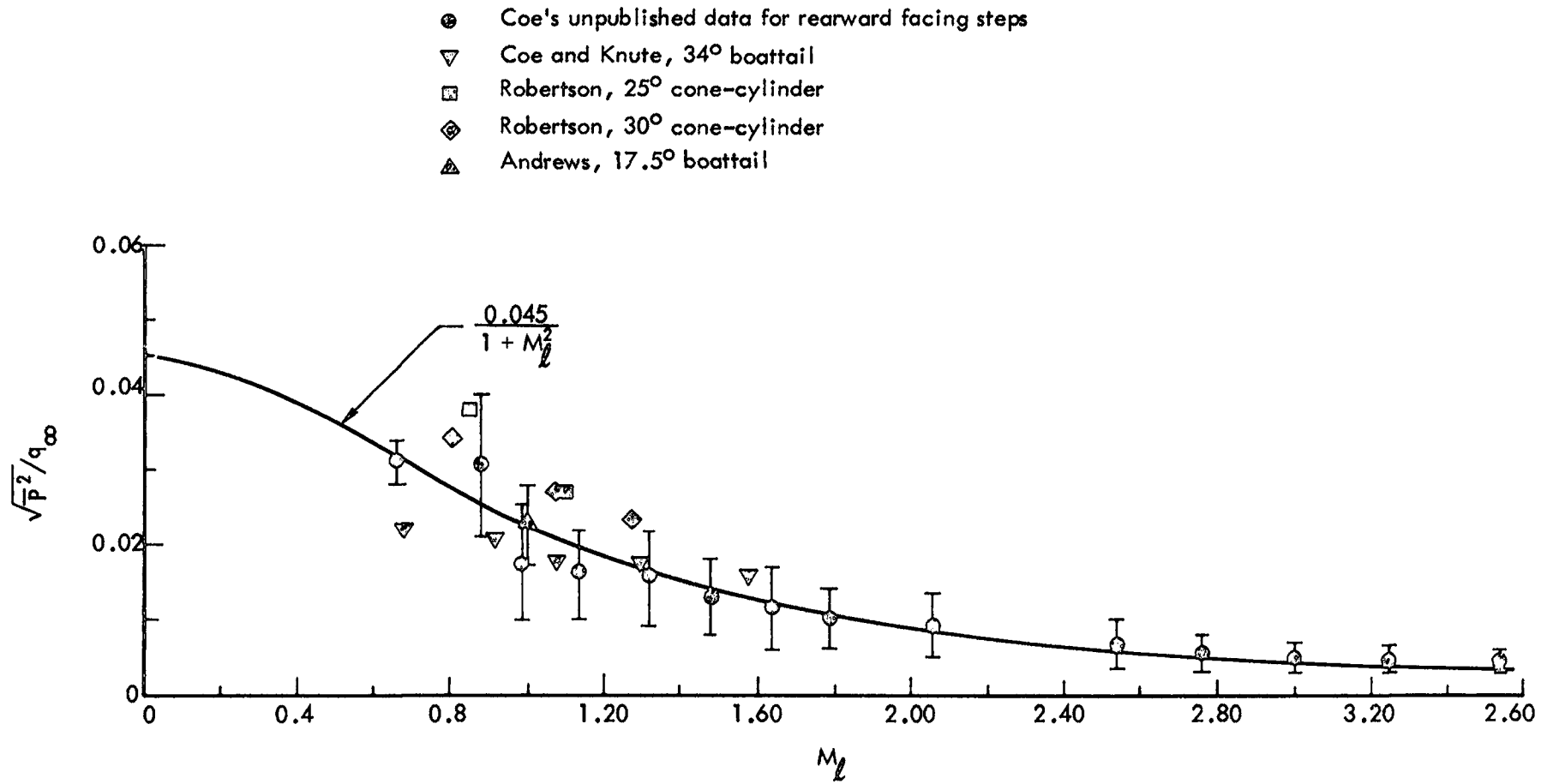
Figure 7. Variation of Normalized RMS Fluctuating Pressure Level with Local Mach Number for Expansion Induced Separated Flow
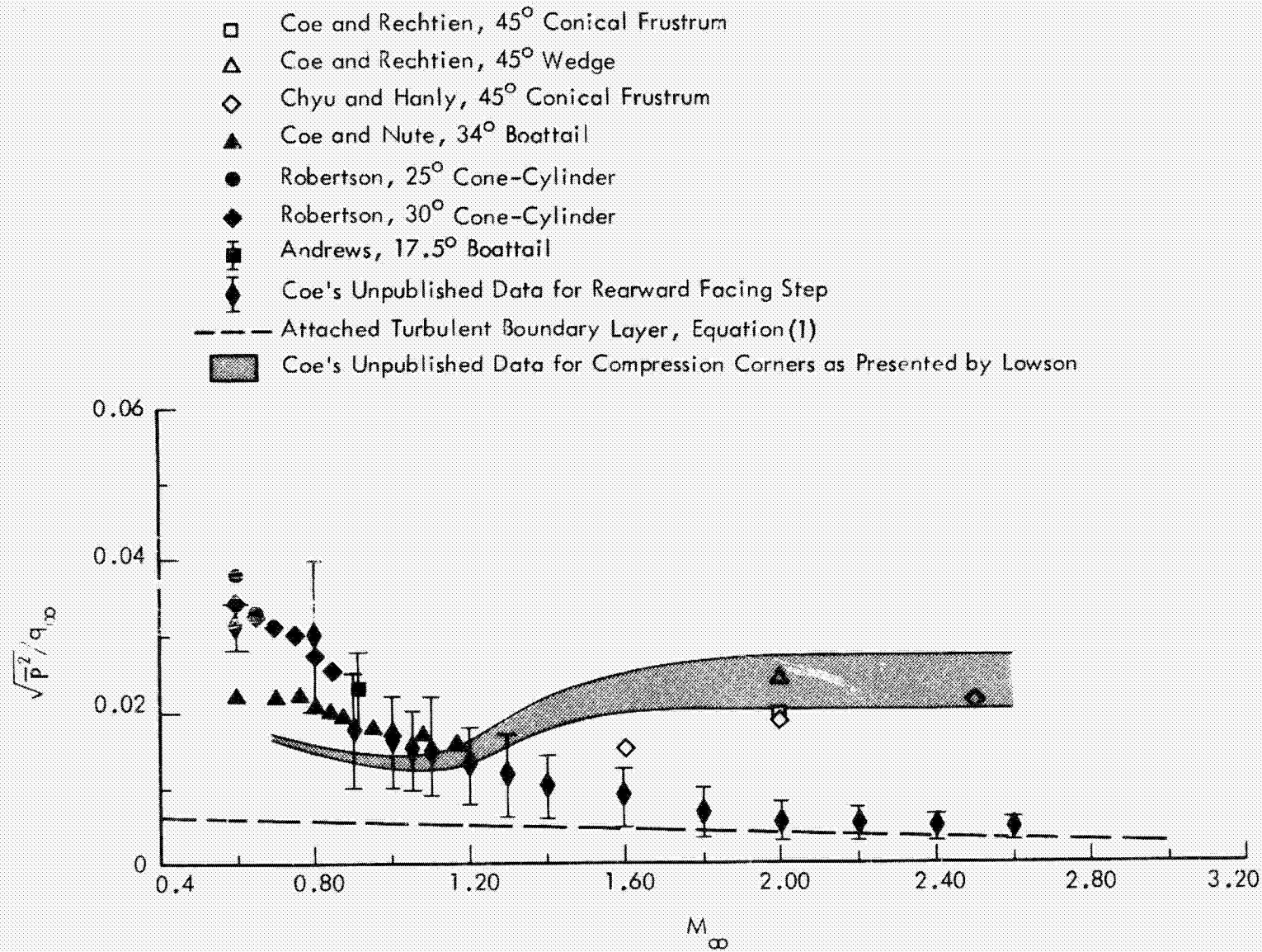
Figure 8. Variation of Normalized RMS Fluctuating Pressure Level with Free-Stream Mach Number for Expansion Induced and Compression Induced Separated Flows
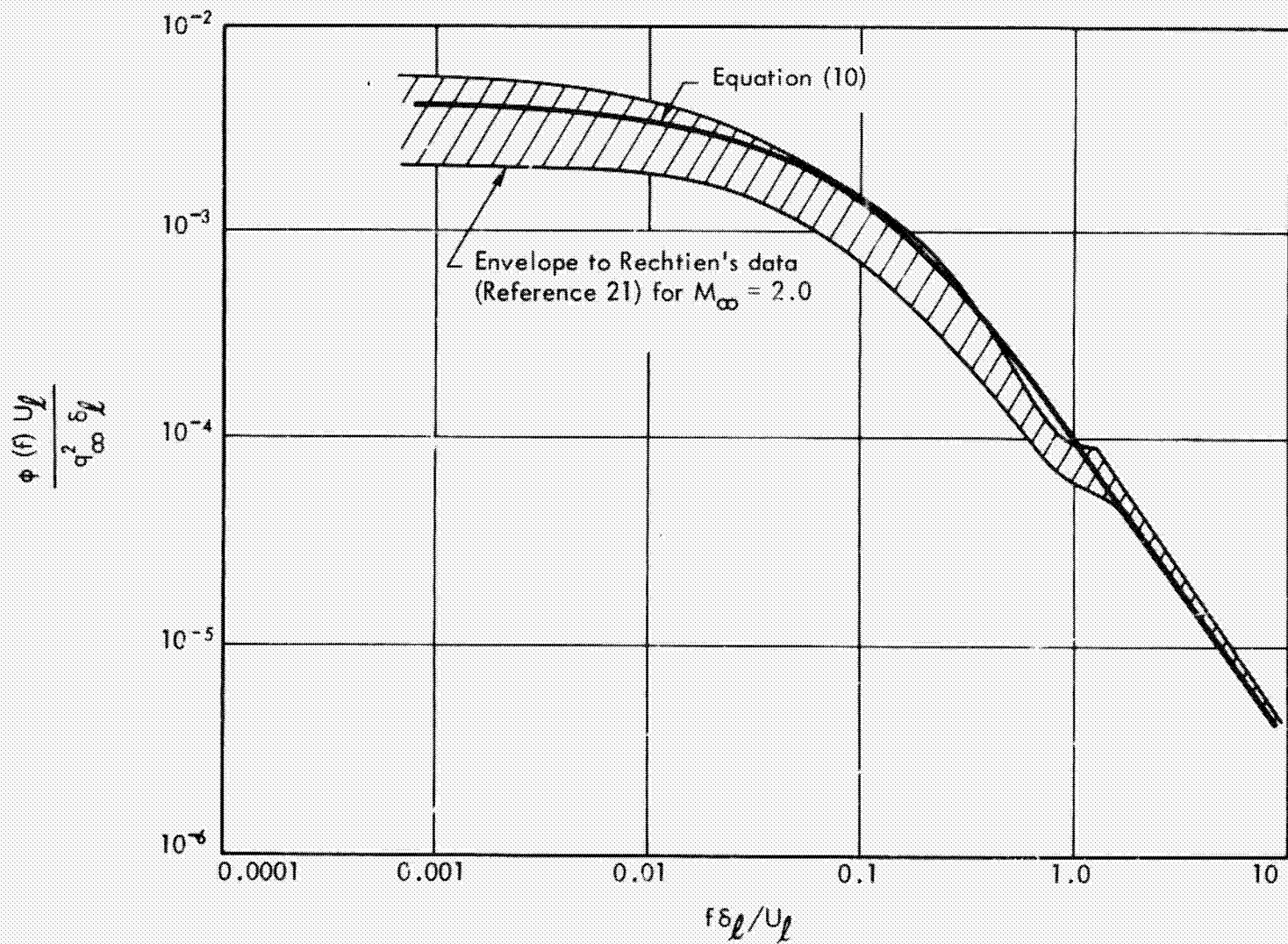
Figure 9. Power Spectrum of Fluctuating Pressures within Separated Flow Regions

$$1.61 \leq \zeta /\delta^* \leq 9.67$$
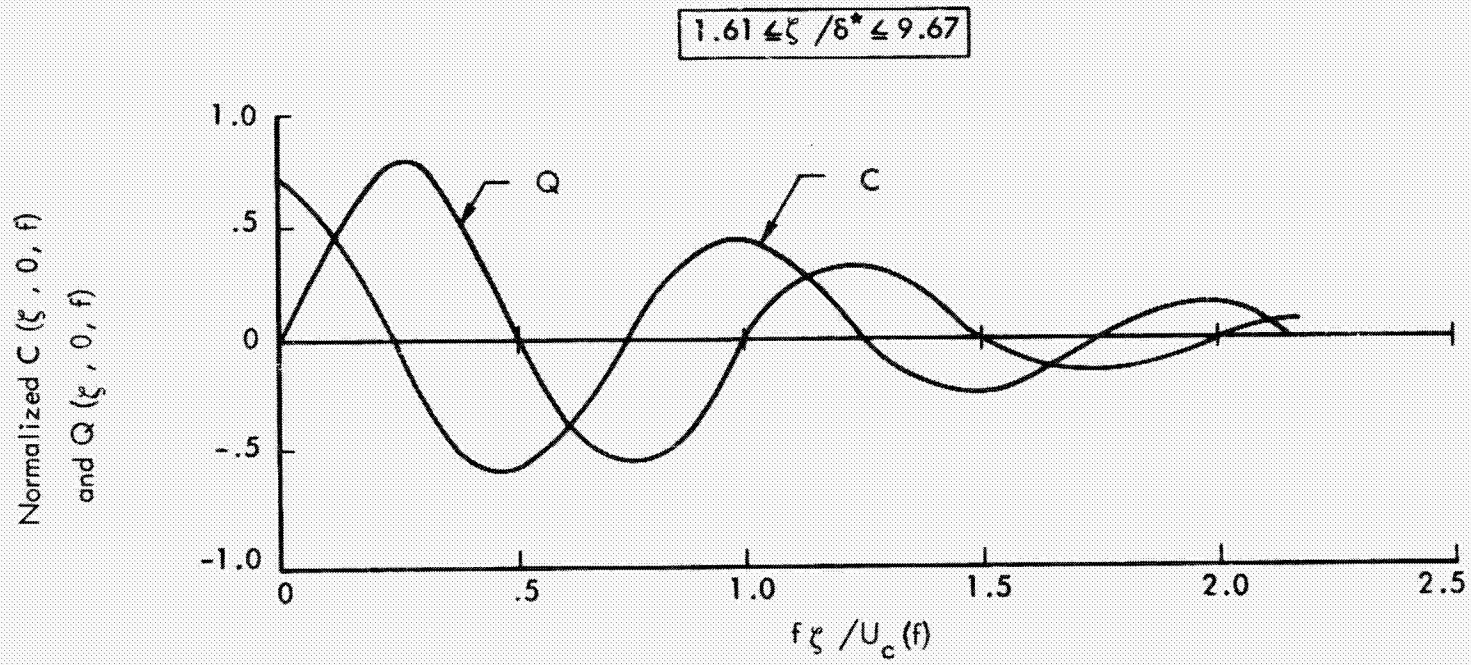
Figure 10. Typical Longitudinal Cross-Spectra of Pressure Fluctuations for Separated Flow (Ref. 14)
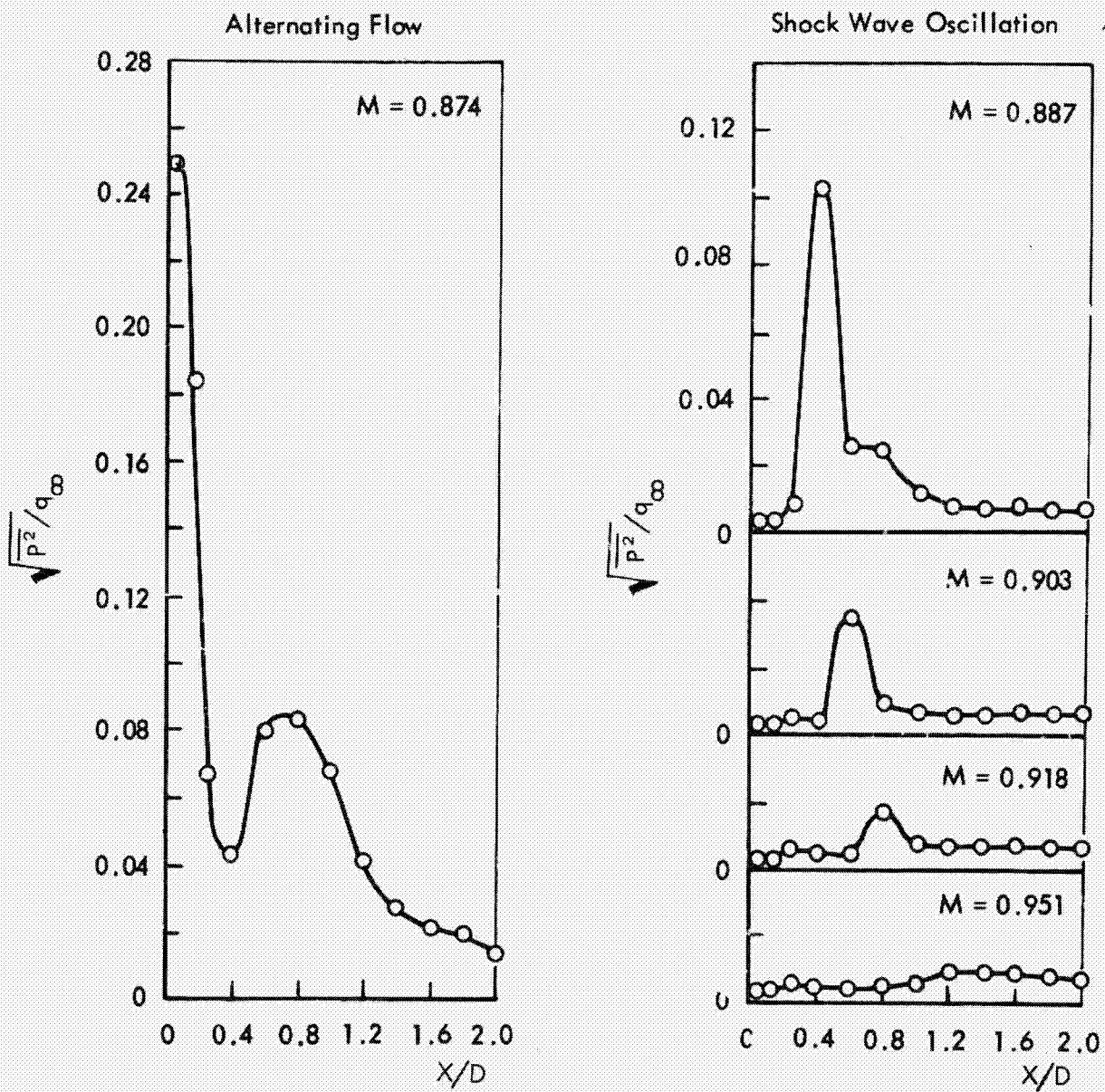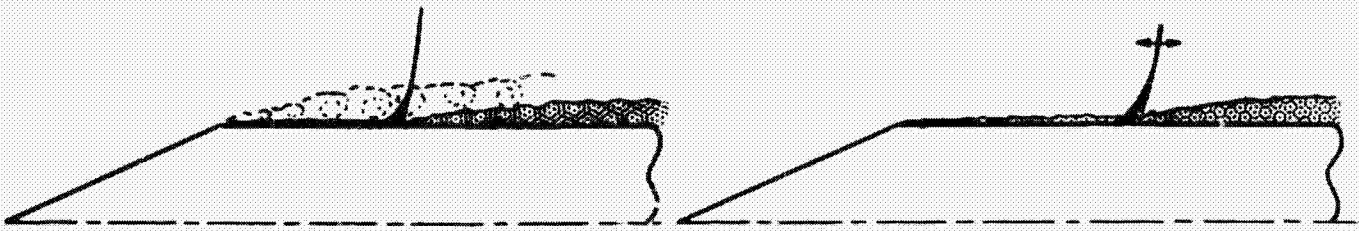
Figure 11. Axial Distribution of Fluctuating Pressures; 25 Degree Cone-Cylinder
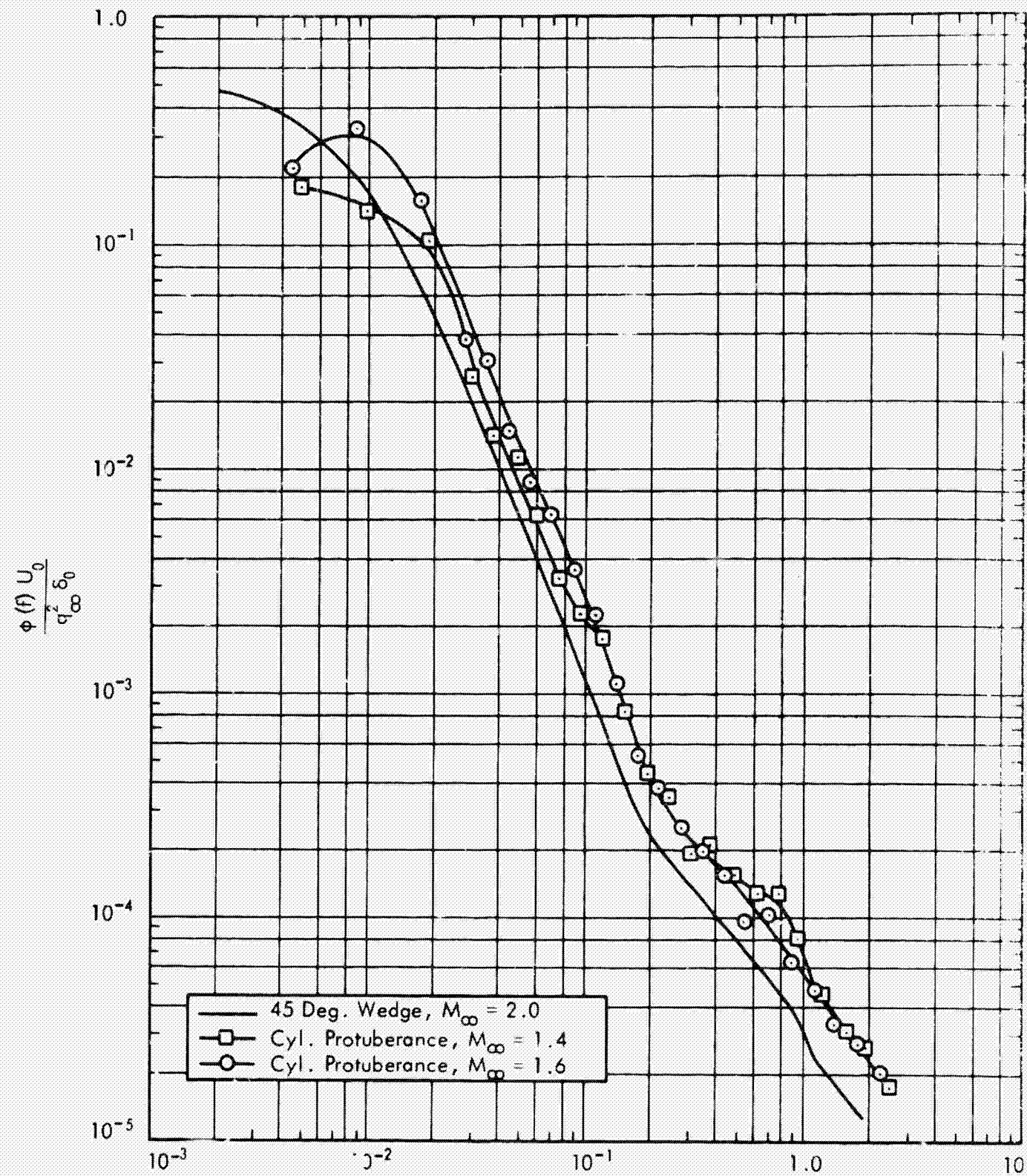
Figure 12. Comparison of Power Spectra for Shock-Wave Oscillation
Induced by Two- and Three-Dimensional Protuberances

294
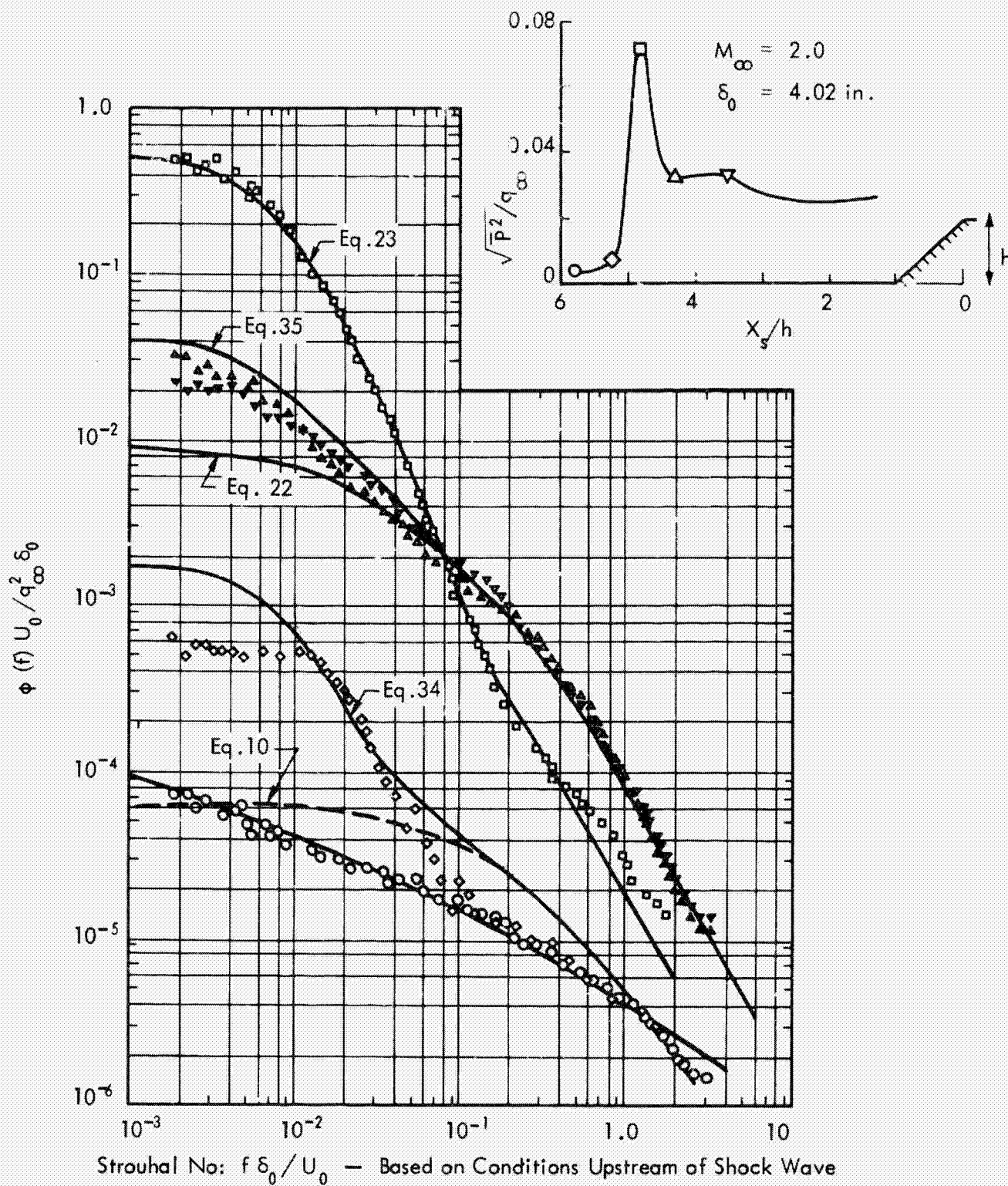
Figure 13. Longitudinal Distribution of Pressure Fluctuations and Typical Power Spectra in Vicinity of Supersonic Flow Separation Ahead of a 45° Wedge
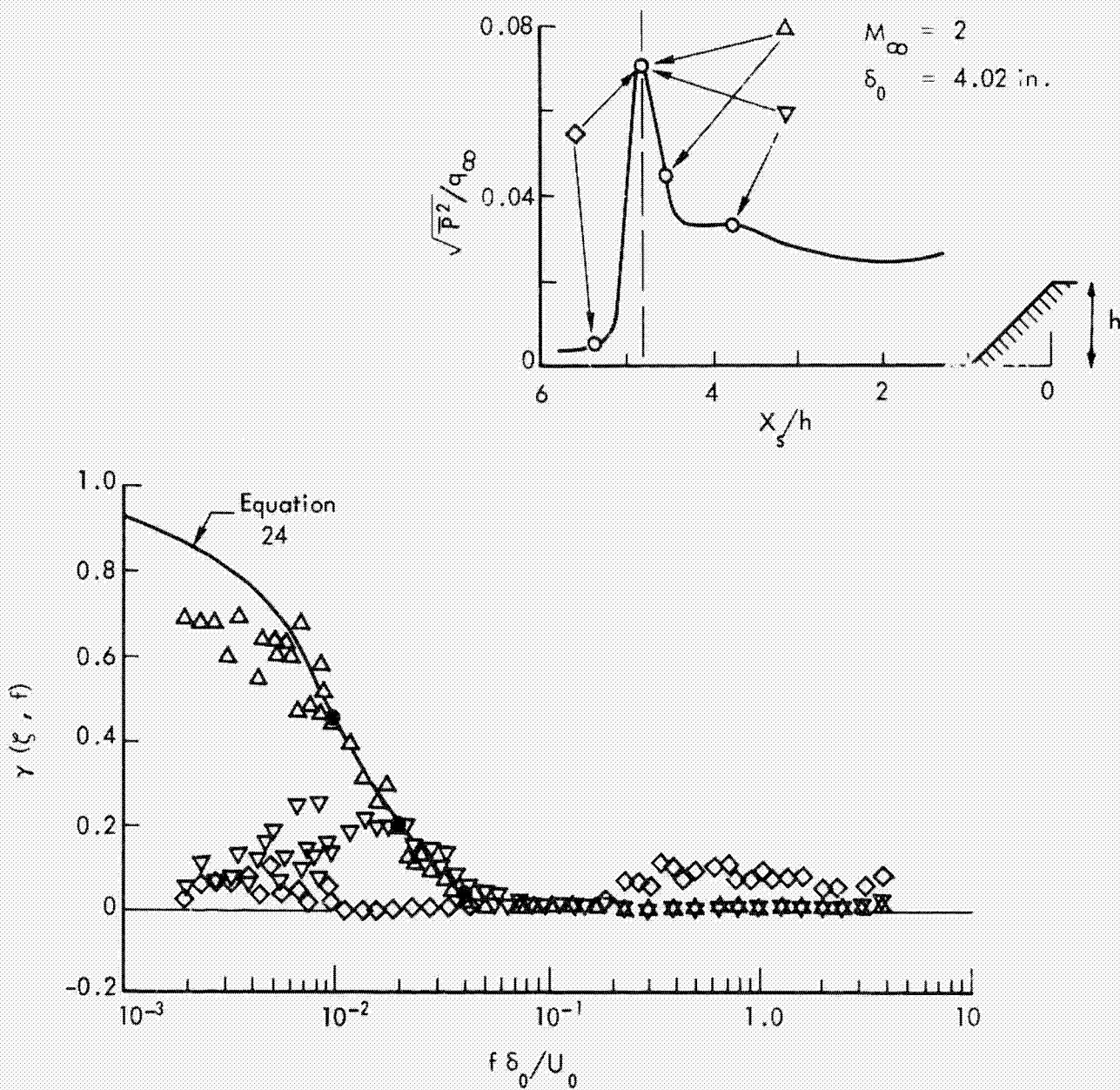
Figure 14. Correlation of Pressure Fluctuations Between Shock Wave and Adjacent Attached and Separated Flows (Reference 20)

APPENDIX C

PREDICTION OF STRUCTURAL RESPONSE AND NOISE REDUCTION

1.0 INTRODUCTION

A brief summary of the final equations for predicting the structural response and noise reduction of shroud structures was presented in Section 3.4 in the main body of this report. In this Appendix the equations for the joint acceptances for the various fluctuating pressure environments are presented. In addition, a more comprehensive description of the Statistical Energy Analysis is presented, together with the equations for the modal densities and coupling loss factors. The general forms for these joint acceptance expressions were originally derived in References 1 and 2, while the statistical energy equations were derived in References 3, 4, and 5.

In Section 2.0 of this Appendix, the general joint acceptance equations for cylindrical shells are presented for uniformly distributed excitation, i.e., a uniform pressure power spectral density over the structural surface. This is followed by a detailed presentation of the axial and circumferential joint acceptances, $j_m^2(\omega)$ and $j_n^2(\omega)$, respectively, for boundary layer turbulence, reverberant acoustic fields, progressive wave ducts, rocket noise, separated flow and shock-wave oscillation. In Sections 3.0 and 4.0, the axial and circumferential joint acceptances are presented for special cases of localized excitation, i.e., cases involving the joint acceptance of the total cylindrical shell when only a portion of the surface is subjected to excitation. Finally in Section 5.0, the relevant equations are presented for the computation of structural response and noise reduction utilizing the Statistical Energy Method.

2.0 JOINT ACCEPTANCE FOR UNIFORMLY DISTRIBUTED EXCITATION

2.1 General Joint Acceptance Equations — The general equations for the axial and circumferential joint acceptances, $j_m^2(\omega)$ and $j_n^2(\omega)$, for the (m n) mode of a cylindrical shell are given by:

$$j_m^2(\omega) = \int_{\bar{x}=0}^{1} \int_{\bar{x}'=0}^{1} C(\zeta; \omega) \cdot \sin m\pi\bar{x} \cdot \sin m\pi\bar{x}' \; d\bar{x} \; d\bar{x}'$$

$$j_n^2(\omega) = \int_{\bar{y}=0}^{1} \int_{\bar{y}'=0}^{1} C(\eta; \omega) \cos 2\pi n\bar{\eta} \; d\bar{y} \; d\bar{y}' \tag{2}$$

299

Expressions (1) and (2) involve double integration over one of the coordinate axes of the cylinder. Since, in both cases, the correlation coefficient is a function of separation distance, and since the modal deflection functions are spatially harmonic, the double integration can be reduced to a single integration, for an arbitrary correlation coefficient, by a transformation of the variables of integration. Consider first the expression for $j_m^2(\omega)$ given by (1). The product $[\sin m\pi\bar{x} \cdot \sin m\pi\bar{x}']$ can be written as

$$\sin m\pi\bar{x} \cdot \sin m\pi\bar{x}' = \frac{1}{2}\left[\cos m\pi\bar{\zeta} - \cos m\zeta\right]$$

$$\bar{\xi} = \bar{x} + \bar{x}' \qquad \bar{x} = \frac{1}{2}\left[\bar{\zeta} + \bar{\zeta}\right]$$

$$\bar{\zeta} = \bar{x} - \bar{x}' \qquad \bar{x}' = \frac{1}{2}\left[\bar{\xi} - \bar{\zeta}\right]$$

In (1), the region of integration is $0 \le x \le 1$, $0 \le x' \le 1$; and this region is shown in Figure 1. If $\bar{\xi}$ and $\bar{\zeta}$ represent the new variables of integration, the transformed region over which the integration is performed is shown in Figure 1. The element of area $d\bar{x}\,d\bar{x}'$ is transformed according to the equation

$$d\bar{x}\,d\bar{x}' = \begin{vmatrix} \dfrac{\partial \bar{x}}{\partial \bar{\xi}} & \dfrac{\partial \bar{x}}{\partial \bar{\zeta}} \\[2mm] \dfrac{\partial \bar{x}'}{\partial \bar{\xi}} & \dfrac{\partial \bar{x}'}{\partial \bar{\zeta}} \end{vmatrix} \cdot d\bar{\xi}\,d\bar{\zeta} = \begin{vmatrix} 1/2 & 1/2 \\ 1/2 & -1/2 \end{vmatrix} \cdot d\bar{\xi}\,d\bar{\zeta} = \left|-\frac{1}{2}\right| d\bar{\xi}\,d\bar{\zeta} = \frac{1}{2}\,d\bar{\xi}\,d\bar{\zeta}$$

By integrating first with respect to $\bar{\xi}$, the limits of integration for the first integral are $\bar{\xi} = |\bar{\zeta}|$ and $\bar{\xi} = 2 - |\bar{\zeta}|$. The limits of integration for the variable $\bar{\zeta}$ are $\bar{\zeta} = -1$ and $\bar{\zeta} = 1$. Thus (1) can be written in the form

$$j_m^2(\omega) = \frac{1}{4}\int_{\bar{\zeta}=-1}^{1} C(\bar{\zeta};\omega)\int_{\bar{\xi}=|\bar{\zeta}|}^{2-|\bar{\zeta}|}\left[\cos m\pi\bar{\zeta} - \cos m\pi\bar{\xi}\right]d\bar{\xi}\,d\bar{\zeta}$$

Performing the first integration gives

$$j_m^2(\omega) = \frac{1}{2}\int_{\bar{\zeta}=-1}^{1} C(\bar{\zeta};\omega)\left[(1 - |\bar{\zeta}|)\cos m\pi\bar{\zeta} + \frac{1}{m\pi}\sin m\pi|\bar{\zeta}|\right]d\bar{\zeta} \tag{3}$$

However, $C(\bar{\zeta}; \omega)$ is an even function of $\bar{\zeta}$ so that Equation (3) reduces to

$$j_m^2(\omega) = \int_{\bar{\zeta}=0}^{1} C(\bar{\zeta};\omega)\left[(1-\bar{\zeta})\cos m\pi\bar{\zeta} + \frac{1}{m\pi}\sin m\pi\bar{\zeta}\right]d\bar{\zeta} \tag{4}$$

A similar transformation applied to (2) gives the general expression for the joint-acceptance of the ring modes

$$j_n^2(\omega) = 2\int_{\bar{\eta}=0}^{1}(1-\bar{\eta})\,C(\bar{\eta};\omega)\cos 2n\pi\bar{\eta}\,d\bar{\eta} \tag{5}$$

The above expression for the case of the breathing modes $(n=0)$ reduces to

$$j_0^2(\omega) = 2\int_{\bar{\eta}=0}^{1}(1-\bar{\eta})\,C(\bar{\eta};\omega)\,d\bar{\eta} \tag{6}$$

2.2 Boundary Layer Turbulence — The space correlation functions for boundary layer turbulence are given by the expressions:

$$C(\bar{\zeta};\omega) = \exp\left[-\delta_x|\bar{\zeta}|\right]\cos\tau_x\bar{\zeta} \tag{7}$$

$$C(\bar{\eta};\omega) = \exp\left[-\delta_y|\bar{\eta}|\right] \tag{8}$$

where

$$\delta_x = .10\frac{L_x\omega}{U_c} + .27\frac{L_x}{\delta_b}$$

$$\tau_x = \frac{L_x\omega}{U_c}$$

$$\delta_y = .72\frac{L_y\omega}{U_c} + 1.95\frac{L_y}{\delta_b} \tag{9}$$

$$\bar{\zeta} = \zeta/L_x$$

$$\bar{\eta} = \eta/L_y$$

The joint acceptance of the axial modes of the cylinder for boundary layer turbulence can be obtained by substituting (7) into (4), performing the necessary integration and simplifying the resulting algebraic expressions, giving

$$j_m^2(\omega) = \frac{2}{(m\pi)^2 \Delta^2}\left[P\left\{ 1 - (-1)^m e^{-\bar{\delta}_x} \cos \bar{\gamma}_x \right\} + 4(-1)^m q \ e^{-\bar{\delta}_x} \sin \bar{\gamma}_x + \frac{m\pi}{2} r\Delta \right] \qquad (10)$$

where

$$\Delta = \left[1 + \left(\frac{\gamma_x}{m\pi}\right)^2 + \left(\frac{\delta_x}{m\pi}\right)^2 \right]^2 - 4\left(\frac{\gamma_x}{m\pi}\right)^2$$

$$P = \left[1 - \left(\frac{\gamma_x}{m\pi}\right)^2 + \left(\frac{\delta_x}{m\pi}\right)^2 \right]^2 - 4\left(\frac{\gamma_x}{m\pi}\right)^2 \left(\frac{\delta_x}{m\pi}\right)^2$$

$$q = \left(\frac{\gamma_x}{m\pi}\right)\left(\frac{\delta_x}{m\pi}\right)\left[1 - \left(\frac{\gamma_x}{m\pi}\right)^2 + \left(\frac{\delta_x}{m\pi}\right)^2 \right] \qquad (11)$$

$$r = \left(\frac{\delta_x}{m\pi}\right)\left[1 + \left(\frac{\gamma_x}{m\pi}\right)^2 + \left(\frac{\delta_x}{m\pi}\right)^2 \right]$$

This expression agrees with that obtained by Wilby in Reference 6.

Using (8) and (5), the comparable expression for the circumferential bending mode is

$$j_n^2(\omega) = \frac{2\delta_y}{\left[(2\pi n)^2 + \delta_y^2\right]} + 2\frac{(2\pi n) - \delta_y}{\left[(2\pi n)^2 + \delta_y^2\right]^2}\left[1 - e^{-\delta_y} \right] \qquad (12)$$

2.3 Reverberant Acoustic Field — It is assumed that the space correlation functions for the reverberant acoustic field can be represented by the expressions:

$$C(\bar{\zeta}; \omega) = \frac{\sin(2\pi \frac{L_x}{\lambda}\bar{\zeta})}{2\pi \frac{L_x}{\lambda}\bar{\zeta}}$$

$$\qquad (13)$$

$$C(\bar{\eta}; \omega) = \frac{\sin(2\pi \frac{L_y}{\lambda}\bar{\eta})}{2\pi \frac{L_y}{\lambda}\bar{\eta}}$$

302

The joint acceptance expression for the axial modes of the cylinder to a reverberant acoustic field is obtained by substituting the first of Equations (13) into (4). The resulting integral contains three terms in the integrand. The first term can be written in terms of cosine integrals, the second term can be integrated directly, and the third term can be written in terms of sine integrals. The joint acceptance equation can thus be expressed as follows:

$$
j_m^2 (\omega) = \frac{1}{(2\pi)^2 m \, L_x/\lambda} \left[\text{Cin} \left\{ \pi \, (m + 2L_x/\lambda) \right\} - \text{Cin} \left\{ \pi \left| m - 2L_x/\lambda \right| \right\} \right]
$$

$$
+ \frac{1}{4\pi L_x/\lambda} \left[\text{Si} \left\{ \pi \, (m + 2L_x/\lambda) \right\} - \text{Si} \left\{ \pi \, (m - 2L_x/\lambda) \right\} \right] \tag{14}
$$

$$
+ \frac{1}{(m\pi)^2} \frac{1 - (-1)^m \cos (2\pi L_x/\lambda)}{1 - (2L_x/m\lambda)^2}
$$

where

$$
\text{Cin} \ (z) = \int_0^z \frac{1 - \cos x}{x} \, dx \qquad \text{(cosine integral)}
$$

$$
\text{Si} \ (z) = \int_0^z \frac{\sin x}{x} \, dx \qquad \text{(sine integral)}
$$

Next, substituting (3) into (5) and performing the integration gives the following expression for the joint acceptance of the circumferential modes to a reverberant acoustic field namely,

$$
j_n^2 (\omega) = \frac{1}{2\pi (L_y/\lambda)} \left[\text{Si} \left\{ 2\pi \, (n + L_y/\lambda) \right\} - \text{Si} \left\{ 2\pi \, (n - L_y/\lambda) \right\} \right]
$$

$$
+ \frac{1}{2 (n\pi)^2} \frac{1 - \cos (2\pi L_y/\lambda)}{1 - (L_y/n\lambda)^2} \qquad \text{at } n \neq 0 \tag{15}
$$

$$
= \frac{\text{Si} \left| 2\pi L_y/\lambda \right|}{\pi L_y/\lambda} - \frac{1 - \cos (2\pi L_y/\lambda)}{2\pi^2 (L_y/\lambda)^2} \qquad \text{at } n = 0
$$

As shown in Reference 7, the sine and cosine integrals can be evaluated numerically by using power series expansions for small values of z ($0 < z < 1$), rational function approximations for intermediate values of z ($1 < z < 50$), and asymptotic expansions for large values of z ($50 < z$). The indicated ranges of the values of z were used

303

in the present analysis; and for these ranges, it was necessary to use at most five terms in the power series and asymptotic expansions to maintain a maximum error of 10^{-7} in the numerical values of the sine and cosine integrals. The approximating expressions used in the numerical evaluations are summarized below:

$$Si(z) = \sum_{n=0}^{\infty} \frac{(-1)^n z^{2n+1}}{(2n+1)(2n+1)!}$$

$$Cin(z) = \sum_{n=0}^{\infty} \frac{(-1)^{n+1} z^{2n}}{(2n)(2n)!}$$

$$Si(z) = \frac{\pi}{2} - f(z)\cos z - g(z)\sin z$$

$$Ci(z) = f(z)\sin z - g(z)\cos z = -\int_z^{\infty} \frac{\cos t}{t}\, dt$$

$$Cin(z) = \gamma + Lnz - Ci(z) \tag{16}$$

$$\gamma = \text{Euler's constant} = .5772156649.$$

$$f(z) = \int_0^{\infty} \frac{e^{-zt}}{t^2+1}\cdot dt \doteq \frac{1}{z}\frac{a_8 z^8 + a_6 z^6 + a_4 z^4 + a_2 z^2 + a_0}{b_8 z^8 + b_6 z^6 + b_4 z^4 + b_2 z^2 + b_0} \qquad 1 < z < \infty$$

$$g(z) = \int_0^{\infty} \frac{te^{-zt}}{t^2+1}\cdot dt \doteq \frac{1}{z^2}\frac{c_8 z^8 + c_6 z^6 + c_4 z^4 + c_2 z^2 + c_0}{d_8 z^8 + d_6 z^6 + d_4 z^4 + d_2 z^2 + d_0} \qquad 1 < z < \infty$$

$$f(z) = \frac{1}{z}\left[1 - \frac{2!}{z^2} + \frac{4!}{z^4} - \dots\right] \qquad 1 \ll z$$

$$g(z) = \frac{1}{z^2}\left[1 - \frac{3!}{z^2} + \frac{5!}{z^4} - \dots\right] \qquad 1 \ll z$$

Numerical values for the constants a_i, b_i, c_i, and d_i appearing in the expressions $f(z)$ and $g(z)$ are tabulated in Table I.

2.4 Non-Decaying Progressive Wave Duct Excitation — Assuming that the sound pressure level is uniform along the ducts, the axial space correlation coefficient $C(\zeta; \omega)$ for the acoustic field is

$$C(\zeta; \omega) = \cos(\omega\zeta/c)$$

or in nondimensional form

$$C(\bar{\zeta}; \omega) = \cos\gamma_x \bar{\zeta} \tag{17}$$

where

$$\gamma_x = \frac{L_x \omega}{c} = 2\pi L_x/\lambda$$

λ = acoustic wave length

c = speed of sound

To obtain the joint acceptance of the axial modes of the cylinder for a non-decaying progressive wave excitation, substitute (17) into (4). Performing the necessary integration leads to

$$j_m^2(\omega) = \frac{2}{(m\pi)^2} \frac{1 - (-1)^m \cos(2\pi L_x/\lambda)}{\left[1 - 4(L_x/m\lambda)^2\right]^2}$$

$$j_m^2(\omega) = \frac{2}{(m\pi)^2} \frac{1 - (-1)^m \cos(2\pi L_x/\lambda)}{\left[1 - (2L_x/m\lambda)^2\right]^2} \tag{18}$$

$$= \frac{2}{(m\pi)^2} \frac{1 - (-1)^m \cos(2\pi L_x f/c)}{\left[1 - (2L_x f/mc)^2\right]^2}$$

The space correlation function for the circumferential modes was not defined explicitly above since the joint acceptance expression can be obtained directly as follows. When a radially directed oscillatory point force acts on the cylinder, the circumferential

305

bending modes will align themselves so that each mode exhibits an antinode at the point of application of the force. It is reasonable that the acoustic field of a single correlated span or duct will cause the circumferential modes to have antinodes located at the center of the duct. Since the sound field for such a duct has a unit circumferential correlation, it is clear that the lateral joint acceptance for one duct is

$$j_n^2(\omega) = \left[\int_{-\Delta/2}^{\Delta/2} \cos 2\pi n \bar{y} \cdot d\bar{y} \right]^2 \tag{19}$$

where Δ is the dimensional width of a duct. If there are N uncorrelated ducts the total joint acceptance is N-times that given by Equation (19) so that

$$j_n^2(\omega) = N \left[\int_{-\Delta/2}^{\Delta/2} \cos 2\pi n \bar{y} \cdot d\bar{y} \right]^2 \tag{20}$$

Performing the integration of Equation (20),

$$\begin{aligned} j_n^2(\omega) &= \frac{1}{N} \left[\frac{\sin n\pi/N}{n\pi/N} \right]^2 \quad n \neq 0 \\ &= \frac{1}{N} \quad\quad\quad\quad n = 0 \end{aligned} \tag{21}$$

Equation (21) has been numerically evaluated for the first ten ring modes for each of the following uncorrelated duct patterns; $N = 1, 2, 4, 8,$ and 16. The results are presented in Table II.

2.5 Rocket Noise — The space correlation functions for the rocket noise environment can be represented by the following expressions:

$$C(\bar{\zeta}; \omega) = \cos \gamma_x \bar{\zeta} \tag{22}$$

$$C(\bar{\eta}; \omega) = \frac{\sin \left(2\pi \frac{L_y}{\lambda^*} \bar{\eta} \right)}{2\pi \frac{L_y}{\lambda^*} \bar{\eta}} \tag{23}$$

where

$$\gamma_x \quad = \quad \frac{\omega L_x}{c} \cdot \sin \beta$$

c =   Speed of sound

β =   Angle between the normal to the incident plane wave and the horizontal

$\lambda^* \quad = \quad 0.1 \, \lambda \, f^{3/4}$

$\lambda \quad = \quad c/f$

Notice that the functional form of Equation (22) is identical to Equation (17) for the non-decaying progressive wave duct, while the functional form of Equation (23) is identical to Equation (13) for the reverberant acoustic field. Thus the axial and circumferential joint acceptance for rocket noise will be identical to Equations (18) and (15), respectively with the appropriate substitutions for γ_x and λ^*.

    2.6 <u>Separated Flow</u> — The space correlation functions for the separated flow environment can be represented by the following expressions:

$$C(\overline{\zeta}; \omega) = \exp\left[-\delta_x \left|\overline{\zeta}\right|\right] \cos \gamma_x \overline{\zeta} \qquad (24)$$

$$C(\overline{\eta}; \omega) = \exp\left[-\delta_y \left|\overline{\eta}\right|\right] \qquad (25)$$

where δ_x, γ_x and δ_y are as defined in Section 3.2.2.5 in the main body of this report. Notice that the functional forms of Equations (24) and (25) are identical to those for the attached boundary layer, i.e., Equations (7) and (8). Thus the axial and circumferential joint acceptances for separated flow are identical to Equations (10) and (12) respectively, with the appropriate substitutions for δ_x, γ_x and δ_y from Section 3.2.2.5.

2.7 Shock Wave Oscillation — The space correlation functions for the shock wave oscillation environment can be represented by the following expressions:

$$C(\overline{\zeta}; \omega) = \exp\left[-\delta_{x \cdot}\left|\overline{\zeta}\right|\right] \cdot \cos \gamma_x \overline{\zeta} \tag{26}$$

$$C(\overline{\eta}; \omega) = 1.0 \text{ (over each of 4 quadrants)} \tag{27}$$

where

$$\delta_x = \frac{3 \cdot 18 \omega L_x}{U_0}$$

$$\gamma_x = \frac{\omega L_x}{U_0}$$

$$U_0 = \text{local velocity upstream of the shock wave}$$

It should be noted that the functional forms defined in Equations (26) and (27) are identical to those for the attached boundary layer and the non-decaying progressive wave duct, respectively. Thus the axial and circumferential joint acceptances for the shock wave oscillation are identical to Equations (10) and (21) respectively, with the appropriate substitutions for δ_x, γ_x, and U_0. Note also that for the shock-wave oscillation, N is equal to 4 in Equation (21).

3.0 AXIAL JOINT ACCEPTANCES FOR CASES INVOLVING LOCALIZED EXCITATION

Consider a pinned-pinned beam, such as that shown in Figure 2, on which a distributed random pressure loading acts over the range $x_1 \leq x \leq x_2$. The center of the loading is located at x_0, and the length of the loading is Δ_x so that

$$x_0 = (x_2 + x_1)/2$$

$$\Delta_x = x_2 - x_1 \tag{28}$$

It is assumed that, within the range $x_1 \le x \le x_2$, the load is homogeneous and is characterized by a space correlation function $C(\zeta; \omega)$ which depends only upon the separation distance ζ between any two points in the range $x_1 \le x \le x_2$. The general equation for the joint acceptance, $j_m^2(\omega)$, of the m-th mode is:

$$j_m^2(\omega) = \frac{1}{L_x^2} \int_{x=x_1}^{x_2} \int_{x'=x_1}^{x_2} C(\zeta; \omega) \cdot \phi_m(x) \cdot \phi_m(x') \, dx \, dx'$$

$$= \int_{\bar{x}=\bar{x}_1}^{\bar{x}_2} \int_{\bar{x}'=\bar{x}_1}^{\bar{x}_2} C(\bar{\zeta}; \omega) \cdot \phi_m(\bar{x}) \cdot \phi_m(\bar{x}') \cdot d\bar{x} \cdot d\bar{x}' \tag{29}$$

$$\phi_m(x) = \phi_m(\bar{x}) = \sin(m\pi x/L_x) = \sin(m\pi\bar{x}) \tag{30}$$

$$\bar{x} = x/L_x \tag{31}$$

Following the procedure described in Section 2.1 above, the double integral in Equation (29) can be reduced to a single integral. This transformation of the integration leads to:

$$j_m^2(\omega) = \frac{1}{4} \int_{\bar{\zeta}=-\bar{A}_x}^{\bar{A}_x} C(\bar{\zeta}; \omega) \int_{\xi=2\bar{x}_1+|\bar{\zeta}|}^{2\bar{x}_2-|\bar{\zeta}|} \left[\cos m\pi\bar{\zeta} - \cos m\pi\bar{\xi} \right] \cdot d\bar{\xi} \cdot d\bar{\zeta}$$

$$= \frac{1}{2} \int_{\bar{\zeta}=-\bar{A}_x}^{\bar{A}_x} C(\bar{\zeta}; \omega) \left[(\bar{A}_x - |\bar{\zeta}|) \cos m\pi\bar{\zeta} - \frac{\cos 2m\pi\bar{x}_0}{m\pi} \sin m\pi(\bar{A}_x - |\bar{\zeta}|) \right] d\bar{\zeta}$$

$$= \int_{\bar{\zeta}=0}^{\bar{A}_x} C(\bar{\zeta}; \omega) \left[(\bar{A}_x - \bar{\zeta}) \cos m\pi\bar{\zeta} - \frac{\cos 2m\pi\bar{x}_0}{m\pi} \sin m\pi(\bar{A}_x - \bar{\zeta}) \right] d\bar{\zeta} \tag{32}$$

The integral in Equation (32) can be further simplified to

$$j_m^2(\omega) = \bar{A}_x^2 \int_{z=0}^{1} C(z; \omega) \left[(1-z) \cos m\pi z - \frac{\cos 2m\pi\bar{x}_0}{m\pi} \sin m\pi(1-z) \right] dz$$

309

or

$$\frac{j_m^2(\omega)}{\overline{\Delta}_x^2} = -\int_0^1 Z \cdot C(z;\omega) \cdot \cos m\pi z \cdot dz$$

$$+ \left[1 - \frac{\cos 2m\pi\overline{x}_0 \cdot \sin m\pi}{m\pi}\right] \int_0^1 C(z;\omega) \cdot \cos m\pi z \cdot dz \qquad (33)$$

$$+ \frac{\cos 2m\pi\overline{x}_0 \cdot \cos m\pi}{m\pi} \int_0^1 C(z;\omega) \cdot \sin m\pi z \cdot dz$$

where

$$\left.\begin{array}{l} z = \overline{\zeta}/\overline{\Delta}_x = \zeta/\Delta_x \\ m = m\,\overline{\Delta}_x \end{array}\right\} \qquad (34)$$

As $\overline{\Delta}_x \longrightarrow 0$, the right-hand side of Equation (33) approaches a finite, non-zero quantity. For example, in the case of a point force applied at x_0, $C(z;\omega) = 1.0$, $m = 0$, the first term in Equation (33) is equal to $(1/2)$, the second is equal to $-\cos 2m\pi\overline{x}_0$, and the third term is equal to $(1/2)\cos 2m\pi\ \overline{x}_0$; and hence

$$\lim_{\Delta_x \to 0} \frac{j_m^2(\omega)}{\overline{\Delta}_x^2} = \frac{1}{2}\left[1 - \cos 2m\pi\overline{x}_0\right] = \sin^2 m\pi\overline{x}_0 \qquad (35)$$

which is the correct result.

Boundary Layer Turbulence Parallel to Flow Axis

The space correlation function, $C(z;\omega)$, selected here for representing localized boundary layer turbulence is:

$$C(z;\omega) = e^{-\delta_x |z|} \cdot \cos \gamma_x z \qquad (36)$$

$$\left.\begin{array}{l} \gamma_x = \omega \Delta_x/U_c \\ \delta_x = a\,\gamma_x + b\,\Delta_x/\delta_b \end{array}\right\} \qquad (37)$$

U_c = convection velocity

δ_b = boundary layer thickness

a, b = constants dependent upon measured characteristics of boundary layer flow field.

310

When the boundary layer is distributed over the entire length of the beam, then $\Delta_x = L_x$ and Equation (37) reduces to those presented in Section 2.2 above.

Upon substituting Equation (36) into Equation (33) and performing the integration gives:

$$
\begin{aligned}
\frac{j_m^2(\omega)}{\overline{\Delta}_x^2} =& \left[\frac{\delta_x\,[\delta_x^2 + (\gamma_x \pm m\pi)^2] + \delta_x^2 - (\gamma_x \pm m\pi)^2}{2\,[\delta_x^2 + (\gamma_x \pm m\pi)^2]^2} \right] e^{-\delta_x} \cos(\gamma_x \pm m\pi) \\[2mm]
&- \left[\frac{\gamma_x \pm m\pi}{2} \cdot \frac{\delta_x^2 + (\gamma_x \pm m\pi)^2 + 2\delta_x}{[\delta_x^2 + (\gamma_x \pm m\pi)^2]^2} \right] e^{-\delta_x} \sin(\gamma_x \pm m\pi) \\[2mm]
&- \frac{\delta_x^2 - (\gamma_x \pm m\pi)^2}{2\,[\delta_x^2 + (\gamma_x \pm m\pi)^2]^{-2}} + \frac{1}{2}\left[1 - \frac{\cos 2m\pi\,\overline{x}_0 \cdot \sin m\pi}{m\pi}\right] \cdot \\[2mm]
&\cdot \left[\frac{\delta_x}{\delta_x^2 + (\gamma_x \pm m\pi)^2} \left\{ 1 - e^{-\delta_x} \cos(\gamma_x \pm m\pi) \right\} \right. \\[2mm]
&\left. + \frac{\gamma_x \pm m\pi}{\delta_x^2 + (\gamma_x \pm m\pi)^2}\, e^{-\delta_x} \sin(\gamma_x \pm m\pi) \right] \\[2mm]
&\pm \frac{\cos 2m\pi\,\overline{x}_0 \cdot \cos m\pi}{2m\pi}\left[\frac{(\gamma_x \pm m\pi)}{\delta_x^2 + (\gamma_x \pm m\pi)^2} \left\{ 1 - e^{-\delta_x} \cos(\gamma_x \pm m\pi) \right\} \right. \\[2mm]
&\left. - \frac{\delta_x}{\delta_x^2 + (\gamma_x \pm m\pi)^2}\, e^{-\delta_x} \sin(\gamma_x \pm m\pi) \right]
\end{aligned}
\tag{38}
$$

Equation (38) contains twice as many terms as are shown; one set is associated with the (+) sign and one set is associated with the (−) sign. The total equation for $j_m^2(\omega)/\overline{\Delta}_x^2$ is obtained by algebraically adding these two sets of terms.

When the boundary layer extends over the entire length of the beam, then $\overline{\Delta}_x = 1.0$, $m = m = $ integer, and Equation (38) can be reduced to:

311

$$j_m^2(\omega) = \frac{1}{2}\left[\frac{(\gamma_x \pm m\pi)^2 - \delta_x^2}{[\delta_x^2 + (\gamma_x \pm m\pi)^2]^2} + \frac{(m\pi \pm \gamma_x)/m\pi}{\delta_x^2 + (\gamma_x \pm m\pi)^2}\right]\left\{1 - (-1)^m\, e^{-\delta_x}\cos\gamma_x\right\}$$

$$+ \left[\frac{-\delta_x(\gamma_x \pm m\pi)}{[\delta_x^2 + (\gamma_x \pm m\pi)^2]^2} \mp \frac{\delta_x/2m\pi}{\delta_x^2 + (\gamma_x \pm m\pi)^2}\right](-1)^m\, e^{-\delta_x}\sin\gamma_x$$

$$+ \frac{\delta_x/2}{\delta_x^2 + (\gamma_x \pm m\pi)^2} \tag{39}$$

where the ($\pm$) sign once again implies a summation of ($+$) terms and ($-$) terms. It is a straightforward exercise to show that Equation (39) can be rewritten in the more condensed form of Equation (10) in Section 2.2 above.

Equations (38) and (39) are applicable to a flat rectangular plate and a cylindrical shell if the flow is directed along the x-axis, which for the shell is parallel to the center line.

When $\bar{\Delta}_x = 1.0$, coincidence between the elastic waves of the m-th mode of the beam and the turbulence wavelengths occurs when $\gamma_x = m\pi$. From Equation (37), the corresponding coincidence frequency is:

$$f_c = \frac{\omega_c}{2\pi} = \frac{m U_c}{2 L_x} = \text{coincidence frequency for m-th mode.} \tag{40}$$

Setting $\gamma_x = m\pi$ in Equation (39) gives the following expression for the joint acceptance, $j_m^2(\omega_c)$, at coincidence:

$$j_m^2(\omega_c) = \frac{1}{2}\left[\frac{(2m\pi)^2 - \delta_x^2}{[\delta_x^2 + (2m\pi)^2]^2} + \frac{2}{\delta_x^2 + (2m\pi)^2} - \frac{1}{\delta_x^2}\right]\left\{1 - e^{-\delta_x}\right\}$$

$$+ \frac{\delta_x/2}{\delta_x^2 + (2m\pi)^2} + \frac{1}{2\delta_x} \tag{41}$$

Aerodynamically slow modes, for which response levels are generally not large, are those modes for which $\gamma_x < m\pi$; while aerodynamically fast modes are defined by the condition $\gamma_x > m\pi$.

312

Progressive Wave Acoustic Excitation

The joint-acceptance for a correlated acoustic wave progressing along the beam at parallel incidence can be obtained from Equation (38) by setting $\delta_x = 0$. If the wave acts over the entire length of the beam, then $\Delta_x = 1.0$ and $\infty = m$, and in this case, Equation (39) reduces to the following well-known equation developed by Powell in Reference 8.

$$j_m^2(\omega) = \frac{2}{(m\pi)^2} \frac{1 - (-1)^m \cos \gamma_x}{\left[1 - (\gamma_x/m\pi)^2\right]^2} \tag{42}$$

It is possible to rewrite Equation (42) in the following alternate form:

$$j_m^2(\omega) = \frac{1}{\left[1 - (f/f_c)\right]^2} \left[\frac{\sin(m\pi\epsilon/2)}{(m\pi\epsilon/2)}\right]^2 \tag{43}$$

ϵ = deviation of excitation frequency, f, from coincidence frequency f_c

$$= \frac{\gamma_x}{m\pi} - 1 = \frac{f}{f_c} - 1 \tag{44}$$

$$f_c = \frac{m c_0}{2 L_x} = \text{coincidence frequency for m-th mode} \tag{45}$$

The fluctuating part of $j_m^2(\omega)$ is controlled by $\left[\sin(m\pi\epsilon/2)/(m\pi\epsilon/2)\right]^2$ and this factor is shown graphically in Figure 3.

Reverberant Acoustic Field

The space correlation function for a localized reverberant acoustic field on the beam is chosen as

$$C(z,\omega) = -\frac{\sin \gamma_x z}{\gamma_x z} \tag{46}$$

$$\gamma_x = \omega \Delta_x/c_0$$

Substituting Equation (46) into Equation (33) and performing the integration gives:

313

$$j_m^2 (\omega) = \frac{\cos (\gamma_x + m \pi) - 1}{2 \gamma_x (\gamma_x + m \pi)} + \frac{\cos (\gamma_x - m \pi) - 1}{2 \gamma_x (\gamma_x - m \pi)}$$

$$+ \frac{1}{2 \gamma_x} \left[1 - \frac{\cos 2 m \pi \overline{x}_0 \cdot \sin m \pi}{m \pi} \right] \cdot \left[Si \, (\gamma_x + m \pi) + Si \, (\gamma_x - m \pi) \right]$$

$$+ \frac{\cos 2 m \pi \, \overline{x}_0 \cdot \cos \, m \pi}{2 \, m \pi \, \gamma_x} \left[Cin \, (\gamma_x + m \pi) - Cin \left| \gamma_x - m \pi \right| \right] \tag{47}$$

where

$$Si \, (z) = \int_0^z \frac{\sin x}{x} \cdot dx$$

$$Cin \, (z) = \int_0^z \frac{1 - \cos x}{x} \cdot dx \tag{48}$$

Various methods for approximating the functions $Si \, (z)$ and $Cin \, (z)$ are discussed in Section 2.3. Equation (47) is applicable for both axes of a flat rectangular plate and for the axial direction along a cylindrical shell.

4.0 CIRCUMFERENTIAL JOINT ACCEPTANCES FOR CASES INVOLVING LOCALIZED EXCITATION

Consider a circular ring which has a distributed random pressure loading over the range $-\Delta y/2 \le y \le \Delta y/2$. Mode shapes of the ring modes that may respond to such an excitation are:

$$\phi_{n1} (y) = \sin (2 \pi n y / L_y)$$

$$\phi_{n2} (y) = \cos (2 \pi n y / L_y)$$

y = circumferential coordinates

L_y = circumferential length of ring

n = number of elastic full-waves around circumference.

Following the procedure in Reference (1), the joint acceptance $j_n^2 (\omega)$ for the n-th mode of the ring can be written in the form:

314

$$j_n^2 (\omega) = \frac{1}{L_y^2} \int_{y=-\Delta y/2}^{\Delta y/2} \int_{y'=-\Delta y/2}^{\Delta y/2} C(\eta;\omega) \cdot \left[\phi_{n2}(y) \cdot \phi_{n2}(y') + \phi_{n1}(y) \cdot \phi_{n1}(y') \right] \cdot dy \cdot dy'$$

$$= \frac{1}{L_y^2} \int_{y=-\Delta y/2}^{\Delta y/2} \int_{y'=\Delta y/2}^{\Delta y/2} C(\eta;\omega) \cdot \cos(2\pi n\eta/L_y) \cdot dy \cdot dy' \tag{49}$$

$\eta = y - y'$ = separation distance around ring

$C(\eta;\omega)$ = space correlation coefficient for homogeneous pressure field.

Equation (49) can be reduced to a single integral by using the same procedure as that described in Section 2.1. The resulting equation is:

$$j_n^2 (\omega) = \bar{\Delta}_y^2 \int_{z=0}^{1} (1-z) \cdot C(z;\omega) \cdot \cos 2n\pi z \cdot dz \tag{50}$$

$$\bar{\Delta}_y = \Delta y/L_y$$

$$n = n \cdot \bar{\Delta}_y$$

Joint acceptance expressions are developed below for correlation functions associated with boundary layer turbulence and a reverberant acoustic field.

Boundary Layer Turbulence

For a boundary layer convected along the axis of a cylindrical shell, the space correlation coefficient around the circumference of the ring is assumed to have the form:

$$C(x;\omega) = e^{-\delta_y |z|} \tag{51}$$

Substituting Equation (51) into Equation (50) and integrating gives:

$$\frac{j_n^2(\omega)}{\bar{\Delta}_y^2} = \frac{(2n\pi)^2 - \delta_y^2}{[\delta_y^2 + (2n\pi)^2]^2} \left[1 - e^{-\delta_y} \cos 2n\pi \right]$$

$$- \frac{4n\pi \delta_y}{[\delta_y^2 + (2n\pi)^2]^2} e^{-\delta_y} \sin 2n + \frac{\delta_y}{\delta_y^2 + (2n\pi)^2} \tag{52}$$

315

Reverberant Acoustic Field

For a reverberant acoustic field the space correlation coefficient aroung the ring is approximated as follows:

$$C(z;\omega) = \frac{\sin \gamma_y z}{\gamma_y z} \tag{53}$$

where

$$\gamma_y = \omega \Delta_y / c_0$$

Substituting Equation (53) into Equation (50) and integrating gives:

$$j_n^2(\omega) = \frac{\overline{\Delta}_y^2}{\gamma_y} \left[Si\{(\gamma_y + 2\pi n)\} + Si\{(\gamma_y - 2\pi n)\} \right]$$

$$+ \frac{\overline{\Delta}_y^2}{2(n\pi)^2} \frac{1 - \cos(4\pi n)\cos(\gamma_y) - (2\pi n/\gamma_y)\sin(4\pi n)\sin(\gamma_y)}{1 - (\gamma_y/2\pi n)^2} \quad , \quad n \neq 0$$

$$= \frac{2\overline{\Delta}_y^2}{\gamma_y} Si\{\gamma_y\} - \Delta_y^2 \frac{2[1 - \cos(\gamma_y)]}{\gamma_y^2} \quad , \quad n = 0 \tag{54}$$

5.0 STATISTICAL ENERGY ANALYSIS OF THE REVERBERANT RESPONSE OF CYLINDERS

A method which can be used to predict the response of structures to an external excitation is offered by the statistical energy analysis (References 3 and 9). This method is based on the fact that the time average power flow between two simple oscillators, linearly coupled and excited by a wide-band excitation, is proportional to the difference in their time—average total energy, the power flow being always from the oscillator of higher energy to that of lower energy. This principle can be expressed by the following equation.

$$\langle P_{12} \rangle = \Phi_{12} \left[\langle E_1 \rangle - \langle E_2 \rangle \right]$$

where

$\langle P_{12} \rangle$ = time average power flow from oscillator 1 to oscillator 2

$\langle E_1 \rangle$ = time average total energy of oscillator 1

$\langle E_2 \rangle$ = time average total energy of oscillator 2

Φ_{12} = coupling factor between the two oscillators. An expression for this factor can be found by using the admittance concept (Reference 9).

This principal can be extended to two vibrating systems, A and B, for which the time average power transferred from A to B can be written in the following form:

$$P_{AB} = \Phi_{AB} \cdot N_A \cdot N_B \left[\frac{E_A}{N_A} - \frac{E_B}{N_B} \right] \qquad (55)$$

where

Φ_{AB} = average mode-to-mode coupling factor between the two subsystems

E_A = average total energy of subsystem A

E_B = average total energy of subsystem B

N_A = number of modes in subsystem A

N_B = number of modes in subsystem B.

The above expression is valid when the subsystems satisfy one of the following conditions (which in most cases are approximately satisfied): (See Reference 9.)

a. The coupling factors between modes are all equal.

b. Modes within the same subsystems have the same time-average total energy.

c. The time-average total energy of a mode is independent of its coupling to any particular mode in the other subsystem.

When a multimodal system is excited in a band of frequencies, its modes can be divided into resonant and non-resonant modes within the band and each of these groups can be divided into groups of modes which satisfy one of the above mentioned conditions. Then, Equation (55) can be applied among the resonant groups. The energy transmission between non-resonant modes and between resonant and non-resonant modes cannot be

317

predicted by the statistical energy analysis and, usually, it is calculated by using classical vibrational analysis. Equation (55) can be written in the following fashion:

$$P_{AB} = \omega \, \eta_{AB} \, n_A \left[\frac{E_A}{n_A} - \frac{E_B}{n_B} \right]$$

where

ω = center frequency of the excitation band

η_{AB} $\equiv \Phi_{AB} \, N_B / \omega$ = coupling loss factor

n_A = average modal density of system A over a band of frequency Δ; it is defined as:

$$n_A = \frac{N_A \, (f + \Delta/2) - N_A \, (f - \Delta/2)}{\Delta}$$

$N_A(f)$ = average number of modes with resonance frequencies below f

n_B = average modal density of system B.

Now, a power balance equation can be written for each vibrating system. These equations will state that the summation of the power received from other systems, the power given to other systems and the power dissipated must be equal to zero in steady state conditions. For example, the power-balance equation for the n-th system of a series has the following form:

$$\omega \, \eta_{n,n+1} \, n_n \left[\frac{E_n}{n_n} - \frac{E_{n+1}}{n_{n+1}} \right] + \omega \, \eta_{n,n-1} \, n_n \left[\frac{E_n}{n_n} - \frac{E_{n-1}}{n_{n-1}} \right] + \omega \, \eta_n \, E_n + P_{n,n-1}^{NR} + P_{n,n+1}^{NR} = 0 \qquad (56)$$

where

$\omega \, \eta_n \, E_n$ = power dissipated

η_n = dissipating loss factor

$P_{n,n-1}^{NR}$ and $P_{n,n+1}^{NR}$ are the power transmitted through nonresonant modes.

If equations similar to Equation (56) are written for each vibrating system of the series, a set of linear equations is obtained. This set can be solved for the energy of the resonant modal group in terms of the coupling and dissipating loss factors, modal densities and power transmitted from non-resonant modal groups. Finally, the response of the vibrating systems can be predicted in the form of power spectral density. In fact, the PSDs of an acoustic field and of a structural system are given in term of the average energy by the following relations:

318

$$S_p(f) = \frac{\rho_0 c_0^2 E}{V \Delta} \tag{57}$$

$$S_a(f) = \frac{\omega^2 E}{M \Delta} \tag{58}$$

Equation (57) gives the sound pressure level spectral density $S_p(f)$ (which is a function of frequency, f) in terms of the average energy, E, within a band of frequency Δ, the density of the medium, ρ_0, the speed of sound, c_0, the volume, V, and the band of frequency, Δ. Equation (58) gives the acceleration spectral density of a structural system $S_a(f)$, in terms of the average energy, E, the mass, M, the band center frequency, ω, and the band of frequency, Δ.

In the case of a cylinder excited by a reverberant acoustic field, the following expression can be derived to predict the response:

$$\frac{S_{a2}}{S_{p1}} = \frac{\pi c_0}{A \rho_s \rho_0} \left[\frac{\eta_{2AF,1} \, \eta_{2AF}}{2\eta_{2AF,1} + \eta_{2AF}} + \frac{\eta_{2AS,1} \, \eta_{2AS}}{2\eta_{2AS,1} + \eta_{2AS}} \right] \left[1 + \frac{S_{p3}}{S_{p1}} \right] \left[\frac{1}{g^2} \right] \left(\frac{g^2}{psi^2} \right) \tag{59}$$

where

S_{a2} = acceleration spectral density

S_{p1} = sound pressure spectral density

$$\frac{S_{p1}}{S_{p3}} = \frac{\eta_{2AS,1} \, \eta_{2AS} + \eta_{1AF,1} \, \eta_{2AF} + \eta_3 \, \eta_3}{\dfrac{\eta_{2AS,1} \, \eta_{2AS}}{2\eta_{2AS,1} + \eta_{2AS}} + \dfrac{\eta_{2AF,1}^2 \, \eta_{2AF}}{2\, \eta_{2AF,1} + \eta_{2AF}}} - 1 \quad (= \text{noise reduction}) \tag{60}$$

c_0 = speed of sound in air

ρ_0 = mass density of air

A = surface area of cylinder

ρ_s = surface mass density of cylinder

g = gravity acceleration

n_{2AF} = modal density of the resonant acoustically fast (AF) modal group

319

n_{2AS} = modal density of the resonant acoustically slow (AS) modal group

n_3 = modal density of the resonance interior space modes

$\eta_{2AF,1}$ = coupling loss factor between the acoustic field and the resonant AF mode group

$\eta_{2AS,1}$ = coupling loss factor between the acoustic field and the resonant AF mode group

η_{2AF} = dissipating loss factor of the resonant AF modal group

η_{2AS} = dissipating loss factor of the resonant AS modal group

η_3 = dissipating loss factor of the interior space modal group

Values of the above factors and modal densities are given by the following expressions:

a) Modal Densities

An expression for the total modal density of a simply supported thin cylindrical shell is given by Bolotin's formula (Reference 3)

$$n_t(\nu) = \frac{\ell \sqrt{3}}{\pi h} \int_0^{\theta_m} \left[1 - \frac{\sin^4 \theta}{\nu^2} \right]^{-\frac{1}{2}} d\theta \tag{61}$$

where

$\nu = \dfrac{f}{f_r}$ = ratio of frequency f to the ring frequency f_r

$f_r = c_L / 2\pi a$

c_L = speed of sound in the material

a = radius of cylinder

h = thickness of shell wall

$$\theta_m = \begin{cases} \sin^{-1} \sqrt{\nu} & \text{if} \quad \nu < 1 \\ \pi/2 & \text{if} \quad \nu \geq 1 \end{cases}$$

The number of AF modes below the frequency ν (for ν ν_c), N_{2AF} is given by (Reference 3):

$$N_{2AF}^{(\nu)} = \frac{2\ell}{\pi a \beta} \int_0^{\theta_m} \left[\frac{\nu_c}{2} - \frac{\nu_c}{2} \left(1 - \frac{4 \sin^4 \theta}{\nu_c^2} \right)^{\frac{1}{2}} \right] d\theta \tag{62}$$

$$\beta = \frac{h}{a\sqrt{12}}$$

$$\nu_c = f_c/f_r$$

f_c = critical frequency ≡ frequency at which the free-bending wave speed in the panel is equal to the speed of sound. Therefore, the critical frequency is found from

$$c_b = \sqrt{\omega_c} \left[\frac{D}{\mu}\right]^{\frac{1}{4}} = c_0$$

or

$$f_c = \frac{c_0^2}{2\pi} \sqrt{\frac{\mu}{D}}$$

where

c_b = bending wave speed

D = flexural rigidity

μ = surface mass density

c_0 = speed of sound in air.

The modal density of the AF modal group can be obtained from Equation (62) as:

$$n_{2AF}^{(\nu)} = \frac{\partial N_{2AF}^{(\nu)}}{\partial \nu} \tag{63}$$

Now, it can be seen from Equations (62) and (63) that n_{2AF} for $1 < \nu < \nu_c$ is zero as shown in Figure 11 of Reference 3.

For frequencies above the critical frequency, all modes are acoustically fast and then

$$n_{2AF}^{(\nu)} = n_t^{(\nu)}$$

The modal density of the AS modal group is given by the difference between the total density and the AF modal density.

An approximate expression for the acoustic volume modal density is

321

$$n_3 = \frac{4\pi^2 f^2 a^2 \ell}{c_0^3}$$

b) Coupling Loss Factors

The coupling factor between the acoustic field and the acoustically fast modes is given by (Reference 3):

$$\eta_{2AF,1} = \frac{\rho_0 c_0}{2\pi f \rho_s}$$

The coupling factor for the AS group (for $f > f_r$ and when the cylinder dimensions are greater than an acoustic wavelength) is (Reference 3):

$$\eta_{2AS,1} = \frac{\rho_0 c_0^2}{2\pi f f_c \rho_s A} \left[2\lambda_0 \, g_1 (f/f_c)^2 + P_r \, g_2 (f/f_c) \right]$$

where

λ_0 = acoustic wavelength

P_r = radiating perimeter = $4\pi a$

$$g_1(f/f_c) = \begin{cases} (4/\pi^4)(1-2f/f_c)\Big/\sqrt{f/f_c \,(1-f/f_c)} & f < 0.5 f_c \\[2mm] 0 & f \geq 0.5 f_c \end{cases}$$
(Reference 10)

$$g_2(f/f_c) = \left\{ (1-f/f_c) \ln\left[(1+\sqrt{f/f_c})/(1-\sqrt{f/f_c})\right] + 2\sqrt{f/f_c} \right\}\Big/ 4\pi^2 (1-f/f_c)^{3/2}$$ (Reference 10)

When the cylinder dimensions are smaller than an acoustic wavelength and for $f \ f_r$, the following coupling factor is used:

$$\eta_{2AS,1} = \frac{\rho_0 c_0^2}{2\pi f f_c \rho_s A} \left(\frac{4}{\pi^4} P_r \sqrt{f/f_c} \right)$$

c) Dissipating Loss Factor

The structural loss factors are given by:

322

$$\eta_{2AF} = \eta_{2AS} = \frac{1}{Q}$$

where Q is the dynamic magnification factor of resonance.

The loss factor of the inside acoustic volume can be expressed in terms of the average absorption coefficient α as

$$\eta_3 = \frac{c_0 \alpha}{4 \pi f a}$$

REFERENCES:

1. White, R.W.,"Predicted Vibration Responses of Apollo Structure and Effects of Pressure Correlation Lengths on Response," Wyle Laboratories Research Staff Report, WR 67-4, March 1967 and Revised March 1968.

2. Bozich, D. and White, R.W., "A Study of the Vibration Responses of Shells and Plates to Fluctuating Pressure Environments," NASA CR-1515, March 1970.

3. Manning, J.E. et al., "Transmission of Sound and Vibration to a Shroud—Enclosed Spacecraft," BBN Report 1431, October 1966.

4. Smith, P.N. and Lyon, R.H., "Sound and Structural Vibration," NASA CR-160, March 1965.

5. Conticelli, V.C., "Study of Vibratory Response of a Payload Subjected to a High Frequency Acoustic Field," work performed under Contract No. NAS8-21260 for Marshall Space Flight Center, May 1969.

6. Wilby, J.F., "The Response of Simple Panels to Turbulent Boundary Layer Excitation," AFFDL-TR-67-70, October 1967.

7. Abromowitz, M., and I.A. Stegun, "Handbook of Mathematical Functions," U.S. Department of Commerce, National Bureau of Standards, Americal Mathematical Series 55, November 1964.

8. Powell, A., "On the Response of Structures to Random Pressures and to Jet Noise in Particular," Chapter 8 of Random Vibration (S.H. Crandall, Ed.), MIT Press, Cambridge, Massachusetts, 1958.

9. Ungar, E.E., "Fundamentals of Statistical Energy Analysis of Vibrating System," Technical Report 66-52, Air Force Flight Dynamics Laboratory, Wright-Patterson Air Force Base, Ohio, May 1966.

10. Maidanik, G., "Response of Ribbed Panels to Reverberant Acoustic Fields," J. Acoust. Soc. Am., No. 34, June 1962.

TABLE I

SUMMARY OF COEFFICIENTS FOR RATIONAL FRACTION
APPROXIMATIONS FOR SINE AND COSINE INTEGRALS

i	a_i	b_i	c_i	d_i
8	1.000000	1.000000	1.000000	1.000000
6	38.027264	40.021433	42.242855	48.196927
4	265.187033	322.624911	302.757865	482.485984
2	335.677320	570.236280	352.018498	1114.978885
0	38.102495	157.105423	21.821899	449.690326

TABLE II

LATERAL JOINT ACCEPTANCE VALUES, $j_n^2(\omega)$, FOR
VARIOUS SYMMETRIC DUCT CORRELATION PATTERNS

(from Reference 1)

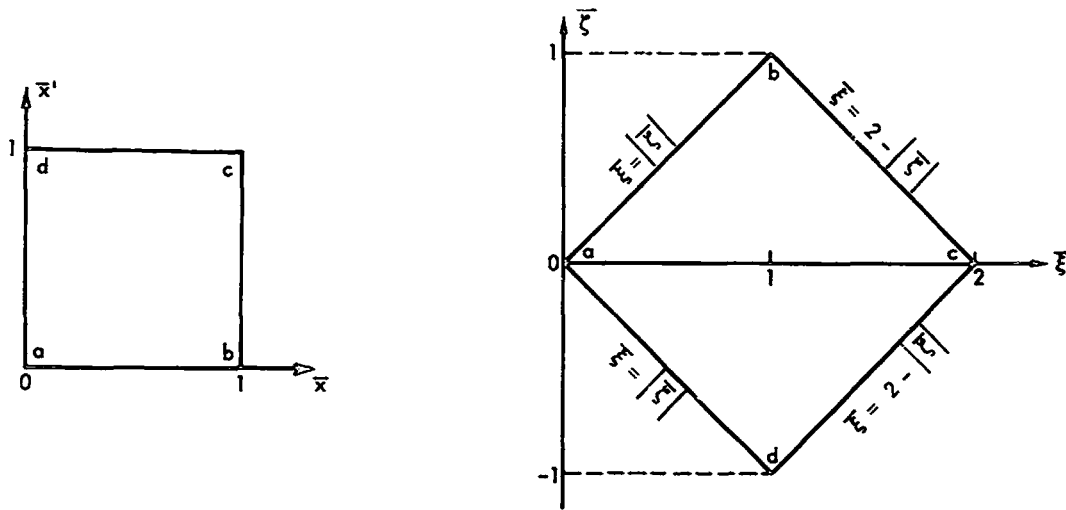| n \ N	1	2	4	8	16
0	1.000	0.5000	0.2500	0.1250	0.0625
2	0.000	0.0000	0.1012	0.1125	0.0598
3	0.000	0.0225	0.0750	0.0775	0.0563
4	0.000	0.0000	0.0000	0.0507	0.0510
5	0.000	0.0081	0.0081	0.0279	0.0451
6	0.000	0.0000	0.0114	0.0114	0.0388
7	0.000	0.0041	0.0042	0.0024	0.0319
8	0.000	0.0000	0.0000	0.0000	0.0255
9	0.000	0.0025	0.0025	0.0015	0.0194
10	0.000	0.0000	0.0041	0.0041	0.0140

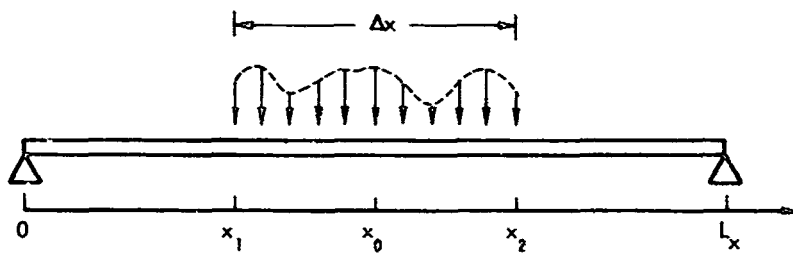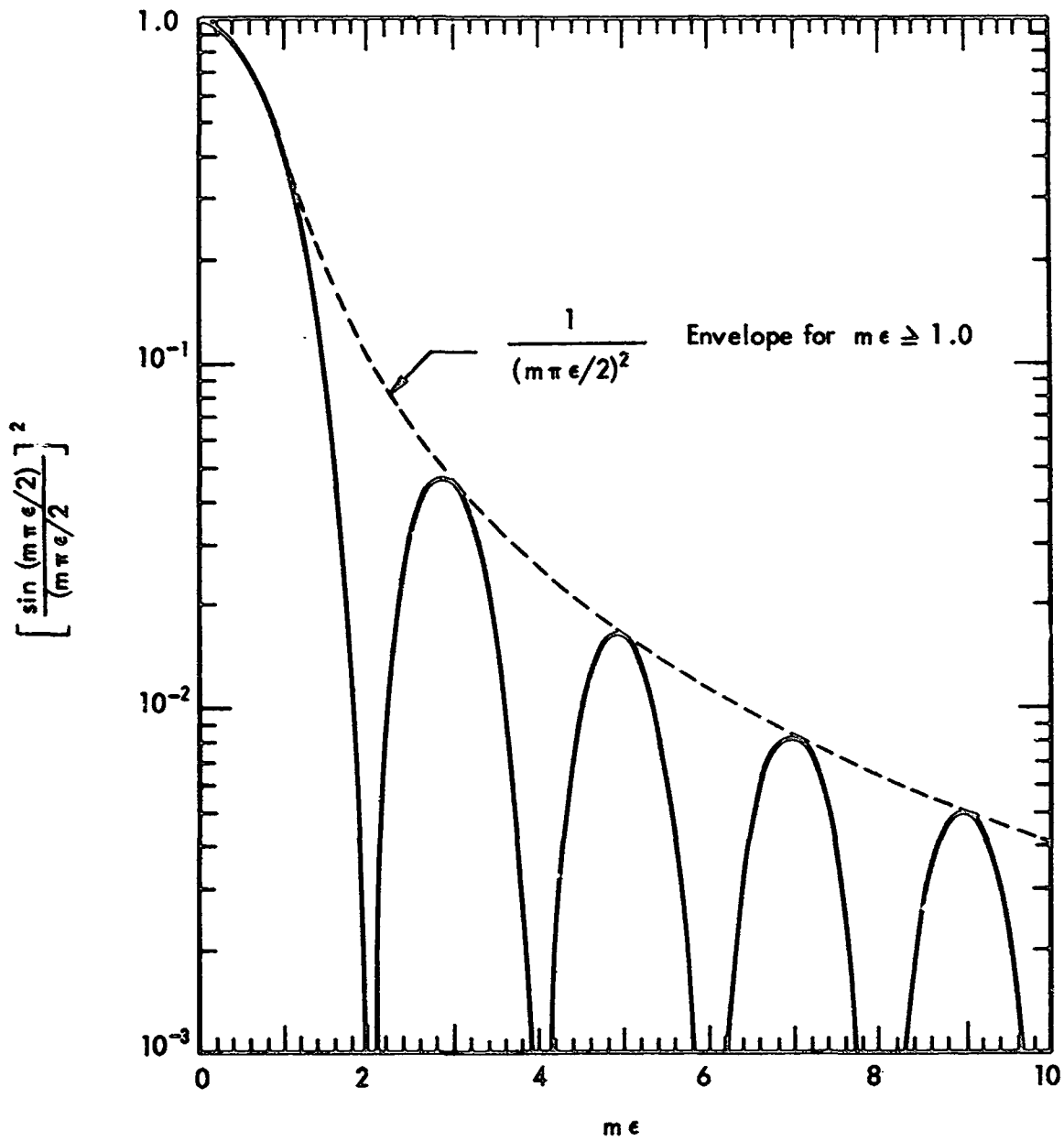Figure 1. Transformation of the Region of Integration for Joint Acceptances

Figure 2. Pinned-Pinned Beam with Localized Excitation

326

$$j_m^2(\omega) = \frac{1}{\left[1 + (f/f_c)\right]^2} \left[\frac{\sin(m\pi\epsilon/2)}{m\pi\epsilon/2}\right]^2, \quad \epsilon = (f/f_c) - 1$$

$f_c = m\,c_0/2L_x$ = wave length coincidence frequency for m-th mode.

Figure 3. Joint Acceptance, $j_m^2(\omega)$, for Progressive Acoustic Wave of Frequency f on Pinned-Pinned Beam of Length L (from Reference 2)

327